VOLUME 79 MARCH 27, 1975 NUMBER 7

JPCHAx

THE JOURNAL OF PHYSICAL CHEMISTRY

PUBLISHED BIWEEKLY BY THE AMERICAN CHEMICAL SOCIETY

THE JOURNAL OF

PHYSICAL CHEMISTRY

AMERICAN CHEMICAL SOCIETY, *1155 Sixteenth St., N.W., Washington, D.C. 20036*

Books and Journals Division

JOHN K CRUM *Director*
VIRGINIA E. STEWART *Assistant to the Director*

CHARLES R. BERTSCH *Head, Editorial Processing Department*
D. H. MICHAEL BOWEN *Head, Journals Department*
BACIL GUILEY *Head, Graphics and Production Department*
SELDON W. TERRANT *Head, Research and Development Department*

All manuscripts should be sent to *The Journal of Physical Chemistry*, Department of Chemistry, University of Minnesota, Minneapolis, Minn. 55455.

Additions and Corrections are published once yearly in the final issue. See Volume 78, Number 26 for the proper form.

Extensive or unusual alterations in an article after it has been set in type are made at the author's expense, and it is understood that by requesting such alterations the author agrees to defray the cost thereof.

The American Chemical Society and the Editor of *The Journal of Physical Chemistry* assume no responsibility for the statements and opinions advanced by contributors.

Correspondence regarding accepted copy, proofs, and reprints should be directed to Editorial Processing Department, American Chemical Society, 20th and Northampton Sts., Easton, Pa. 18042. Department Head: CHARLES R. BERTSCH. Associate Department Head: MARIANNE C. BROGAN. Assistant Editor: CELIA B. MCFARLAND. Editorial Assistant: JOSEPH E. YURVATI.

Advertising Office: Centcom, Ltd., 50 W. State St., Westport, Conn. 06880.

Business and Subscription Information

Send all new and renewal subscriptions *with payment* to: Office of the Controller, 1155 16th Street, N.W., Washington, D.C. 20036. Subscriptions should be renewed promptly to avoid a break in your series. All correspondence and telephone calls regarding changes of address, claims for missing issues, subscription service, the status of records, and accounts should be directed to Manager, Membership and Subscription Services, American Chemical Society, P.O. Box 3337, Columbus, Ohio 43210. Telephone (614) 421-7230. For microfiche service, contact ACS Journals Department, 1155 16th St. N.W., Washington, D.C. 20036. Telephone (202) 872-4444.

On changes of address, include both old and new addresses with ZIP code numbers, accompanied by mailing label from a recent issue. Allow four weeks for change to become effective.

Claims for missing numbers will not be allowed (1) if loss was due to failure of notice of change in address to be received before the date specified, (2) if received more than sixty days from date of issue plus time normally required for postal delivery of journal and claim, or (3) if the reason for the claim is "issue missing from files."

Subscription rates (hard copy or microfiche) in 1975: $20.00 for 1 year to ACS members; $80.00 to nonmembers. Extra postage $4.50 in Canada and PUAS, $5.00 other foreign. Supplementary material (on microfiche only) available on subscription basis, 1975 rates: $15.00 in U.S., $19.00 in Canada and PUAS, $20.00 elsewhere. All microfiche airmailed to non-U.S. addresses; air freight rates for hard-copy subscriptions available on request.

Single copies for current year: $4.00. Rates for back issues from Volume 56 to date are available from the Special Issues Sales Department, 1155 Sixteenth St., N.W., Washington, D.C. 20036.

Subscriptions to this and the other ACS periodical publications are available on microfilm. For information on microfilm write Special Issues Sales Department at the address above.

Notice to Authors last printed in the issue of January 16, 1975

THE JOURNAL OF
PHYSICAL CHEMISTRY

Volume 79, Number 7 March 27, 1975

JPCHA 79(7) 671–764 (1975)

ISSN 0022-3654

COMMUNICATIONS TO THE EDITOR

There is no supplementary material for this issue

* In papers with more than one author, the asterisk indicates the name of the author to whom inquiries about the paper should be addressed.

AUTHOR INDEX

THE JOURNAL OF
PHYSICAL CHEMISTRY

Registered in U. S. Patent Office © Copyright, 1975, by the American Chemical Society

VOLUME 79, NUMBER 7 MARCH 27, 1975

Ion–Molecule Reactions in Amines. Photoionization of Propyl-, Ethyl-, Diethyl-, and Triethylamine[1a]

J. M. Brupbacher,[1b] C. J. Eagle,[1c] and E. Tschuikow-Roux*

Department of Chemistry, The University of Calgary, Calgary, Alberta, Canada T2N 1N4 *(Received August 6, 1974)*

Photoinduced ion–molecule reactions of primary ions occurring in the ethylamines and propylamine have been investigated in the pressure range 1–20 mTorr using a Kr resonance lamp (10.03 and 10.6 eV) as the excitation source. Thermal rate constants (T = 298°K) have been determined for the reactions $R_{3-n}{}^+NH_n + R_{3-n}NH_n \rightarrow R_{3-n}{}^+NH_{n+1} + R_{3-n}NH_n(-H)$ (k_1) and $R_{2-n}(CH_2)^+NH_n + R_{3-n}NH_n \rightarrow R_{2-n}(CH_2)NH_n(-H) + R_{3-n}{}^+NH_{n+1}$ (k_2) where n = 0, 1, and 2 for R = C_2H_5 and n = 2 for R = C_3H_7. For the ethylamines the values for k_1 were found to be 18.3, 12.5, and 7.05 × 10^{-10} cm^3 sec^{-1} and for k_2, 19.7, 13.6, and 1.28 × 10^{-10} cm^3 sec^{-1} for n = 2, 1, and 0, respectively. For propylamine the corresponding values for k_1 and k_2 are 15.6 and 22.4 × 10^{-10} cm^3 sec^{-1}. The values of k_1 are slightly less than those previously reported for the methylamines and are shown to be consistent with the predictions for an ion–induced dipole model for ion–molecule reactions which assumes a collision complex in which the polar molecule is aligned with the ion and takes into account intrinsic differences in the N–H and C–H hydrogen-transfer rates. The observed change in k_2 with increasing ethyl substitution is explained on the basis of the structure of the primary ion, $R_{2-n}(CH_2)^+NH_n$.

Introduction

Previous studies of ion–molecule reaction rates occurring in simple amine systems have been largely restricted to the methylamine series. Thermal rate coefficients for the reactions

$$(CH_3)_{3-n}\overset{+}{N}H_n + (CH_3)_{3-n}NH_n \longrightarrow (CH_3)_{3-n}\overset{+}{N}H_{n+1} + (CH_3)_{3-n}NH_n(-H) \qquad n = 0,\ 1,\ 2 \qquad (1)$$

have been determined at several excitation energies.[2–5] These rate constants were noted to be only weakly dependent on the excitation energy and were observed to decrease with increasing methyl substitution. Theoretically predicted rate constants based on ion-induced dipole[6] and ion–dipole models[7] were found to be in poor agreement with experimental values.

In the case of the ethylamines, the ion–molecule reactions have been investigated at excitation energies from 8.5 to 12.5 eV.[8] The reactions observed in ethylamine include the parent ion–parent neutral interaction

$$C_2H_5\overset{+}{N}H_2 + C_2H_5NH_2 \xrightarrow{k_1} C_2H_5\overset{+}{N}H_3 + C_2H_5NH\cdot \qquad (2)$$

and the reactions of the fragment ions

$$CH_2\overset{+}{N}H_2 + C_2H_5NH_2 \xrightarrow{k_2} C_2H_5\overset{+}{N}H_3 + CH_2NH\cdot \qquad (3)$$

$$CH_3CH\overset{+}{N}H_2 + C_2H_5NH_2 \xrightarrow{k_3} C_2H_5\overset{+}{N}H_3 + CH_3CHNH\cdot \qquad (4)$$

Analogous reactions were observed in the cases of diethyl- and triethylamine. At relatively low excitation energies (10 eV) only reactions 2 and 3 occur; however, the rates of these reactions were not determined. Similar processes were observed in the photoionization of n-propyl- and n-butylamine.

Although the analogous reaction to (1) for ammonia has been shown to proceed mainly via proton transfer from the parent ion to the neutral molecule rather than by hydrogen atom transfer to the ion,[9] a recent study by Isakov and Potapov[8] on $(C_2H_5)_3N$-CH_3OD mixtures at ionizing energies below the appearance potential of CH_3OD has clearly demonstrated the hydrogen atom acceptor character of $(C_2H_5)_3{}^+N$ ions. This suggests that the unit mass transfer reactions occurring in higher order alkylamines may proceed to a significant extent via a hydrogen atom transfer pathway.

In order to gain a better understanding of the reaction processes in simple amine systems, the ethylamines and n-

propylamine have been reexamined with the aim to determine the rate constants for the elementary reactions in these systems.

Experimental Section

All experiments were carried out using a high-pressure (10^{-3} to 0.3 Torr) photoionization mass spectrometer similar in design to that reported by Sieck, *et al.*[10,11] The apparatus consisted of three major parts: (a) a vacuum chamber which houses the reaction cell, ion detection equipment, and a photoionization source (Figure 1); (b) an electronic module; and (c) a gas handling system, including pressure control and monitoring devices.

The reaction cell was constructed from stainless steel having a cylindrical inner chamber 15 mm long and 8 mm in diameter. Both ends of the cell were sealed via O rings with LiF windows which could be readily exchanged. The exit pinhole (diameter = 0.25 mm), mounted so as to be also easily interchanged, was located in a segment of stainless steel foil of 0.15 mm thickness situated across from the gas inlet to the cell.

The ion detection system consisted of a quadrupole mass spectrometer electronic module (Finnigan Model 3000) with a separate quadrupole assembly and an ion source which had been modified to permit electrical coupling to the reaction cell. When ions and neutral molecules emerged from the field free region of the reaction cell through the pinhole, a small voltage gradient focused the ions into the quadrupole field. The steep change in pressure brought about by the expansion of the reaction mixture into the housing assured that the ion–molecule reactions occurring outside of the cell were negligible. The reaction cell was maintained at +5 V while the three focusing plates were kept at 0, −70, and 0 V.

Relative ion concentrations were recorded as a function of cell pressure on a uv oscillograph which allowed the simultaneous recording of spectra at three preamplifier gains, each differing by a factor of 10. The spectra were recorded at a slow rate (1.6 amu/sec) to permit time averaging of each relative ion concentration. Pressure fluctuations in the cell during the recording process were found to be less than 0.05 mTorr.

The vacuum chamber was evacuated using a 6-in. oil diffusion pump coupled to a freon-cooled baffle. A separate gas handling system was used to evacuate the reaction cell. Ultimate pressure in the vacuum chamber was typically 1×10^{-7} Torr as measured on a discharge vacuum gauge. Vacuum in the chamber could be maintained below 5×10^{-6} Torr with 100 mTorr in the reaction cell. Pressure measurements in the reaction cell were made to the nearest 0.1 mTorr using a capacitance manometer (MKS Type 170M electronic unit and Type 310 AH-10 pressure head). Pressure in the reaction cell could be adjusted and also maintained at a constant level by use of a variable leak (Granville-Phillips Series 203) located in the transfer line between the gas handling system and the reaction cell.

Photoionization of the ethylamines was achieved using a Kr resonance lamp (10.03 and 10.6 eV) as the light source. The energy of the 10.03-eV line, which accounts for about 90% of the total lamp intensity, was 28.8, 27.0, 46.6, and 58.3 kcal mol^{-1} in excess of the ionization potential for propyl-, ethyl-, diethyl-, and triethylamine, respectively. The quartz tube extension on the lamp was fitted with an aluminum covering to shield the quadrupole rods and electron multiplier from spurious microwave and uv radiation, as well as to eliminate the possibility of photoionization occurring outside of the cell.

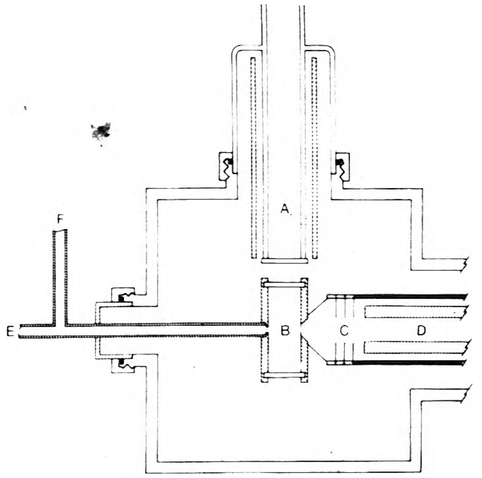

Figure 1. Schematic diagram of the photoionization mass spectrometer: (A) krypton resonance lamp, (B) reaction cell, (C) ion focusing plates, (D) quadrupole assembly, (E) to variable leak, (F) to capacitance manometer.

The ethylamines used were reagent grade and were injected into the gas handling system shortly before use, outgassed, and multiply distilled in vacuo. Mass spectral analysis of the purified compounds showed no impurities.

Determination of Rate Constants. For single component systems the rate coefficient for the loss of a specific primary ion, P_i^+, by two-body reaction is given in terms of the fractional ion current, f_i, by (Appendix A)

$$\ln f_i = -(k_i \tau / RT) P \qquad (5)$$

where P is the total pressure and T is the absolute temperature. The reaction time, τ, can be associated with the mean residence time of the primary ions in the reaction cell. At low pressures, in the molecular flow region, τ is not a function of pressure. Consequently, in the molecular flow region, the rate coefficient, k_i, can be determined from the slopes of plots of $\ln f_i$ *vs.* P. Parenthetically it may be noted, however, that with increasing pressure the nature of the flow through the pinhole changes and τ is expected to become pressure dependent. Any change in τ with pressure would manifest itself as curvature in these plots.

From the above discussion, it is clear that in order to calculate absolute rate constants from plots of fractional ion current *vs.* pressure it is necessary to know the residence time of the particular primary ion. However, experimental determination of residence times is imprecise. For this reason, rate constants were determined relative to a standard reaction by the procedure outlined below.

From plots of $\ln f_i$ *vs.* P, eq 5, slopes can be obtained for the standard and unknown reactions. These slopes, denoted by b_0 and b_i, respectively, satisfy the relationship $b = -k\tau/RT$. Combination of these expressions for the slopes gives the ratio

$$b_i/b_0 = (k_i/k_0)(\tau_i/\tau_0) \qquad (6)$$

Assuming that the residence time of a primary ion is inversely proportional to the ion velocity[13] given by $\bar{c} = [(8kT)/(\pi m)]^{1/2}$, one obtains

$$k_i = (b_i/b_0)(m_0/m_i)^{1/2} k_0 \qquad (7)$$

The reaction, $NH_3^+ + NH_3 \rightarrow NH_4^+ + NH_2$, has been extensively studied by various techniques[9,12-17] and was consequently chosen as the standard for this investigation.

The rate constant for this process was taken as $k_{\mathrm{NH_3}} = 2.1 \times 10^{-9}$ cm^3 sec^{-1} which is the value reported by Sieck, et al.,[17] for ammonium ions produced by photon impact at 10.6 eV. After photoionization of $\mathrm{NH_3}$ at 116.5 nm in the pressure range 1–15 mTorr, a plot of $\log[I_{\mathrm{NH_3}^+}/(I_{\mathrm{NH_3}^+} + I_{\mathrm{NH_4}^+})]$ *vs.* P was made and the slope, b_0, was determined. This slope was used in conjunction with eq 7 to determine the rate constants for the amine reactions. The value of $\tau_{\mathrm{NH_3}^+}$ calculated from eq 5 was 1.9 μsec.

Using the above procedure, rate constants of 15.3 and 10.2 × 10^{-10} cm^3 sec^{-1} were obtained for the hydrogen transfer reactions in dimethyl- and trimethylamine, respectively. Although the exact calibration procedure used by the previous investigators[5] was not stated for these systems, a value of 1.4 × 10^{-9} cm^3 sec^{-1} was reported earlier by these authors for the ammonia reaction.[11] Multiplication of their rate constants for dimethyl- and trimethylamine by the factor $2.1 \times 10^{-9}/1.4 \times 10^{-9} = 1.5$, yields values of 15.3 and 8.3 × 10^{-10} cm^3 sec^{-1}, respectively. These results are in good agreement with the results reported in the present work.

In the pressure range 1–20 mTorr, the mass spectra of the ethylamines show only three major ions. These ions are the primary parent ion of mass m, a cracking ion of mass $m - 15$ corresponding to the loss of a methyl group from the parent molecule, and a secondary ion of mass $m + 1$ formed by two-body reaction.

Two processes have been proposed for the formation of this $m + 1$ ion[8]

$$\mathrm{R_{3-\mathit{n}}\overset{+}{N}H_{\mathit{n}} + R_{3-\mathit{n}}NH_{\mathit{n}} \xrightarrow{k_1} R_{3-\mathit{n}}\overset{+}{N}H_{\mathit{n}+1} + R_{3-\mathit{n}}NH_{\mathit{n}}(-H)} \qquad (8)$$

$$\mathrm{R_{2-\mathit{n}}(CH_2)\overset{+}{N}H_{\mathit{n}} + R_{3-\mathit{n}}NH_{\mathit{n}} \xrightarrow{k_2} R_{2-\mathit{n}}(CH_2)NH_{\mathit{n}}(-H) + R_{3-\mathit{n}}\overset{+}{N}H_{\mathit{n}+1}} \qquad (9)$$

where R represents the $\mathrm{C_2H_5}$ group and $n = 0$, 1, or 2 for triethyl-, diethyl-, and ethylamine, respectively.

Since the process

$$\mathrm{C_2H_4\overset{+}{N}H_2 + C_2H_5NH_2 \longrightarrow C_2H_5\overset{+}{N}H_3 + C_2H_4NH} \qquad (10)$$

is known to occur only at excitation energies above 11.5 eV[8] this reaction need not be considered in the present study. Further, in the cases of diethyl and triethylamine, the $m - 1$ ion is observed to be present in exceedingly low concentration, indicating that the analogous processes to reaction 10 are unimportant in these systems.

In order to calculate the rate constants for reactions 8 and 9, it is necessary to separate the $m + 1$ ion intensity into contributions from the two processes. This can be done by consideration of the charge balance in reactions 8 and 9.

$$[\mathrm{R_{3-\mathit{n}}\overset{+}{N}H_{\mathit{n}}}]_0 = [\mathrm{R_{3-\mathit{n}}\overset{+}{N}H_{\mathit{n}}}]_p + [\mathrm{R_{3-\mathit{n}}\overset{+}{N}H_{\mathit{n}+1}}]_p - [\mathrm{R_{3-\mathit{n}}\overset{+}{N}H_{\mathit{n}+1}}]_b \qquad (11)$$

$$[\mathrm{R_{2-\mathit{n}}(CH_2)\overset{+}{N}H_{\mathit{n}}}]_0 = [\mathrm{R_{2-\mathit{n}}(CH_2)\overset{+}{N}H_{\mathit{n}}}]_p + [\mathrm{R_{3-\mathit{n}}\overset{+}{N}H_{\mathit{n}+1}}]_b \qquad (12)$$

where $[\mathrm{R_{3-\mathit{n}}{}^+NH_{\mathit{n}}}]_0$ and $[\mathrm{R_{2-\mathit{n}}(CH_2)^+NH_{\mathit{n}}}]_0$ represent the concentrations of the m and $m - 15$ ions prior to bimolecular reaction; $[\mathrm{R_{3-\mathit{n}}{}^+NH_{\mathit{n}}}]_p$, $[\mathrm{R_{3-\mathit{n}}{}^+NH_{\mathit{n}+1}}]_p$, and $[\mathrm{R_{2-\mathit{n}}(CH_2)^+NH_{\mathit{n}}}]_p$ are the observed concentrations of these ions at a given pressure, and $[\mathrm{R_{3-\mathit{n}}{}^+NH_{\mathit{n}+1}}]_b$ is the concentration of the $m + 1$ ion formed by reaction 9.

Combination of these expressions gives the ratio, β, of the two primary ion intensities observed in the absence of bimolecular reaction.

$$\beta = \frac{[\mathrm{R_{2-\mathit{n}}(CH_2)\overset{+}{N}H_{\mathit{n}}}]_0}{[\mathrm{R_{3-\mathit{n}}\overset{+}{N}H_{\mathit{n}}}]_0} \qquad (13a)$$

$$= \frac{[\mathrm{R_{2-\mathit{n}}(CH_2)\overset{+}{N}H_{\mathit{n}}}]_p + [\mathrm{R_{3-\mathit{n}}\overset{+}{N}H_{\mathit{n}+1}}]_b}{[\mathrm{R_{3-\mathit{n}}\overset{+}{N}H_{\mathit{n}}}]_p + [\mathrm{R_{3-\mathit{n}}\overset{+}{N}H_{\mathit{n}+1}}]_p - [\mathrm{R_{3-\mathit{n}}\overset{+}{N}H_{\mathit{n}+1}}]_b} \qquad (13b)$$

In terms of the observed ion intensities, eq 13b may be rewritten as

$$I_b = \frac{\beta(I_m + I_{m+1}) - I_{m-15}}{(\beta + 1)} \qquad (14)$$

where I_b is the intensity of $m + 1$ ion arising from reaction 9. The resulting expressions for the fractional ion currents of the two primary ions at any pressure are $f_{m-15} = I_{m-15}/(I_{m-15} + I_m)$ and $f_m = I_m/(I_m + I_{m+1} - I_b)$.

For a particular amine the value of β can be determined by plotting the ratio $I_{m-15}/(I_m + I_{m+1})$ *vs.* pressure, and extrapolating the resulting curve to zero pressure. The intercept, $I_{m-15}{}^0/I_m{}^0$, which is the ratio of the primary ion intensities in the absence of bimolecular reactions, corresponds to β. Once β is known the fractional currents of the primary ions at any pressure can readily be calculated.

Results and Discussion

Plots of ln f_i *vs.* P for both primary and secondary ions are shown in Figures 2–4 for ethyl-, diethyl-, and triethylamine, respectively. The plot for n-propylamine was essentially identical with that of ethylamine and is omitted. The values of the thermal rate constants for the loss of the primary ions, k_1 and k_2, are listed in Table I. Also included are the previously reported values (revised) for the analogous methylamines.[5] Listed in Table II are the predicted values for these reactions based on ion-induced dipole ($k_{i\alpha}$) and ion–dipole ($k_{i\mu}$) interactions and their combination which correspond to the "locked-in" dipole theory,[7,12] and the average-dipole-orientation (ADO) theory.[18–20]

The observed values of k_1 agree with the general trend established for the methylamines, i.e., k_1 decreases with increasing alkyl substitution. The value of k_1 for ethylamine coincides with that for methylamine and both values are close to the predictions of the ADO theory. However, the values of k_1 for the two tertiary amines are significantly lower than the expected values based upon this theory.

The values of the rate constants for the proton transfer reaction, k_2, decrease with increasing ethyl substitution as was also observed in the case of k_1 (Table I) and are close to $k_{2,\mathrm{ADO}}$ for ethyl- and diethylamine. However, the rate constant for triethylamine is very low compared to $k_{2,\mathrm{ADO}}$. This observation is consistent with the results obtained for k_2 for the analogous trimethylamine case.[5] This discrepancy cannot be accounted for simply on the basis of the ion acidity since the decreased acidity of the ion with increasing ethyl substitution is approximately matched by increased basicity of the substrate molecule. The low value of k_2 can, however, be interpreted on the basis of the structure of the primary ion, $(\mathrm{C_2H_5})_{2-n}(\mathrm{CH_2})^+\mathrm{NH}_n$. McLafferty[21] has indicated that for primary amines the observed $m - 15$ ion arises through the sequence

$$\mathrm{R{:}CH_2{:}\ddot{N}H_2 \xrightarrow[-e]{h\nu} R{:}CH_2{:}\overset{+\cdot}{N}H_2 \longrightarrow R\cdot CH_2{=}\overset{+}{N}H_2}$$

$$\mathrm{R\cdot CH_2{=}\overset{+}{N}H_2 \longrightarrow R\cdot + CH_2{=}\overset{+}{N}H_2}$$

$$\underset{\mathrm{I}}{\mathrm{CH_2{=}\overset{+}{N}H_2}} \longleftrightarrow \underset{\mathrm{II}}{\mathrm{\overset{+}{C}H_2{-}NH_2}}$$

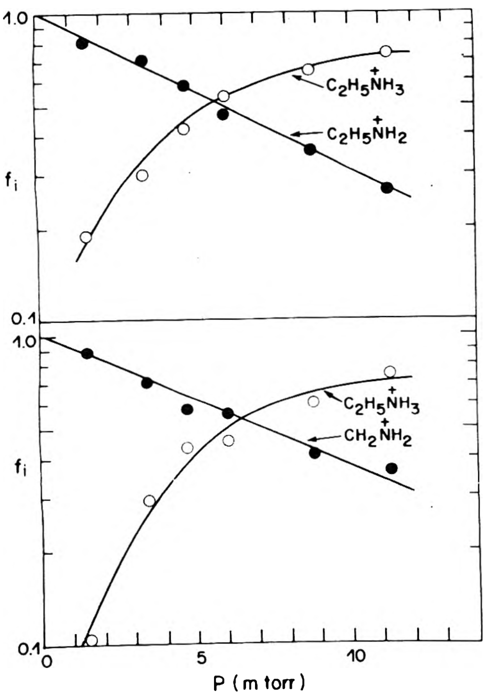

Figure 2. Plots of log f_i *vs.* pressure for ethylamine: upper plot corresponds to hydrogen transfer reaction, $C_2H_5{}^+NH_2 + C_2H_5NH_2 \rightarrow C_2H_5{}^+NH_3 + C_2H_5NH_2(-H)$; lower plot corresponds to proton transfer reaction, $CH_2{}^+NH_2 + C_2H_5NH_2 \rightarrow CH_2NH + C_2H_5{}^+NH_3$. The values of f_i are the average of three experimental determinations at each pressure.

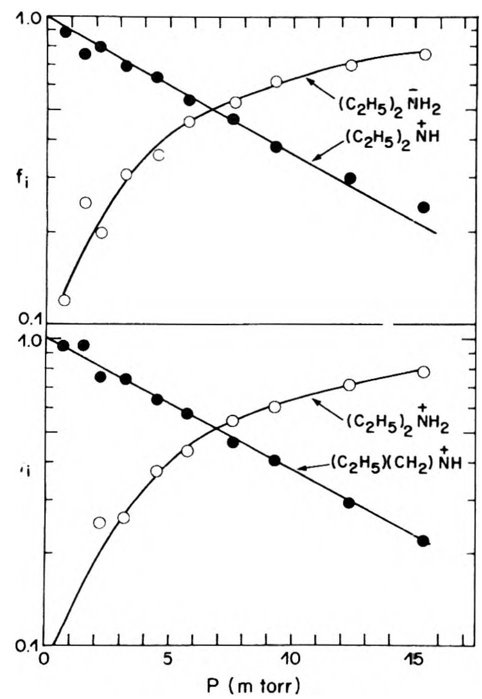

Figure 3. Plots of log f_i *vs.* pressure for diethylamine: upper plot corresponds to hydrogen transfer reaction, $(C_2H_5)_2{}^+NH + (C_2H_5)_2NH \rightarrow (C_2H_5)_2{}^+NH_2 + (C_2H_5)_2NH(-H)$; lower plot corresponds to proton transfer reaction, $(C_2H_5)(CH_2)^+NH + (C_2H_5)_2NH \rightarrow (C_2H_5)(CH_2)N + (C_2H_5)_2{}^+NH_2$. The values of f_i are the average of three experimental determinations at each pressure.

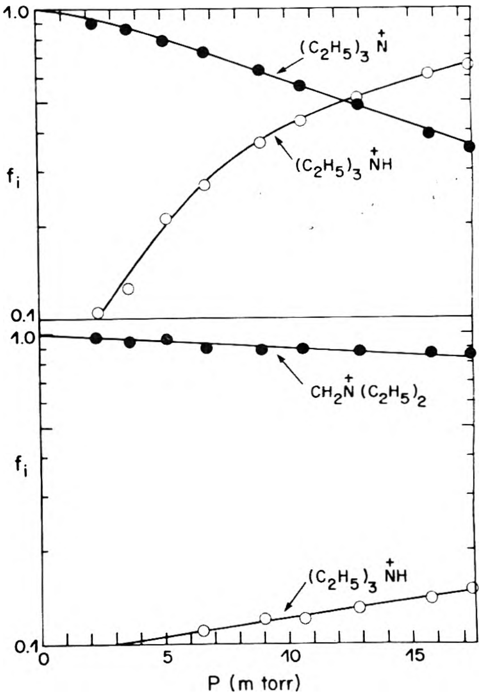

Figure 4. Plots of log f_i *vs.* pressure for triethylamine: upper plot corresponds to hydrogen transfer reaction, $(C_2H_5)_3{}^+N + (C_2H_5)_3N \rightarrow (C_2H_5)_3{}^+NH + (C_2H_5)_3N(-H)$; lower plot corresponds to proton transfer reaction, $(CH_2)^+N(C_2H_5)_2 + (C_2H_5)_3N \rightarrow (CH_2)N(C_2H_5)(C_2H_4) + (C_2H_5)_3{}^+NH$. The values of f_i are the average of three experimental determinations at each pressure.

TABLE I: Rate Constants[a,b] for Alkylamines

$R_{3-n}NH_n$	k_1	Ref	k_2	Ref
CH_3NH_2	18.3	*c*		*d*
$(CH_3)_2NH$	15.3	*c*		*d*
	15.3	*e*		
$(CH_3)_3N$	8.3	*c*	*f*	*c*
	10.2	*e*		
$C_2H_5NH_2$	18.3	*e*	19.7	*e*
$(C_2H_5)_2NH$	12.5	*e*	13.6	*e*
$(C_2H_5)_3N$	7.05	*e*	1.28	*e*
$C_3H_7NH_2$	15.6	*e*	22.4	*e*

[a] Estimated reproducibility in k_1 is 5%; however, the values of k_2 are only reproducible to about 10% due to lower intensities of the cracking ion. [b] Units of k_1 and k_2 are 10^{-10} cm^3 sec^{-1}. [c] Values of k_1 taken from ref 5 and adjusted by multiplying by the factor 1.5 (see text). [d] For methyl- and dimethylamine cracking of the primary ion does not occur at 10.0-eV excitation energy. [e] This work. [f] No reaction was found between $(CH_3)_2{}^+NCH_2$ and $(CH_3)_3N$, although resonance hydride (H^-) transfer would not have been detected.

By analogy, the general structure for this ion in ethylamines would be

III IV

R = H, C_2H_5

where the alkyl stabilized iminium ion III more accurately describes the bulk of these ions since nitrogen is significantly more electronegative than carbon and structure IV is an unstabilized primary carbonium ion. For triethylamine, $R_1 = R_2 = C_2H_5$, the positively charged nitrogen has no transferable proton. Hence, the slow but observable rate of proton transfer must occur through the small contribution of the carbonium ion IV to the primary ion structure

TABLE II: Theoretical Thermal Rate Constants[a,b] for Amines and Comparison

$R_{3-n}NH_n$	$k_{i\alpha}$[c]	$k_{i\mu}$[d]	$k_{i\alpha}$ + $k_{i\mu}$[e]	c[f]	$k_{i,ADO}$[g]	$k_{i,obsd}$	$k_{1,\alpha}$
			(i = 1)				
NH_3	12.0	46.6	58.6	0.215	22.0	21.3	21.3
CH_3NH_2	13.0	34.0	47.0	0.180	19.1	18.3	17.6
$(CH_3)_2NH$	12.5	22.0	34.5	0.139	15.5	15.3	14.0
$(CH_3)_3N$	12.0	11.0	33.0	0.066	12.8	10.2	10.2
$C_2H_5NH_2$	12.1	23.8	45.9	0.156	15.8	18.3	16.5
$(C_2H_5)_2NH$	12.1	14.1	26.2	0.100	13.5	12.5	11.7
$(C_2H_5)_3N$	12.0	8.6	20.6	0.048	12.4	7.05	6.90
$C_3H_7NH_2$	11.8	19.9	31.7	0.140	14.6	15.6	16.5
			(i = 2)				
$C_2H_5NH_2$	13.6	26.6	40.2	0.156	17.7	19.7[h]	
$(C_2H_5)_2NH$	12.9	10.0	22.9	0.100	13.9	13.6	
$(C_2H_5)_3N$	12.6	8.9	21.5	0.058	13.1	1.28	
$C_3H_7NH_2$	14.9	24.3	39.2	0.140	18.3	22.4[h]	

[a] Values of $k_{i,\alpha}$ and $k_{i,\mu}$ were calculated using bond polarizabilities and dipole moments tabulated in ref 23 and 24, respectively. [b] Units of k are 10^{-10} cm^3 sec^{-1}. [c] Ion-induced dipole contribution. [d] Ion-dipole contribution. [e] "Locked-in" dipole theory. [f] The values of c have been calculated using data provided in ref 20. [g] Average-dipole-orientation (ADO) theory, $k_{i,ADO} = k_{i,\alpha} + ck_{i,\mu}$. [h] Poor agreement obtained between $k_{2,ADO}$ and $k_{2,obsd}$ is a direct consequence of the very small extent of fragmentation in the primary amine ions.

or from the carbon atom α to the positively charged nitrogen. However, for n-propyl-, ethyl-, and diethylamine transferable protons are available in structure III and a rapid reaction is observed.

The observation that the structure of the ion can play an important role in the rate of proton-transfer reactions supports the view of Su and Bowers[19] that the slow rate observed for the reaction $(CH_3)_3C^+ + NR_3 \rightarrow (CH_3)_2CCH_2 + H^+NR_3$ results from structural factors in the reactant ion and not from any inadequacy in the ADO theory itself.

When both ion-induced dipole and ion-dipole interactions are considered, the collision rate constant k_i, is given as the sum of the two contributing terms: $k_{i,\alpha}$, the pure polarization theory rate constant and the ion-dipole collision term, $k_{i,\mu}$, multiplied by a mixing parameter, c_i, which indicates the extent of contribution of the permanent dipole term to the overall rate constant

$$k_{i,ADO} = k_{i,\alpha} + c_i k_{i,\mu} = (a\alpha/\mu)^{1/2} + c_i(b\mu_D/\mu^{1/2}) \tag{15}$$

where a and b are constants; α and μ_D are the polarizability and dipole moment of the molecules, respectively, and μ is the reduced mass of the ion-molecule collision complex.[18] Current treatment of collision frequencies includes both terms in eq 15. The values of c_i and hence $k_{i,ADO}$ can be readily calculated using parameters summarized in ref 20. These values are given in Table II for all reactions relevant to this study. It is noteworthy that $k_{i,ADO}$ for the hydrogen (or proton) transfer reaction in $(CH_3)_3N$ and $(C_2H_5)_3N$ are significantly greater than the experimental result. This suggests that the reaction efficiency is low.

If the rate constant for an ion-molecule reaction is assumed to be the collision rate constant, $k_{i,ADO}$, the effects of internal molecular structure on reaction rate are ignored. A more complete model must include some type of correction for these effects. In the case of amines, in a typical collision complex formed at low ion velocity, the polar amine is most likely aligned with the ion.[2] In such a configuration, both the N-H and α C-H hydrogen atoms on the substrate molecule are in a geometrically favorable position for hydrogen transfer.[22] It is clear that aside from statistical considerations these two transfer processes would also be expected to differ due to differences in reactivity and stereochemistry. It is relatively easy to account for these factors semiempirically.

In trimethylamine (TMA), hydrogen atom transfer can only occur from the C-H bonds on the α carbons; whereas, in ammonia only transfer of N-H hydrogen is possible. In other primary and secondary alkylamines both types of transfer are possible and the observed reaction rate is a composite of the rates of these processes (neglecting contributions of H from the β carbons, etc.).

The rate constants for hydrogen transfer in ammonia per N-H bond can be defined as $k_{NH_3}/3$ where k_{NH_3} is the observed rate constant for this reaction. In the case of amines, it is assumed here that the rate of hydrogen transfer per N-H bond is given by $k_{NH_3}/3$ multiplied by an appropriate factor to account for the difference in the collision rates in ammonia and the particular amine. Since the values of c_i in eq 15 are low in the amine reactions, it has, for simplicity, been assume that $k_{i,ADO} \approx (a\alpha/\mu)^{1/2}$. Using this approximate expression the collision correction factor is $(\mu_{NH_3}\alpha_A/\mu_A\alpha_{NH_3})^{1/2}$ where μ and α refer to the reduced mass and polarizability of NH_3 and the amine (denoted by subscript A). Further, if n is the number of N-H bonds in the amine the rate constant for hydrogen transfer is given by

$$k_{N-H} = n\left(\frac{\mu_{NH_3}\alpha_A}{\mu_A\alpha_{NH_3}}\right)^{1/2}\left(\frac{k_{NH_3}}{3}\right) \tag{16}$$

Similarly, the rate constant (per C-H bond) for hydrogen transfer from the α carbon in TMA may be written as $k_{TMA}/9$ where k_{TMA} is the observed rate constant. Hence, this contribution for any other amine is

$$k_{C-H} = j\left(\frac{\mu_{TMA}\alpha_A}{\mu_A\alpha_{TMA}}\right)^{1/2}\left(\frac{k_{TMA}}{9}\right) \tag{17}$$

where j is the number of μ-carbon hydrogen bonds.

Thus the total rate of hydrogen transfer for an amine is then

$$k_{i,\alpha}' = k_{\mathrm{N-H}} + k_{\mathrm{C-H}} = \left(\frac{\alpha_{\mathrm{A}}}{\mu_{\mathrm{A}}}\right)^{1/2}\left[n\left(\frac{\mu_{\mathrm{NH_3}}}{\alpha_{\mathrm{NH_3}}}\right)^{1/2}\left(\frac{k_{\mathrm{NH_3}}}{3}\right) + j\left(\frac{\mu_{\mathrm{TMA}}}{\alpha_{\mathrm{TMA}}}\right)^{1/2}\frac{k_{\mathrm{TMA}}}{9}\right] \tag{18}$$

In the present model, the rate constant is seen to be proportional to the pure polarization theory (Langevin) collision number, as is reflected by the term $(\alpha_{\mathrm{A}}/\mu_{\mathrm{A}})^{1/2}$, multiplied by a second factor which reflects the internal structure of the molecule.

The values of $k_{1,\alpha}'$ for both methyl- and ethylamines are compared with the experimental results in Table II. The calculated values agree well with the experimental results but are generally slightly lower than the observed rate constant, $k_{1,\mathrm{obsd}}$. This observation is understandable in light of the fact that the ion–dipole contribution to the total collision frequency has been neglected in the formulation of $k_{1,\alpha}'$. The correct prediction of a very low value of k_1 for the triethylamine system lends further support to the present model.

The agreement obtained between $k_{1,\alpha}'$ and the observed k_1 values for the methyl- and ethylamines seems to indicate that this class of unit mass transfer reactions in amines, at low ion velocities, involves a collision complex in which the polar molecule is aligned with the ion and the actual hydrogen or proton transfer rate is determined by the number and intrinsic reactivity of those hydrogens which are in a geometrically favorable position for reaction. Consequently, any theoretical model which predicts collision rates only will generally be inadequate in describing the chemistry of hydrogen transfer reactions.

Acknowledgment. The authors are grateful to Professors P. Kebarle and D.A. Armstrong for helpful discussions. They are also indebted to Dr. K.O. McFadden and Mr. J.D. Malinsky for their assistance in the construction of the apparatus.

Appendix A

As a result of photoionization of a substrate material, R_i, several different primary ions, P_i^+ and neutrals, N_i, may result from the process

$$R \xrightarrow[-e]{h\nu} \sum_{i=1}^{n} P_i^+ + \sum_{i=1}^{n} N_i$$

Once formed, each of these primary ions may undergo ion–molecule reactions with any suitable substrate present in the reaction mixture. The reactions of one particular primary ion can be summarized as follows:

$$\begin{array}{l} P_i^+ + R_1 \xrightarrow{k_1} S_1^+ + N_1 \\ P_i^+ + R_2 \xrightarrow{k_2} S_2^+ + N_2 \\ \quad\vdots \qquad \vdots \qquad\quad \vdots \qquad \vdots \\ P_i^+ + R_L \xrightarrow{k_L} S_L^+ + N_L \end{array}$$

where R_i represents the different reactive substrates that may be present in the reaction mixture and S_i^+ and N_i represent the various secondary ions and neutrals formed. For this reaction scheme, the rate of loss of a specific primary ion, P_i^+, must be given by

$$\mathrm{d}[P_i^+]/\mathrm{d}t = -\sum_{i=1}^{L} k_i[R_i][P_i^+] \tag{A1}$$

where k_i represents the total rate constant for the loss of P_i^+ by reaction with R_i. Integration of eq A1 over the reaction time τ gives the expression

$$\ln\frac{[P_i^+]_\tau}{[P_i^+]_0} = -\sum_{i=1}^{L} k_i[R_i]\tau \tag{A2}$$

On the basis of charge conservation, it can be seen from the above scheme that $[P_i^+]_0 = [P_i^+]_\tau + \Sigma_i[S_i^+]_\tau$, where $[S_i^+]_\tau$ is the concentration of a particular secondary ion at time τ. Since ion currents are proportional to ion concentration

$$\ln\frac{I_{P_i^+}}{I_{P_i^+} + \sum_{i=1}^{L} I_{S_i^+}} = -\sum_{i=1}^{L} k_i[R_i]\tau \tag{A3}$$

where I_y is the observed total ion current for species y at time τ. Equation A3 may be rewritten in terms of mole fractions as follows:

$$\ln f_i = -\sum_{i=1}^{L}\frac{k_i X_i P\tau}{RT} \tag{A4}$$

where $f_i = I_{P_i^+}/(I_{P_i^+} + \Sigma_i I_{S_i^+})$, P is the total pressure, T is the absolute temperature, and X_i is the mole fraction of the ith component in the reaction mixture. For single component systems eq A4 further simplifies to

$$\ln f_i = -(k_i\tau/RT)P \tag{A5}$$

References and Notes

(1) (a) Work supported by the National Research Council of Canada. (b) Postdoctorate Fellow 1972–1974. (c) Postgraduate Fellow.

(2) M. J. Henchman. *Discuss. Faraday Soc.*, **39**, 63 (1965).

(3) M. S. B. Munson, *J. Phys. Chem.*, **70**, 2034 (1966).

(4) E. G. Jones and A. G. Harrison, *Can. J. Chem.*, **45**, 3119 (1967).

(5) L. Hellner and L. W. Sieck, *Int. J. Chem. Kinet.*, **5**, 177 (1973).

(6) G. Gioumousis and D. P. Stevenson, *J. Chem. Phys.*, **29**, 294 (1958).

(7) T. F. Moran and W. H. Hamill, *J. Chem. Phys.*, **39**, 1413 (1963).

(8) L. I. Isakov and V. K. Potapov, *Russ. J. Phys. Chem.*, **47**, 42 (1973).

(9) W. T. Huntress, Jr., and R. F. Pinizzotto, Jr., *J. Chem. Phys.*, **59**, 4742 (1973).

(10) L. W. Sieck, S. K. Searles, and P. Ausloos, *J. Amer. Chem. Soc.*, **91**, 7627 (1969).

(11) L. W. Sieck and S. K. Searles, *J. Amer. Chem. Soc.*, **92**, 2937 (1970).

(12) A. G. Harrison and J. C. J. Thynne, *Trans. Faraday Soc.*, **62**, 2804 (1966).

(13) S. K. Gupta, E. G. Jones, A. G. Harrison, and J. J. Myher, *Can. J. Chem.*, **45**, 3107 (1967).

(14) G. A. W. Derwish, A. Galli, A. Gairdini-Guidoni, and G. G. Volpi, *J. Chem. Phys.*, **39**, 1599 (1963).

(15) C. E. Melton, *J. Chem. Phys.*, **45**, 4414 (1966).

(16) W. T. Huntress, M. M. Mosesman, and D. D. Elleman, *J. Chem. Phys.*, **54**, 843 (1971).

(17) L. W. Sieck, L. Hellner, and R. Gordon, Jr., *Chem. Phys. Lett.*, **10**, 502 (1971).

(18) T. Su and M. T. Bowers, *J. Chem. Phys.*, **58**, 3027 (1973).

(19) T. Su and M. T. Bowers, *J. Amer. Chem. Soc.*, **95**, 1370 (1973).

(20) T. Su and M. T. Bowers, *Int. J. Mass Spectrom. Ion Phys.*, **12**, 347 (1973).

(21) F. N. McLafferty, "Interpretation of Mass Spectra," W. A. Benjamin, New York, N.Y., 1967.

(22) The term hydrogen transfer here and elsewhere for reaction between parent ion and parent neutral is used synonymously to denote unit-mass transfer since in the absence of isotopic labeling it is not possible to distinguish between this mechanism and proton transfer for this class of reactions. Since the molecule and ion are identical in the number and type of hydrogen atoms, the statistical treatment outlined here is applicable to either mechanism, i.e., hydrogen or proton transfer.

(23) R. J. W. LeFèvre, "Advances in Physical Organic Chemistry," Vol. III, Academic Press, New York, N.Y., 1965.

(24) R. D. Nelson, Jr., D. R. Lide, Jr., and A. A. Maryott, *Nat. Stand. Ref. Data Ser., Nat. Bur. Stand.* **No. 10** (1967).

Oxidation of Chloroethylene[1a]

Eugenio Sanhueza[1b] and Julian Heicklen*

Department of Chemistry and Center for Air Environment Studies, The Pennsylvania State University, University Park, Pennsylvania 16802

(Received July 19, 1974; Revised Manuscript Received December 16, 1974)

Publication costs assisted by the Center for Air Environment Studies

The chlorine-atom initiated oxidation of C_2H_3Cl produces $CH_2ClCCl(O)$, $CHClO$, CO, and HCl as products. $\Phi\{CHClO\}$ and $\Phi\{CO\}$ are, respectively ~2.4 and 0.7, independent of reaction parameters. Their production can be explained through the oxidation of $CH_2ClCHCl$ radicals. $\Phi\{CH_2ClCCl(O)\}$ is produced in a long-chain process which decreases in importance as $[O_2]/[Cl_2]$ increases. It can be explained through the chain oxidation of CH_2ClCCl_2 radicals which are produced via $CH_2ClCHCl + Cl_2 \rightarrow CH_2ClCCl_2 + HCl$ (20). This reaction competes with the oxidation of $CH_2ClCHCl$: $CH_2ClCHCl + O_2 \rightarrow CH_2ClCHClO_2$ (12) with $k_{20}/k_{12} = 10 \pm 4$. The reaction of $O(^3P)$ with C_2H_3Cl proceeds through an energetic intermediate, $C_2H_3ClO^*$, which can rearrange to either C_2 carbonyl compound: $C_2H_3ClO^* \rightarrow CH_2ClCH(O)$; $C_2H_3ClO^* \rightarrow CH_3CCl(O)$. These compounds are produced with the excess energy retained, so that they can decompose to radical fragments, if not first stabilized by collision. $\Phi\{CH_2ClCH(O)\}/\Phi\{CH_3CCl(O)\}$ is about 4. The other products observed were CO, HCl, CH_4, and polymer. In the presence of O_2, the $O(^3P)$–C_2H_3Cl reaction does not give the C_2 carbonyl compounds or CH_4. However CO, $CHClO$, HCl, and $HCOOH$ are produced. Presumably the O reacts directly with the intermediate: $C_2H_3Cl^* + O_2 \rightarrow CHClO + CH_2O_2$ (30a), $C_2H_3ClO^* + O_2 \rightarrow CO + HCl + CH_2O$ (30b) with channel 30a being dominant. The CH_2O_2 either rearranges to $HCOOH$ or decomposes to $CO + H_2O$.

Introduction

Studies have been made on the chlorine-atom and $O(^3P)$-initiated oxidation of C_2Cl_4,[2-6] C_2Cl_3H,[7-9] CCl_2CH_2,[10,11] and *cis-* and *trans-*$CHClCHCl$.[12,13] All of these molecules oxidize by a long-chain free-radical process which can be summarized as

$$Cl + \text{olefin} \longrightarrow R \tag{1}$$

$$R + O_2 \longrightarrow RO_2 \tag{2}$$

$$2RO_2 \longrightarrow 2RO + O_2 \tag{3a}$$

$$\longrightarrow (RO)_2 + O_2 \tag{3b}$$

$$RO \longrightarrow 2P_1 + Cl \tag{4a}$$

$$\longrightarrow P_2 + Cl \tag{4b}$$

where P_1 and P_2 are one- and two-carbon atom carbonyl compounds, respectively. Reaction 4a is a composite reaction which requires additional oxygen.

On the other hand, C_2H_4 does not oxidize through a long chain, and the details of the oxidation are quite different. Bertrand et al.[14] reported that the chlorine-atom initiated oxidation has a chain length less than 2 at room temperature. The reaction of $O(^3P)$ with C_2H_4 has been extensively examined. Cvetanović[15] summarized the early data and showed that the general process is

$$O(^3P) + C_2H_4 \longrightarrow \overline{CH_2CH_2O}^* \tag{5}$$

$$\overline{CH_2CH_2O}^* \longrightarrow CH_3CHO^* \tag{6}$$

$$\overline{CH_2CH_2O}^* + M \longrightarrow \overline{CH_2CH_2O} + M \tag{7}$$

$$CH_3CHO^* \longrightarrow CH_3 + HCO \tag{8}$$

$$CH_3CHO^* + M \longrightarrow CH_3CHO + M \tag{9}$$

Only very limited information is available on C_2H_3Cl, a molecule whose structure is intermediate between C_2H_4 and the more highly chlorinated ethylenes. Bertrand et al.[14] studied the oxidation of $CH_2ClCHCl$, the radical expected from the addition of chlorine atoms to C_2H_3Cl. They prepared the $CH_2ClCHCl$ radical from CH_2ClCH_2Cl by hydrogen-atom abstraction, and they found the chain length of the oxidation to be less than 2. They did not report the products of the reaction.

The reaction of $O(^3P)$ with C_2H_3Cl was studied by Huie et al.,[16] who obtained a rate coefficient of $5.2 \times 10^8\ M^{-1}\ \text{sec}^{-1}$. They also reported that CH_2O was a product of the reaction.

In this communication, we extend our work on the oxidation of chloroolefins to C_2H_3Cl. Both the chlorine-atom and $O(^3P)$-initiated oxidations are reported.

Experimental Section

The experimental procedure has been described previously.[5,9,17] The chlorine atoms were generated from the photolysis of Cl_2 at 3660 Å and the $O(^3P)$ atoms from the Hg-sensitized photolysis of N_2O at 2537 Å.

The C_2H_3Cl was from the Matheson Co. Before use, it was distilled at −80° and collected and degassed at −196°. Its infrared spectrum showed no impurity peaks.

The olefin and products were monitored by in situ infrared spectroscopy during a run, utilizing the bands and peak extinction coefficients (to base 10) shown in Table I.

N_2, CO, and CH_4 were analyzed by gas chromatography after the irradiation was terminated.

In the reaction of $O(^3P)$ with C_2H_3Cl in the presence of O_2, the reaction cell was shaken periodically during each run to minimize the inhibition observed in previous work with the other chloroethylenes.

Results

In the chlorine-atom initiated oxidation of C_2H_3Cl, the products are $CH_2ClCCl(O)$, $CHClO$, CO, and HCl. Perhaps

TABLE I: Extinction Coefficients

Molecule	Band, cm^{-1}	10^3 × peak extinction coefficient, $Torr^{-1}$ cm^{-1}
C_2H_3Cl	1640	3.55
CHClO	1805	15.0
$CH_2ClCCl(O)$	1860	9.82
$CH_2ClCH(O)$	1770	6.00
$CH_3CCl(O)$	1860	14.0
HCOOH	1805	7.36

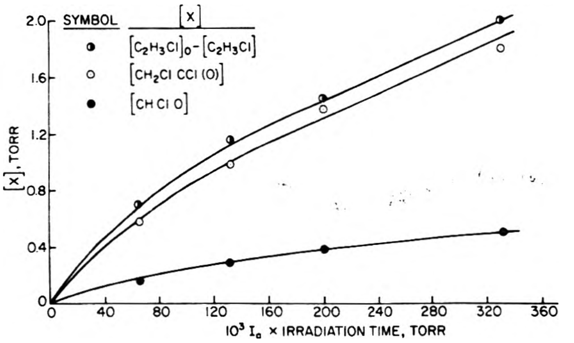

Figure 1. Plots of C_2H_3Cl consumption and $CH_2ClCCl(O)$ and CHClO production vs. the product of the initial absorbed intensity and the irradiation time in the chlorine-atom initiated oxidation of C_2H_3Cl at 31° for $[C_2H_3Cl]_0$ = 2.67 Torr, $[O_2]_0$ = 3.06 Torr, $[Cl_2]_0$ = 3.53 Torr, $[N_2]$ = 176 Torr, and an initial absorbed intensity of 0.43 mTorr/sec.

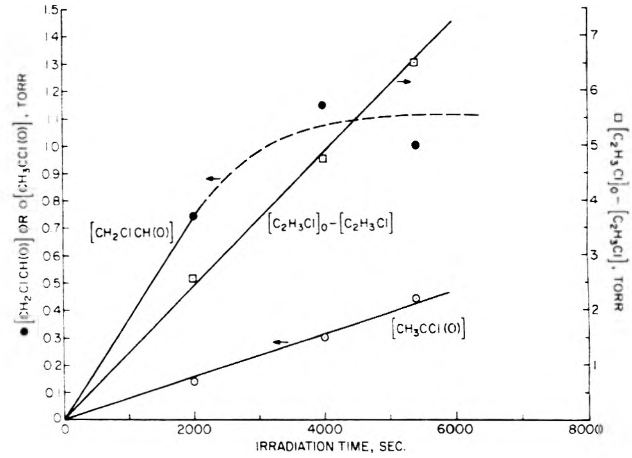

Figure 2. Plots of C_2H_3Cl consumption and $CH_2ClCH(O)$ and $CH_3CCl(O)$ production vs. irradiation time in the reaction of $O(^3P)$ with C_2H_3Cl at 25° for $[C_2H_3Cl]_0$ = 6.6 Torr, $[N_2O]$ = 400 Torr, and an initial absorbed intensity of 1.0 mTorr/sec. Note two different ordinate scales.

some $CH_3CCl(O)$ is also produced, but it is not possible to know for sure since its carbonyl infrared band is identical with that for $CH_2ClCCl(O)$. The results are summarized in Table II, assuming no production of $CH_3CCl(O)$. The quantum yield of C_2H_3Cl disappearance, $-\Phi\{C_2H_3Cl\}$, and $CH_2ClCCl(O)$ production, $\Phi\{CH_2ClCCl(O)\}$ are strongly dependent on the ratio $[O_2]/[Cl_2]$. They decrease as the values of the ratio increase. The lower limiting value of $-\Phi\{C_2H_3Cl\}$ appears to approach ~2, while that for $\Phi\{CH_2ClCCl(O)\}$ is even lower. There may be some dependence in $\Phi\{CHClO\}$, but it is not marked. Except for one run, it varies between 2 and 4. For the runs with the shortest conversion times, CO was measured immediately at the termination of the run. It is believed that the CO is a true initial product, and does not come from the decay of CHClO.

There is a time dependence during the run, and this is shown in Figure 1, which contains plots of olefin consumption and carbonyl product formation vs. duration of exposure for a typical run. The inhibition of the reaction as the run proceeds is evident. It almost surely comes from the fact that the Cl_2 (and thus the absorbed intensity, I_a) is depleted during the irradiation, as required by mass balance considerations. For example, when $[CH_2ClCCl(O)]$ reaches a pressure of 1.5 Torr, about 50% of the Cl_2 should have been removed, and the rate of $CH_2ClCCl(O)$ production has dropped to about one-half of its initial value.

The reaction of $O(^3P)$ with C_2H_3Cl gives as products: CO, $CH_2ClCH(O)$, $CH_3CCl(O)$, HCl, CH_4, and polymer. There was no evidence for C_2H_6 ($\Phi\{C_2H_6\} < 0.02$), CHClO ($\Phi\{CHClO\} < 0.1$), or CH_2O. No attempt at analysis was made for H_2. The results are listed in Table III. They are reported in comparison to N_2 production, to obtain yields per $O(^3P)$ atom. The yield of C_2H_3Cl removal is clearly >1. For high total pressure ($[N_2O]$ ~ 400 Torr), $R\{CO\}/R\{N_2\}$ = 0.25, $R\{CH_2ClCH(O)\}/R\{N_2\} \approx 0.40$, and $P\{CH_3CCl(O)\}/R\{N_2\} \approx 0.09$. At low total pressure, the respective values are 0.40, 0.25–0.35, and ~0.07. At either high or low pressure, all of the $O(^3P)$ atoms have not been accounted. Presumably the unaccounted fraction has gone into the polymer or H_2O. Figure 2 shows the time history for one set of conditions. The C_2H_3Cl consumption and $CH_3CCl(O)$ production rates are constant. However the $CH_2ClCH(O)$ production rate falls off at long irradiations, indicating that it is being removed from the reaction mixture, probably by free-radical attack on the aldehydic hydrogen.

In the presence of O_2, the $O(^3P)$–C_2H_3Cl reaction produces CHClO, CO, HCl, and HCOOH. Surprisingly the C_2 carbonyl compounds are not produced ($\Phi\{CH_2ClCH(O)\} < 0.2$ and $\Phi\{CH_3CCl(O)\} < 0.03$). CH_4 also is not produced ($\Phi\{CH_4\} < 0.01$). The results are in Table IV. Considerable difficulties were encountered in obtaining these results. Even though the cell was shaken during the experiments, inhibition occurred. Even the N_2 rates decreased. Thus some material was produced which inhibited the Hg-sensitized decomposition of N_2O. It was difficult to obtain N_2 production rates in the presence of a large excess of O_2, so this parameter was measured only in the run at lowest O_2 pressure. The quantum yields reported are all low because they are based on final product concentrations, but initial values of I_a. For the two runs where initial rates of C_2H_3Cl consumption were used, $-\Phi\{C_2H_3Cl\}$ is much larger (about a factor of 2). The results for $\Phi\{CHClO\}$ are even further complicated, because HCOOH interferes with the analysis, and the values reported assume no HCOOH production, which does not appear to be correct. Finally after all the CHClO had decomposed, $\Phi\{CO\}$ and $\Phi\{HCOOH\}$ could be measured, but we cannot tell what fraction represents initial products, and what fraction secondary products. In spite of these difficulties, it appears that the results are unaffected by changes in the reaction conditions.

The inhibition effect with extent of irradiation is shown in Figures 3 and 4 for C_2H_3Cl consumption and CHClO production, respectively. From Figure 4 it can be seen that the inhibition effect increases with the O_2 pressure, possi-

TABLE II: Chlorine-Atom Initiated Oxidation of C_2H_3Cl at 31° [a]

$[O_2]/[Cl_2]$	$[O_2]$, Torr	$[Cl_2]$, Torr	$[C_2H_3Cl]$, Torr	I_a,[b] mTorr/sec	Irradiation time, sec	$-\Phi\{C_2H_3Cl\}$[c]	$\Phi\{CH_2ClCCl(O)\}$[c]	$\Phi\{CHClO\}$[c]	$\Phi\{CO\}$[d]
0.374	3.14	8.39	4.55	1.03	100	20	15.2	2.8	0.72
0.445	3.77	8.47	7.45	1.04	100	20	16.0	3.8	0.73
0.846	6.90	8.16	5.18	1.00	550	13	8.3	3.0	
0.865	3.02	3.49	28.86	0.43	600		19.0	6.7	
0.867	3.06	3.53	2.67	0.43	765	11	8.6	2.4	
2.22	18.4	8.30	5.02	1.03	150	7.0	4.0	2.8	0.71
2.80	4.40	1.57	5.24	0.193	3600	5.0	2.4	1.6	
2.81	23.2	8.27	4.66	1.04	100		3.4	2.2	0.66
3.95	3.25	0.82	6.0	0.101	4250	4.0	1.8	2.2	
8.60	27.0	3.14	3.14	0.43	2000	4.4	2.0	2.4	
18.64	150.6	8.08	25.4	0.99	1300	2.0	0.6	1.9	
20.57	167.0	8.12	6.2	1.00	1000	3.0	1.0	1.9	

[a] 142–176 Torr of N_2 present in all runs. [b] I_a based on the quantum yield of consumption of C_2Cl_4 = 300 in the chlorine-atom initiated oxidation of C_2Cl_4. [c] From initial rates. [d] Analysis for CO at the termination of the run.

TABLE III: Reaction of $O(^3P)$ with C_2H_3Cl at 25°

$[C_2H_3Cl]$, Torr	$[N_2O]$, Torr	$R\{N_2\}$, mTorr/sec	Irradiation time, sec	$-R\{C_2H_3Cl\}/R\{N_2\}$	$R\{CO\}/R\{N_2\}$	$R\{CH_2ClCH(O)\}/R\{N_2\}$	$R\{CH_3CCl(O)\}/R\{N_2\}$
1.25	847	0.89	1,350	1.10	0.26	0.37	
2.35	36	0.70	2,100	1.50	0.39	0.25	~0.07
4.30	412	0.08	10,800	1.50	0.25	0.40	0.09
5.10	35	0.35	1,300	1.97	0.40	0.35	
6.37[a]	373	0.52	2,500	1.56	0.25	0.50	0.09
6.60[b]	400			1.22[c]		0.37[c]	0.076[c]
11.16	411	0.66	2,000	1.63	0.24	0.43	0.09

[a] $R\{CH_4\}/R\{N_2\}$ = 0.033. [b] This run taken to 100% conversion. I_a = 1.0 mTorr/sec at the beginning of the run. The ratio of CH_4 produced to C_2H_3Cl consumed was 0.03. [c] From Figure 2.

TABLE IV: Reaction of $O(^3P)$ with C_2H_3Cl in the Presence of O_2 at 25°

$[O_2]$, Torr	$[C_2H_3Cl]$, Torr	$[N_2O]$, Torr	I_a,[a] mTorr/sec	Irradiation time, sec	$-\Phi\{C_2H_3Cl\}$[b,c]	$\Phi\{CO\}$[b,d]	$\Phi\{HCOOH\}$[b,d]	$\Phi\{CHClO\}$[e]
2.7	2.82	460	0.96	1754	0.92 (1.54)	0.70[f]	0.48[f]	0.93
3.0	3.60	400	0.102	7400	0.80	0.60	0.53	
5.65	3.80	346	0.90	2400	0.78 (1.65)	1.00	0.46	0.93
12.0	11.65	409	0.90	700		0.52	0.69	0.83
87.0	3.31	362	0.96	800	0.71	0.49	0.50	0.64

[a] I_a at the beginning of the run as determined in separate actinometry experiments from the N_2 produced in the irradiation of N_2O in the presence of ~1% C_2F_4. [b] Quantum yields are based on the total C_2H_3Cl consumed or product produced during the run divided by the initial I_a. [c] Values in parentheses are based on initial rates obtained from Figure 3, and represent true initial quantum yields. [d] Analyses for CO and HCOOH were performed about 1 hr after the termination of radiation so that all the CHClO had decomposed. [e] $\Phi\{CHClO\}$ based on the initial growth rate of the 1805-cm^{-1} band, assuming that this band was entirely due to CHClO. HCOOH has a band in the same place, and if any of the band is due to HCOOH, then $\Phi\{CHClO\}$ would be reduced, and the value reported lies between $\Phi\{CHClO\}$ and $\Phi\{CHClO\}$ + $\{HCOOH\}$ since the extinction coefficient for HCOOH is 7.36×10^{-3} $Torr^{-1}$ cm^{-1} compared to that of 15.0×10^{-3} $Torr^{-1}$ cm^{-1} for CHClO. [f] $R\{CO\}/R\{N_2\}$ = 1.24, $R\{HCOOH\}/R\{N_2\}$ = 0.85.

bly because some of the $O(^3P)$ atoms react with O_2 to produce O_3 which attacks the mercury.

Discussion

The production of CO and CHClO in the chlorine-atom initiated oxidation can be explained by a mechanism analogous to that for the more-highly substituted chloroethylenes

$$Cl_2 + h\nu \longrightarrow 2Cl \tag{10}$$

$$Cl + C_2H_3Cl \longrightarrow CH_2ClCHCl \tag{11}$$

$$CH_2ClCHCl + O_2 \longrightarrow CH_2ClCHClO_2 \tag{12}$$

$$2CH_2ClCHClO_2 \longrightarrow 2CH_2ClCHClO + O_2 \tag{13a}$$

$$\longrightarrow (CH_2ClCHClO)_2 + O_2 \tag{13b}$$

$$CH_2ClCHClO \longrightarrow CH_2Cl + CHClO \tag{14a}$$

$$\longrightarrow CH_2Cl + CO + HCl \tag{14b}$$

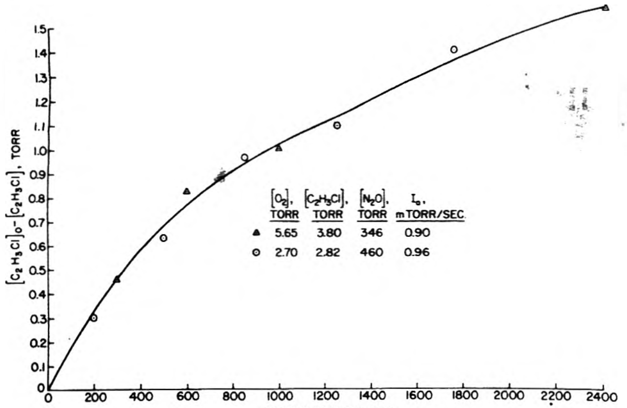

	$[O_2]$, TORR	$[C_2H_3Cl]$, TORR	$[N_2O]$, TORR	I_a, mTORR/SEC
▲	5.65	3.80	346	0.90
○	2.70	2.82	460	0.96

Figure 3. Plots of C_2H_3Cl consumption vs. irradiation time in the reaction of $O(^3P)$ with C_2H_3Cl in the presence of O_2 at 25° for two of the runs in Table IV.

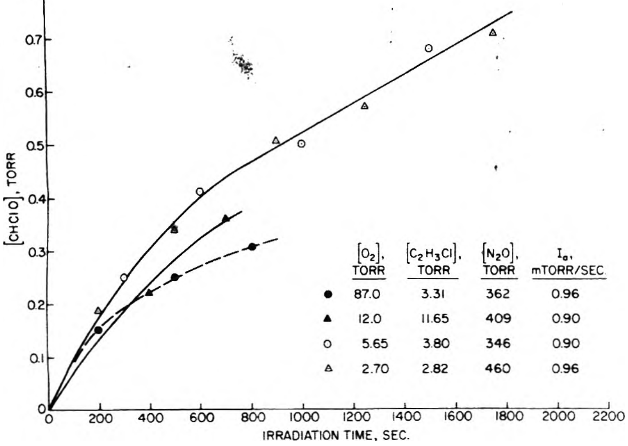

	$[O_2]$, TORR	$[C_2H_3Cl]$, TORR	$[N_2O]$, TORR	I_a, mTORR/SEC
●	87.0	3.31	362	0.96
▲	12.0	11.65	409	0.90
○	5.65	3.80	346	0.90
△	2.70	2.82	460	0.96

Figure 4. Plots of CHClO production vs. irradiation time in the reaction of $O(^3P)$ with C_2H_3Cl In the presence of O_2 at 25° for four of the runs in Table IV.

The CH_2Cl always gives CHClO in a terminating reaction[17]

$$CH_2Cl + O_2 \longrightarrow CH_2ClO_2 \tag{15}$$

$$2CH_2ClO_2 \longrightarrow 2CH_2ClO + O_2 \tag{16}$$

followed by

$$CH_2ClO_2 + CH_2ClO \longrightarrow 2CHClO + H_2O \tag{17}$$

or

$$CH_2ClO + O_2 \longrightarrow CHClO + HO_2 \tag{18}$$

$$CH_2ClO_2 + HO_2 \longrightarrow CHClO + H_2O + O_2 \tag{19}$$

The mechanism predicts that

$$\Phi\{CHClO\} + \Phi\{CO\} + 4\Phi\{(CH_2ClCClO)_2\} = 4 \tag{I}$$

$$\Phi\{(CH_2ClCClO)_2\} = k_{13b}/k_{13} \tag{II}$$

$$\Phi\{CO\}/\Phi\{CHClO\} = k_{14b}/(2k_{14a} + k_{14b}) \tag{III}$$

where $k_{13} \equiv k_{13a} + k_{13b}$. The results indicate that $\Phi\{CHClO\} + \Phi\{CO\} \sim 3.1 \pm 0.5$. If the 3.1 value is accepted, then $\Phi\{(CH_2ClCClO)_2\}$ should be ~0.2, an amount too small for us to detect. However with this value $k_{13b}/k_{13} \sim 0.2$. The ratio $\Phi\{CO\}/\Phi\{CHClO\} \sim 0.29$, so that $k_{14b}/k_{14} \sim 0.45$.

The production of $CH_2ClCCl(O)$ represents a process quite different from the oxidation of the more highly substituted chloroethylenes in two ways: (1) the incorporation of a second chlorine atom in the molecule requires the participation of Cl_2 in the reaction and (2) $\Phi\{CH_2ClCCl(O)\}$ depends on the ratio $[O_2]/[Cl_2]$. The latter point suggests a competition between O_2 and Cl_2 for one of the radical intermediates. The simplest explanation is to add the following reaction to the mechanism.

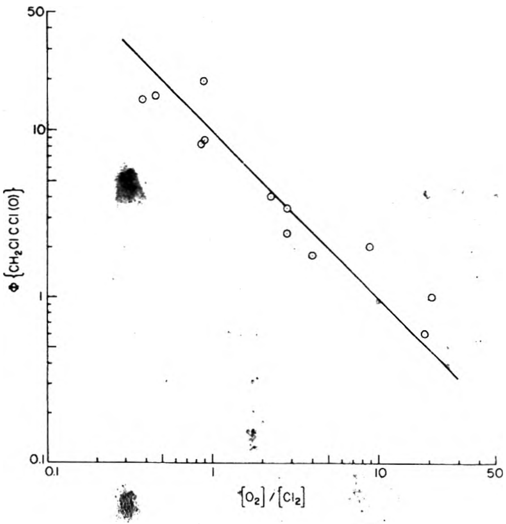

Figure 5. Log–log plot of $\Phi\{CH_2ClCCl(O)\}$ vs. $[O_2]/[Cl_2]$ in the chlorine-atom initiated oxidation of C_2H_3Cl at 31°.

$$CH_2ClCHCl + Cl_2 \longrightarrow CH_2ClCCl_2 + HCl \tag{20}$$

The CH_2ClCCl_2 radical will react as it does in the CH_2CCl_2 system to give almost exclusively $CH_2ClCCl(O)$ in chain carrying steps[10,11]

$$CH_2ClCCl_2 + O_2 \longrightarrow CH_2ClCCl_2O_2 \tag{21}$$

$$2CH_2ClCCl_2O_2 \longrightarrow 2CH_2ClCCl_2O + O_2 \tag{22}$$

$$CH_2ClCCl_2O \longrightarrow CH_2ClCCl(O) + Cl \tag{23}$$

The mechanism then predicts

$$\Phi\{CH_2ClCCl(O)\} = k_{20}[Cl_2]/k_{12}[O_2] \tag{IV}$$

Figure 5 is a log–log plot of $\Phi\{CH_2ClCCl(O)\}$ vs. $[O_2]/[Cl_2]$. The plot can be fitted reasonably by a line of slope −1.0. The intercept gives $k_{20}/k_{12} = 10 \pm 4$.

The reaction of $O(^3P)$ with C_2H_3Cl can be explained by a scheme analogous to that for C_2H_4

$$O(^3P) + C_2H_3Cl \longrightarrow C_2H_3ClO^* \tag{24}$$

$$C_2H_3ClO^* \longrightarrow CH_2 + CO + HCl \tag{25a}$$

$$\longrightarrow CH_2ClCH(O)^* \tag{25b}$$

$$\longrightarrow CH_3CCl(O)^* \tag{25c}$$

$$CH_2ClCH(O)^* \longrightarrow CH_2Cl + HCO \tag{26}$$

$$CH_2ClCH(O)^* + M \longrightarrow CH_2ClCH(O) + M \tag{27}$$

$$CH_3ClCH(O)^* \longrightarrow CH_3 + Cl + CO \tag{28}$$

$$CH_3CCl(O)^* + M \longrightarrow CH_3CCl(O) + M \tag{29}$$

The excited intermediate, $C_2H_3ClO^*$, can decompose or rearrange to one of the aldehydes which still contain the excess energy of reaction. If not deactivated they decompose to radical fragments. Thus at higher pressure relatively more aldehydes and less CO are produced. The radical fragments react with the C_2H_3Cl to form the polymeric material. Presumably some of the CH_3 radicals abstract a hydrogen atom to give the small amount of CH_4 produced. Reaction 25a has been included for completeness, but in fact there is no evidence that it actually occurs. Apparently the $C_2H_3ClO^*$ is never deactivated to the epoxide, since no epoxide was found. We found no evidence for CH_2O, though Huie et al. did.[16] They worked at very high concentrations of $O(^3P)$, and presumably the CH_2O they found came from the $O(^3P)$ reaction with CH_3 radicals, which is unimportant in our system.

In the presence of O_2 a very surprising result occurs, namely, no C_2 carbonyl compounds are produced. The O_2 must intercept the intermediate in a scheme such as

$$C_2H_3ClO^* + O_2 \longrightarrow CHClO + CH_2O_2 \qquad (30a)$$

$$\longrightarrow HCl + CO + CH_2O_2 \qquad (30b)$$

The CH_2O_2 can either rearrange to HCOOH or decompose to $CO + H_2O$

$$CH_2O_2 \longrightarrow HCOOH \qquad (31a)$$

$$\longrightarrow CO + H_2O \qquad (31b)$$

From the data in Table IV, it is difficult to assess the relative importance of the products observed. However a reasonable designation for the initial quantum yields is $\Phi\{CO\} \sim 0.6$, $\Phi\{HCOOH\} \sim 0.85$, and $\Phi\{CHClO\} \sim 0.6$. With this assessment

$$k_{30a}/k_{30} = \Phi\{CHClO\} \sim 0.6 \qquad (V)$$

$$k_{31a}/k_{31} = \Phi\{HCOOH\} \sim 0.8 \qquad (VI)$$

Acknowledgment. We wish to thank Dr. James Meagher for useful discussions and help in this study. This work was supported by the Environmental Protection Agency through Grant No. R800949 and the Center for Air Environment Studies at Penn State University for which we are grateful.

References and Notes

(1) (a) CAES Report No. 371-74. (b) Fulbright Fellow.

(2) (a) R. G. Dickinson and J. A. Leermakers, *J. Am. Chem. Soc.*, **54**, 3852 (1932); (b) R. G. Dickinson and J. L. Carrico, *ibid.*, **56**, 1473 (1934).

(3) C. Schott and H. J. Schumacher, *Z. Phys. Chem.*, **B49**, 107 (1941).

(4) G. Huybrechts, J. Olbrects, and K. Thomas, *Trans. Faraday Soc.*, **63**, 1647 (1967).

(5) E. Mathias, E. Sanhueza, I. C. Hisatsune, and J. Heicklen, Center for Air Environment Studies Report No. 304-73, Penn State University (1974); *Can. J. Chem.*, **52**, 3852 (1974).

(6) E. Sanhueza and J. Heicklen, Center for Air Environment Studies Report No. 305-73, Penn State University (1974); *Can. J. Chem.*, **52**, 3870 (1974).

(7) K. L. Muller and H. J. Schumacher, *Z. Phys. Chem.*, **B37**, 365 (1937).

(8) G. Huybrechts and L. Meyers, *Trans. Faraday Soc.*, **62**, 2191 (1966).

(9) E. Sanhueza and J. Heicklen, *Int. J. Chem. Kinet.*, **6**, 553 (1974).

(10) E. Sanhueza and J. Heicklen, Center for Air Environment Studies Report No. 353-74, Penn State University (1974); *J. Photochem.*, in press.

(11) E. Sanhueza and J. Heicklen, Center for Air Environment Studies Report No. 360-74, Penn State University (1974); *J. Photochem.*, in press.

(12) K. L. Muller and H. J. Schumacher, *Z. Phys. Chem.*, **B35**, 455 (1937).

(13) E. Sanhueza and J. Heicklen, Center for Air Environment Studies Report No. 364-74, Penn State University (1974); *Int. J. Chem. Kinet.*, in press.

(14) L. Bertrand, L. Exsteen-Meyers, J. A. Franklin, G. Huybrechts, and J. Olbregts, *Int. J. Chem. Kinet.*, **3**, 89 (1971).

(15) R. J. Cvetanović, *Adv. Photochem.*, **1**, 115 (1963).

(16) R. E. Huie, J. T. Herron, and D. D. Davis, *Int. J. Chem. Kinet.*, **4**, 521 (1972).

(17) E. Sanhueza and J. Heicklen, Center for Air Environment Studies Report No. 349-74, Penn State University (1974); *J. Phys. Chem.*, **79**, 7 (1975).

Photooxidation and Fluorescence of Cerium(III) in Aqueous Sulfuric Acid Solutions[1]

R. W. Matthews

A.A.E.C. Research Establishment, Sutherland, 2232, New South Wales, Australia

and T. J. Sworski*

Chemistry Division, Oak Ridge National Laboratory, Oak Ridge, Tennessee 37830

(Received April 18, 1974; Revised Manuscript Received November 1, 1974)

Publication costs assisted by the Energy Research and Development Administration

The fluorescence of cerium(III) is quenched by persulfate with concomitant photooxidation of cerium(III). Stern–Volmer constants for the quenching of cerium(III) fluorescence are in good agreement with Stern–Volmer constants for the photooxidation of cerium(III), conclusive evidence that photooxidation is induced by the quenching process. We propose that the quenching of cerium(III) fluorescence by persulfate is an irreversible electron transfer reaction: $(Ce^{III})^* + S_2O_8^{2-} \rightarrow Ce^{IV} + SO_4^{2-} + SO_4^-$. There is no marked effect of oxygen on the photooxidation of cerium(III). Therefore, there is no significant quantum yield of H atoms from the quenching of cerium(III) fluorescence by hydrogen ion.

Introduction

Photochemical oxidation[2] of cerium(III) to cerium(IV) in acidic aqueous solutions occurs with concomitant production[3] of hydrogen. Heidt and McMillan[4] presented excellent kinetic evidence that reaction of "excited cerium(III)" with hydrogen ion yields an intermediate, with a maximum quantum yield of 0.0007, that oxidizes cerium(III) with concomitant hydrogen production. They postulated that this intermediate was the ion $(H_2O)_5Ce\text{–}OH\text{–}H_2^{4+}$, but did not eliminate the possibility that it may be the oxidizing ion[5] H_2^+.

The presence of hydrogen ion was found necessary both for the quenching of cerium(III) fluorescence and the initiation of polymerization in the polymerization of methyl acrylate,[6] acrylonitrile,[6,7] and methacrylic acid[7] photosensitized by cerium(III). Quenching of cerium(III) fluorescence by hydrogen ion was attributed[6,7] to reaction of "excited cerium(III)" with hydrogen ion to produce H atoms, which combine in the absence of monomer to yield the hydrogen observed by Heidt and coworkers. Quantum yields as high as 0.0302 for polymer chains were reported.[7] High quantum efficiencies for production of H atoms would not be inconsistent with the kinetic results of Heidt and McMillan[4] only if every H atom were to reduce cerium(IV).[8]

Since the postulation[9] that photoionization of cerium(III) occurs in silicate glasses has been substantiated,[10,11] the possibility has been suggested[12] that H atoms in acidic aqueous solutions may result from photoionization of cerium(III) with subsequent scavenging of electrons by hydrogen ions.

We previously studied[13] the oxidation of cerium(III) by peroxymonosulfuric acid and peroxydisulfuric acid in air-saturated sulfuric acid solutions induced by ^{60}Co γ radiation. The H atoms react either with oxygen to yield HO_2 radicals, which reduce[3] cerium(IV), or with the peroxysulfuric acids to yield HSO_4 radicals, which oxidize[14] cerium(III). The role of H atoms was quantitatively evaluated; $G_H + G_{e_{aq}^-}$[15] and the relative rate constants for reaction of H atom with oxygen, peroxymonosulfuric acid, and peroxydisulfuric acid were determined. During the course of these studies, we discovered that the oxidation of cerium(III) by peroxysulfuric acids was photosensitized by cerium(III).

In this paper we report the dependence of both the photooxidation and fluorescence of cerium(III) on persulfate concentration in 0.4 *M* sulfuric acid solutions. Our initial objective was to evaluate the role of H atoms in the photolysis of cerium(III) in acidic aqueous solutions.

Experimental Section

Materials. Cerous sulfate octahydrate (G. Frederick Smith) was purified by precipitation as previously described.[13] Ceric sulfate (G. Frederick Smith), ammonium persulfate (Merck GR and May and Baker AR grade), ferric chloride, and ferrous sulfate (May and Baker AR grade), potassium oxalate, and 2-propanol (Ajax Chemicals Ltd. AR grade), ammonium sulfate (Standard Laboratories Pty. Ltd. AR grade), and argon (Commonwealth Industrial Gases special dry grade) were all used without further purification. Sulfuric acid (Ajax Chemicals Ltd. AR grade) was used as supplied in some experiments; in others, it was diluted with water and allowed to stand for several weeks in the presence of low concentrations of cerium(IV) before use. Water from a Manesty still was further distilled in a two-stage all-silica still before use.

Solutions. Solutions containing cerium(III), ammonium persulfate, and sulfuric acid were prepared using stock solutions. The ammonium persulfate stock solution was freshly prepared before each experimental run, and the required amount added to each solution immediately prior to photolysis. This was done to ensure that acid hydrolysis of the persulfate was negligible.[16] For those runs in which the sulfuric acid containing cerium(IV) was used, the solutions were allowed to stand overnight to allow oxidation of impurities before addition of ammonium persulfate.

In some experiments, solutions were deaerated by bubbling argon through the solution before and during photolysis. In other experiments, solutions were deaerated by bubbling argon through them in an apparatus similar to that described by Boyle et al.[17] by which a photolysis cell could be filled with deaerated solution and capped.

In some experiments, solutions were not stirred *during* photolysis, but were stirred prior to absorbance measurements between intermittent irradiations either by means of small air bubbles or in the case of deaerated solutions by means of a small silica disk. In other experiments, some degree of stirring was achieved by bubbling argon through the solution during photolysis.

In the majority of experiments, the solutions were stirred by a rapidly rotating glass propeller. A solution was contained in a 2-cm cylindrical cell fitted with a plastic stopper. The glass stirring propeller fitted snugly through a hole drilled in the stopper and was attached by means of rubber tubing and a screw to a metal shaft. The shaft was driven by means of an "O" ring belt operated by a laboratory stirrer. The cell with propeller could be quickly disconnected from the driving shaft and the propeller raised out of the light path, without removing the stopper, for the absorbance measurements.

Analyses. Cerium(III) and cerium(IV) concentrations were determined spectrophotometrically by absorbance measurements using either a Unicam SP500 or a Cary Model 16 spectrophotometer with cell compartments thermostatted at 25°. A molar extinction coefficient of 685 at 254 nm was used for cerium(III).[18] A molar extinction coefficient of 5600 at 320 nm for cerium(IV) in 0.4 *M* sulfuric acid was used;[19] for other sulfuric acid concentrations, the molar extinction coefficients reported by Boyle[20] were used.

Apparatus. The light source for both the fluorescence and photooxidation of cerium(III) was the 150-W xenon lamp of a Farrand spectrofluorometer. For the photooxidation experiments, solutions were contained in silica cylindrical spectrophotometer cells; the cell compartment of the spectrofluorometer was modified to accept these cells. The photooxidation of cerium(III) was followed as a function of photolysis time by using intermittent irradiations and transferring the cell back and forth between the spectrofluorometer and a spectrophotometer.

No variation in lamp intensity was observed during a typical experimental run lasting 5 hr, but marked differences resulted from switching off and restarting the lamp. Therefore, experiments to determine the effects of a specific variable were made in a single run. No significance should be attached to differences in rates of photooxidation observed in different runs.

Actinometry. Ferrioxalate actinometry was done by the method of Hatchard and Parker[21] using a quantum yield of 1.24 for iron(II) at 300 nm.

Results

The absorption spectrum of cerium(III) in aqueous solutions has six bands with maxima at 201, 211, 221, 239, 253, and 296 nm.[22] These bands are attributed[23] to 4f → 5d transitions. Cerium(III) in aqueous solutions fluoresces[24,25] with an excitation maximum at 260 nm (and a secondary peak at 295 nm) and a fluorescence emission maximum at 350 nm.[26]

We determined the excitation spectrum for both the fluorescence and the photooxidation of cerium(III) in a 0.4 *M* sulfuric acid solution containing 0.03 *M* cerium(III) and 0.01 *M* persulfate. These spectra were identical with an excitation maximum at 300 nm and a fluorescence emission

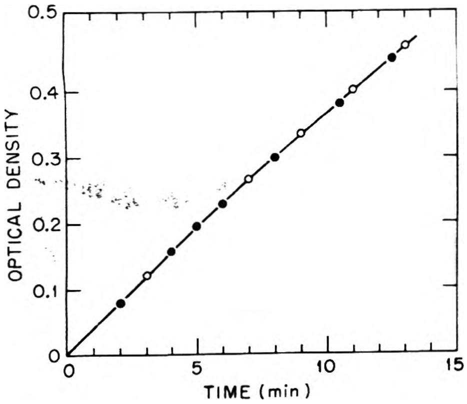

Figure 1. Photooxication of cerium(III) in aqueous 0.4 *M* sulfuric acid solutions containing 0.03 *M* cerium(III) and 0.01 *M* persulfate, evidenced by increased absorbance of solutions at 320 nm: (○) deaerated solutions; (●) aerated solutions.

maximum at 350 nm. Our excitation spectra were "uncorrected"; our failure to confirm either an excitation maximum at 260 nm[26] or even significant fluorescence with an excitation wavelength of 254 nm[27] is probably due to differences in emission characteristics of the light sources and response characteristics of the photomultipliers. Our research, therefore, was carried out with an excitation band centered at 300 nm and either 10- or 20-nm band widths.

Fluorescence of Cerium(III). Relative fluorescence intensities for air-saturated 0.4 *M* sulfuric acid solutions containing either 0.03 or 0.003 *M* cerium(III) were measured as a function of persulfate concentration. The observed fluorescence intensity F_{obsd} decreases with increase in persulfate concentration. For any particular persulfate concentration, F_{obsd} decreases with time of photolysis owing to absorption of both excitation and fluorescence light by increasing concentrations of cerium(IV). This decrease was negligible during the time required to insert a sample and measure F_{obsd}.

The absorbance of the cerium(III) solutions increases with increase in persulfate concentration owing to absorption of the excitation band by persulfate. The molar extinction coefficients for cerium(III) ($\epsilon_{\mathrm{Ce^{III}}}$) and persulfate ($\epsilon_{\mathrm{S_2O_8^{2-}}}$) for the 295–305-nm excitation band were found to be 30 and 2, respectively. All F_{obsd} values were normalized to F_{norm} values that would have been obtained if the cerium(III) in all solutions, at any particular cerium(III) concentration, had absorbed the same amount of light. F_{norm} values are given by

$$F_{\mathrm{norm}} = F_{\mathrm{obsd}}\left(\frac{1 - 1/\mathrm{antilog}\ A_0}{1 - 1/\mathrm{antilog}\ A_s}\right)\left(1 + \frac{\epsilon_{\mathrm{S_2O_8}^{2-}}[\mathrm{S_2O_8}^{2-}]}{\epsilon_{\mathrm{Ce}^{\mathrm{III}}}[\mathrm{Ce}^{\mathrm{III}}]}\right) \qquad \mathrm{(I)}$$

A_0 and A_s denote the absorbances of the cerium(III) solutions in the absence and presence of persulfate, respectively.

Photooxidation of Cerium(III). The experimental data shown in Figure 1 for the photooxidation of cerium(III) in 0.4 *M* sulfuric acid solutions containing 0.03 *M* cerium(III) and 0.01 *M* persulfate were obtained in a single run to determine the effect of oxygen. No effect of oxygen was detectable. The solutions were contained in 2-cm cylindrical cells using a 10-nm band width. The solutions were not stirred during photolysis, but were stirred prior to absorbance measurements using either a small air bubble for the aerated solution or a small silica disk for the deaerated solution. Figure 1 shows that the rate of cerium(IV) production decreases with increase in time of photolysis. This is attributable[27] to absorption of the excitation band by cerium(IV). We assume that the rate of cerium(IV) production is given to a good approximation by

$$\frac{\mathrm{d}[\mathrm{Ce^{IV}}]}{\mathrm{d}t} = R_{\mathrm{obsd}}\left(\frac{1 - 1/\mathrm{antilog\ ABST}}{1 - 1/\mathrm{antilog\ ABS0}}\right)\Bigg/ \left(1 + \frac{\epsilon_{\mathrm{S_2O_8}^{2-}}[\mathrm{S_2O_8}^{2-}] + \epsilon_{\mathrm{Ce}^{\mathrm{IV}}}[\mathrm{Ce^{IV}}]}{\epsilon_{\mathrm{Ce}^{\mathrm{III}}}[\mathrm{Ce^{III}}]}\right) \qquad \mathrm{(II)}$$

R_{obsd} denotes the initial rate of cerium(IV) production. ABS0 and ABST denote the initial absorbance and the absorbance at any given time, respectively.

The changes in cerium(III) and persulfate concentrations with time of photolysis are given by

$$\mathrm{d}[\mathrm{Ce^{III}}]/\mathrm{d}t = -\,\mathrm{d}[\mathrm{Ce^{IV}}]/\mathrm{d}t \qquad \mathrm{(III)}$$

$$\mathrm{d}[\mathrm{S_2O_8}^{2-}]/\mathrm{d}t = -0.5\,\mathrm{d}[\mathrm{Ce^{IV}}]/\mathrm{d}t \qquad \mathrm{(IV)}$$

R_{obsd} values were obtained by numerical integration of eq II–IV using an IBM Model 360 computer.

For deaerated solutions with a 10-nm band width, R_{obsd} values were determined with theoretical curves for cerium(IV) production that represented the data well when using our measured molar extinction coefficients of 500, 30, and 2 for cerium(IV), cerium(III), and persulfate, respectively.

For aerated solutions with a 20-nm band width, the use of our measured molar extinction coefficients of 500, 25, and 2 for cerium(IV), cerium(III), and persulfate, respectively, yielded theoretical curves having somewhat less curvature than the data. The slightly exaggerated curvature in the data probably arises from failure to adequately stir the solution to maintain a homogeneous solution at the higher rate of cerium(IV) production. R_{obsd} values were obtained with theoretical curves that represented the data well when using a molar extinction coefficient of 20 for cerium(III).

R_{obsd} values were determined as a function of cerium(III) concentration in 0.4 *M* sulfuric acid solutions containing 0.01 *M* persulfate. The solutions were contained in 2-cm cylindrical cells with continuous stirring by a glass propeller during photolysis using a 10-nm band width. The R_{obsd} values listed in Table I were normalized to R_{norm} values that would have been obtained if a constant amount of light had been absorbed initially by cerium(III) in all of the solutions. The ratios of light absorbed by cerium(III) in each solution relative to that absorbed by cerium(III) in the 0.090 *M* cerium(III) solution are 0.712, 0.874, 0.984, and 0.998 for the 0.009, 0.015, 0.030, and 0.060 *M* cerium(III) solutions, respectively. The R_{norm} values listed in Table I indicate that the quantum efficiency for photooxidation of cerium(III) is independent of cerium(III) concentration. Therefore, we do not confirm the conclusion[27] that there is self-quenching of cerium(III) fluorescence at high cerium(III) concentrations.

The thermal oxidation of cerium(III) by persulfate[28] was insignificant under our experimental conditions.

The oxidation of cerium(III) by persulfate can also be photosensitized by persulfate. Photolysis of persulfate in aqueous solutions yields sulfate radicals[29,30] that oxidize[14,31] cerium(III). The oxidation of cerium(III) photosensitized by persulfate was not quantitatively taken into account, but was minimized by the choice of solute concen-

TABLE I: Dependence of Photooxidation Rate on Cerium(III) Concentration in 0.4 M Sulfuric Acid, $[S_2O_8^{2-}] = 0.01\ M$

$[Ce^{III}]$, $M\ 10^2$	R_{obsd}, $M\ sec^{-1} \times 10^8$	R_{norm}, $M\ sec^{-1} \times 10^8$
0.9	2.59	3.64
1.5	3.08	3.51
3.0	3.47	3.53
6.0	3.62	3.63
9.0	3.62	3.62

trations. Less than 5% of the total light absorbed in solutions was absorbed by persulfate at its highest concentration of 0.02 M in 0.03 M cerium(III) solutions.

Reduction of cerium(IV) by persulfate may be photosensitized by cerium(IV). Photolysis of cerium(IV) in aqueous solutions yields[33] OH radical that reacts[34] with persulfate to yield the HO_2 radical that reduces[8] cerium(IV). The reaction of OH radical with persulfate is inhibited[34] by sulfuric acid, owing to reaction of OH radical with sulfuric acid to yield the HSO_4 radical.[35] Under our experimental conditions, most of the OH radicals oxidize cerium(III). Therefore, no net reaction would result from light adsorbed by cerium(IV) in our solutions.

Photooxidation of cerium(III) was barely detectable in solutions containing no persulfate. The rate of photooxidation was small, being an order of magnitude less than the rates observed with the lowest persulfate concentrations used and approximately equal to the experimental error for determinations of photooxidation rates. For this reason, photooxidation of cerium(III) in the presence of persulfate was assumed to be entirely oxidation of cerium(III) by persulfate photosensitized by cerium(III).

Actinometry. Actinometry was carried out only during that experimental run in which R_{obsd} values were determined as a function of persulfate concentration for deaerated solutions with 10-nm band width. The light absorbed by the solutions in that experimental run corresponded to a rate of (6.1 ± 0.2) × 10^{-8} M sec^{-1} for cerium(III) excitation.

Discussion

The dependence of both the photooxidation and fluorescence of cerium(III) on persulfate concentration is quantitatively explicable by the following reaction mechanism:

$$Ce^{III} + h\nu \longrightarrow (Ce^{III})^* \tag{1}$$

$$(Ce^{III})^* \longrightarrow Ce^{III} + h\nu \tag{2}$$

$$(Ce^{III})^* + H_3O^+ \longrightarrow Ce^{III} + H_3O^+ \tag{3}$$

$$(Ce^{III})^* + S_2O_8^{2-} \longrightarrow Ce^{IV} + SO_4^{2-} + SO_4^- \tag{4}$$

$$Ce^{III} + SO_4^- \longrightarrow Ce^{IV} + SO_4^{2-} \tag{5}$$

Our reaction mechanism requires that the dependence of F_{norm} on persulfate concentration adhere to

$$F_{norm} = F^0/\left(1 + \frac{k_4[S_2O_8^{2-}]}{k_2 + k_3[H^+]}\right) \tag{V}$$

F^0, the fluorescence intensity in the absence of persulfate, is equal to $F^*/(1 + k_3[H^+]/k_2)$. F^* denotes the fluorescence intensity in the absence of both persulfate and hydrogen ion. Our reaction mechanism also requires that the dependence of R_{obsd} on persulfate concentration adhere to

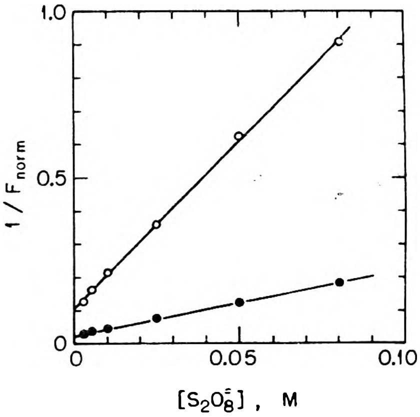

Figure 2. Stern–Volmer type plot for quenching of cerium(III) fluorescence by persulfate in (○) 0.003 and (●) 0.03 M cerium(III) solutions in aqueous 0.4 M sulfuric acid.

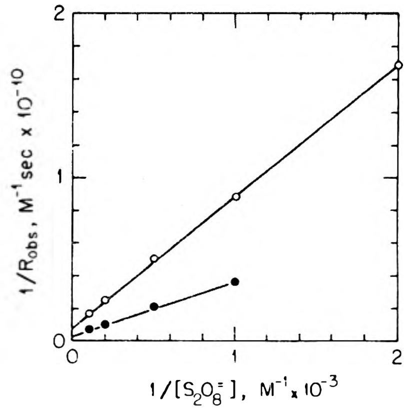

Figure 3. Stern–Volmer type plot for photooxidation of cerium(III) by persulfate in (○) deaerated and (●) aerated 0.03 M cerium(III) solutions in aqueous 0.4 M sulfuric acid.

$$R_{obsd} = 2R^*/\left(1 + \frac{k_2 + k_3[H^+]}{k_4[S_2O_8^{2-}]}\right) \tag{VI}$$

R^* denotes the rate of cerium(III) excitation.

The experimental data adhere well to eq V and VI as shown by Figures 2 and 3, respectively. The experimental data were fit to eq V and VI by the method of least squares using the computer program of Lietzke.[36] Equal absolute error was assumed for all of the experimental data.

Least-squares analysis yielded values for F^0 of 48.6 ± 0.3 and 9.11 ± 0.05 and values for $k_4/(k_2 + k_3[H^+])$ of 98.9 ± 2.5 and 93.5 ± 2.0 M^{-1} for 0.03 and 0.003 M cerium(III) solutions, respectively. Least-squares analysis yielded values for $2R^*$ of (31.3 ± 0.6) × 10^{-8} and (11.74 ± 0.20) × 10^{-8} M sec^{-1} and values for $k_4/(k_2 + k_3[H^+])$ of 90.5 ± 3.4 and 102.7 ± 3.0 M^{-1} for the aerated and deaerated solutions, respectively. The values for $k_4/(k_2 + k_3[H^-])$ obtained for the fluorescence of cerium(III) are in good agreement with the values obtained for the photooxidation of cerium(III), conclusive evidence that the photooxidation of cerium(III) is induced by the quenching of cerium(III) fluorescence by persulfate.

For deaerated solutions, the values for R^* of (5.87 ± 0.10) × 10^{-8} M sec^{-1} obtained from eq VI is equal within standard errors with the value for R^* of (6.1 ± 0.2) × 10^{-8} M sec^{-1} obtained by actinometry. A limiting quantum yield of unity is indicated for reaction of $(Ce^{III})^*$ with persulfate at high persulfate concentrations, consistent with our reaction mechanism.

Quenching of $(Ce^{III})^*$ *by Persulfate.* Cerium(III) complexes with a variety of organic ligands are reportedly[37,38] not capable of fluorescing, fluorescence being characteristic only of uncomplexed cerium(III). Quenching of cerium(III) fluorescence by persulfate is not due to complex formation. We reject this mechanism of quenching for two reasons. First, the absorption spectra of cerium(III) solutions in the presence and absence of persulfate provide no evidence for a cerium(III)–persulfate complex. This evidence is not definitive, but is in sharp contrast with the bathochromic shift in the cerium(III) absorption spectrum of complexing organic ligands.[37] Second, the fraction of $(Ce^{III})^*$ that reacts with 0.01 M persulfate is about 0.5 even when the concentration of cerium(III) is as high as 0.09 M and fraction of cerium(III) that is complexed can not be greater than 1/9. The fraction of $(Ce^{III})^*$ that reacts with 0.01 M persulfate from our photooxidation studies is $15.0/31.3 = 0.479$ and $14.7/31.3 = 0.470$ for aerated solutions and $5.96/11.74 = 0.508$ for deaerated solutions. Table I shows that the fraction of $(Ce^{III})^*$ that reacts with 0.01 M persulfate is independent of cerium(III) concentration from 0.009 to 0.09 M.

Quenching of cerium(III) fluorescence by persulfate does not occur via energy transfer to yield "excited persulfate" that dissociates to yield sulfate radicals:

$$(Ce^{III})^* + S_2O_8^{2-} \longrightarrow Ce^{III} + (S_2O_8^{2-})^* \qquad (6)$$

$$(S_2O_8^{2-})^* \longrightarrow SO_4^- + SO_4^- \qquad (7)$$

We reject this mechanism of quenching for two reasons. First, the quantum yield of 0.6 reported[39] for the photochemical decomposition of persulfate would not be consistent with our determination of a maximum quantum yield of 2 for the photooxidation of cerium(III). Second, significant photooxidation was observed in a solution containing 0.03 M cerium(III), 0.01 M persulfate, and 0.1 M 2-propanol in 0.4 M sulfuric acid. Relative rate constants[40] for reaction of sulfate radical with cerium(III) and 2-propanol indicate that more than half of the sulfate radicals would react with 2-propanol in this solution to yield a radical that reduces[41] cerium(IV). If two sulfate radicals were formed by the sequence of reactions 6 and 7, instead of one sulfate radical according to reaction (4), no net photooxidation of cerium(III) would be observed.

We propose that the quenching of $(Ce^{III})^*$ by persulfate is an irreversible electron transfer process[42] according to reaction 4. Reaction 4 may occur through intermediate formation of $S_2O_8^{3-}$. If so, the lifetime of $S_2O_8^{3-}$ must be very short since the electron transfer process is not reversible.

Quenching of $(Ce^{III})^*$ *by Hydrogen Ion.* The absence of any detectable oxygen effect on the photooxidation of cerium(III) by persulfate, evidenced by Figure 1, is conclusive evidence that there is no significant quantum yield for either H atom or e_{aq}^-. This conclusion is based on our experience[13] in the oxidation of cerium(III) by persulfate in 0.4 M sulfuric acid solutions induced by ^{60}Co γ radiation. We observed for air-saturated solutions containing 0.003 M cerium(III), 0.0001 M cerium(IV), and 0.01 M persulfate that the fraction of H and e_{aq}^- scavenged by persulfate in competition with oxygen was only about 0.05, a marked oxygen effect.

We confirm the proposal of Heidt and McMillan[4] that hydrogen ion can quench $(Ce^{III})^*$ with no net chemical reaction. We find no evidence to support either the proposal[6,7] that hydrogen ion quenches $(Ce^{III})^*$ with concomitant formation of H atom or the proposal[12] that H atom results from photoionization of cerium(III).

The absence of any significant quantum yield for H atom production indicates that the polymerization of methyl acrylate,[6] acrylonitrile,[6,7] and methacrylic acid[7] photosensitized by cerium(III) can not be attributed[6,7] to addition of H atoms to olefinic double bonds. We suggest that polymerization is induced by an electron transfer reaction between $(Ce^{III})^*$ and the carbonium ion[43] that results from protonation of the olefinic double bond:

$$M + H_3O^+ \rightleftarrows MH^+ + H_2O \qquad (8)$$

$$(Ce^{III})^* + MH^+ \longrightarrow Ce^{IV} + MH \qquad (9)$$

The sequence of reactions 8 and 9 is consistent with the kinetic scheme of Hussain and Norrish[7] who postulated a third-order reaction:

$$(Ce^{III})^* + H^+ + M \longrightarrow Ce^{IV} + MH \qquad (10)$$

The limiting quantum yield of unity for reaction of $(Ce^{III})^*$ with persulfate at high persulfate concentrations is inconsistent with the quenching of $(Ce^{III})^*$ by hydrogen ion through complex formation of cerium(III) with hydrogen ion. We therefore support the mechanism of Heidt and McMillan[4] in which hydrogen ion quenches $(Ce^{III})^*$ through a kinetic encounter. Our proposal of electron transfer processes for quenching of $(Ce^{III})^*$ by persulfate and carbonium ions according to reactions 4 and 9 leads us to consider a reversible electron transfer process for the quenching of $(Ce^{III})^*$ by hydrogen ion through transitory formation of H_3O:[44]

$$(Ce^{III})^* + H_3O^+ \longrightarrow [Ce^{IV} + H_3O] \longrightarrow Ce^{III} + H_3O^+ \qquad (11)$$

Should some H_3O radicals escape geminate reaction with cerium(IV), they might be precursors of hydrogen production. However, we have no evidence to refute the suggestion of Heidt and McMillan[4] that H_2^+ plays an important role in hydrogen production.

Acknowledgments. We wish to thank Drs. P. Airey and D. Sangster for helpful discussions during this work.

References and Notes

(1) Research supported by both the U.S. Atomic Energy Commission under contract with Union Carbide Corporation and the Australian Atomic Energy Commission.

(2) L. J. Heidt and M. E. Smith, *J. Am. Chem. Soc.*, **70**, 2476 (1948).

(3) L. J. Heidt, *Proc. Am. Acad. Arts Sci.*, **79**, 228 (1951).

(4) L. J. Heidt and A. F. McMillan, *J. Am. Chem. Soc.*, **76**, 2135 (1954).

(5) J. Weiss, *Nature (London)*, **165**, 728 (1950).

(6) F. H. C. Edgecombe and R. G. W. Norrish, *Nature (London)*, **197**, 282 (1963).

(7) F. Hussain and R. G. W. Norrish, *Proc. Roy. Soc., Ser. A*, **275**, 161 (1963).

(8) T. J. Hardwick, *Can. J. Chem.*, **30**, 23 (1952).

(9) S. D. Stookey, *Ind. Eng. Chem.*, **41**, 856 (1949).

(10) J. S. Stroud, *J. Chem. Phys.*, **35**, 344 (1961).

(11) A. J. Cohen and H. L. Smith, *Science*, **137**, 981 (1962).

(12) A. W. Adamson, W. L. Waltz, E. Zinato, D. W. Watts, P. D. Fleischauer, and R. D. Lindholm, *Chem. Rev.*, **68**, 541 (1968).

(13) R. W. Matthews, H. A. Mahlman, and T. J. Sworski, *J. Phys. Chem.*, **74**, 2475 (1970).

(14) T. J. Sworski, *Radiat. Res.*, **6**, 645 (1957).

(15) G_H and $G_{e_{aq}^-}$ denote the number of H atoms and hydrated electrons, respectively, formed per 100 eV absorbed in solution.

(16) H. Palme, *Z. Anorg. Allg. Chem.*, **112**, 97 (1920).

(17) J. W. Boyle, S. Weiner, and C. J. Hochanadel, *J. Phys. Chem.*, **63**, 892 (1959).

(18) H. L. Greenhaus, A. M. Feibush, and L. Gordon, *Anal. Chem.*, **29**, 1531 (1957).

(19) R. W. Matthews, *Int. J. Appl. Radiat. Isotopes*, **22**, 199 (1971).
(20) J. W. Boyle, *Radiat. Res.*, **17**, 427 (1962).
(21) C. G. Hatchard and C. A. Parker, *Proc. Roy. Soc., Ser. A*, **235**, 518 (1956).
(22) L. J. Heidt and J. Berestecki, *J. Am. Chem. Soc.*, **77**, 2049 (1955).
(23) C. K. Jφrgensen and J. Brinen, *Mol. Phys.*, **6**, 629 (1963).
(24) H. Gobrecht, *Ann. Phys.*, **31**, 181 (1938).
(25) P. C. Mukerji, *Z. Phys.*, **109**, 673 (1938).
(26) G. F. Kirkbright, T. S. West, and C. Woodward, *Anal. Chim. Acta*, **36**, 298 (1966).
(27) W. A. Armstrong, D. W. Grant, and W. G. Humphreys, *Anal. Chem.*, **35**, 1300 (1963).
(28) S. Fronaeus and C. O. Ostman, *Acta Chem. Scand.*, **9**, 902 (1955).
(29) M. Tsao and W. K. Wilmarth, *J. Phys. Chem.*, **63**, 346 (1959).
(30) L. Dogliotti and E. Hayon, *J. Phys. Chem.*, **71**, 2511 (1967).
(31) L. Dogliotti and E. Hayon, *J. Phys. Chem.*, **71**, 3802 (1967).
(32) M. H. Mariano, *Anal. Chem.*, **40**, 1662 (1968).
(33) J. Weiss and D. Porret, *Nature (London)*, **139**, 1019 (1937).
(34) A. Buu and J. Pucheault, *J. Chim. Phys.*, **63**, 1037 (1966).
(35) T. J. Sworski, *J. Am. Chem. Soc.*, **78**, 1768 (1956).
(36) M. H. Lietzke, ORNL-3259 (March 31, 1962).
(37) N. S. Poluektov and A. I. Kirilov, *Opt. Spectrosc.*, **23**, 413 (1967).
(38) H. Boden, *Nature (London)*, **222**, 161 (1969).
(39) L. J. Heidt, *J. Chem. Phys.*, **10**, 297 (1942).
(40) R. W. Matthews, H. A. Mahlman, and T. J. Sworski, *J. Phys. Chem.*, **76**, 1265 (1972).
(41) T. J. Sworski, R. W. Matthews, and H. A. Mahlman, *Adv. Chem. Ser.*, **No. 81**, 164 (1968).
(42) K. H. Grellman, A. R. Watkins, and A. Weller, *J. Phys. Chem.*, **76**, 469 (1972).
(43) F. C. Whitmore, *Ind. Eng. Chem.*, **26**, 94 (1934).
(44) J. L. Magee, *Radiat. Res. Suppl.*, **4**, 20 (1964).

Mechanism of the High Temperature Decomposition of Propane

Assa Lifshitz* and Michael Frenklach[1]

Department of Physical Chemistry, The Hebrew University, Jerusalem, Israel *(Received August 27, 1974)*

The mechanism of the thermal decomposition of propane around 1200°K is discussed, and results of computer calculations are compared with previously reported data on propane decomposition behind reflected shocks. A reaction scheme of 11 reactions provides a good description of the system at low extent of reaction. The kinetic scheme includes initiation step, chain propagations, unimolecular decompositions of free radicals, and a recombination reaction. The decompositions of ethylene and propylene to produce acetylene, allene, and propyne are not included in this discussion since these three products begin to appear at much higher temperatures. The rate of production of hydrogen, methane, ethylene, ethane, and propylene, its dependence on the propane concentration, and its temperature dependence can be very well reproduced by the computer calculations. The system was found to be highly dependent on the rate of the initiation reaction 1 and the chain propagation step 2. The best fit was obtained for: $C_3H_8 \rightarrow CH_3 + C_2H_5$, $k_1 = K_1k_{-1}$, $k_{-1} = 10^{12.4}$ (1) and $CH_3 + C_3H_8 \rightarrow CH_4 + C_3H_7(i,n)$, $k_2 = 10^{12.55} \exp(-10.3 \times 10^3/RT)$ (2) in units of cc, mole, sec. The disappearance rates of the five radicals in the system via transfer, unimolecular decompositions, and recombinations are compared and discussed.

I. Introduction

Recently, we have presented experimental data on the decomposition of propane behind reflected shocks in a single pulse shock tube.[2a] In this article a short summary of these results and a discussion of the mechanism of the high temperature decompositions of propane are presented.

In the single pulse shock tube[2b] a reaction mixture is heated to a desired temperature by a reflected shock wave, it is maintained and reacts at that temperature for a short period of time (~1 msec) and is then rapidly cooled with a set of expansion waves. Samples are later taken from the shock tube and are analyzed by conventional techniques. The reaction mixture passes through three phases in the shock tube: an incident shock heating, a reflected shock heating, and a cooling phase. It is first subjected to the incident shock heating. In this phase the temperature is lower by a few hundred degrees than the reflgcted shock temperature so that negligible reaction takes place. The second phase is the one behind the reflected shock wave. Here the temperature is high enough for a measurable chemical conversion to take place during 1 msec. This phase is isothermal except for temperature changes which may result from the chemical reaction itself. Most of the contribution to the chemical conversion comes from this phase. The third phase is the cooling phase; the temperature decreases at a rate of approximately 5 × 10^5 °K/sec. The elementary steps with high activation energies such as the initiation reactions are quenched very rapidly. The free radical chains continue to propagate until they are completely quenched. Although the main contribution to the measured chemical conversion comes from the reflected shock region, the cooling phase may affect the product distribution. A modeling program which simulates the experiment must take into account the latter two phases.

At low extents of reaction where the concentration of propane is almost unchanged, the rates of production of the various products, as will be shown later, are characterized by three parameters α, β, and E, and can be represented by an equation of the type

$$d[P_i]/dt = 10^{\alpha_i} \exp[-E_i/RT][C_3H_8]_0^{\beta_i} \qquad (I)$$

It is the purpose of this study to find the appropriate reaction scheme and rate constants that will reproduce these parameters for each one of the products in the tem-

TABLE I: Parameters α, β, and E for the Five Primary Products

Product	α	β	E, kcal/mol	Rate of production, mol cc^{-1} sec^{-1} [a]
H_2	15.70	1.41	63.2	5.17×10^{-5}
CH_4	15.52	1.65	54.8	4.17×10^{-5}
C_2H_4	15.52	1.38	62.5	6.88×10^{-5}
C_2H_6	14.74	1.24	67.3	1.07×10^{-5}
C_3H_6	13.76	1.45	52.0	3.70×10^{-5}

[a] For group of experiments with 1.6% C_3H_8 run at $p_1 \simeq 200$ Torr and $T = 1200$°K.

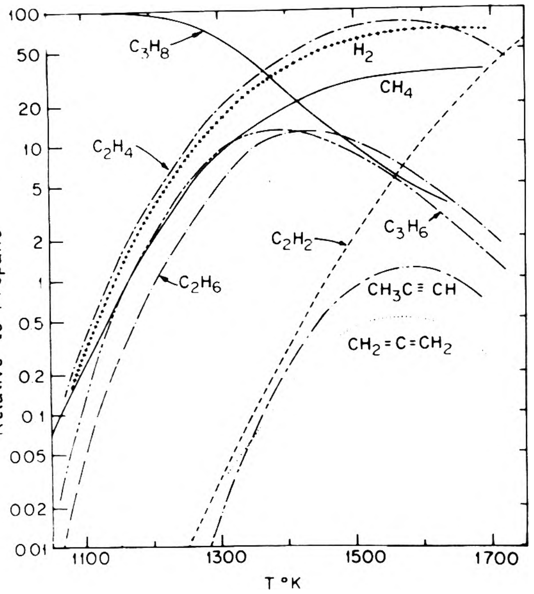

Figure 1. Distribution of reaction products (experimental) in a mixture of 1.6% propane in argon. Initial pressure $p_1 = 200$ Torr. Allene, propyne, and acetylene begin to show up at temperatures far above 1250°K which is beyond the limit of the computer modeling.

perature range over which eq I was found to hold experimentally. A comparison between the low and the high temperature mechanism for the decomposition of propane will also be presented.

II. Summary of the Experimental Results

Mixtures of 0.4 and 1.6% propane in argon were shocked over the temperature range 1050–1700°K and the reaction products were quantitatively analyzed. Five of the eight products (CH_4, C_2H_4, C_2H_6, C_3H_6 and H_2) were observed over the entire temperature range. The other three (C_2H_2, $CH_3C{\equiv}CH$, and $CH_2{=}C{=}CH_2$) were observed in measurable quantities only in the higher temperature range of this study. The experimental product distribution for a mixture of 1.6% propane in argon is shown in Figure 1. In view of the very high sensitivity of the analyses, two orders of magnitude variation in the rate of production of the first five products could be observed before any appreciable decomposition of propane (a few per cent) took place. This was true over the temperature range 1050–1250°K. Under these conditions, at practically constant reactant (C_3H_8, Ar) concentrations, pseudo-zero-order plots were made, in which the logarithms of the rate of production of CH_4, C_2H_4, C_2H_6, C_3H_6, and H_2 were plotted against $1/T$. Over the temperature range 1050–1250°K these plots yielded straight lines. An example for methane is shown in Figure 2. The three different symbols on this plot correspond to three groups of experiments run at different compositions and pressures. These three groups provided the basis for the evaluation of the "reaction orders" and activation energies for the rate of production of each one of the five reaction products mentioned above. The fact that the squares and the circles appear on a single line indicates a zero-order dependence on the argon. This was found also for the other four reaction products. The triangles (Figure 2) which correspond to a mixture containing four times more propane show a higher rate of production of methane. The vertical distance between the lines provides a rough estimate of the power dependence on propane. The exact value of this parameter (β) and the temperature dependence in the equation

$$\Delta[CH_4]/\Delta t = 10^{\alpha} \exp(-E/RT)[C_3H_8]^{\beta} \qquad \text{(II)}$$

was obtained by a regression analysis of all the tests run between 1050 and 1250°K. Table I lists the parameters α, β, and E for all the five primary products.

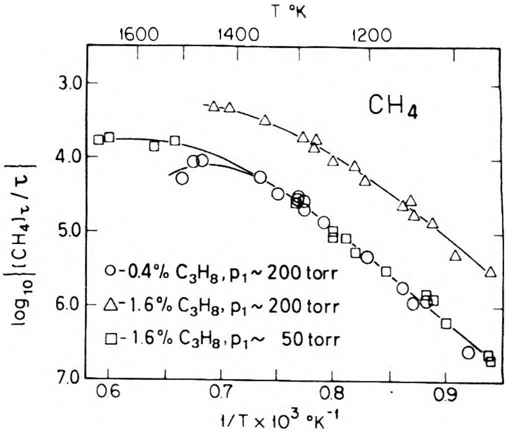

Figure 2. A plot of log $[CH_4]/\tau$ vs. $1/T$ for three groups of experiments as listed in the figure. The lines bend very little below 1250°K. The distance between the two lines provides an indication of the power dependence on the initial propane concentration.

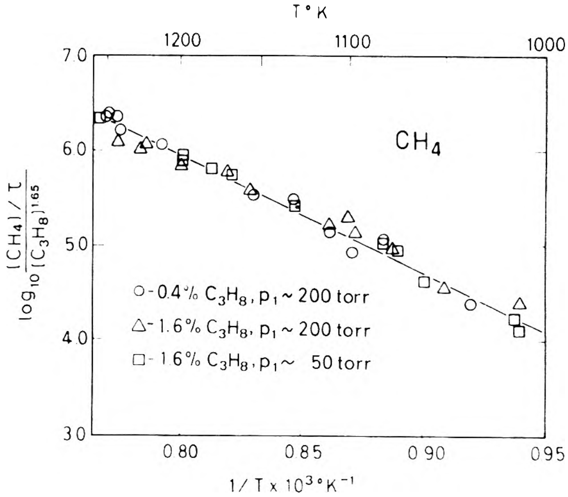

Figure 3. A plot of log $([CH_4]/\tau)/[C_3H_8]_0^{1.65}$ vs. $1/T$ for all the test runs below 1300°K. All the data points when normalized by $[C_3H_8]_0^{1.65}$ coincide to a single line. The slope of the line and the 1.65 power dependence are the parameters which the computer experiments must reproduce.

TABLE II: Reaction Scheme and Rate Constants for the Decomposition of Propane

Reaction	Rate constants, cc, mol, sec	Ref
I. Initiation		
1. $C_3H_8 \longrightarrow CH_3 + C_2H_5$	$k_{-1} = 2.4 \times 10^{12}$	This work
II. Chain propagation		
2A. $CH_3 + C_3H_8 \longrightarrow CH_4 + i\text{-}C_3H_7$	$10^{12.55} \exp(-10.3 \times 10^3/RT)$	This work
2B. $CH_3 + C_3H_8 \longrightarrow CH_4 + n\text{-}C_3H_7$		
3A. $H + C_3H_8 \longrightarrow H_2 + i\text{-}C_3H_7$	$10^{13.8} \exp(-8.0 \times 10^3/RT)$	8
3B. $H + C_3H_8 \longrightarrow H_2 + n\text{-}C_3H_7$		
III. Unimolecular decompositions of free radicals		
4A. $i\text{-}C_3H_7 \longrightarrow C_2H_4 + CH_3$	$10^{12.11} \exp(-34.5 \times 10^3/RT)$	16
4B. $n\text{-}C_3H_7 \longrightarrow C_2H_4 + CH_3$	$10^{13.8} \exp(-33.2 \times 10^3/RT)$	16
5A. $i\text{-}C_3H_7 \longrightarrow C_3H_6 + H$	$10^{14.3} \exp(-41.3 \times 10^3/RT)$	16
5B. $n\text{-}C_3H_7 \longrightarrow C_3H_6 + H$	$10^{13.8} \exp(-38.0 \times 10^3/RT)$	16
6. $C_2H_5 \longrightarrow C_2H_4 + H$	$10^{13.5} \exp(-40.7 \times 10^3/RT)$	16
IV. Termination		
7. $CH_3 + CH_3 \rightleftarrows C_2H_6$	2.4×10^{13}	3

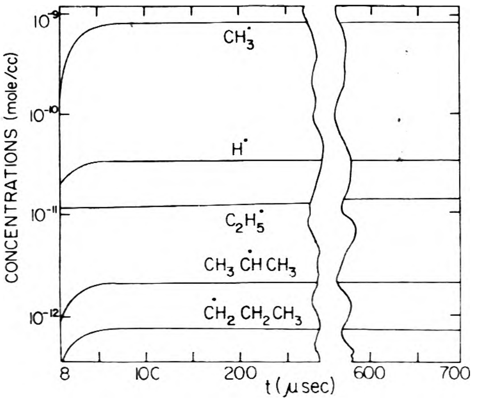

Figure 4. Calculated profiles of the five radicals which are present in the reaction system. They reach a steady-state concentration at the very early stages of the reaction.

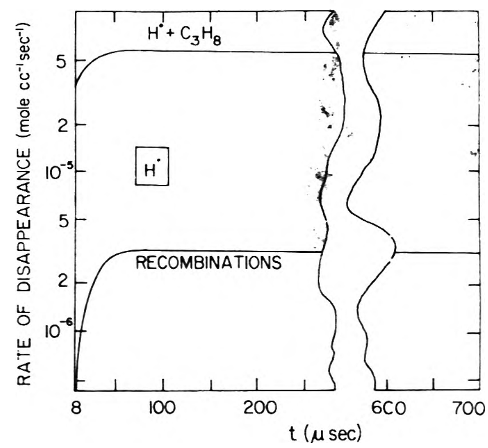

Figure 5. The rates at which hydrogen atoms react via the various channels. The transfer reaction $H + C_3H_8 \rightarrow H_2 + C_3H_7(n,i)$ is considerably faster than all the possible recombinations involving H atom.

Figure 3 shows that when the rate of production of methane is normalized by $[C_3H_8]^{\beta=1.65}$ (see Table I), the points of all three groups of experiments coincide to a single line.

III. Discussion

A. Introductory Remarks. The kinetic scheme which describes the decomposition of propane consists of four types of chemical reactions: (1) initiation; (2) transfer (propagation); (3) unimolecular decomposition of unstable free radicals; and (4) recombination reactions. The scheme which will be discussed here does not include the decomposition of ethylene and propylene to yield allene, propyne, and acetylene. These three products began to appear in measurable quantities in a dwell time of approximately 1 msec far above 1300°K. Over this temperature range the experimental kinetic parameters no longer represent the rate of production of the five reaction products mentioned above. The following scheme describes the system only over the temperature range 1050–1250°K.

B. Reaction Scheme. Of the overall scheme of 29 chemical reactions which participate in the decomposition of propane only 11 are important and are needed to provide a full description of the system. The 11 reactions and their rate constants are listed in Table II. As may be seen, there is only one initiation step and one termination. There are four propagation steps and five reactions involving decomposition of unstable free radicals. This final reaction scheme was constructed by the elimination of elementary steps which were found to have no influence on the distribution of reaction products and on their temperature and composition dependence.

There are five free radicals in the system, the calculated profiles of which are shown in Figure 4. They all reach a steady-state concentration in the very early stages of the reaction. Since the decomposition of propane is a chain reaction carried by these five free radicals, it is of interest to examine and compare the various channels by which these radicals react. In fact, the competition between the parallel reactions which remove each radical from the system determine to a great extent its overall behavior. The elimination of many elementary steps from the overall reaction scheme of 29 reactions was based on the comparison between the decompositions, recombinations, and transfer reactions that these radicals undergo. In Figures 5–9 calculated rates of disappearance of the five free radicals during the entire reaction time are shown. These, as well as the profiles shown in Figure 4, were calculated using the complete scheme of 29 steps in both the forward and the reverse reactions.

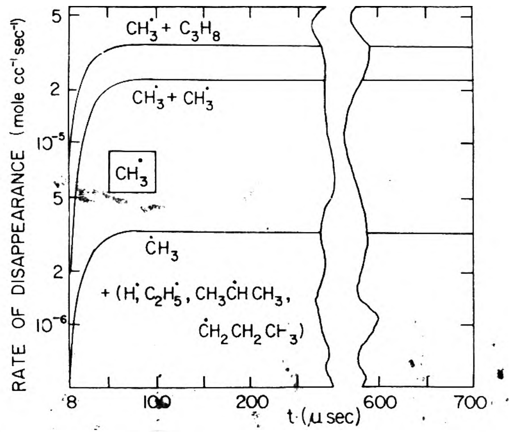

Figure 6. The rates of reaction of methyl radicals. The $CH_3 + CH_3$ recombination is comparable in its rate to the $CH_3 + C_3H_8 \rightarrow CH_4 + C_3H_7(n,i)$ transfer. All other recombinations are more than an order of magnitude slower and are therefore eliminated from the reaction scheme.

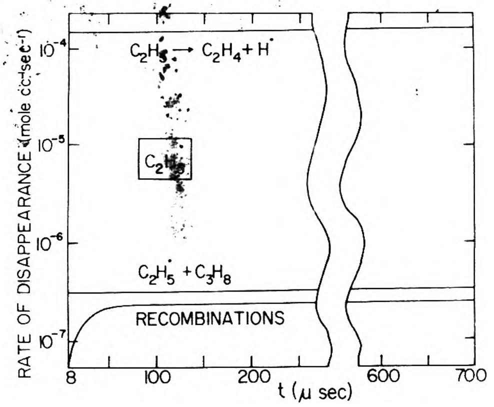

Figure 7. Reactions of the ethyl radicals. Only the unimolecular decomposition is considered. Recombinations and transfer are very slow and are neglected.

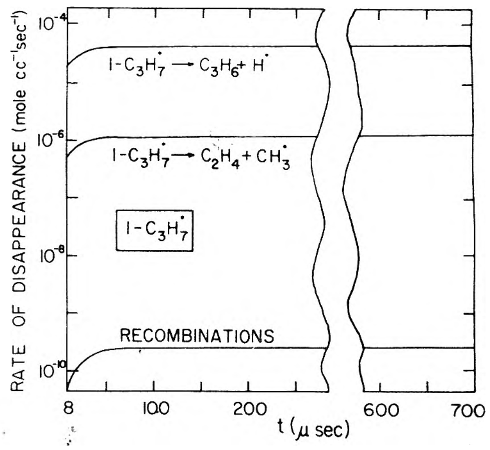

Figure 8. The rate of disappearance of i-C_3H_7. The two unimolecular decomposition channels are many orders of magnitude faster than the recombinations which are eliminated from the reaction scheme.

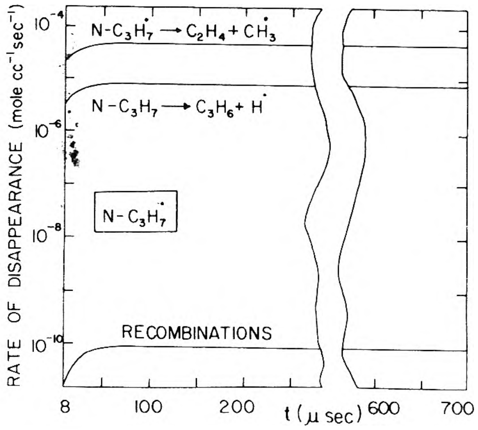

Figure 9. The disappearance rate of n-C_3H_7. Here too only the two decompositions are left.

Since there are five free radicals in the system there are 15 possible recombination reactions which in principle lead to chain termination. It may be seen in Figures 5-9, however, that there is only one recombination step which can compete with the other channels of disappearance. This is the $CH_3 + CH_3 \rightleftharpoons C_2H_6$ reaction. In all the other cases the recombinations are too slow to compete either with the unimolecular decompositions or with the transfer reactions of the type $R + C_3H_8 \rightarrow RH + C_3H_7$. In these calculations we assigned to the recombination rate constants values ranging from 1 to 2 × 10^{11} cc mol^{-1} sec^{-1} depending on the size of the recombining radicals (except for the $CH_3 + CH_3$ step, $k = 2.4 \times 10^{13}$ cc mol^{-1} sec^{-1} [3] and the $CH_3 + H$ step which, under our experimental conditions, is 2.4 × 10^{12} cc mol^{-1} sec^{-1} [4]). It has recently been shown that the recombination reaction $C_2H_5 + C_2H_5$ proceeds with a rate constant of 3 × 10^{11} cc mol^{-1} sec^{-1}.[5-7] This is approximately 100 times lower than the rate constant of the $CH_3 + CH_3$ recombination. More complicated free radicals recombine probably with an even lower rate constant. It is believed that the rate constants chosen for the various recombinations provide an upper limit for their rates. Any disproportionation/recombination ratio of the present radicals is considerably lower than unity[8] and does not change the general picture.

We have therefore eliminated 14 recombinations from the original reaction scheme and left only the $CH_3 + CH_3$ step. No change in the computer output was noticed when these reactions were not considered. After the elimination of the unimportant recombinations, the following are the only channels for reaction.

(1) *H Atom.* The transfer reactions $H + C_3H_8 \rightarrow H_2 + C_3H_7(n,i)$.

(2) *CH_3 Radical.* The $CH_3 + CH_3$ recombination and the two $CH_3 + C_3H_8 \rightarrow CH_4 + C_3H_7$ transfer reactions. These reactions have comparable rates (Figure 6) and must be considered.

(3) *C_2H_5 Radical.* This radical as well as the two propyl radicals have an additional reaction channel which is the unimolecular decomposition. Figure 7 shows that under the experimental conditions of the described experiment the transfer reactions $C_2H_5 + C_3H_8 \rightarrow C_2H_6 + C_3H_7(n,i)$ are very slow compared to the unimolecular decomposition $C_2H_5 \rightarrow C_2H_4 + H$ and are therefore negligible. This is supported also by the observed isotopic distribution of the various ethanes and ethylenes in studies where a mixture of 0.8% C_3D_8 and 0.8% C_3H_8 in argon was shocked to a temperature around 1100°K.[2a] No scrambled ethylenes (CH_2–CD_2) were observed whereas the ratio CH_3CH_3:CH_3CD_3:CD_3CD_3 was 1:2:1 without any C_2H_5D and C_2D_5H present. This indicates that the ethylene retains its original skeleton whereas ethane is a result of methyl radicals recombi-

TABLE III: A Comparison between the Calculated and Observed Parameters with the Reaction Scheme Shown in Table II

Parameter		CH_4	C_2H_4	C_2H_6	C_3H_6	H_2
C_i, mol/cc after 700 μsec 1200°K	calcd	$2.9E-8$	$5.0E-8$	$1.0E-8$	$3.4E-8$	$4.4E-8$
	exptl	$2.9E-8$	$4.9E-8$	$7.5E-9$	$2.6E-8$	$3.6E-8$
Activation energy E_a, kcal/mol	calcd	55.1	63.9	86.5	60.4	64.4
	exptl	54.8	62.5	67.3	52.0	63.2
β_i power dependence on $[C_3H_8]_0$	calcd	1.61	1.34	1.08	1.43	1.33
	exptl	1.65	1.38	1.24	1.45	1.41

nation, and not of the reaction $C_2H_5 + C_3H_8 \rightarrow C_2H_6 + C_3H_7(n,i)$.

(4) *(n,i)-C_3H_7 Radicals*. Normal and isopropyl radicals can isomerize in a transfer type reaction. $n\text{-}C_3H_7 + C_3H_8 \rightleftarrows i\text{-}C_3H_7 + C_3H_8$. The steady-state concentrations of the iso- and the normal propyls, however, are very close to their concentration ratio at equilibrium. In addition, the pseudo-first-order rate constant of the isomerization ($10^{12.1} \exp(-17 \times 10^3/RT)[C_3H_8]_0{}^9$) is several orders of magnitude lower than that of the unimolecular decompositions. The introduction of this step into the reaction scheme had no effect on the results. Again, the only reactions that contribute to the overall reaction scheme are the unimolecular decompositions to $C_2H_4 + CH_3$ and $C_3H_6 + H$.

Together with one initiation step $C_3H_8 \rightarrow CH_3 + C_2H_5$ it brings the number of reactions which are needed to describe the system to 11. These are listed in Table II. (The initiation step $C_3H_8 \rightarrow C_3H_7 + H$ is much slower than the $C_3H_8 \rightarrow CH_3 + C_2H_5$ step and is therefore neglected[10].)

C. Reaction Parameters. The purpose of the computer modeling was not only the elimination of unimportant elementary steps but also to find out whether the suggested scheme and the set of rate constants are consistent and capable of reproducing the set of parameters which were found experimentally and are listed in Table I. One should demand that the reaction scheme by a series of computer experiments will reproduce the following sets of parameters: (1) the power dependence of the rates on the initial propane concentration for each one of the five reaction products; (2) the concentrations of the reaction products at the end of the experimental dwell time of 700 μsec; (3) the "activation energies;" (4) the ratio $[CH_4]/[C_2H_6]$ after 700 μsec. This ratio is very sensitive to the relative rates of reactions 2 and 7.

The experimental results show that the extent of decomposition of propane below 1250°K is only a few per cent. We have therefore neglected all the back reactions in the final calculations except for the $CH_3 + CH_3 \rightleftarrows C_2H_6$ step which approaches equilibrium. Also, owing to the small extent of reaction, we did not consider in the final scheme transfer reactions involving products such as $CH_3 + H_2 \rightarrow CH_4 + H$, etc... These were shown to be insignificant in view of the relatively low concentration of all the reaction products relative to the reactant propane.

We have run three calculations for each reaction scheme which was tested. These will be referred to as "calculated shocks." They are (1) 1.6% C_3H_8, P_1 = 200 Torr, T = 1200°K; (2) 0.4% C_3H_8, P_1 = 200 Torr, T = 1200°K; and (3) 1.6% C_3H_8, P_1 = 200 Torr, T = 1100°K. A comparison between the calculated shocks 1 and 2 gave the value of β for each one of the reaction products and the comparison between shocks 1 and 3 gave the value of E. The concentrations of the products after 700 μsec as well as the ratio $[CH_4]/[C_2H_6]$ are given for calculated shock 1 (Table III).

There are two points to mention regarding the calculations. The reaction time is given a period of 700 μsec in which the only possible change in temperature is due to the chemistry and not to the gas dynamics. The change in temperature in calculated shock 1 was less than 10°K during the 700-μsec reaction time so it was indeed an isothermal period. After the initial isothermal period of 700 μsec the system was cooled adiabatically and reversibly at a linear rate of approximately 0.5°K/μsec, until it was completely frozen. The differential equation for the concentration of component i, C_i, during the cooling phase, is given by

$$\frac{d[C_i]}{dt} = \sum_{j=1}^{m} \alpha_{ij}\{\text{rate}_j(\text{b}) - \text{rate}_j(\text{f})\} + \frac{C_i}{(\gamma - 1)T}\frac{dT}{dt} \tag{III}$$

where m is the number of chemical reactions and α_{ij} is the stoichiometric coefficient for component i in the jth reaction. It is zero when this component does not participate in the jth reaction. It is positive when it appears on the left-hand side of the chemical reaction and it is negative when it appears on the right-hand side. The rate constants k_j were reviewed and corrected for the change in temperature following every integration step. We have used Treanor's method in our numerical integration.[11] The concentrations which are shown in Table III as "concentration after 700 μsec" are actually those at the end of the entire cooling phase. For the sake of comparison with the experiment they are normalized by the overall concentration change due to expansion. The picture during the cooling phase shows a very sharp decrease in the free radical concentrations but very little change in the concentration of the products. Only a few per cent is added during the cooling phase. We also found that the system is but very little sensitive to the exact cooling rate (dT/dt) provided the latter is high enough.

The rate constants used in the calculations were taken from various sources in the literature as listed in Table II. The rate constant reported for the two transfer reactions 2 and 3 is that for the rate of disappearance of propane. The ratio of the rate of production of the isopropyl radical to the normal isomer k_i/k_n was taken as $10^{-0.62} \exp(+2700/RT)$.[9]

In our first series of calculations we used a value for the rate constants k_1 as has been suggested by previous investigators. Leathard and Purnell[10] calculated k_1 from the relation $k_1 = k_{-1}K_1$ where k_{-1} was assumed equal to $2k_7$. Our calculations using this rate constant gave very poor agreement between the parameters obtained by the experimental and the calculated shocks. The following disagreement has resulted from these calculations.

(1) A value of 0.4 was obtained for the ratio $[CH_4]/[C_2H_6]$ compared to a value of 4 observed experimentally (see Figure 1). The disaggreement factor was 16.

(2) The concentrations of C_2H_6, C_2H_4, and H_2 were high by a factor of 4–12 compared to what had been observed experimentally.

(3) The power dependence on the initial propane concentration ranged between 1.06 and 1.12; a serious disagreement with the experiment (see Table I).

Since the system as a whole is highly sensitive to the value of k_1, a value of $k_{-1} = 2k_7$ is clearly incorrect. By decreasing the value of k_1, one decreases the steady-state concentration of CH_3. The rate of reaction 7 which is the main supplier of ethane is proportional to $[CH_3]^2$ whereas that of reaction 2, which forms methane, is proportional to $[CH_3]$. It is therefore expected that decreasing k_1 will increase the ratio $[CH_4]/[C_2H_6]$.

It has recently been shown that the $C_2H_5 + C_2H_5$ recombination proceeds with a rate constant roughly 100 times lower than that of the $CH_3 + CH_3$ recombination.[5] On the assumption that k_{-1} lies somewhere between these two k's, we have decreased the rate constant k_{-1} up to a point where the ratio $[CH_4]/[C_2H_6]$ in calculated shock 1 matched the experimental value of 4. This required the reduction of k_{-1} by a factor of a few hundred. Under these conditions, then, the concentrations of the reaction products were far lower than the ones observed experimentally and the activation energies were on the average 20 kcal/mol higher than the experimental ones. It was impossible to find agreement for all the four sets of parameters together by adjusting the value of k_{-1} alone.

Before one varies rate constants in order to try and match the calculations with the experiment, one should examine the sensitivity of the system to the various rate constants which appear in the reaction scheme. It is easy to show that the rates of reactions 3 and 6, for example, are almost independent of their respective rate constants. They behave in such a manner because the C_2H_5 and the H radicals reach a steady-state concentration at the very early stages of the reaction (see Figure 4) and each radical then reacts through *only one channel*. The rates of reactions 3 and 6 are determined by the rates at which C_2H_5 and H are formed. A variation in the rate constants of reactions 3 or 6 will result in the variation of the steady-state concentrations of the radicals but will leave the rates unchanged. Indeed, there was no effect whatsoever on the results when k_6 was varied tenfold. In the decomposition reactions 4 and 5 the adjustments of the relative rates of the A and B channels (see Table II) will vary the ratio $[C_3H_6]/[C_2H_4]$ and $[CH_4]/[H_2]$ but not the general picture and the disagreement mentioned above. Moreover, the rate constants of reactions 4 and 5 are pretty well known and a drastic change in its values is unjustified.

It seems therefore that the only rate constant which might affect the calculations (in addition to that of reaction 1) is that of reaction 2. This *propagation* reaction competes for the CH_3 radicals with a *termination* reaction (7). The variation of k_2 is therefore expected to change the calculated parameters.

A number of values have been suggested in the literature for k_2: $10^{12.64} \exp(-17.5 \times 10^3/RT)$,[9] $10^{12.57} \exp(-15.9 \times 10^3/RT)$,[10] and $10^{11.9} \exp(-10.3 \times 10^3/RT)$[14] which yield at 1200°K: $10^{9.46}$, $10^{9.86}$, $10^{10.03}$, respectively. We used the highest reported value in our initial calculations but found it still too low to provide a match with the experiment. We can show now that the value of $10^{9.86}$ which was evaluated by Leathard and Purnell was too low by at least a factor of 5. They evaluated k_2 from a relation

$$k_2 = (C/K_1^{1/2})(k_7/k_{-1})^{1/2} \qquad \text{(IV)}$$

and assumed k_{-1} equal to $2k_7$, i.e., $10^{13.7}$ cc mol^{-1} sec^{-1}. K_1 is the equilibrium constant of reaction 1 and C is an experimental measured quantity. As has been mentioned above and will be shown later, k_{-1} is roughly of the order of $10^{12.4}$ cc mol^{-1} sec^{-1}. This error in k_{-1} produces a factor of 5 error in k_2. Although we cannot comment in detail on the other two reported values of k_2 we believe that they are also too low.

In view of this finding regarding k_2, we have made the following changes in our scheme. Since k_1 and k_2 are interconnected, as a first trial we chose k_1 according to the criterion suggested by Benson[5]

$$k_{(CH_3+C_2H_5)} = 2\{k_{(CH_3+CH_3)}k_{(C_2H_5+C_2H_5)}\}^{1/2} = 5.2 \times 10^{12} \text{ cc mol}^{-1} \text{ sec}^{-1}$$

and increased k_2 to match the ratio $[CH_4]/[C_2H_6]$ with the experimental value. This required a factor of 4. Following these changes the overall picture became very good. The best agreement, however, was obtained by choosing $k_{-1} = 10^{12.4}$ cc mol^{-1} sec^{-1} and increasing k_2 by a factor of 4.5. We could not tell how the 4.5 is divided between A and E and increased the A factor by 4.5. The agreement now is demonstrated in Table III for the five reaction products CH_4, C_2H_4, C_2H_6, C_3H_6, and H_2. The picture is very good indeed except for ethane, for which the calculated activation energy is considerably higher than the experimental one and for propylene where E is slightly higher. It is unclear whether the errors lie in the calculations or are experimental ones.

D. Low Temperature Regime. Whereas there is only one detailed study of propane decomposition above 1000°K,[2a] its low temperature decomposition has been studied and discussed quite extensively.[9,10,12-15] In the low temperature regime the initiation step is still reaction 1 but in view of the high activation energy of this step the steady-state concentration of the methyl and ethyl radicals is extremely low. Recombination of methyl radicals is therefore negligible. Also, the decomposition reaction $C_2H_5 \rightarrow C_2H_4 + H$ is slow ($E_a = 40.7$ kcal/mol). The channels for the removal of these two radicals are therefore $CH_3 + C_3H_8 \rightarrow CH_4 + C_3H_7$ and $C_2H_5 + C_3H_8 \rightarrow C_2H_6 + C_3H_7$. Since the reaction $CH_3 + CH_3$ hardly occurs and C_2H_5 is not regenerated along the chain, the per cent of ethane found at low temperatures was very minute. These observations were confirmed by our reaction scheme of 29 reactions when it was run on the computer at 800°K. Also, it has been shown at the low temperature regime, and contrary to the high temperature mechanism, that $[H_2] = [C_3H_6]$ and $[CH_4] = [C_2H_4]$ over a relatively wide range of pressures. This is rationalized by the fact that these four substances are formed only via the propyl radical decompositions and that there is no contribution from the C_2H_5 decomposition. These equalities were found in our low temperature calculations, to three significant figures.

It is believed that the complete reaction scheme describes the system over a wide range of temperatures. There are a number of reactions which are very important at low temperatures but become negligible when the system is examined at higher temperatures.

References and Notes

(1) In partial fulfillment of the requirements for a Ph.D. Degree. Thesis to be submitted to the Senate of the Hebrew University by M.F.

(2) (a) A. Lifshitz, K. Scheller, and A. Burcat, *Proc. 7th Int. Shock Tube Symp.*, 690 (1973); (b) A. Lifshitz, S. H. Bauer, and E. L. Resler, Jr., *J. Chem. Phys.*, **38,** 2056 (1963).

(3) F. K. Truby and J. K. Rice, *Int. J. Chem. Kinet.*, **V,** 721 (1973).

(4) R. Hartig, J. Troe, and H. Gg. Wagner, *Symp. (Int.) Combust.*, [*Proc.*], *13th, 1970*, 147 (1971).

(5) R. Hiatt and S. W. Benson, *J. Amer. Chem. Soc.*, **94,** 25 (1972).

(6) R. Hiatt and S. W. Benson, *J. Amer. Chem. Soc.*, **94,** 6886 (1972).

(7) P. D. Pacey and J. H. Purnell, *Int. J. Chem. Kinet.*, **IV,** 651 (1972).

(8) A. F. Trotman-Dickenson and G. S. Milne, *Nat. Stand. Ref. Data Ser., Nat. Bur. Stand.*, **No. 9,** 108 (1967).

(9) D. A. Leathard and J. H. Purnell, *Proc. Roy. Soc., Ser. A*, **306,** 553 (1968).

(10) D. A. Leathard and J. H. Purnell, *Proc. Roy. Soc., Ser. A*, **305,** 517 (1968).

(11) L. Lapidus and J. H. Seinfeld, "Numerical Solution of Ordinary Differential Equations," Academic Press, New York, N.Y., 1971, p 270.

(12) K. J. Laidler, N. H. Sagert, and B. W. Wojciechowski, *Proc. Roy. Soc., Ser. A*, **270,** 242 (1962).

(13) K. J. Laidler, N. H. Sagert, and B. W. Wojciechowski, *Proc. Roy. Soc., Ser. A*, **270,** 254 (1962).

(14) M. M. Papic and K. J. Laidler, *Can. J. Chem.*, **49,** 535 (1971).

(15) M. M. Papic and K. J. Laidler, *Can. J. Chem.*, **49,** 549 (1971).

(16) S. W. Benson and H. E. O'neal, *Nat. Stand. Ref. Data Ser., Nat Bur. Stand.*, **No. 21** (1970).

Condensed-Phase Photochemistry of Propylene

William A. Guillory*[1]

Department of Chemistry, University of Utah, Salt Lake City, Utah 84112

and Samuel G. Thomas, Jr.

Department of Chemistry, Drexel University, Philadelphia, Pennsylvania 19104

(Received August 12, 1974)

Publication costs assisted by the National Science Foundation

The vacuum-ultraviolet photolysis of propylene (C_3H_6) in argon, nitrogen, CO, and CO-doped argon matrices has been performed between 8 and 10 K. The results of these experiments suggest that the photodecomposition of propylene occurs principally from the absorption of the 1215-Å hydrogen resonance line. Although this energy is above the ionization threshold (9.6 eV), no evidence of ionization was observed. The major products of photolysis are methylacetylene, allene, methane, and acetylene, which presumably result from three primary processes: $C_3H_6 + h\nu \rightarrow CH_4 + C_2H_2$ (1); $C_3H_6 + h\nu \rightarrow H_2 + CH_2{=}C{=}CH_2$ (2); and $C_3H_6 + h\nu \rightarrow H_2 + CH_3C{\equiv}CH$ (3). Processes 1, 3, and possibly 2 are also the major reactions resulting from photolysis at 1745, 1634, 1580, and 1495 Å with various vacuum-ultraviolet resonance lamps. Based on relative intensities, process $1 > 3 > 2$ as a result of photolysis with the 1215-Å line, but $1 > 2 \simeq 3$ for the other resonance line sources.

I. Introduction

The photolysis of propylene in the gas phase both below and above its ionization potential has been previously studied.[2-4] Becker, Okabe, and McNesby[2a] carried out the photolysis at 1470 and 1236 Å producing the following major products: acetylene, ethylene, hydrogen, methane, ethane, propane, propyne, allene, isobutane, and C_4-unsaturated hydrocarbons. Photolysis has also been performed with the 1849-Å Hg line[2b,3] to give many of the same products. In a recent study performed in this laboratory on the photolysis of cyclobutanone,[5] propylene, produced as a primary product, was observed to undergo secondary photolysis. The secondary photolysis processes suggested in that study are confirmed in more detail and are the subject of this publication.

The advantages and disadvantages of the matrix photolysis technique with band pass filtered and resonance lamp sources have been discussed in the cyclobutanone work.[5] In this particular study the primary photodecomposition products, methylacetylene, allene, methane, and acetylene, are all stable products and easily identified from their known infrared spectra. The infrared spectra of these species provided a direct means, based on ratios of optical densities, to compare the relative importance of the primary photochemical processes as a function of exciting energy. Information about the mechanism of photodecomposition was also obtained.

II. Experimental Section

The propylene (C_3H_6) was obtained from Air Products and Chemicals, Inc. and used without further purification. Although the argon and carbon monoxide matrix gases (99.99% purity) were also used without further purification, the nitrogen matrix gas (99.99% purity) was passed through a molecular sieve which was contained in a coiled copper tube and immersed in liquid nitrogen to remove water impurity.

The ratios of the matrix to active materials (M:A) were either 400:1, 600:1, or 800:1. Sample mixtures were delivered through a Granville-Phillips leak valve, generally at a

TABLE I: Summary of Absorptions (cm^{-1}) in the Ar:C_3H_6 = 400:1 Experiments

Before photolysis	After photolysis[a]	Assignment
	3335 mw	$CH_3C\equiv CH$
	3323 mw	
	3299 w	C_2H_2
	3287 m	
3090 s		C_3H_6
3078 mw		
3035 m		C_3H_6
3025 mw		
2993 m		C_3H_6
2982 s		
2941 s		C_3H_6
2922 s		C_3H_6
2889 m		C_3H_6
2867 w		C_3H_6
2859 m		
	1954 w	$CH_2{=}C{=}CH_2$
1819 ms		C_3H_6
1648 ms		C_3H_6
1452 vs		C_3H_6
1438 s		C_3H_6
1414 mw		C_3H_6
1372 mw		C_3H_6
	1333 w	C_2H_2
	1303 mw	CH_4
	1247 mw	
1042 ms		C_3H_6
997 s		C_3H_6
987 mw		
931 m		C_3H_6
915 m		C_3H_6
909 vs		
899 vw		
	838 mw	$CH_2{=}C{=}CH_2$
	800 mw	
786 w		
	741 vw	C_2H_2
	735 s	
	628 s	$CH_3C\equiv CH$
577s		C_3H_6
	330 vw	$CH_3C\equiv CH$

[a] After 5 hr of simultaneous deposition and photolysis with a hydrogen resonance lamp (LiF).

rate of 1 mm/min or less from a 2.5-l. volume. The cryogenic instrument used was an Air Products closed-cycle helium Displex refrigerator.

The photolysis of the matrix-isolated species was accomplished by subjecting the samples on the cold CsI window to direct radiation through CaF_2, LiF, or Suprasil II vacuum-ultraviolet windows. Microwave powered hydrogen, bromine, and nitrogen flow discharge lamps were used as photolysis sources.[6] The spectral characteristics of the hydrogen, bromine, and nitrogen discharge lamps have been discussed in previous publications.[7-9]

The infrared spectra were recorded on Perkin-Elmer 621 and 180 spectrophotometers. The resolution and frequency accuracy are estimated to be better than 1 cm^{-1} between 200 and 2000 cm^{-1}, and 2 cm^{-1} between 2000 and 4000 cm^{-1}.

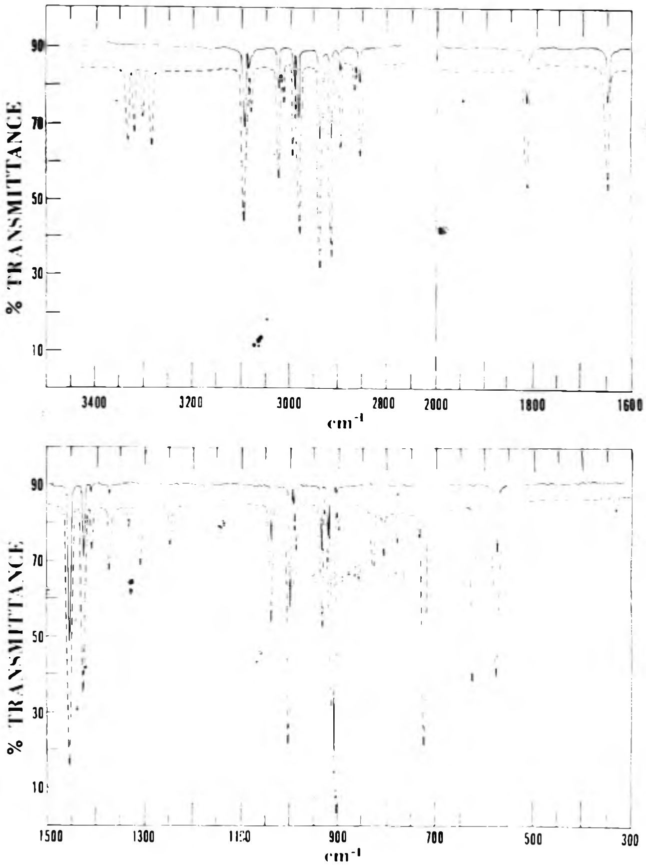

Figure 1. Infrared spectra of Ar:C_3H_6 = 400:1: (a, ——) deposition at 8 K, mm/min for 70 min from a 2.5-l. volume; (b, - - - - -) simultaneous deposition and photolysis for 5 hr with a hydrogen discharge lamp (LiF).

III. Results

The infrared spectrum of a film of Ar:C_3H_6 = 400:1 before photolysis is shown in the solid trace of Figure 1 and summarized in the first column of Table I. The spectrum of the unphotolyzed sample agrees well with the gas-phase spectrum reported by Sadtler Research Laboratories, Inc.[10] with consideration given for the usual slight matrix shifts.

When the Ar:C_3H_6 = 400:1 film was subjected to radiation from a microwave powered hydrogen resonance lamp, new absorptions appeared due to the production of methylacetylene,[11] acetylene,[12] allene,[13] and methane.[14] These results are summarized in the last two columns of Table I and shown as a dashed trace in Figure 1.

Excitation into a possible Rydberg series 1500–1420 Å and the continuous $\pi \rightarrow \pi^*$ 1900–1500-Å band[15,16] of C_3H_6 (Ar:C_3H_6 = 400:1) was performed with the 1743-, 1745-, and 1495-Å resonance lines of a microwave powered nitrogen resonance lamp through the CaF_2 transmitting window. A bromine resonance lamp (1634 and 1580 Å) was also used for excitation of C_3H_6 (Ar:C_3H_6 = 800:1) into the $\pi \rightarrow \pi^*$ band. The products resulting from photolysis in these experiments were the same as those obtained with the hydrogen resonance lamp except for a significantly lower efficiency of conversion. The production of allene relative to acetylene and methylacetylene was also observed to increase as compared to their relative concentrations using the hydrogen resonance source.

In order to help clarify the mechanism of photodecomposition as a function of the exciting wavelengths, a series of photolysis experiments was performed with propylene isolated in nitrogen, CO, and CO-doped argon matrices. Systematic excitation into the vacuum-uv absorption bands of C_3H_6 isolated in N_2 matrices with the various resonance line sources resulted in the production of the same photolysis products cited above. No absorptions attributable to diazomethane (CH_2N_2)[17] were observed in these experiments, suggesting the absence of methylene as an important intermediate in the photochemical reactions at these wavelengths. Similar experiments involving CO and CO-doped argon matrices again resulted in the generation of the same products previously observed. The absence of absorptions due to HCO[18] in these experiments suggest that H atom detachment plays a minimal role in the major photodecompositions observed here. In addition, no absorptions due to ketene[19] (CH_2CO) were observed, which again suggests that CH_2 is not a major fragment produced in these experiments.

IV. Discussion

The results of photolysis with a hydrogen resonance lamp of propylene isolated in argon indicated new absorptions in the infrared due to methylacetylene, acetylene, allene, and methane. Performing the same experiment with bromine and nitrogen discharge lamps showed similar new features with the exception of significantly lower conversion efficiencies. On the basis of the gas-phase vacuum-uv photochemistry of C_3H_6,[20] the following reactions could be important in this system and serve as a basis for discussion:

$$C_3H_6 + h\nu \longrightarrow CH_4 + C_2H_2 \tag{1}$$

$$C_3H_6 + h\nu \longrightarrow H_2 + CH_2{=}C{=}CH_2 \tag{2}$$

$$C_3H_6 + h\nu \longrightarrow H_2 + CH_3C{\equiv}CH \tag{3}$$

$$C_3H_6 + h\nu \longrightarrow H + C_3H_5 \tag{4}$$

$$C_3H_6 + h\nu \longrightarrow CH_2 + C_2H_4 \tag{5}$$

$$C_3H_6 + h\nu \longrightarrow CH_3 + C_2H_3 \tag{6}$$

$$C_2H_3 \longrightarrow C_2H_2 + H \tag{6a}$$

$$C_3H_6 + h\nu \longrightarrow C_3H_6^+ + e^- \tag{7}$$

Photolysis of C_3H_6 with the 1215-Å line of the hydrogen resonance lamp above the ionization potential (9.6 eV) might appear to favor the occurrence of process 7. However, we obtained no evidence in this study to support the ionization process. The reason that it probably does not occur in these experiments is that it is as important to have an electron acceptor as it is to have an energy source which exceeds the ionization potential of the species of interest. The absence of infrared absorptions, after photolysis, attributable to ethylene and the methyl radical, suggests that (5) and (6) are unimportant in this study. Additional experiments, which indicated the absence of CH_2 and H atom generation, also confirm that (4), (5), and (6a) do not occur to any significant extent. The major primary processes occurring as a result of photolysis with the hydrogen, nitrogen, and bromine resonance lamps appear to be (1), (2), and (3). The absence of any significant HCO production in the CO matrix experiments again suggests no H-atom detachment and that (2) and (3) occur exclusively via molecular detachment at these wavelengths.

On the basis of the relative intensities of the products with the various resonance line sources, the 1215-Å photolysis source is the most efficient in effecting processes 1, 2, and 3. Based on the relative optical densities of the most intense vibrational fundamentals of acetylene, methylacetylene, and allene, $(1) > (3) > (2)$ with the H-resonance source, and $(1) > (3) \simeq (2)$ with the other resonance line sources.

Acknowledgment. We gratefully acknowledge support of this work by the National Science Foundation through Grants No. GP-34141 X and GP-44109 X.

References and Notes

(1) Alfred P. Sloan Foundation Fellow.

(2) (a) D. A. Becker, H. Okabe, and J. R. McNesby, *J. Phys. Chem.*, **69**, 538 (1965); (b) S. Aral, S. Shida, and T. Nishikawa, *Bull. Chem. Soc. Jpn.*, **39**, 2548 (1966).

(3) P. Borrell, A. Cervenka, and J. W. Turner, *J. Chem. Soc. B*, 2293 (1971).

(4) E. Tschuikow-Roux, *J. Phys. Chem.*, **71**, 2355 (1967).

(5) S. G. Thomas and W. A. Guillory, *J. Phys. Chem.*, **78**, 1461 (1974).

(6) D. Davis and W. Braun, *Appl. Opt.*, **7**, 2071 (1968).

(7) S. G. Thomas, Jr., and W. A. Guillory, *J. Phys. Chem.*, **77**, 2469 (1973).

(8) R. Isabel and W. A. Guillory, *J. Chem. Phys.*, **55**, 1197 (1971).

(9) G. H. Andrews, Jr., and W. A. Guillory, *J. Chem. Phys.*, in press.

(10) Sadtler Research Laboratories, Inc., IR 6403, 1962 Philadelphia, Pa.

(11) T. Shimanouchi, Tables of Molecular Vibrational Frequencies Consolidated Volume I, U.S. Government Printing Office, Washington, D.C., 1972, p 116, and references therein.

(12) G. H. Andrews, Jr., and W. A. Guillory, unpublished data.

(13) G. Herzberg, "Molecular Spectra and Molecular Structure. II. Infrared and Raman Spectra of Polyatomic Molecules", Van Nostrand, New York, N.Y., 1945, p 339, and references therein.

(14) B. Meyer, "Low Temperature Spectroscopy", American Elsevier, New York, N.Y., 1971, p 371, and references therein.

(15) W. C. Price and W. T. Tutte, *Proc. Roy. Soc., Ser. A*, **174**, 207 (1940).

(16) J. A. R. Samson, F. F. Marmo, and K. Watanabe, *J. Chem. Phys.*, **36**, 783 (1962).

(17) C. B. Moore and G. C. Pimentel, *J. Chem. Phys.*, **41**, 3504 (1964).

(18) D. Milligan and M. E. Jacox, *J. Chem. Phys.*, **41**, 3032 (1964).

(19) C. B. Moore and G. C. Pimentel, *J. Chem. Phys.*, **38**, 2816 (1963).

(20) J. G. Calvert and J. N. Pitts, "Photochemistry", Wiley, New York, N.Y., 1966, p 505.

Rates of Electron Exchange between Tetracyanoethylene (TCNE) and TCNE^- and between Tetracyanoquinodimethide (TCNQ) and TCNQ^- and Rate of Heisenberg Spin Exchange between $\mathrm{TCNE}^{\cdot -}$ Ions in Acetonitrile[1,2]

Myron A. Komarynsky and Arthur C. Wahl*

Department of Chemistry, Washington University, St. Louis, Missouri 63130

(Received July 22, 1974; Revised Manuscript Received November 27, 1974)

Publication costs assisted by the National Science Foundation

The following rate constants at ~25° and activation energies for electron exchange in acetonitrile have been determined by ESR line-shape measurements: TCNE–$\mathrm{TCNE}^-(\mathrm{Li}^+)$, $k = 1.7 \times 10^9\ M^{-1}\ \mathrm{sec}^{-1}$, $E_{\mathrm{act}} = 2.0$ kcal/mol; TCNE–$\mathrm{TCNE}^-(\mathrm{K}^+)$, $k = 2.2 \times 10^9\ M^{-1}\ \mathrm{sec}^{-1}$; TCNQ–$\mathrm{TCNQ}^-(\mathrm{Li}^+$ or $\mathrm{K}^+)$, $k = 3.3 \times 10^9\ M^{-1}\ \mathrm{sec}^{-1}$, $E_{\mathrm{act}} = 1.9$ kcal/mol. For the Heisenberg spin exchange process the rate constants determined at ~25° are $\mathrm{TCNE}^-(\mathrm{Li}^+)$, $k = 1.4 \times 10^9\ M^{-1}\ \mathrm{sec}^{-1}$; $\mathrm{TCNE}^-(\mathrm{Na}^+$ or $\mathrm{K}^+)$, $k = 3.3 \times 10^9\ M^{-1}\ \mathrm{sec}^{-1}$. Since the reactions are at least partially encounter controlled, the measured rate constants listed above should be considered lower limits for the exchange processes not limited by diffusion.

Introduction

The rates of electron exchange between tetracyanoethylene (TCNE) and its radical anion (TCNE^-) and between tetracyanoquinodimethide (TCNQ) and its radical anion (TCNQ^-) are of interest as examples of electron-exchange reactions without coulombic repulsion between reactants that are quite flat in shape. (The TCNE dimensions in Å are ~3 × 7 × 7, and those for TCNQ are ~3 × 7 × 11.) The Heisenberg spin-exchange reaction should occur without reorganizational free energy of activation,[3] since the reactants are identical in shape and charge. Also, knowledge of the spin-exchange rate is necessary for investigation of the electron-exchange rate at high anion concentrations where both exchange processes affect the ESR line shape. This article reports the results of our investigation of the rates of these processes by ESR line-shape measurements.

In 1960 Phillips, Rowell, and Weissman[4] reported the rate constant for electron exchange to be $k_e = 2.1 \times 10^8\ M^{-1}\ \mathrm{sec}^{-1}$ for the TCNE–TCNE^- system in tetrahydrofuran (THF) at ~25°, and in 1962 Phillips, Rowell, Foster, and Chesnut[5] observed that $k_e \simeq 10^9\ M^{-1}\ \mathrm{sec}^{-1}$ for the TCNQ–TCNQ^- system in acetonitrile (MeCN) at ~23°. More recently (1969) Eastman, Kooser, Das, and Freed[6] reported on extensive investigation of the Heisenberg spin-exchange process and found $k_s = (4.1 \pm 0.6) \times 10^9\ M^{-1}\ \mathrm{sec}^{-1}$ for the K^+ salt of TCNE^- in dimethoxyethane (DME) at 15°; the rate was also large in THF. Last year, while our work was in progress, additional investigations of the TCNE–TCNE^- system and the effects of ion pairing were reported by Watts, Lu, Chen, and Eastman;[7,8] they found for DME at 15° $k_e = 2.6 \times 10^8\ M^{-1}\ \mathrm{sec}^{-1}$ and an activation energy of $E_{\mathrm{act}} = 5.2$ kcal/mol, and for MeCN at 15° $k_e = 3.2 \times 10^9\ M^{-1}\ \mathrm{sec}^{-1}$ (value corrected for diffusion) and $E_{\mathrm{act}} = 2.3$ kcal/mol. Also, Ogasawara, Takaoka, and Hayashi[9] investigated the counterion effect on the rate of electron exchange between TCNE and TCNE^- in DME and in THF and observed values of k_e between (1 and 2) × $10^8\ M^{-1}\ \mathrm{sec}^{-1}$ at 20° and values of E_{act} between 2 and 8 kcal/mol.

The investigations mentioned above were all carried out at low concentrations, where individual hyperfine lines broaden with increasing concentration; and the results were interpreted by use of the equation derived for the slow-exchange limit.[10] Our investigation was carried out at higher concentrations, where the hyperfine lines had coalesced into a single line (see Figure 1), which narrows with increasing concentration in approaching the fast-exchange limit. Our results were interpreted by comparing measured line shapes with those calculated by the density matrix formulation using the computer program written by Norris.[11] Our measurements were made in MeCN because the electron-exchange rates were larger and the reactants were more soluble and/or stable in this solvent than in the other solvents investigated (methanol, formic acid, dimethylformamide, THF, and DME).

Very recently, after our original manuscript had been submitted for publication, Haren, Luz, and Shporer[12] reported measurement of the TCNQ–TCNQ^- electron-exchange reaction by methods similar to ours described above; their results of $k = 3.9 \times 10^9\ M^{-1}\ \mathrm{sec}^{-1}$ at 22° and $E_{\mathrm{act}} = 2.2\ \mathrm{kcal\ mol}^{-1}$ with MeCN as solvent are consistent with our results, as will be discussed.

Results

The results of our measurements at ~25° are summarized in Figures 2–4; the lines represent least-squares fits of the data by the equation

$$1/\tau\ (\mathrm{gauss}) = kc/1.76 \times 10^7 \tag{1}$$

by use of the computer program ORGLS,[13] τ being the lifetime of the paramagnetic species, k the second-order rate constant, and c the concentration plotted as abscissa in Figures 2–4. The lines represent the data quite well over a large range of concentrations, showing, as assumed in the derivation eq 1, that the rates are proportional to the first power of the reactant concentration, c ($[\mathrm{TCNE}^-]$ for the spin-exchange reaction and [TCNE] or [TCNQ] for the electron-exchange reactions).

The assumed first-order dependence of the electron-exchange rate on $[\mathrm{TCNE}^-]$ was checked in a series of experiments at high LiTCNE concentration (~10^{-2} to ~10^{-1} M, two-to-three orders of magnitude higher than normally

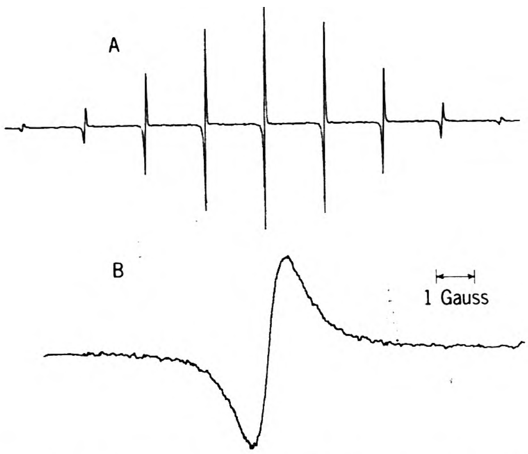

Figure 1. ESR spectra of ~10^{-4} *M* KTCNE (A) and of ~10^{-4} *M* KTCNE + 0.025 *M* TCNE (B), at greater amplification than in A.

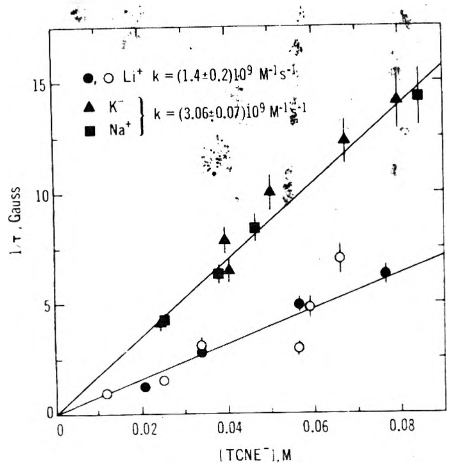

Figure 2. Heisenberg spin-exchange between $TCNE^-$ ions in MeCN at ~25°. Unfilled circles represent data for samples prepared by reduction of TCNE in MeCN by LiI; filled symbols represent data for samples prepared by reduction of TCNE by the appropriate alkali metal.

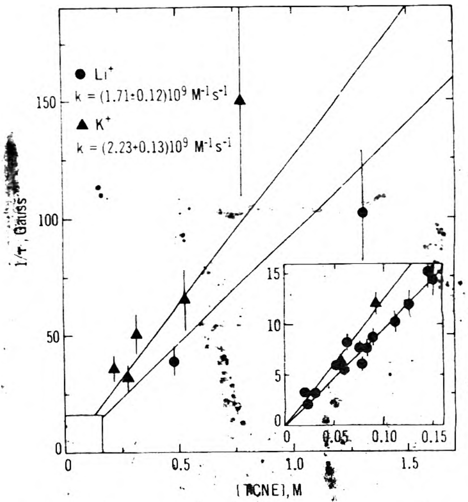

Figure 3. Electron exchange between $TCNE^-$ and TCNE in MeCN at ~25°. $TCNE^-$ was prepared by reduction of TCNE by the appropriate alkali metal.

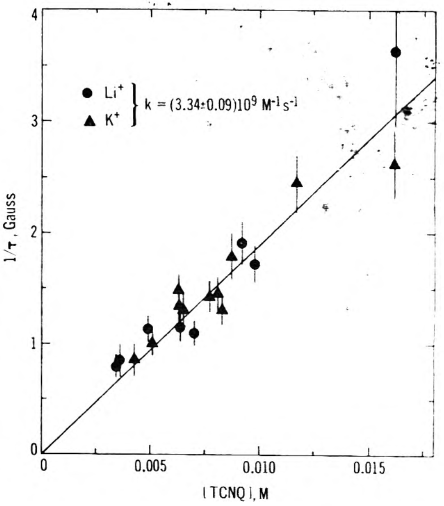

Figure 4. Electron exchange between $TCNQ^-$ and TCNQ in MeCN at ~25°. $TCNQ^-$ was prepared by reduction of TCNQ in MeCN by LiI or KI.

used) and at high TCNE concentrations (~1 *M*), to minimize the contribution of the Heisenberg spin-exchange reaction, for which corrections were made by use of the following equation:

$$\frac{1}{\tau_e} = \frac{1}{\tau} - \frac{1}{\tau_s} \qquad (2)$$

The symbols τ, τ_e, and τ_s represent, respectively, the measured lifetime of $TCNE^-$ and the lifetimes of $TCNE^-$ with respect to the electron- and spin-exchange reactions, τ_s being calculated from eq 1 and the value of $k_s = 1.4 \times 10^9$ M^{-1} sec^{-1} from Figure 2. The equation should be applicable if the electron- and spin-exchange processes are uncorrelated, as they most probably are. The results are summarized in Table I, and, although there is considerable spread in the values due to uncertainties of ~25% in the measurements due to the small line widths (~0.1 to ~0.2 G) of the collapsed lines and due to volume changes on addition of TCNE, the values are consistent with the value of 1.7×10^9 M^{-1} sec^{-1} obtained at low (~10^{-4} *M*) $TCNE^-$ concentrations (Figure 3) showing that the rate dependence on $[TCNE^-]$ is indeed first order.

Further evidence for the first-order dependence on $[TCNE^-]$ and for the validity of eq 2 was obtained from three experiments with KTCNE–TCNE mixtures in which both electron- and Heisenberg spin exchange affected the line shapes appreciably. The data are given in Table II, and, as can be seen, there is agreement, within experimental uncertainties, between measured and calculated values of $1/\tau$, the calculated values being derived from eq 1 and the values of $k_s = 3.06 \times 10^9$ M^{-1} sec^{-1} (from Figure 2) and $k_e = 2.23 \times 10^9$ M^{-1} sec^{-1} (from Figure 3).

The temperature dependence of the electron-exchange rates was investigated by lowering the temperature of individual samples from ~25° to a lower temperature (between 3 and −25°) and remeasuring the ESR spectrum. For the LiTCNE–TCNE system the average calculated activation energy is 2.0 ± 0.1 kcal/mol, and for the Li,KTCNQ–TCNQ system it is 1.9 ± 0.2 kcal/mol. The uncertainties given are standard deviations of the average values derived from six or seven measurements. Inclusion of estimates of systematic errors would probably increase the uncertainties to ~1 kcal/mol. Sine the temperature dependence of the rate constants is small, careful temperature control was unnecessary.

The uncertainties in the $1/\tau$ values were estimated as-

TABLE I: Rate of Electron Exchange at High TCNE⁻ Concentrations[a]

[LiTCNE], M	[TCNE], M	$1/\tau$, G	$1/\tau_s$, G	k_e, 10^9 M^{-1} sec^{-1}
0.0095	0.76	67	0.8	1.5
0.021	0.79	81	1.7	1.8
0.030	0.03	114	2.5	1.9
0.045	0.71	110	3.7	2.6
0.052	0.77	98	4.3	2.1
0.086	0.58	41	7.1	1.0
			Av	1.8

[a] Temperature ~25°.

TABLE II: Comparison of Measured and Calculated $1/\tau$ Values at Relatively High TCNE and KTCNE Concentrations at ~25°

[KTCNE], M	[TCNE], M	Measd $1/\tau$, G	Calcd $1/\tau$, G Spin	Electron	Sum
0.0188	0.069	11.8 ± 1.3	3.3	8.7	12.0
0.0180	0.173	29.0 ± 4.8	3.1	21.9	25.0
0.0275	0.020	6.9 ± 0.7	4.8	2.5	7.3

suming a 10% uncertainty in line-width measurements and ±0.03 G in ΔH, the difference between the collapsed line width and the initial hyperfine line width (usually ~0.05 G before addition of TCNE or TCNQ, and assumed to be 0.05 G for the spin-exchange measurements), i.e.

$$\sigma_{1/\tau} \simeq \frac{1}{\tau}\left\{(0.1)^2 + \left(\frac{0.03}{\Delta H}\right)^2\right\}^{1/2} \tag{3}$$

The uncertainties in the rate constants given in Figures 2–4 are standard deviations obtained as output from the least-squares computer program.

Discussion

Our observed rate constant $k_e = 2.2 \times 10^9\ M^{-1}\ \text{sec}^{-1}$ at ~25° for the TCNE–KTCNE electron-exchange reaction in CH_3CN is consistent with the value of Watts, Lu, Chen, and Eastman,[7] $k_e = 2.6 \times 10^9\ M^{-1}\ \text{sec}^{-1}$ (uncorrected for diffusion, and corrected to 25° for comparison). Also the activation energy of 2.0 kcal/mol that we determined using the lithium salt is similar to the value of 2.3 kcal/mol that they reported for the potassium salt.

For the TCNQ–TCNQ⁻ system in MeCN, our measured rate constant of $k = 3.3 \times 10^9\ M^{-1}\ \text{sec}^{-1}$ at ~25° and activation energy of 1.9 kcal/mol are consistent with the values of $k_e = 4.0 \times 10^9\ M^{-1}\ \text{sec}^{-1}$ (corrected to 25° for comparison) and 2.2 kcal/mol recently reported by Haren, Luz, and Shporer.[12] Both values of k_e are consistent with the early order-of-magnitude estimate of $k_e = {\sim}10^9\ M^{-1}\ \text{sec}^{-1}$ by Phillips, Rowell, Foster, and Chesnut.[5]

The consistency of the data with eq 1 as reactant concentrations are varied shows that there is no appreciable deviation from a second-order rate law, first order with respect to each reactant concentration, for the considerable range of concentrations investigated. This observation is somewhat surprising for the TCNE⁻ spin-exchange reaction since the activated complex has twice the charge of the reactants, and according to the Brønsted–Bjerrum theory,[14] the rate constants should increase with increasing electrolyte concentration due to changes in activity coefficients. The lack of observable change in k_s as the electrolyte concentration is increased from ~0.02 to ~0.08 M indicates either that changes in the activity coefficient ratio are small or that the reaction is largely encounter controlled, a possibility discussed later. The apparent constancy of k_e for the TCNE–TCNE⁻ system to ~0.5 M TCNE, and possibly higher, indicates that there is no appreciable association of TCNE⁻ with TCNE in MeCN, as was reported to occur in 2-methyltetrahydrofuran, but was later retracted.[15,16]

The somewhat smaller values of k_e and k_s for Li^+ salts of TCNE⁻ than for Na^+ or K^+ salts is an interesting effect, but the cause is unknown. The effect is not observed for electron exchange between TCNQ and TCNQ⁻. Ion association between Li^+ and TCNE⁻ should lower k_e by increasing the Franck–Condon restrictions, but it would increase k_s by lowering coulombic repulsion, the reverse of what is observed.

The rates of electron and spin exchange in MeCN are at least partially, and perhaps largely, encounter controlled. An estimate of the encounter controlled limit derived for different uncharged, spherical reactants of the same size in a continuous dielectric medium is given by[17]

$$k_d = \frac{8RT}{3000\eta} = 1.9 \times 10^{10}\ M^{-1}\ \text{sec}^{-1}\ (\text{for } CH_3CN \text{ at } 25°) \tag{4}$$

η being the viscosity of the solution, R the gas constant, and T the absolute temperature. For chemically identical reactants, as for the spin-exchange reaction, k_d is one-half of the above value.[6] If these are reasonable estimates for the flat molecules and ions involved in the reactions investigated, the rate constants for the exchange processes not limited by diffusion would be 10–50% larger than the observed rate constants by the relationship[18]

$$\frac{1}{k} = \frac{1}{k_{obsd}} - \frac{1}{k_d} \tag{5}$$

The observed activation energies are very similar to the activation energy of 2.0 kcal/mol for diffusion in MeCN (the temperature dependence of $1/\eta$) suggesting that the exchange reactions could be largely encounter controlled; if so, the rate constants for the exchange processes not hindered by diffusion could be much larger than the observed ones.

It is of interest to compare the observed k_e values, which, as discussed above, are lower limits for the electron-exchange processes, with the Marcus theory for electron-transfer reactions,[3] since the reactions involve a neutral molecule and, therefore, only reorganizational free energy of activation ($\Delta G_0^\ddagger$) is required. Unfortunately, the only detailed model through which the Marcus theory has been applied involves spherical reactants in a continuous, unsaturated dielectric medium,[3] and the reactants of interest are flat. However, the comparison of measured rate constants with those calculated from theory are given in Table III.

The lack of agreement for the electron-transfer reactions may well be due to the inadequacy of the model, and, as Marcus[19] pointed out, if electron transfer occurs with the reactants face to face, the solvent reorganization free energy of activation will be less than for touching spheres since there is no intervening solvent in the activated complex. A crude calculation using a point-dipole-in-a-sphere model,[19-21] the sphere having the same volume as the two reactants, indicates that $\Delta G_0^\ddagger$ could be a factor of 2 or more less than that for the touching spheres model, and thus the

TABLE III: Comparison of Measured and Calculated Rate Constants[a]

Reactants	k_e, M^{-1} sec^{-1}	
	Measd	Calcd[b]
TCNE$^-$–TCNE	2.2×10^9	1.4×10^6
TCNQ$^-$–TCNQ	3.3×10^9	6.4×10^6

[a] Solvent is MeCN at 25°. [b] Marcus theory[3] applied to touching spheres, having the same volumes as the reactants, in a continuous, unsaturated dielectric medium, with the assumption that the internal reorganization free energy of activation is negligible.

calculated rate constants could be two orders-of-magnitude or more larger and nearer the measured values. However, it seems unlikely that the Heisenberg spin-exchange reaction occurs with the reactants face to face, as suggested by Marcus[19] for the electron-exchange reactions, because the free energy of activation would be large due to the work required to remove solvent from between the reactants and to bring like charged reactants together without an intervening dielectric medium.

Experimental Section

TCNE and TCNQ, purchased from Eastman Organic Chemicals, were sublimed and stored under vacuum. For some experiments, crystals of TCNE were grown by resublimation of the original sublimate at ~80° in an evacuated tube having ~10° temperature differential between the ends. Most salts of TCNE$^-$ were prepared by reduction of sublimed TCNE in dry THF by the appropriate freshly sublimed alkali metal in an evacuated chamber. After filtration under vacuum to remove any solid impurities, the solvent and excess TCNE were vaporized at ~90° to leave the pure dry salt, which was stored under vacuum. The dry salts and the sublimed TCNE or TCNQ reacted only slowly with air, so transfers and weighings of the solids could be made without difficulty, but since solutions reacted rapidly with air, especially those containing the salts, MeCN was distilled under vacuum onto a dry salt. After ESR measurements of the resulting solution had been completed, the solution was transferred to another arm of the evacuated vessel containing solid TCNE or TCNQ behind a break seal, which was broken, the solid dissolved, and ESR measurements were made on this new solution.

MeCN solutions of KTCNQ and LiTCNQ and some of the LiTCNE solutions were made by reduction of TCNQ or TCNE in solution with KI or LiI under vacuum.

The MeCN solvent, purchased from Fisher, was dried over silica gel for several days, refluxed over CaH_2 for ~12 hr, and distilled through a dry system into a flask containing molecular sieves or fresh CaH_2. After degassing by freezing and pumping, the MeCN was distilled at room temperature into a storage flask on the vacuum line containing dry molecular sieves.

The ESR measurements were made with a Varian Model E-3 spectrometer, which has a modulation frequency of 100 kHz. For each initial width of the central hyperfine line for the pure paramagnetic species (e.g., 0.04, 0.05, 0.06 G), simulated spectra were calculated[11] for a number of selected $1/\tau$ values, and plots were made of ΔH, the change in line width, vs. $1/\tau$; then, $1/\tau$ values were determined from measured ΔH values by use of the plots. The hyperfine interaction constants measured for the pure dilute radical anions and used in calculations of the simulated spectra are a_N = 1.53 G for TCNE$^-$ and a_N = 0.96 G, a_H = 1.38 G for TCNQ$^-$. Although these measured values may differ somewhat from other reported and possibly more accurate values, the measured values are appropriate for use in the line-shape calculations since small errors in the calibration of the spectrometer tend to cancel. For a few experiments at the lower concentrations or temperatures, the coalesced line had sufficient structure to prevent determination of a line width; in these cases a measured line was compared directly with a number of simulated spectra, and a $1/\tau$ value was chosen between those for the simulated spectra "bracketing" the measured one. Spectra change rapidly with $1/\tau$, in this "intermediate" region and very precise values of $1/\tau$ can be determined if sufficient simulated spectra are calculated for comparison.

No correction for the effect of dipolar interaction between the radical anions on line shapes has been applied since the effect is believed to be small. For example, Eastman, Kooser, Das, and Freed[6] have shown that this effect is very much smaller than the effect of Heisenberg spin exchange and had a negligible effect on their experimentally determined spin-exchange rate in DME. They showed that the ratio of the dipolar to spin-exchange effect was independent of concentration and was proportional to the square of the viscosity; thus the ratio would be even smaller for MeCN (η = 0.34 cP) than for DME (η = 0.46 cP). Also, we have observed only a single line 2.0 G in width in the ESR spectrum of powdered solid NaTCNE, showing that the hyperfine lines, which are spread over ~12 G in well-resolved spectra of dilute solutions of the radical anions (see Figure 1A), had coalesced into a narrowed line due to Heisenberg spin exchange, not merely broadened due to dipolar interactions. Using this result and assuming a 6-Å distance between adjacent spin sites, we estimate, using appropriate published equations,[22,23] that the dipolar interaction energy is two orders-of-magnitude less than the spin-exchange interaction energy in the solid. It seems unlikely that the dipolar effect could be appreciably greater in solution, a conclusion consistent with the calculations of Eastman *et al.*[6]

Acknowledgments. It is a pleasure to thank Professor S.I. Weissman for his helpful advise during the course of this investigation and for his valuable comments concerning this article. Professor M.P. Eastman made a number of helpful comments concerning the article, and it is a pleasure to thank him also. The assistance of Mr. E.S. Yang during the early phase of this investigation is gratefully acknowledged.

References and Notes

(1) Supported by the National Science Foundation under Grant No. GP-28260X.

(2) Presented in part at the 167th National Meeting of the American Chemical Society, Los Angeles, Calif., April 1–4, 1974.

(3) R. A. Marcus, *J. Chem. Phys.*, **43**, 679 (1965).

(4) W. D. Phillips, J. C. Rowell, and S. I. Weissman, *J. Chem. Phys.*, **33**, 626 (1960).

(5) W. D. Phillips, J. C. Rowell, H. Foster, and D. B. Chesnut, reported by L. R. Melby, R. J. Harder, W. R. Herter, W. Mahler, R. E. Benson, and W. E. Mochel, *J. Am. Chem. Soc.*, **84**, 3374 (1962).

(6) M. P. Eastman, R. G. Kooser, M. R. Das, and J. H. Freed, *J. Chem. Phys.*, **51**, 2690 (1969).

(7) M. T. Watts, M. L. Lu, R. C. Chen, and M. P. Eastman, *J. Phys. Chem.*, **77**, 2959 (1973).

(8) M. T. Watts, M. L. Lu, and M. P. Eastman, *J. Phys. Chem.*, **77**, 625 (1973).

(9) M. Ogasawara, H. Takaoka, and K. Hayashi, *Bull. Chem. Soc. Jpn.*, **46**, 35 (1973).

(10) R. L. Ward and S. I. Weissman, *J. Am. Chem. Soc.*, **79**, 2086 (1957).
(11) J. R. Norris, *Chem. Phys. Lett.*, **1**, 333 (1967).
(12) N. Haran, Z. Luz, and M. Shporer, *J. Am. Chem. Soc.*, **96**, 4788 (1974).
(13) L. A. Busing and H. A. Levy, Oak Ridge National Laboratory Report No. ORNL-TM-271, 1962 (unpublished).
(14) See, for example, S. W. Benson, "The Foundations of Chemical Kinetics", McGraw-Hill, New York, N.Y., 1960, pp 525–528.
(15) M. Itoh, *J. Am. Chem. Soc.*, **92**, 886, 7239 (1970).
(16) M. Itoh, *Bull. Chem. Soc. Jpn.*, **45**, 1947 (1972).
(17) See, for example, E. F. Caldin, "Fast Reactions in Solution", Wiley, New York, N.Y., 1964, p 12.
(18) R. A. Marcus, *J. Chem. Phys.*, **43**, 3477 (1965).
(19) R. A. Marcus, personal communication.
(20) R. A. Marcus, *J. Chem. Phys.*, **38**, 1858 (1963).
(21) R. A. Marcus, *J. Chem. Phys.*, **43**, 1261 (1965).
(22) J. H. Van Vleck, *Phys. Rev.*, **74**, 1168 (1948), eq 14.
(23) P. W. Anderson and P. R. Weiss, *Rev. Mod. Phys.*, **25**, 269 (1953), eq 29.

Formation of Ion Pairs in Irradiated Charge-Transfer Systems

Masahiro Irie,*[1a] Setsuko Irie,[1b] Yukio Yamamoto,[1a] and Koichiro Hayashi[1a]

The Institute of Scientific and Industrial Research, Osaka University, Suita, Osaka, 565, Japan *(Received August 29, 1974)*

Radiation effects on the electron donor–acceptor (EDA) complex, especially the ion-pair formation process in the glassy state at 77°K, are studied. The yield of the radical anion of pyromellitic dianhydride (PMDA) in *n*-butyl chloride-2-methyltetrahydrofuran matrix containing PMDA is increased by the addition of ethylbenzene, which is known to form a stable EDA complex with PMDA. The absorption spectrum of the radical anion thus formed has a peak at 668 nm and a rather broad band width. The peak position and the band width are different from that of the free-radical anion and similar to the anion formed by photoillumination of the complex which indicates that the radical anion exists as an ion pair and has considerable interaction with the countercation. The effects of sensitizers and quenchers prove that the excited EDA complex formed by radiation dissociates into separated ion pairs in their highly excited singlet states.

Introduction

The physicochemical processes in the excited states of electron donor–acceptor (EDA) complexes have been attracting much attention from theoretical as well as experimental points of view. Recent progress in laser photolysis techniques has enabled direct observation of the dynamic behaviors of the transient species and extensive studies dealing with the excited EDA complex have been carried out.[2] It is now well established that the EDA complex dissociates into a separated ion pair in its singlet or/and triplet excited states in a polar solvent.[3,4] In some complexes, intersystem crossing and ionization processes were reported to occur in their nonrelaxed excited states.[5–7]

Although many studies have been made on the photoexcited states of the EDA complexes as mentioned above, the excited states formed by ionizing radiation have not yet been revealed.[8,9] The highly excited states of the complexes formed by radiation are expected to be in very polar states which dissociate readily into separated ion pairs, as observed in the photoexcited complexes.

In this study the radiation effects on the EDA complex, especially the ion-pair formation process by radiation in the glassy state at 77°K, are studied to clarify the nature of the excited states of the complexes formed by radiation in comparison with that of photoexcited states.

Experimental Section

Purification of 2-methyltetrahydrofuran and *n*-butyl chloride were described before.[10] Benzene, ethylbenzene, mesitylene, and piperylene were fractionally distilled twice. Zone-refined naphthalene was used as received. Pyromellitic dianhydride (PMDA) was purified by sublimation before use.

Samples were irradiated in darkness by Co-60 γ rays at a dose rate of 1.2×10^{19} eV/g hr at 77°K. Absorption spectra were measured with a Hitach EPS-3T spectrophotometer. The extinction coefficient of the free-radical anion of PMDA produced by radiation is obtained to be 3.0×10^4 M^{-1} cm^{-1} at 664 nm by comparison with the value of the trapped electron of 2.6 in pure 2-methyltetrahydrofuran.[11] G values of the paired radical anion formed from EDA complexes were determined by comparing the absorption area with that of the above free-radical anion.

Results and Discussion

I. Radical Ions from PMDA–Ethylbenzene Complex. According to the criterion proposed by Hamill et al.,[12] stable radical cations of the solutes are obtained in *n*-butyl chloride by γ irradiation at 77°K and radical anions in 2-methyltetrahydrofuran. In *n*-butyl chloride, electrons ejected by radiation are stabilized as Cl^- by a dissociative electron attachment reaction. In 2-methyltetrahydrofuran, on the other hand, positive charges, counterparts of the ejected electrons, are regarded to be trapped in the protonated form of the solvent.[13,14] Therefore, both electrons and positive charges generated as a consequence of the ionization of the solvent by radiation are considered to be captured immediately by surrounding solvent molecules in an equimolar mixture of these two matrices and neither radical cations nor anions of the solutes are expected to be formed. Actually, no absorption due to radical ions was detected in the equimolar mixture containing 2.0×10^{-2} M

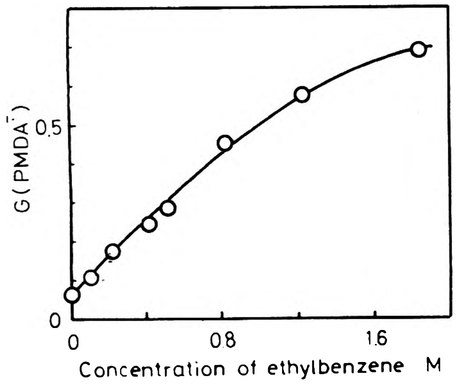

Figure 1. Dependence of the radiation chemical yields, *G* values, of the radical anion of pyromellitic dianhydride on the concentration of ethylbenzene added to the mixed matrices of *n*-butyl chloride and 2-methyltetrahydrofuran (molar ratio 1:1) containing 2.5×10^{-2} *M* pyromellitic dianhydride at 77°K.

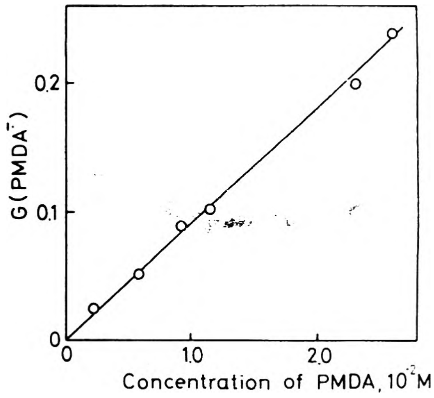

Figure 2. Dependence of the yields, *G* values, of the radical anion of pyromellitic dianhydride on the concentration of pyromellitic dianhydride added to the mixed matrices of *n*-butyl chloride and 2-methyltetrahydrofuran (molar ratio 1:1) containing 0.41 *M* ethylbenzene at 77°K.

biphenyl irradiated with a dose of 6×10^{18} eV/g at 77°K. Unless otherwise noted, this matrix was used to avoid direct ionization as a formation process of the radical ions.

In the matrix containing 2.5×10^{-2} *M* PMDA, however, radical anions of PMDA, which has an absorption peak about 670 nm,[15] were observed, though its radiation chemical yield, *G* value, is as low as 0.06. This ion was not detected in the absence of 2-methyltetrahydrofuran. The result suggests that the interaction between PMDA and 2-methyltetrahydrofuran in the excited states enables the generation of the radical anion by radiation. Direct capture of the ejected electron by PMDA was negligible for the above system because of the much lower concentration of PMDA compared with that of *n*-butyl chloride.

To clarify the ion formation process the effects of the addition of benzene derivatives, which are well known to have a distinct interaction with PMDA to form a stable EDA complex,[15] were examined. Figure 1 shows the dependence of the yield of the radical anion of PMDA on the concentration of ethylbenzene added to the matrices containing 2.5×10^{-2} *M* PMDA. The yield increased with increasing concentration of ethylbenzene so that the concentration of the PMDA–ethylbenzene complex increased. Ten times the yield was obtained by the addition of 1.2 *M* ethylbenzene. This result unequivocally indicates that the increase is due to the ionic dissociation of the excited complex formed by radiation. Low-energy radiation, too low to ionize the solvent molecules directly but enough to excite them, should raise the EDA complex to excited states resulting in the formation of ions, although it is lost wastefully in the absence of the complex. The concentration of PMDA also affects the yield, as shown in Figure 2. Upon increasing its concentration the yield of the ions increases.

Increases in the yield are observed by the addition of other aromatic compounds which are able to form an EDA complex with PMDA as well as ethylbenzene. The relative yields of the radical anion are shown in Table I. Simple correlation of the yield with the equilibrium constant to form the complex does not hold in this case. It is a very complicated problem to discuss the difference in the yield quantitatively because the degree of the charge separation in the excited states of the complex and the cross section of the excitation of the complex must both be considered. However, it is worthwhile to note that the naphthalene complex has higher yield than benzene derivatives.[16]

II. Ion-Pair Formation by Radiation. The ions formed from excited EDA complexes by photoillumination as well as radiation in the glassy state are considered to exist in pairs. To elucidate the structure of these ion pairs, absorption spectra of the ions were investigated in detail. Figure 3 shows the spectra of the radical anion of PMDA formed in three different ways: (i) γ irradiation of 2-methyltetrahydrofuran containing only PMDA; (ii) γ irradiation; and (iii) photoillumination (γ >350 nm) of the mixed solvent containing the PMDA–ethylbenzene complex.

In the first case the ions are considered to be formed through direct capture of ejected electrons by uncomplexed PMDA. Ions thus formed are regarded to be free[12] and have a sharp peak at 664 nm.

On the other hand, the anion formed by photoillumination has an absorption peak at a longer wavelength of 672 nm and its line width is appreciably broad. The difference is presumably due to the effect of the electric field of the countercation. Theoretical consideration predicts that the higher electric field shifts the peak to a longer wavelength and makes the spectrum broader.[17,18]

The radical anion formed from the complex by radiation has a peak at 668 nm and a rather broad band width. The peak position and the band width indicate that the radical anion exists as an ion pair and has a considerable interaction with the countercation, though it is not as strong as the ion pair formed by photoillumination. The highly excited state of the precursor of the ions formed by radiation possibly results in a longer distance between the ion pairs because of the larger enthalpy change involved in the ionic dissociation process.

III. Ionic Dissociation Mechanism. The effect of several triplet sensitizers or quenchers was studied to reveal the precursor of radical ions, viz., whether it is a singlet or triplet excited state of the complex. When the radical ions are formed from the triplet state, the yield should be affected by the addition of the sensitizers or quenchers. Table II summarizes the results obtained for photoillumination and γ irradiation along with the triplet energy levels of the additives used.[19] For photoillumination the yield increased by the addition of acetophenone and benzophenone, though it decreased by piperylene and fluorenone. This result clearly indicates that the radical ion is formed from the triplet state by photoillumination and its energy level lies between 2.97 and 2.55 eV. For γ irradiation, on the other hand, piperylene and fluorenone have no influence on the yield, though it was increased by the addition of acetophenone

TABLE I: Relative Yield of the Radical Anion of PMDA in 2-Methyltetrahydrofuran–*n*-Butyl Chloride Glass at 77°K

Complex	Yield
Benzene–PMDA	1
Ethylbenzene–PMDA	0.9
Mesitylene–PMDA	0.8
Naphthalene–PMDA	1.5

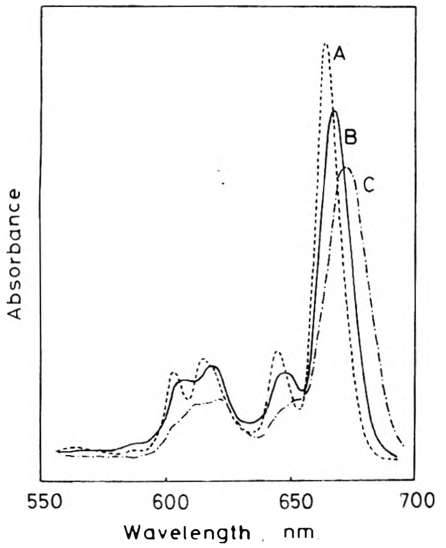

Figure 3. Absorption spectrum of radical anion of pyromellitic dianhydride formed by three different irradiation techniques: (A) γ irradiation of 2-methyltetrahydrofuran containing only pyromellitic dianhydride; (B) γ irradiation; and (C) photoillumination ($\lambda > 350$ nm) of the mixed matrices of *n*-butyl chloride and 2-methyltetrahydrofuran (molar ratio 1:1) containing the pyromellitic dianhydride–ethylbenzene complex.

and benzophenone. The ineffectiveness of piperylene and fluorenone suggests that the precursor of the radical ion in radiation is different than that in photoillumination. The increase in the yield observed by the addition of acetophenone and benzophenone is probably due to additional radical ions formed by another process, such as the triplet energy transfer from them to the complex.[3]

The quenching efficiency of piperylene was followed quantitatively as shown in Figure 4. The yield of the anion decreased with increasing concentration of piperylene for photoillumination. The quenching was not observed in the concentration range examined for γ irradiation. This result shows that the complex excited by radiation is not in the triplet or lowest excited singlet state but in an electronically higher singlet state which dissociates into ions before internal conversion to the lowest singlet state or intersystem crossing to a triplet state occurs. The possibility of dissociation in the lowest excited singlet state is removed because the complex excited by photoillumination in the singlet state does not dissociate in this state but in the triplet state after intersystem crossing.[2]

The higher excited singlet state of the complex is presumably formed by singlet energy transfer from the excited solvent molecules formed by radiation, the energy of which is estimated from its absorption spectrum to be as large as 5 eV. The complex excited to such a high energy level is considered to be in either a charge separated state[20] or in a very polar state, and readily dissociates into ion pairs by weak perturbation, such as bond polarizations of the polar solvents which are favorable for the stabilization of the ion pairs.

TABLE II: Effect of Additives on the Yield of the Radical Anion of PMDA

Additives	E_T, eV	Photoillumination	γ irradiation
Acetophenone	3.19	Increased	Increased
Benzophenone	2.97	Increased	Increased
Piperylene	2.55	Decreased	Unchanged
Fuorenone	2.32	Decreased	Unchanged

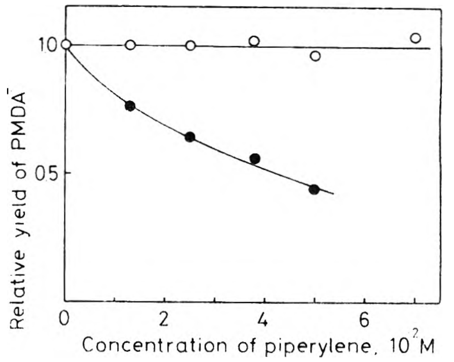

Figure 4. Quenching of the formation of the radical anion of pyromellitic dianhydride by the addition of piperylene in the mixed matrices of *n*-butyl chloride and 2-methyltetrahydrofuran (molar ratio 1:1) at 77°K containing 0.41 *M* ethylbenzene and 2.5×10^{-2} *M* pyromellitic dianhydride at 77°K: (●) photoillumination ($\lambda > 350$ nm); (○) γ irradiation with a dose of 6.0×10^{18} eV/g.

Acknowledgment. The authors express their thanks to Dr. G. Bakale, Hahn-Meitner-Institute, Berlin, for kindly reading the manuscript.

References and Notes

(1) (a) Institute of Scientific and Industrial Research, Osaka University. (b) Radiation Center of Osaka Prefecture.
(2) M. Ottolenghi, *Acc. Chem. Res.*, **6**, 153 (1973).
(3) M. Irie, H. Masuhara, K. Hayashi, and N. Mataga, *J. Phys. Chem.*, **78**, 341 (1974).
(4) Y. Achiba, S. Katsumata, and K. Kimura, *Chem. Phys. Lett.*, **13**, 213 (1972).
(5) N. Orbach, U. Novros, and M. Ottolenghi, *J. Phys. Chem.*, **77**, 2831 (1973).
(6) Y. Taniguchi and N. Mataga, *Chem. Phys. Lett.*, **13**, 596 (1972).
(7) M. Shimada, H. Masuhara, and N. Mataga, *Chem. Phys. Lett.*, **15**, 364 (1972).
(8) E. J. Land, J. T. Richards, and J. K. Thomas, *J. Phys. Chem.*, **76**, 3805 (1972).
(9) K. Tsuji, K. Yoshida, and K. Hayashi, *J. Chem. Phys.*, **46**, 2808 (1967).
(10) H. Yoshida, M. Noda, and M. Irie, *Polym. J.*, **2**, 359 (1971).
(11) D. R. Smith and J. J. Pieroni, *Can. J. Chem.*, **41**, 2141 (1965).
(12) W. H. Hamill, "Radical Ions," E. T. Kaiser and L. Kevan, Ed., Interscience, New York, N.Y., 1968, p 321.
(13) D. R. Smith and J. H. Pieroni, *Can. J. Chem.*, **43**, 876 (1965).
(14) F. S. Dainton and G. A. Salmon, *Proc. Roy. Soc., Ser. A*, **285**, 310 (1965).
(15) Y. P. Pilette and K. Weiss, *J. Phys. Chem.*, **75**, 3805 (1971).
(16) H. Masuhara, M. Shimada, N. Tsujino, and N. Mataga, *Bull. Chem. Soc. Jpn.*, **44**, 3310 (1971).
(17) K. Kimura, S. Katsumata, and K. Suwada, *J. Phys. Chem.*, **76**, 639 (1972).
(18) M. Irie, M. Shimizu, and H. Yoshida, *Chem. Phys. Lett.*, **25**, 102 (1974).
(19) C. A. Parker, "Photoluminescene in Solutions," Elsevier, New York, N.Y., 1968, p 324.
(20) C. Fuchs, F. Heisel, and R. Voltz, *J. Phys. Chem.*, **76**, 3867 (1972).

Low-Temperature Pulse Radiolysis. III. Ionic Species Produced from Aliphatic Ketones

Shigeyoshi Arai,* Mikio Hoshino, and Masashi Imamura

The Institute of Physical and Chemical Research, Wako-shi, Saitama 351, Japan

(Received September 5, 1974)

Publication costs assisted by the Institute of Physical and Chemical Research

Absorption spectra of transient species produced at low temperatures by pulse radiolysis of pure acetone have been measured. Similar measurements have been carried out for 11 aliphatic ketones including acetone in tetrahydrofuran and/or 2-methyltetrahydrofuran solutions. The absorption bands at 500 and 750 nm in pure acetone are assigned to monomer anions and cations of acetone, respectively, on the basis of the effects of various scavengers and on comparisons with spectra observed for pulse irradiated tetrahydrofuran solutions of acetone at 178°K and γ irradiated glassy n-butyl chloride solutions of acetone at 77°K. The molar extinction coefficient of an acetone anion at 500 nm has been determined to be $5 \times 10^3\ M^{-1}\ \mathrm{cm}^{-1}$. The pulse irradiation of ethereal solutions of aliphatic ketones produces intense transient absorption bands in the visible and near-infrared regions. The peak is located at 500 nm for acetone, 510 nm for methyl ethyl ketone, 600 nm for methyl isopropyl ketone, 560 nm for methyl isobutyl ketone, 550 nm for diethyl ketone, 520 nm for diisopropyl ketone, 775 nm for cyclopentanone, 580 nm for cyclohexanone, 680 nm for cycloheptanone, 775 nm for cyclooctanone, and 640 nm for cyclododecanone. All the absorption bands are ascribed to molecular anions of these ketones.

Introduction

Previous papers[1-6] on pulse radiolysis of aromatic hydrocarbons in acetone solutions have shown that both cations and anions of solute molecules are produced in fairly high yields. The formation of solute ions is regarded as being due to charge transfer from radiation-produced solvent ions to solute molecules. The absorption spectra of ionic species produced by radiolysis of acetone have been measured using a matrix isolation technique,[7] and more recently using a nanosecond pulse radiolysis technique.[8,9] The bands at 460 and 740 nm have been assigned to molecular anions and cations of acetone, respectively. However, there is some ambiguity as to the assignments; the spectrum reported[10,11] for molecular anions of acetone produced in alkaline aqueous solutions does not show a band around 460 nm. It has been suggested[12] that the band at 740 nm is due to dimer cations of acetone.

The present study was undertaken to obtain further information relating to ionic species produced in the pulse radiolysis of acetone. Lifetimes of the ionic species become considerably longer at low temperatures, and their optical absorptions are easily observed using a microsecond pulse radiolysis technique. In addition, pulse radiolysis of tetrahydrofuran solutions of acetone at low temperatures and γ radiolysis of n-butyl chloride solutions of acetone at 77°K were carried out for the purpose of clear identification of the absorption bands. The study has then been extended to 10 other aliphatic ketones in tetrahydrofuran and/or 2-methyltetrahydrofuran solutions. The spectra of the molecular anions of these ketones are presented.

Experimental Section

A Mitsubishi Van de Graaff accelerator was used as the source of electron pulses. The accelerating voltage was 2.7–2.8 MeV and the pulse widths were 0.5, 1.0, 2.0, and 5.0 μsec. The current of up to 200 mA was varied to give suitable absorptions of the transient species. Experimental procedures and optical detection systems were described in previous papers.[13,14]

Two types of the low-temperature apparatus (A and B) were used. The temperature of a sample was variable down to 140°K for the A type, while constant (approximately 100°K) for the B type. The main part of the A type was a rectangular thermostatic box with a thin aluminum window for the electron beam and an evacuated quartz cell as a window for the analyzing light beam. The temperature was controlled by a flow of cooled nitrogen gas. The temperature was measured with an uncertainty of less than ±3°K with a copper–constantan thermocouple attached to a reaction vessel. The reaction vessel used for the A type consisted of a rectangular optical cell made of high-purity quartz and a glass bulb for degassing the solution. The inside dimensions of the cell were 22 by 22 by 12 mm deep in the direction of the electron beam. Since the light beam traversed the optical cell twice, the total length of the optical path was 44 mm. The optical cell and a part of the side arm were placed inside the thermostatic box.

The B type was essentially the same as that shown in Figure 1 of ref 14, except that the copper block on which the optical cell was mounted was slightly slanted from the horizontal, so that the liquid inside the cell did not flow.

Tetrahydrofuran (THF), 2-methyltetrahydrofuran (MTHF), and acetone were obtained from Wako Pure Chemical Industries. THF was fractionally distilled after being dried with metallic sodium. The middle fraction was stored over sodium and potassium alloy in vacuo in the presence of a small amount of anthracene. Necessary amounts of THF for preparing samples were distilled in vacuo from the stock solution. MTHF was purified in a same manner. Acetone was fractionally distilled after being refluxed over anhydrous sodium sulfate for several hours, and dried with molecular sieve. Other aliphatic ketones were of the best quality commercially available. The ketones, except for cyclooctanone and cyclododecanone, were dried with anhydrous sodium sulfate, before distillation in vacuo rejecting the first and last thirds. Cyclooctanone and cyclododecanone (both solids at room temperature) were used without further purification. All the solutions were prepared, without exposure to air, on a vacuum line

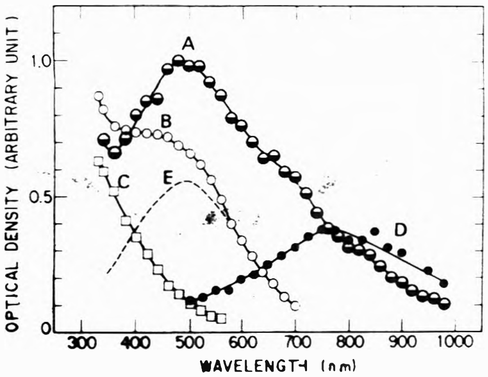

Figure 1. Absorption spectra observed at 193°K on pulse radiolysis of pure acetone (A); acetone containing 0.1 *M* triethylamine (B); acetone containing 0.1 *M* triethylamine and 0.1 *M* water (C); and acetone saturated with nitrous oxide (D). All the spectra were determined immediately after the pulse. Spectrum E is the difference between B and C.

equipped with a distillation still and a graduated glass tube for a volumetric measurement.

Results

Acetone. The pulse irradiation of acetone at room temperature produces a weak absorption starting at about 600 nm and increasing to the transmission limit, 330 nm. As the temperature of acetone is decreased the absorption increases in intensity and the decay becomes much slower. Figure 1 shows the absorption spectrum at 193°K, which has a peak at 500 nm and a long tail extending to 1000 nm. The behavior of the decay curves indicates the presence of several absorbing species as discussed below.

Figure 1 also shows the absorption spectrum obtained with acetone containing 0.1 *M* triethylamine as a cation scavenger. The absorption in the infrared region removed by adding triethylamine is attributed to either molecular cations of acetone or some species resulting from the cation. The spectrum in the presence of triethylamine consists of, at least, two absorbing species, because the decay at 330 nm is much slower than that at 500 nm in the same solution. Furthermore, the absorption around 500 nm is almost completely removed by the addition of 0.1 *M* water as shown in Figure 1. The difference between the spectra with and without water gave an absorption band with a peak at about 500 nm, which is in agreement with the band assigned to a molecular anion of acetone in previous papers.[7-9] The suppression of this absorption band by nitrous oxide, as shown in Figure 1, also suggests that the absorbing species is an acetone anion or a product from the anion.

Our previous paper[2] has shown that both anions and cations of solute molecules are produced by pulse radiolysis of aromatic hydrocarbons in acetone solutions. In the present study, the lifetime of the absorption at 500 nm was found to be shortened by adding a small amount of anthracene to solutions of triethylamine in acetone. The absorption due to anthracene anions at 720 nm built up concurrently in the same solution. This result shows that the absorbing species at 500 nm are anionic. The yield of the anthracene anion reaches a saturation value at concentrations $>3 \times 10^{-3}$ *M* anthracene. By comparing the absorbance at 500 nm for pure acetone with that at 720 nm for an acetone solution of 5×10^{-3} *M* anthracene containing 0.1 *M* triethylamine and using the molar extinction coefficient of the anthracene anion at 720 nm[15] (1.0×10^4 M^{-1} cm^{-1}), the molar extinction coefficient of the acetone anion at 500 nm is estimated to be 5×10^3 M^{-1} cm^{-1}.

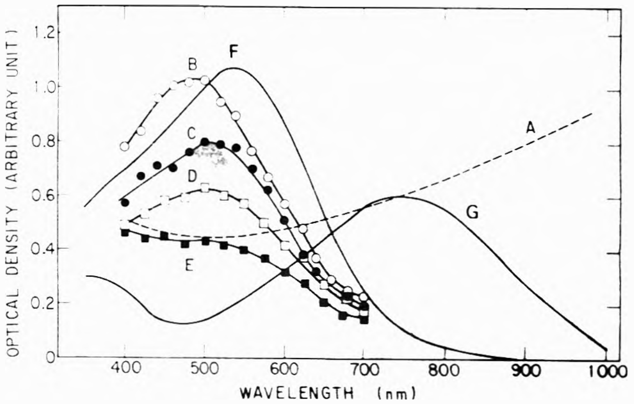

Figure 2. Absorption spectra obtained at 178°K with pure THF (A); and with THF solutions of 7.4×10^{-1} *M* acetone (B); 2.2×10^{-1} *M* acetone (C); 4.2×10^{-3} *M* acetone (D); and 6.0×10^{-4} *M* acetone (E). Spectra A, B, C, and D were determined immediately after the pulse, while E was determined 2 μsec after the pulse. Spectra F and G were obtained at 77°K on γ radiolysis of *n*-butyl chloride and *n*-butyl chloride solution of 0.5 *M* acetone, respectively.

It is well established that the solvated electron is one of the main products in radiolysis of THF.[16,17] The hydrated electron is known to be very reactive toward acetone[18] and so, the molecular anion of acetone is expected to be formed at an early stage in solutions of acetone in THF. Figure 2 presents the absorption spectra obtained on the pulse radiolysis of 7.4×10^{-1}, 2.2×10^{-1}, 4.2×10^{-3}, and 6.0×10^{-4} *M* acetone in THF. The peak of each spectrum is located at 500 nm regardless of the concentration, although the peak height decreases with a decrease in concentration. When the solution of 6.0×10^{-4} *M* was irradiated at 168°K, the absorption due to the solvated electron was observable during the initial 10 μsec. The spectrum determined at the end of the pulse was very similar to that obtained with pure THF, but subsequently changed into the spectrum observed at 178°K for the same solution. These results are in agreement with the suggestion already made that the absorption at 500 nm is due to molecular anions of acetone produced by the reaction between the solvated electron and an acetone molecule. The rate constant is determined to be 6×10^8 M^{-1} sec^{-1} from the decay curve at 900 nm shown in Figure 3. The decay curves at 625 and 500 nm are also shown in Figure 3. The implication of these curves will be discussed later.

The irradiation of acetone saturated with nitrous oxide produces the absorption band centered at 740 nm (see Figure 1). The band is almost identical with the band assigned to a molecular cation of acetone in the previous paper.[7] γ Irradiations of glassy solutions of various organic molecules in butyl chloride are frequently used for the preferential production of solute cations. The spectrum obtained for acetone using this technique is included in Figure 2. The spectrum is the same as that produced by pulse radiolysis of acetone saturated with nitrous oxide.

The effects of triethylamine, water, anthracene, and nitrous oxide lead to the conclusion that the spectrum observed for pure acetone consists of three absorption bands with peaks at <330, 500, and 750 nm and each band corresponds to a different transient species. Figure 3 presents decay curves of the absorptions at 340, 500, and 750 nm in pure acetone as well as the absorption at 500 nm in acetone

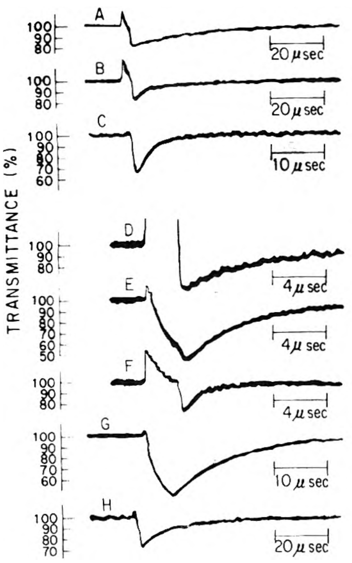

Figure 3. Decay curves of absorptions at 500 (A), 625 (B), and 900 nm (C) obtained with THF solution of 6.0×10^{-4} M acetone at 168°K; decay curves of absorptions at 340 (D), 500 (E), and 740 nm (F) obtained with pure acetone at 193°K; decay curve of absorption at 500 nm (G) obtained with acetone containing 0.1 M triethylamine at 193°K; and decay curve of absorption at 500 nm (H) obtained with THF solution of 0.74 M acetone at 178°K.

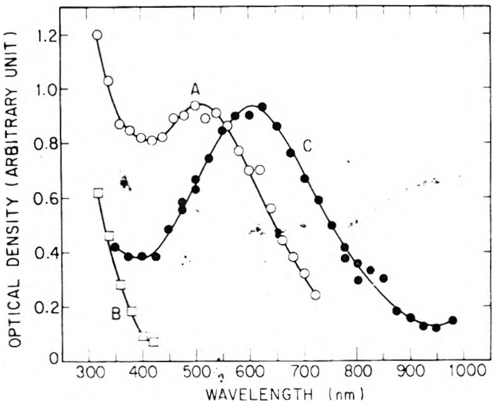

Figure 4. Absorption spectra obtained with 0.25 M methyl ethyl ketone in THF at 178°K (A and B); and 0.40 M methyl isopropyl ketone in MTHF at 100°K (C). Spectra A, B, and C were determined immediately, at 20 μsec, and at 15 μsec after the pulse, respectively.

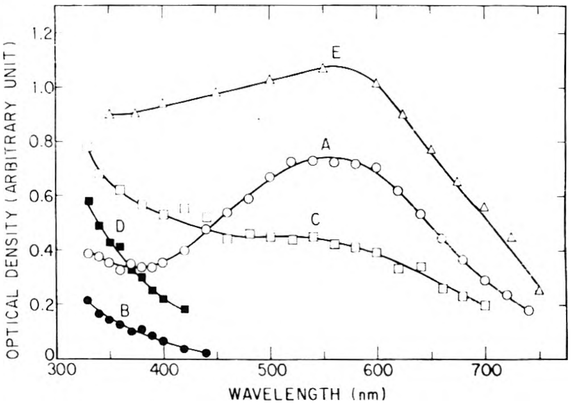

Figure 5. Absorption spectra obtained with 0.22 M methyl isobutyl ketone in THF at 178°K (A and B); 0.16 M diethyl ketone in THF at 178°K (C and D); and 0.40 M diethyl ketone in MTHF at 100°K (E). Spectra A, B, C, D, and E were determined immediately, at 25 μsec, immediately, at 8 μsec, and at 5 μsec after the pulse, respectively.

containing 0.1 M triethylamine and the absorption at 500 nm in THF containing 0.74 M acetone. The decay curve for the band at 340 nm fits a second-order rate law, suggesting that the absorbing species, which are most probably neutral radicals, recombine bimolecularly. The other decay curves fit neither a first- nor second-order rate law. The ionic species corresponding to these absorptions probably disappear by a combination of reactions with solvent molecules, impurities, and/or products. The neutralization reaction between acetone anions and acetone cations does not occur to a significant extent in pure acetone since their decays at 500 and 750 nm are considerably different from each other. The addition of triethylamine increases the lifetime of the absorption at 500 nm. This implies that cationic species may be replaced with a less reactive cation in the presence of triethylamine.

Methyl Ethyl Ketone. Figure 4 illustrates the transient absorption spectra observed at 178°K for 0.25 M methyl ethyl ketone in THF. The spectrum determined immediately after the pulse has a peak at 510 nm, similar to acetone in THF. The absorption at 510 nm decays according to a first-order rate law with a half-life of about 3.5 μsec. The absorbing species probably react with impurities. In the present study, however, no effort has been made to elucidate the decay mechanism. The time necessary for the optical density to decrease to one-half of its initial value ($\tau_{1/2}$) will be given in each case. When the decay fits a first-order rate law, $\tau_{1/2}$ will be described as a half-life. The decay curves at λ <420 nm show the definite contribution of another absorbing species with a longer lifetime; its spectrum can be determined separately after the absorption at longer wavelengths disappears, as shown in Figure 4.

Methyl Isopropyl Ketone. Figure 4 also presents the absorption spectra observed at 100°K for 0.40 M methyl isopropyl ketone in MTHF. In a very early stage the absorption due to the solvated electron appears in the infrared region, but disappears completely within about 20 μsec. On the other hand, the absorption at around 600 nm apparently increases during the initial period of 20 μsec, although the largest part is formed simultaneously with the pulse irradiation. Therefore, absorbing species at 600 nm are formed, at least in part, by the reaction of the solvated electron with a solute molecule. The absorption spectrum determined 15 μsec after the pulse exhibits the peak at 600 nm, which decays with $\tau_{1/2}$ of 220 μsec after reaching a maximum.

Methyl Isobutyl Ketone. Figure 5 shows the absorption spectra obtained for 0.22 M methyl isobutyl ketone in THF at 178°K. The essential features are the same as those for methyl ethyl ketone. The peak of the spectrum is at 560 nm. The decay curve at 560 nm fits neither a first-order nor second-order rate law, giving 4.0 μsec as the value of $\tau_{1/2}$.

Diethyl Ketone. Figure 5 also presents the absorption spectra obtained for 0.16 M diethyl ketone in THF at 178°K and 0.4 M diethyl ketone in MTHF at 100°K. In the spectrum for the former solution an absorption band due to short-lived species exists in the visible region although it is not well separated from the strong uv band due to long-lived species. In the spectrum for the latter solution, the peak is at 550 nm.

Diisopropyl Ketone. Figure 6 shows the absorption spectra observed at 100°K for 0.28 M diisopropyl ketone in

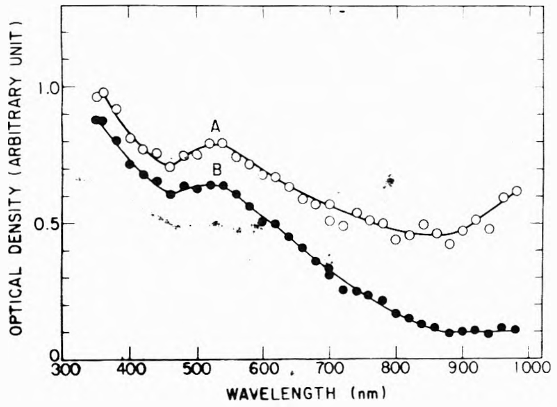

Figure 6. Absorption spectra obtained with 0.28 M diisopropyl ketone in MTHF at 100°K. Spectra A and B were determined immediately and at 75 μsec after the pulse, respectively.

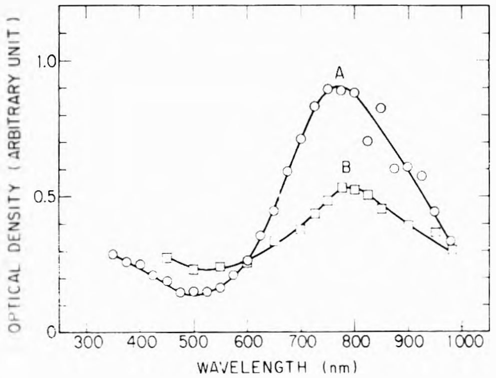

Figure 7. Absorption spectra obtained with 0.43 M cyclopentanone in MTHF at 100°K (A); and 1.6 × 10^{-3} M cyclopentanone in MTHF at 178°K (B). Spectra A and B were determined at 15 μsec and immediately after the pulse, respectively.

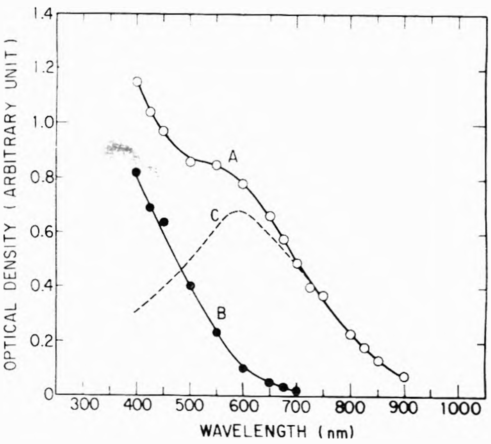

Figure 8. Absorption spectra obtained with 3.2 × 10^{-2} M cyclohexanone in MTHF at 143°K. Spectra A and B were determined at 1 and 15 μsec after the pulse, respectively. Spectrum C is the difference between A and B.

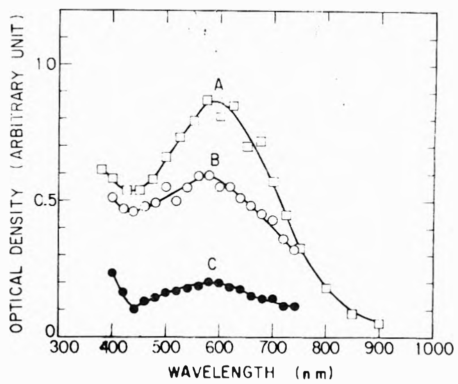

Figure 9. Absorption spectra obtained with 0.37 M cyclohexanone in MTHF at 100°K (A) and 0.20 M cyclohexanone in ethanol at 100°K (B and C). Spectra A, B, and C were determined at 15, 5, and 120 μsec after the pulse, respectively.

MTHF. The absorption due to the solvated electron is seen in the spectrum determined immediately after the pulse. The peak of the visible band is located at about 520 nm, although the tail of the intense uv band overlaps considerably.

Cyclopentanone. Figure 7 shows the absorption spectra observed at 100°K for 0.43 M cyclopentanone in MTHF and at 178°K for 1.6 × 10^{-3} M cyclopentanone in MTHF. Gas chromatographic analysis revealed that the cyclopentanone used contained a few per cent impurity. However, the absorption produced from the impurity cannot be considered to contribute significantly to the spectrum determined immediately after the pulse in the solution when the concentration of the cyclopentanone is as low as 1.6 × 10^{-3} M. Further, since both solutions show practically the same absorption band at 775 nm, the possibility that the band arises from the impurity is excluded. The value of $\tau_{1/2}$ is 200 μsec in the former solution and 3 μsec in the latter.

Cyclohexanone. Figures 8 and 9 present absorption spectra obtained with 3.2 × 10^{-2} M cyclohexanone in MTHF at 143°K, 0.37 M cyclohexanone in MTHF at 100°K, and 0.2 M cyclohexanone in ethanol at 100°K. The decay curves observed for the first solution suggest the presence of three transient species with quite different lifetimes. Of these species, the first one is ascribed to the solvated electron since it absorbs light in the infrared region and its absorbance increases with an increase in wavelength. The second one absorbs light in the visible region and decays according to a first-order rate law with a half-life of 4 μsec. Judging from the location and the short lifetime of the absorption, this species can be asigned to the anion of cyclohexanone. The third one mainly absorbs light in the wavelength region shorter than 450 nm, and decays very slowly with $\tau_{1/2}$ of about 100 μsec. This absorption is probably due to neutral radicals. The spectrum of the second species can be determined by subtracting spectrum B from spectrum A, as shown in Figure 8. The absorption band attributed to the second species is observed more directly for 0.37 M cyclohexanone in MTHF at 100°K, where its lifetime is considerably increased (see Figure 9). A similar absorption band appears in the irradiated ethanol solution of cyclohexanone and the peak wavelength is independent of time.

Cycloheptanone. The absorption spectrum observed at 158°K for 7.7 × 10^{-2} M cycloheptanone in MTHF is shown in Figure 10. The spectrum has a peak at 680 nm and the decay curve obtained at the same wavelength agrees with first-order kinetics with a half-life of 6.5 μsec.

Cyclooctanone. Figure 10 presents the absorption spectrum observed at 143°K for 1.6 × 10^{-3} M cyclooctanone in MTHF. The peak is located at 775 nm and the decay curve fits a first-order rate law with a half-life of 15 μsec.

Cyclododecanone. Figure 10 also presents the absorption spectrum observed at 173°K for 8.9 × 10^{-3} M cyclododecanone in MTHF. The peak is located at 640 nm and the ab-

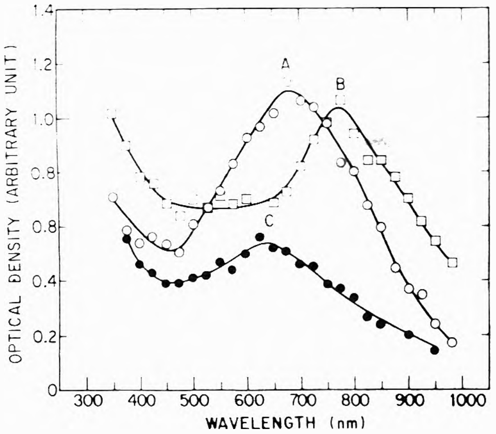

Figure 10. Absorption spectra obtained with 7.7 × 10^{-2} *M* cycloheptanone in MTHF at 158°K (A); 1.6 × 10^{-3} *M* cyclooctanone in MTHF at 143°K (B); and 8.9 × 10^{-3} *M* cyclododecanone in MTHF at 173°K (C). All spectra were determined 2 μsec after the pulse.

sorption disappears by first-order kinetics with a half-life of 3.8 μsec.

Discussion

In the previous study[2] on pulse radiolysis of acetone solutions, we have interpreted the formation of ions and excited states of aromatic molecules in solutions in terms of the following primary process

$$CH_3COCH_3 \longrightarrow CH_3COCH_3^+, CH_3COCH_3^-, {}^1CH_3COCH_3, {}^3CH_3COCH_3, \text{and neutral fragments} \quad (1)$$

where $CH_3COCH_3^+$, $CH_3COCH_3^-$, ${}^1CH_3COCH_3$, and ${}^3CH_3COCH_3$ represent the molecular cation, molecular anion, first excited singlet state, and lowest triplet state of acetone, respectively. In addition, we have reported the following values as their yields: G(free ions) = 1.5, $G({}^1CH_3COCH_3)$ = 0.31, and $G({}^3CH_3COCH_3)$ = 1.1, where G(free ions) is the sum of the yields for both the free cation and anion. These values are in fairly good agreement with the independent measurements by other groups.[4-6] It is realized that ionic processes contribute significantly to the radiolysis of acetone.

The effects of triethylamine and nitrous oxide on the spectrum of irradiated pure acetone indicate that the absorption band at 500 nm can be ascribed to either monomer anions of acetone or species produced from the monomer anion. The same band was observed for irradiated THF solutions of acetone. Since the reaction

$$e_{sol}^- + CH_3COCH_3 \longrightarrow CH_3COCH_3^- \quad (2)$$

is expected to take place in THF solutions, the absorption band at 500 nm is most likely assigned to molecular anions of acetone. In the THF solution of 6.0 × 10^{-4} *M* acetone irradiated at 168°K the initial spectrum agrees with the spectrum of the solvated electron in THF, but the subsequent spectrum shows a 500-nm band. This spectral change can be explained by reaction 2. The decay curve at 900 nm corresponds to the decay of the solvated electron by reaction 2, and its rate constant can be determined to be 6 × 10^8 M^{-1} sec^{-1}. The decay curve at 625 nm apparently consists of the short-lived absorption due to the solvated electron and the long-lived one due to the anion of acetone. On the other hand, the decay at 500 nm behaves as if there were only one absorbing species. This behavior is, however, considered to result from a balance between the decay of the absorption due to the solvated electron and the concurrent growth of the absorption due to the molecular anion of acetone. If the absorption at 500 nm is formed independently of the solvated electron, the rapid decay of the absorption due to the solvated electron should be observable in the initial part of the decay curve. The behavior of the decay curve at 500 nm also suggests that the molar extinction coefficients of the solvated electron and the anion of acetone are roughly equal to each other. The absolute absorption spectrum of the solvated electron in THF has been measured at room temperature in the wavelength region from 555 to 2200 nm.[17] Although the extinction coefficient at 500 nm is not shown in their measurement, its value may be close to that at 555 nm (4 × 10^3 M^{-1} cm^{-1}) because the absorption does not decrease appreciably between 500 and 555 nm. Since the spectrum of the solvated electron generally shifts to shorter wavelengths as the temperature decreases, the extinction coefficient at 168°K must be somewhat larger than that at room temperature. Therefore, the molar extinction coefficient of 5 × 10^3 M^{-1} cm^{-1} determined for the molecular anion of acetone is consistent with the suggestion mentioned above.

The decreasing lifetime of the absorption at 500 nm with an increase in anthracene concentration as well as the concomitant formation of the absorption due to anthracene anions supports the occurrence of the reaction proposed in the previous paper:[2]

$$CH_3COCH_3^- + \text{anthracene} \longrightarrow CH_3COCH_3 + \text{anthracene}^- \quad (3)$$

The removal of acetone anions by water may be due to the reaction:

$$CH_3COCH_3^- + H_2O \longrightarrow (CH_3)_2COH + OH^- \quad (4)$$

The anion of acetone has been studied in aqueous systems. Asmus et al.[10] found that the transient spectrum produced by pulse radiolysis of aqueous solutions of 2-propanol saturated with nitrous oxide changes depending on the pH value of the solution. This change has been attributed to the dissociation of α-2-propanol radicals formed by the following mechanism

$$H_2O \longrightarrow e_{aq}^-, H, OH, \text{etc.}$$

$$e_{aq}^- + N_2O \longrightarrow N_2 + OH + OH^-$$

$$OH \text{ or } H + (CH_3)_2CHOH \longrightarrow H_2O \text{ or } H_2 + (CH_3)_2COH$$

$$(CH_3)_2COH \longrightarrow (CH_3)_2CO^- + H^+$$

Molecular anions of acetone are consequently favored at high pH's. The typical spectrum reported[11] on the aqueous solution of 0.1 *M* 2-propanol at pH 13.3 decreases continuously with an increase in wavelength up to 450 nm. Being different from the present results, the spectrum does not show the absorption band with a peak at around 500 nm. The discrepancy between these observations might be attributed to the effect of the solvent on the spectrum.

Absorption spectra of anions of aromatic ketones, in fact, are known to show a large solvent shift. The benzophenone anion, for example, exhibits an absorption peak at 630 nm in hydroxylic solvents and 780 nm in ethereal solvents. Our previous study[19] on the benzophenone anion produced at 100°K by pulse radiolysis of ethanol solutions has clearly demonstrated that the initial spectrum has a peak at 780 nm, but gradually shifts to shorter wavelengths as reorientation of solvent molecules around the anion proceeds. In contrast to this result the absorption spectrum observed for the cyclohexanone anion in ethanol glass at 100°K does not show a spectral shift even at a few hundred of microsecond after the pulse. This fact excludes the possibility of a solvent shift of the spectra of anions of aliphatic ketones in hydroxylic solvents. In addition the difference between the spectra obtained with aqueous solutions and with THF solutions seems too large to be interpreted in terms of a simple solvent effect. At this moment we cannot explain the difference.

Dimer cations of organic compounds produced by reaction 5 were first found in the esr study[20] of dichloromethane solutions of naphthalene containing antimony pentachloride as an oxidizing agent. Subsequently, a number of studies, especially spectroscopic and kinetic, have been made using a pulse radiolysis technique[21-23] and a matrix isolation technique.[12,24] Badger and Brocklehurst[24] have suggested that the absorption band reported by Shida and Hamill[7] is due to dimer cations of acetone. In the present study glassy *n*-butyl chloride and glassy *n*-butyl chloride solutions of acetone were γ irradiated at 77°K to confirm this identification. As shown in Figure 2, irradiated pure *n*-butyl chloride had an absorption band at 530 nm, while irradiated *n*-butyl chloride solution of 0.5 *M* acetone had an absorption band at 740 nm, almost the same as that obtained with pulse irradiated acetone saturated with nitrous oxide. *n*-Butyl chloride solutions of acetone at concentrations between 0.05 and 0.4 *M* exhibited bands at both 530 and 740 nm. The intensity of the band at 530 nm decreased and that at 740 nm increased with increasing concentration of acetone. No other bands were found in the wavelength region from 350 to 1200 nm. Moreover, an enhancement of the band at 740 nm did not occur during warming the solutions. Their colors faded out without change in tint. These results rather indicate that the band at 740 nm can be assigned to molecular cations of acetone.

$$\mathrm{M}^{+} + \mathrm{M} \longrightarrow \mathrm{M}_2^{+} \qquad (5)$$

All the absorption bands in the visible or near-infrared region observed in other aliphatic ketones are assigned to molecular anions of the solute ketones as the analogy with acetone. The peak wavelengths of these absorption bands are tabulated in Table I. Anions of alkyl ketones with a large alkyl group tend to exhibit the absorption bands at long wavelengths except for diisopropyl ketone. On the other hand, locations of the absorption bands due to anions of cycloketones show no relationship with the number of carbon atoms. We have been unable to correlate the absorption bands with physical parameters of the parent ketones such as dielectric constants, dipole moments, or their optical transitions in the uv.

TABLE I: Peak Wavelengths of Anions of Aliphatic Ketones

Anion	Wavelength, nm
Acetone	500
Methyl ethyl ketone	510
Methyl isopropyl ketone	600
Methyl isobutyl ketone	560
Diethyl ketone	550
Diisopropyl ketone	520
Cyclopentanone	775
Cyclohexanone	580
Cycloheptanone	680
Cyclooctanone	775
Cyclododecanone	640

Electron affinities of aliphatic ketones in the liquid phase are still unknown. However, our previous study[2] has demonstrated that biphenyl anions are formed by electron transfer from acetone anions in irradiated solutions when biphenyl is added at concentrations higher than 0.1 *M*. This result implies that the electron affinity of acetone is comparable to that of biphenyl. The anion of biphenyl is easily photobleached by visible light. In the case of acetone the threshold energy of photobleaching may be somewhat higher than that expected from the electron affinity because the Franck–Condon state of acetone resulting from photoionization of its anion is different from the usual state of acetone. However, the optical transition involving the electron in the highest orbital probably appears in the visible region. The similar argument can be applied to other aliphatic ketones electron affinities of which may be smaller than that of acetone. It is probable that anions of aliphatic ketones have their absorption bands in the visible or near-infrared region.

Acknowledgment. The authors wish to thank Dr. A. Kira for his performance of matrix isolation experiments and frequent discussions throughout this study.

References and Notes

(1) S. Arai and L. M. Dorfman, *J. Phys. Chem.*, **69**, 2239 (1965).
(2) S. Arai, K. Kira, and M. Imamura, *J. Chem. Phys.*, **54**, 5073 (1971).
(3) A. Kira, S. Arai, and M. Imamura, *Int. J. Radiat. Phys. Chem.*, **5**, 127 (1973).
(4) M. A. J. Rodgers, *Trans. Faraday Soc.*, **67**, 1029 (1971).
(5) E. Hayon, *J. Chem. Phys.*, **53**, 2353 (1970).
(6) S. A. Chaudhri and K. -D. Asmus, *J. Phys. Chem.*, **76**, 26 (1972).
(7) T. Shida and W. H. Hamill, *J. Am. Chem. Soc.*, **88**, 3683 (1966).
(8) M. A. J. Rodgers, *J. Chem. Soc., Faraday Trans. 1*, **68**, 1278 (1972).
(9) A. J. Robinson and M. A. J. Rodgers, *J. Chem. Soc., Faraday Trans. 1*, **69**, 2036 (1973).
(10) K. -D. Asmus, A. Henglein, A. Wigger, and G. Beck, *Ber. Bunsenges. Phys. Chem.*, **70**, 756 (1966).
(11) M. Simic, P. Neta, and E. Hayon, *J. Phys. Chem.*, **73**, 3794 (1969).
(12) B. Badger and B. Brocklehurst, *Trans. Faraday Soc.*, **66**, 2939 (1970).
(13) A. Kira, S. Arai, and M. Imamura, *Rep. Inst. Phys. Chem. Res.*, **47**, 139 (1971).
(14) S. Arai, S. Tagawa, and M. Imamura, *J. Phys. Chem.*, **78**, 519 (1974).
(15) P. Balk, G. J. Hoijtink, and J. W. H. Schreurs, *Recl. Trav. Chim. Pays-Bas*, **76**, 813 (1957).
(16) L. M. Dorfman, F. Y. Jou, and R. Wageman, *Ber. Bunsenges. Phys. Chem.*, **75**, 681 (1971).
(17) F. Y. Jou and L. M. Dorfman, *J. Chem. Phys.*, **58**, 4715 (1973).
(18) S. Gordon, E. J. Hart, M. S. Matheson, J. Rabani, and J. K. Thomas, *Discuss. Faraday Soc.*, **36**, 193 (1963).
(19) M. Hoshino, S. Arai, and M. Imamura, *J. Phys. Chem.*, **78**, 1473 (1974).
(20) I. C. Lewis and L. S. Singer, *J. Chem. Phys.*, **43**, 2712 (1965).
(21) A. Kira, S. Arai, and M. Imamura, *J. Chem. Phys.*, **54**, 4890 (1971).
(22) A. Kira, S. Arai, and M. Imamura, *J. Phys. Chem.*, **76**, 1119 (1972).
(23) M. A. J. Rodgers, *Chem. Phys. Lett.*, **9**, 107 (1971).
(24) B. Badger and B. Brocklehurst, *Trans. Faraday Soc.*, **65**, 2576, 2578, 2588 (1969).
(25) C. Denian, A. Déroulède, F. Kieffer, and J. Rigant, *Luminescence*, **3**, 325 (1971).

High-Energy Ion–Molecule Reactions at Nonzero Scattering Angles

T. Ast, D. T. Terwilliger, R. G. Cooks,* and J. H. Beynon

Department of Chemistry, Purdue University, West Lafayette, Indiana 47907 *(Received November 1, 1974)*

Publication costs assisted by the National Science Foundation

Energy loss spectra are reported for the 10/10* reaction of argon ions upon argon at various nonzero scattering angles using a new mass spectrometric technique. The spectra obtained are in good agreement with those obtained by conventional methods. Trajectory calculations were performed in order to determine the scattering angles and the instrument transmission function. An alternative scanning technique is also described whereby a particular process can be monitored as the scattering angle is varied.

Introduction

We have previously shown that it is possible to study ion–molecule reactions at nonzero scattering angles in a double-focusing mass spectrometer.[1] We now show that this approach allows the approximate determination of relative cross sections differential in both scattering angle and kinetic energy. The usefulness of kilovolt energy ion–molecule reactions should be augmented by these developments. These reactions are already a source of information on the quantum state composition of ion beams,[2] ion structure,[3] double ionization potentials,[4] energy levels in inaccessible species,[5] molecular structure,[6] reaction kinetics for highly energized species,[7] and other aspects of ion chemistry.[3a,6]

Principle of the Method

Consider a conventional double focusing mass spectrometer (ion source/electric sector/magnetic sector/detector) operated to transmit stable ions generated in the ion source at an accelerating voltage V, an electric sector voltage E, and a magnetic field strength B. For simplicity, assume that the reactant ion does not change its charge in the collision process. In the conventional mode of operation of the mass spectrometer, specification of the instrument geometry and of the parameters V and B specifies any reaction occurring in the second field-free region. If the beam is able to pass through the electric sector, the value of E is linked to the value of V and is thus not generally thought of as an independent variable. But this is not to say that the electric sector is superfluous when reactions occurring in the second field-free region are being studied. It could serve for prior energy selection of the reactant beam, although we are not aware that any such experiments have been performed in the second field-free region. More importantly, for experiments involving scattering collisions both in and following the electric sector, the sector can be used to select the scattering angle at which measurements are made. If the beam suffers angular deflection upon collision, the required ratio of accelerating voltage to electric sector voltage is changed; each new ratio specifies a particular small range of scattering angles in the collision process for which the product ions are transmitted and collected, though not along the central path through the spectrometer. The range of angles involved is discussed below.

In the earlier study,[1] it was shown that if the magnetic field was set so as to detect ions of mass-to-charge ratio (m) at normal values of V and E, and V was then scanned to higher values, peaks due to scattered ions of mass to charge ratios ($m - 1$), ($m - 2$), etc. could be detected at the same magnetic setting. As the voltage was scanned in the opposite direction, peaks due to ions of mass-to-charge ratios ($m + 1$), ($m + 2$), etc. were similarly observed. The structure observed in some of the peaks corresponded to different energy losses suffered by the scattered ions.

The main advantage of this method is that interference of the main ion beam can be avoided by studying reactions at nonzero scattering angles. However, due to hysteresis and nonlinearity it is difficult to adjust the magnet setting by amounts smaller than one mass unit; this made the study of low mass ions virtually impossible. For this reason, a new experimental method has been developed.

Consider a normal beam of ions of mass-to-charge ratio m which is transmitted through the double-focusing mass spectrometer set at accelerating voltage V, electric sector voltage E, and magnetic field B. If the value of E is reduced by a small amount to a new value E', the ions will no longer follow the central path and will not be transmitted through the electric sector. However, if a collision gas is now introduced, the beam can be deflected through a small angle and its trajectory altered enabling it to pass through the electric sector, as well as through the energy resolving β slit. If no kinetic energy were lost in the collision (vide infra), the ions would still have the kinetic energy corresponding to the original value of V, and they would thus be transmitted through the magnet and recorded as ions of mass-to-charge ratio m. If the accelerating voltage is now scanned upward, peaks due to ions which have suffered kinetic energy loss in the collision will appear at values $V + \Delta V$ where ΔV corresponds to the amount of kinetic energy lost. The value of E' controls the allowed scattering angles; scanning of the accelerating voltage will also influence the scattering angle to some extent (see below). The plot obtained represents an energy loss spectrum corresponding to a small range of scattering angles.

Results and Discussion

All the measurements were made on a Hitachi-Perkin Elmer RMH-2 mass spectrometer under the following conditions: accelerating voltage 8 kV, electron energy 70 eV, electron current 1 mA. Both the β slit and final resolving slit were kept as narrow as the sensitivity permitted. The collision gas was introduced into the second field-free region at a pressure of 1×10^{-5} Torr from where it diffused into the electric sector (ESA pump was shut off during the experiment).

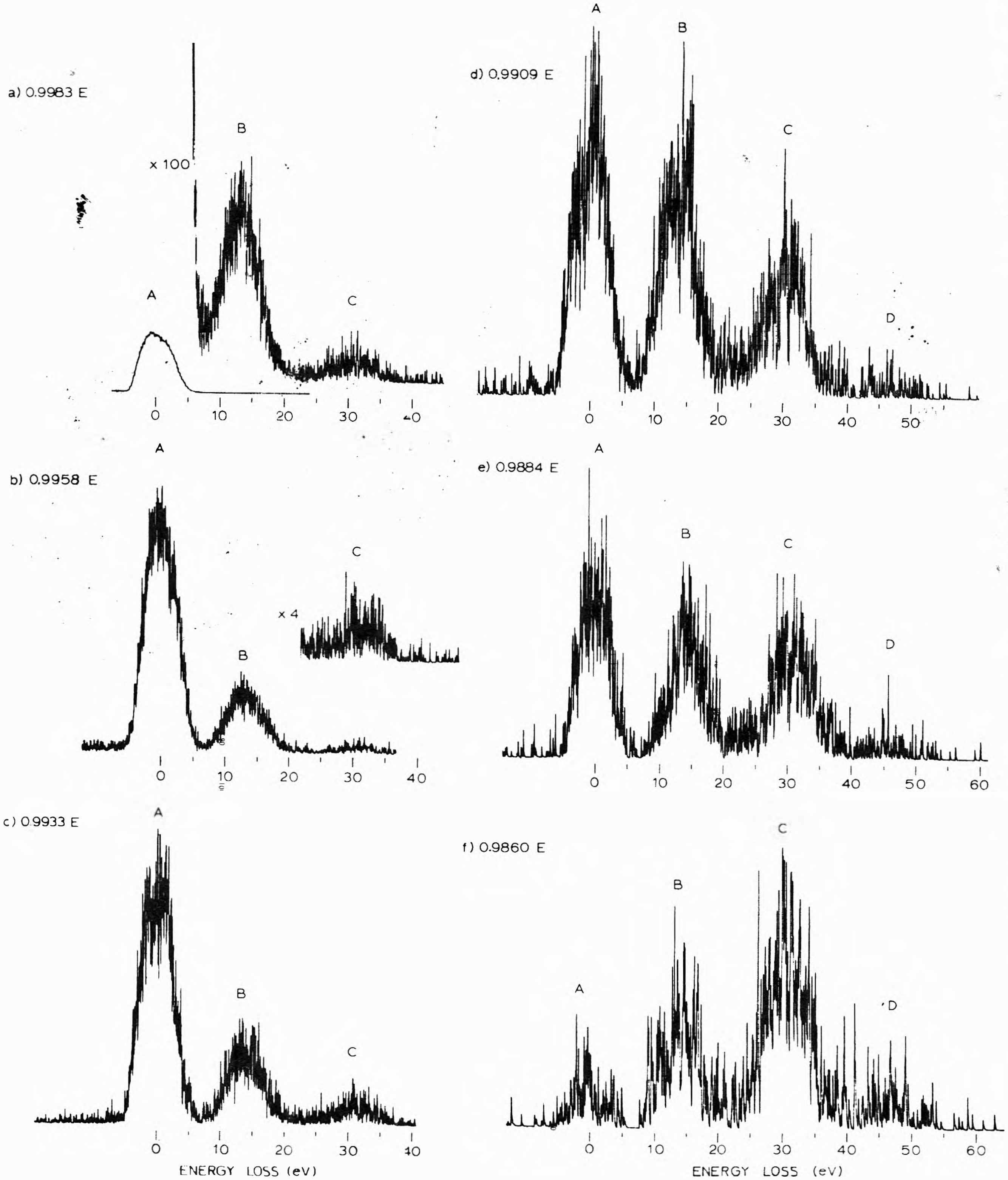

Figure 1. The curves marked a–f show a series of translational energy loss spectra for the reaction of $Ar^{\cdot +}$ ions with Ar plotted at different values of electric sector voltage and hence at different scattering angles. The peaks marked A in each plot correspond to ions that have been scattered elastically, the peaks marked B, C, and D correspond to ions that have undergone inelastic collisions without alteration of charge but in which the target molecules have gained excitational energy.

Because data were already available[8] from conventional scattering experiments, reaction 1 was chosen for study. In

$$Ar^{+} + Ar \longrightarrow Ar^{+} + Ar^{*(+)} \qquad (1)$$

this reaction the target atom can be excited, ionized, or both. The choice of argon also eliminates the potential complicating effects of the presence of ions other than those of a single mass-to-charge ratio.

Figure 1 shows the kinetic energy loss spectra for reaction 1 obtained by the accelerating voltage scan method at different values of the electric sector voltage E'. Peak A represents elastically scattered ions and peaks B, C, and D are due to inelastic processes. All energy loss measurements are made with reference to the elastic peak A. The kinetic energy losses associated with the elastically scattered ions which give peak A are negligible because of the small scattering angles involved (see below). Furthermore, at the ion energies employed kinetic energy transfer to the target in the inelastic reactions is also negligible.[9] Thus, the relative energy losses shown in Figure 1 approximately equal the amount, Q, of kinetic energy transferred to internal energy for the process in question.

Our results for reaction 1 are in agreement with those obtained by a conventional study[8] of reaction 1 covering various scattering angles (0.5–13°) in the kinetic energy range 500–3000 eV. Peaks corresponding in energy loss values to peaks A–C in Figure 1 were observed. Peak B was attributed to the excitation of the target to levels such as ($3p^5\,4s$) with $Q = 11.5$ eV, ($3p^5\,4p$) with $Q = 12.9$ eV, etc. up to the ionization limit of $Q = 15.75$ eV. Peak C was associated with excitation of the target atom to autoionizing levels, such as ($3s\,3p^6\,4s\,{}^1P$) with $Q = 25.8$ eV, ($3s\,3p^6\,4s\,{}^1S$) with $Q = 26.7$ eV, ($3s\,3d^6\,4p\,{}^1D$) with $Q = 27.55$ eV, etc., as well as to the production of excited Ar^+ ions such as Ar^+ ($3p^4\,3d$) with $Q = 32.05$ eV. In addition to these peaks, we also observe a fourth peak D centered at $Q \approx 47$ eV, which apparently corresponds to the process in which the target atom is doubly ionized. The ^3P, ^1D, and ^1S states of Ar^{2+} lead to predicted energy loss values of 43.4, 45.1, and 47.5 eV, respectively, in good agreement with the experimentally observed value.

Although energy loss spectra are readily obtained as described above it was necessary to perform detailed trajectory calculations in order to establish the scattering angles and the instrumental transmission properties.

Consider a collision between an ion m_1^+ and a neutral m_2 in which m_1^+ is scattered through an angle θ in the plane of analysis of the mass spectrometer without change of charge and in which an amount Q of translational energy of the system is converted into internal energy. The final velocity (v_1) of m_1^+ is given in terms of its initial velocity (v_0) by

$$v_1/v_0 = [\mu \cos \theta + \{(1 + \mu\epsilon - \mu^2(1 - \epsilon) \sin^2 \theta)/(1 - \epsilon)\}^{1/2}]/(\mu + 1) \quad (2)$$

where $\epsilon = Q/(Q + 1/2 m_1 v_0^2)$ and $\mu = m_1/m_2$. Writing $x = v_0/v_1$, eq 2 can be rewritten

$$\cos \theta = \frac{(\mu x^2 + \mu + 1)(1 - \epsilon) - x^2}{2x\mu(1 - \epsilon)} \quad (3)$$

The value of x is calculated from the value of V and the value of $V + \Delta V$ and the scattering angle θ through which the detected ions have been deflected in the collisions can then be calculated. Trajectory calculations similar to those used to calculate metastable peak shapes[10] were used to determine the position where an ion scattered at any point along its path impinges on the β-slit plane. The point of scattering was then iterated to the value necessary to permit the ion to pass through the β slit. Generally, it was found that there are two such points, one near the entrance to the electric sector and one located near the exit of the electric sector or in the second field-free region itself. In general, due to the finite width of the β slit and the resolving power of the magnetic sector, there is a range of positions from which scattering can be observed.

TABLE I: Results of Scattering Angle Calculations[a]

E'/E	Q, eV	Range of scattering angles obsd, deg	Calcd rel abundance	ΔV, eV
0.9983	0	0.10–0.82	707	0.03
	13	0.04–0.83	664	13.09
	32	0.04–0.87	608	32.30
	48	0.04–1.05	169	49.19
0.9958	0	0.25–0.86	643	0.18
	13	0.27–0.87	604	13.26
	32	0.04–0.90	552	32.41
	48	0.04–0.95	520	48.70
0.9933	0	0.39–0.92	588	0.45
	13	0.42–0.93	553	13.54
	32	0.44–0.97	507	32.73
	48	0.04–1.00	473	48.91
0.9860	0	0.82–1.19	473	1.87
	13	0.85–1.21	446	15.00
	32	0.89–1.24	409	34.18
	48	0.91–1.27	384	50.42

[a] E' represents the value to which the electric sector was set for the experiment, E being the normal value of electric sector voltage corresponding to transmission of the unscattered ion beam of mass m. Q is the energy defect of the reaction in the scattering collision, ΔV the calculated value by which the accelerating voltage needs to be increased to observe the process. Some of the apparent inconsistencies in the scattering angles are discussed in the text.

The calculations were performed assuming a constant cross section as a function of scattering angle in order to determine the instrument transmission. Results are given in Table I, and they show the following. (i) There is a range of scattering angles corresponding to each E' value. This range is larger for the small electric sector offset values, for example, 0.04–0.83° for $E'/E = 0.9983$, and smaller for the large electric sector offset values, 0.89–1.24° for $E'/E = 0.9860$. Both examples quoted refer to peak C. (ii) The range of scattering angles shows a very small variation between peaks A, B, C, and D observed at a particular E' value. For example, in the experiment performed with the electric sector value offset to $0.9860E$, the range of scattering angles is calculated to be 0.89–1.24° for peak C and 0.91–1.27° for peak D. Therefore, to a good approximation, ions giving rise to peaks A–D in each particular experiment (Figure 1a–f) can be considered as being scattered through the same range of angles. (iii) Instrument transmission falls off with increasing scattering angle and kinetic energy loss but the total change involved is small (less than a factor of 2). (iv) The error involved in approximating the energy defect Q by the energy loss measured relative to the elastic peak never exceeds 0.6 eV and is thus smaller than the experimental error. (v) The scattering angle does not necessarily increase monotonically with increasing electric sector offset as can be seen for the peak with Q of 48 eV. Since the reactant ion fragments within the electric sector the electric sector voltage necessary to transmit the ion scattered at an angle of 0° will be somewhat less than E and will, of course, vary with the collision point. The minimum scattering angles will occur for values of E' closest to this lowered value; this effect can be seen for $Q = 48$ eV in Table I, where the scattering angles are smallest for $E'/E \approx 0.9958$. Similarly, as long as E' is between the lowered value mentioned above, and E, there will be some collision point corresponding to zero or near zero scattering angles. This can also be observed in the table. (The large number of 0.04° scattering angles is due to round off errors in the computer, as the scattering angle is calculated by subtracting two large near equal numbers, and is of no physical significance.) When E' is decreased still further ($E'/E = 0.9860$) the near zero angles disappear.

The scattering angles involved in this study are fairly small. They never exceeded 1.3°. Larger electric sector offset values would have caused larger scattering angles, but the signal strengths were low in this region. However, even for this narrow range of scattering angles, it was found that the cross sections for the elastic and various inelastic collision peaks are an extremely sensitive function of θ. The large energy loss reactions giving peaks C and D (Figure 1) increase in abundance relative to the reactions with smaller energy losses as $|E - E'|$ and, hence the scattering angle, is increased. Completely analogous results were obtained when $E' > E$ although this procedure is less desirable because at some point in the accelerating voltage scan the main beam of unreacted ions is transmitted.

The method described shows the variation of energy loss spectra with the scattering angle; however, a small range of scattering angles is always involved (rather than a single value), which makes it difficult to follow the behavior of the cross section for a particular process as the function of the scattering angle θ. Therefore, a new experiment was performed in which the accelerating voltage is set to the value $V + \Delta V$, corresponding to a particular peak in the kinetic energy loss spectrum (for example, $\Delta V = 13$ eV if we want to study peak B). When the electric sector voltage is now scanned the scattering angle is being continuously changed and the resulting plot shows the variation of the cross section as the function of θ. The experimental curve for the elastic scattering (peak A) shows oscillatory structure, previously noted by Barat *et al.*[8]

Conclusions

The study of high-energy ion–molecule reactions at zero scattering angles in a mass spectrometer is a rapidly developing subject. It is now apparent that a double-focusing mass spectrometer in which the electric sector and accelerating voltage are independently variable can also be used to give detailed information concerning ion–molecule collisions in which nonzero scattering of the ion beam occurs. An immediate advantage of nonzero scattering is that it brings into the compass of the mass spectrometer the study of reactions of the general type 10/10* in which the neutral is excited (or even ionized) but in which the fast particle does not change the number of charges it carries. Without the use of scattering angle as a parameter, the product ion beam is difficult to distinguish and resolve from the main beam of unreacted ions. More generally we have shown that kinetic energy loss spectra can be determined for particular scattering angles and that reaction cross sections for particular elementary reactions can be followed as a function of scattering angle. The procedure does not appear to be applicable to scattering angles larger than a few degrees and there is a considerable range of allowed angles at small electric sector offsets. The importance of the latter factor is probably minimized by the propensity for cross sections to fall off rapidly with increasing scattering angle. Moreover, the control which can be exercised over scattering angle is sufficient to cause marked changes in the relative cross sections for particular processes.

Acknowledgment. We thank the National Science Foundation for support of this work.

References and Notes

(1) R. G. Cooks, K. C. Kim, and J. H. Beynon, *Chem. Phys. Lett.*, **23**, 190 (1973).
(2) (a) F. C. Fehsenfeld, J. Appell, P. Fournier, and J. Durup, *J. Phys. B*, **6**, L268 (1973); (b) T. Ast, J. H. Beynon, and R. G. Cooks, *J. Amer. Chem. Soc.*, **94**, 6611 (1972).
(3) (a) T. Keough, T. Ast, J. H. Beynon, and R. G. Cooks, *Org. Mass Spectrom.*, **7**, 245 (1973); (b) F. W. McLafferty and I. Sakai, *ibid.*, **7**, 971 (1973); (c) J. H. Beynon and R. G. Cooks, *Adv. Mass Spectrom.*, **6**, 835 (1974).
(4) (a) J. Appell, J. Durup, F. C. Fehsenfeld, and P. Fournier, *J. Phys. B*, **6**, 197 (1973); (b) T. Ast, J. H. Beynon, and R. G. Cooks, *Int. J. Mass Spectrom. Ion Phys.*, **11**, 490 (1973).
(5) K. C. Kim, M. Uckotter, J. H. Beynon, and R. G. Cooks, *Int. J. Mass Spectrom. Ion Phys.*, **15**, 23 (1974).
(6) R. G. Cooks and J. H. Beynon in "Mass Spectrometry", A. Maccoll, Ed., MTP, International Review of Science, Physical Chemistry Series, Series Two, in press.
(7) R. G. Cooks, L. Hendricks, and J. H. Beynon, submitted for publication.
(8) M. Barat, J. Bandon, M. Abignoli, and J. C. Houver, *J. Phys. B*, **3**, 230 (1970).
(9) R. G. Cooks, J. H. Beynon, R. M. Caprioli, and G. R. Lester, "Metastable Ions", Elsevier, Amsterdam, 1973, pp 130–134.
(10) D. T. Terwilliger, J. F. Elder, Jr., J. H. Beynon, and R. G. Cooks, *Int. J. Mass Spectrom. Ion Phys.*, in press.

Optical Absorption Spectra of γ-Irradiated 3,4-Polyisoprene and 1,2-Polybutadiene

H. Zott and H. Heusinger*

Institut für Radiochemie der Technischen Universität München, D-8046 Garching, West Germany

(Received October 17, 1974)

Publication costs assisted by Institute für Radiochemie der Technischen Universität München

The optical absorption spectra of γ-irradiated 3,4-polyisoprene and 1,2-polybutadiene were investigated. Allyl radicals, dienes, and diene ions could be observed.

In connection with investigations in the radiolysis of 1,2-polybutadiene (1,2-PB) and 3,4-polyisoprene (3,4-PI)[1-4] uv-absorption measurements of the two polydienes have been made after γ irradiation. The polymer samples were γ irradiated and measured at $T = -196°$ and room temperature. Both unirradiated and γ-irradiated 3,4-PI

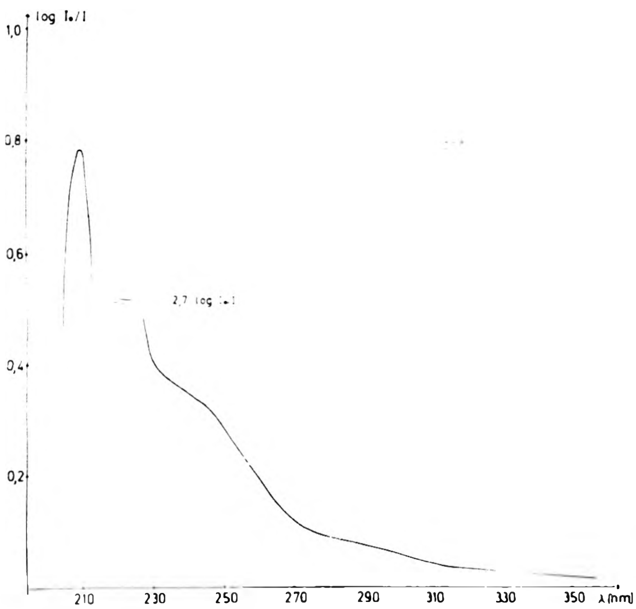

Figure 1. Uv absorption spectrum of 3,4-PI γ irradiated and measured at room temperature, dose 9.5 × 10^{20} eV/g.

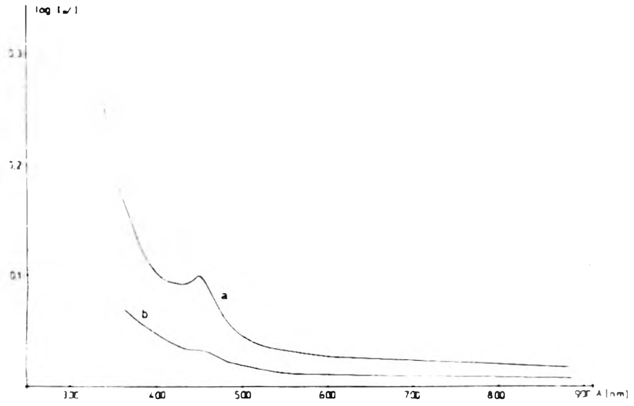

Figure 2. Optical absorption spectra of 3,4-PI γ irradiated and measured at $T = -196°$, dose 2.4 × 10^{20} eV/g: (a) immediately after γ irradiation; (b) after bleaching with filtered light (350 nm $\leq \lambda \leq$ 550 nm).

and 1,2-PB show a very strong absorption band with λ_{max} 205 nm (Figure 1) due to the π–π* transition of the double bond in the side chain:

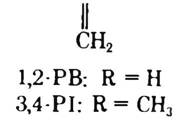

1,2-PB: R = H
3,4-PI: R = CH_3

In addition to this strong absorption the uv spectrum of 3,4-PI γ irradiated and measured at room temperature shows two shoulders at λ 234 and 290 nm (Figure 1). The absorption at λ 234 nm is assigned to dienes. The broad, weak shoulder with an absorption center of about 290 nm should be due to trienes and dienyl radicals[5] though the latter are less probable because dienyl radicals have not been found by ESR measurements.[4] After γ irradiation of 3,4-PI at −196° there are further bands with λ_{max} 250 and 450 nm, the latter being of very low intensity (Figure 2). The weak absorption at λ 450 nm is bleachable with filtered light of 350 nm $\leq \lambda \leq$ 550 nm (Figure 2). After γ irradiation of 1,2-PB we observed the same absorption bands except for a blue shift of the weak absorption to 443 nm. By the addition of 0.5 wt % anthracene to 3,4-PI the absorption at λ 450 nm is nearly suppressed and an additional weak long wave absorption at λ 710 nm due to anthracene ions is observed (Figure 3). The absorption with λ_{max} 250 nm at low temperature must be assigned to the doublet transition of allyl radicals. This is in good agreement with the calculated excitation energy of 5.29 eV for the doublet transition of the allyl radical by Longuet-Higgins and Pople.[6] The formation of allyl radicals by γ irradiation of 3,4-PI and 1,2-PB is established by ESR measurements as well.[4]

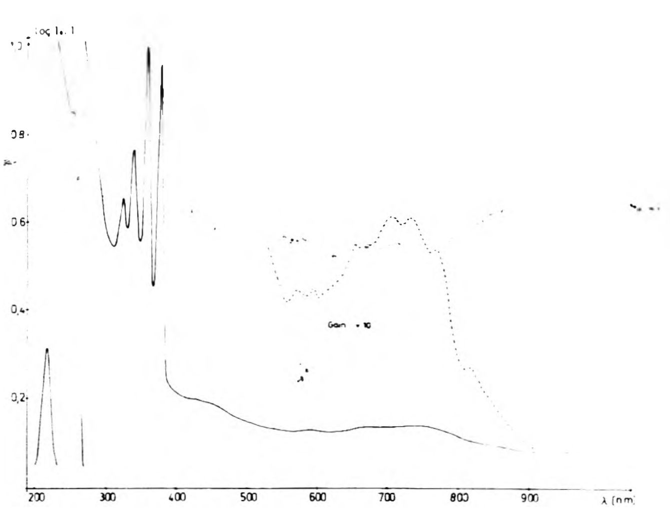

Figure 3. Optical absorption spectrum of 3,4-PI with 0.5 wt % of anthracene as additive, dose 1.9 × 10^{20} eV/g, γ irradiated and measured at $T = -196°$.

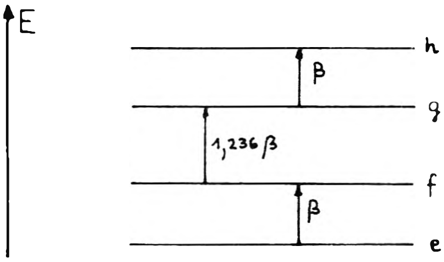

Figure 4. HMO energy levels of the π electrons of dienes (β is the resonance integral).

The absorption bands of 3,4-PI at λ 234 and 450 nm are due to dienes for which Kaufmann[3] has proposed a radiation induced formation. Dienes are also found by infrared spectroscopy.[3] The HMO energy levels for the π electrons of dienes are shown in Figure 4. The absorption at 234 nm is due to the π–π* transition f → g of a substituted diene. For diene anions and cations additional transitions g → h and e → f appear with less energy which correspond to the observed absorption bands of 3,4-PI at 450 nm and 1,2-PB at 443 nm.

The optical bleaching of these absorption bands by intensive light of the same wavelengths indicates the presence of anions. Because of the greater electron affinity anthracene is a more efficient electron scavenger than dienes and therefore the formation of diene anions is suppressed when anthracene is used as an additive. The presence of anthracene anions in such samples has been confirmed by ESR measurements as well.[4] No direct proof for the existence of diene cations can be given.

References and Notes

(1) H. Katzer and H. Heusinger, *Makromol. Chem.*, **163**, 195 (1973).
(2) A. v. Raven and H. Heusinger, *J. Polym. Sci.*, in press.
(3) R. Kaufmann, Thesis, Technical University Munich, 1974.
(4) H. Zott and H. Heusinger, *Macromolecules*, in press.
(5) D. C. Waterman and M. Dole, *J. Phys. Chem.*, **74**, 1906 (1970).
(6) H. C. Longuet-Higgins and J. A. Pople, *Proc. Phys. Soc.*, **68**, 591 (1955).

Internal Energy of Product Ions Formed in Mass Spectral Reactions. The Degrees of Freedom Effect[1]

P. F. Bente, III,[2a,b] F. W. McLafferty,* D. J. McAdoo,[2a,c] and C. Lifshitz[2d]

Department of Chemistry, Cornell University, Ithaca, New York 14850

(Received June 28, 1974; Revised Manuscript Received December 23, 1974)

The factors affecting the distribution of internal energy values, $P(E)$, in secondary ions produced in the ion source of a mass spectrometer have been studied through experimental and theoretical investigations of the degrees of freedom (DOF) effect on the metastable to precursor intensity ratio for a common metastable transition (m*) in a homologous series of molecular ions ($M\cdot^+$). An experimental study of the $C_3H_6O\cdot^+$ and metastable intensities for the process $M\cdot^+ \rightarrow C_3H_6O\cdot^+ \rightarrow C_2H_3O^+$ (m*) for 16 2-alkanones ranging from $C_6H_{12}O$ to $C_{31}H_{62}O$ showed a linear relationship between $[m^*(C_3H_6O\cdot^+ \rightarrow C_2H_3O^+ + CH_3\cdot)]$ and the reciprocal of the number of internal degrees of freedom in $M\cdot^+$. Theoretical calculations of the DOF effect used the 2-alkanone photoelectron spectra and the optical approximation of Meisels to obtain $P(E)_{M\cdot^+}$. Rate constants for formation of $C_3H_6O^+$, and other competing pathways as a function of molecular ion internal energy, $k(E)$, were calculated using Rice–Ramsperger–Kassel–Marcus theory. The $P(E)_{C_3H_6O\cdot^+}$ functions were calculated by assuming statistical randomization of the excess internal energy between the $C_3H_6O\cdot^+$ and the neutral fragment. The resulting calculated DOF plot was linear and had a slope in excellent agreement with the experimental results. The decreasing average internal energy of $C_3H_6O\cdot^+$ with increasing size of $M\cdot^+$ arises because increasingly large neutral fragments carry away a larger fraction of the $M\cdot^+$ internal energy. Offsetting this is an increasing abundance of tight complex fragmentations of $M\cdot^+$ which compete with $C_3H_6O\cdot^+$ formation at low $M\cdot^+$ internal energies, causing the average internal energy of those $M\cdot^+$ ions which fragment to give $C_3H_6O\cdot^+$ to be higher for larger $M\cdot^+$ ions. The general factors which affect $P(E)$ of product ion A^+ are (1) $P(E)_{M\cdot^+}$; (2) reactions competitive with A^+ formation; and (3) the partitioning of excess energy between A^+ and the neutral fragment.

Mass spectral ion abundances have been interpreted in terms of fragmentation rate constants as a function of ion internal energies, $k(E)$, and the internal energy values of the precursor ions, $P(E)$.[3,4] Calculations of $k(E)$ using the Rice–Ramsperger–Kassel–Marcus theory[5] have provided satisfactory agreement with experiment.[4–7] For *molecular* ions, $M\cdot^+$, useful approximations to $P(E)_{M\cdot^+}$ can be derived from the photoelectron spectrum of the corresponding molecule.[6,7] However, such methods will not yield information about $P(E)$ of a primary product ion, such as A^+; for the reaction sequence $M\cdot^+ \rightarrow A^+ \rightarrow D^+$, prediction of $[D^+]$ using $k(E)_{A^+\rightarrow D^+}$ from RRKM calculations requires a knowledge of $P(E)_{A^+}$. The following factors should be important in determining $P(E)_{A^+}$: (i) $P(E)_{M\cdot^+}$; (ii) $k(E)$ for $M\cdot^+ \rightarrow A\cdot^+$; (iii) the $k(E)$ functions for competing decompositions of $M\cdot^+$ ($M\cdot^+ \rightarrow B^+, C^+, \ldots$); and (iv) partitioning of excess energy between the A^+ ion and the neutral lost.[3,6,8,9] A qualitative assessment of these factors has been made;[10] this paper presents quantitative calculations to test further these assumptions.

A further reason for this study is to investigate the origin of the so-called "degrees-of-freedom effect".[10–13] For the fragment ion A^+ found in each of the mass spectra of a homologous series of molecules and the metastable decomposition of A^+ forming the daughter ion D^+ in a field-free region of the mass spectrometer, $m^*(A^+ \rightarrow D^+)$, the abundance ratio $[m^*(A^+ \rightarrow D^+)]/[A^+]$ is found to decrease as the size of the molecule increases. In fact, for all of over 30 homologous series of a wide variety of compounds examined in this laboratory the logarithm of $[m^*(A^+ \rightarrow D^+)]/[A^+]$ is found (Figures 1 and 2) to give within experimental error a linear correlation with the reciprocal of the number of internal degrees of freedom of the molecule (DOF = $3n - 6$, where n is the number of atoms in $M\cdot^+$). This correlation is notable because of its generality, especially considering all of the competing factors which affect $P(E)_{A^+}$.[10] Further, the linearity of the correlation predicts a finite value for $[m^*]/[A^+]$ for an infinite molecular size, meaning that some A^+ ions formed from such a molecular ion will still have sufficient internal energy to fragment at a rate of

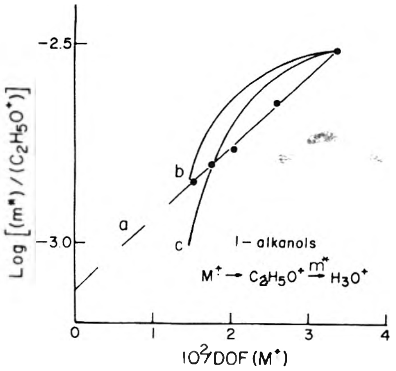

Figure 1. The degree-of-freedom (DOF) effect in 1-alkanols: (a) experimental results of ref 11; (b,c) calculated results of ref 14 assuming $E_0(C_2H_5O^+ \rightarrow H_3O^+)$ = 3.4 and 3.7 eV, respectively.

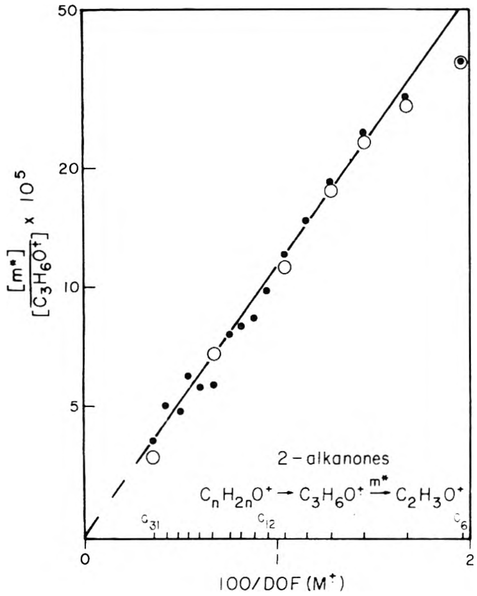

Figure 2. The DOF effect for 2-alkanones: ●, experimental values; O, calculated values (see text), using calculation II for C_6, C_7, and C_8, and calculation I for the remaining compounds.

$\sim 10^6$ sec^{-1} in the metastable drift region. Although it is perhaps a moot question whether an infinitely large molecular ion will indeed fragment to give any A^+ ions, the existence of a finite intercept[11] could imply that the excess internal energy of the fragmenting $M\cdot^+$ ion is not randomized between the very large neutral fragment and the A^+ ion, contrary to the assumptions of the quasiequilibrium theory (vide infra).[3] In a calculation of the DOF effect for $C_2H_5O^+$ ions formed from 1-alkanols, Lin and Rabinovitch[14] predicted a nonlinear DOF effect in which log $[m^*]/[A^+]$ approaches $-\infty$ as 1/DOF approaches zero (Figure 1). The model used assumed statistical partitioning (randomization) of the excess energy of $M\cdot^+$ between the $C_2H_5O^+$ ion and the alkyl neutral fragment, and the disagreement of the calculated results with experiment (Figure 1) at high DOF values could be due to the failure of this assumption. The disagreement could also arise from their assumption that $P(E)_{M\cdot+}$ is independent of the size of $M\cdot^+$; apparently no study comparing $P(E)_{M\cdot+}$ functions for a homologous series of molecules has been reported previously.

We present here experimental and theoretical studies on $P(E)$ of the primary product $C_3H_6O\cdot^+$ ions formed from 2-alkanones ranging in size from $C_6H_{12}O$ to $C_{31}H_{62}O$. $P(E)_{C_3H_6O\cdot+}$ is probed experimentally by comparing the abundance of metastable A^+ ions having the narrow range of internal energies required for methyl loss in the field-free drift region to the abundance of the lower energy $C_3H_6O\cdot^+$ ions which reach the detector undecomposed $[m^*(C_3H_6O\cdot^+ \rightarrow C_2H_3O^+ + CH_3\cdot)]/[C_3H_6O\cdot^+]$. This system is well suited for experimental study and the quasiequilibrium theory calculations for several reasons. The $C_3H_6O\cdot^+$ ions, which are of high abundance in all these 2-alkanones, are formed by γ-hydrogen rearrangement involving a six-membered ring transition state which has been shown to be highly specific for several lower molecular weight 2-alkanones.[6] A substantial body of experimental data exists for the 2-alkanones including studies by photoionization and charge exchange, and for the product $C_3H_6O\cdot^+$ ion including studies of its structure and decomposition.[6,9,15–17] The energy requirement for the reaction $C_3H_6O\cdot^+ \rightarrow C_2H_3O^+ + CH_3\cdot$ has a relatively high value of 1.2 eV,[17,18] so that the $[m^*(C_3H_6O\cdot^+ \rightarrow C_2H_3O^+)]$ value provides a measure of the abundance of $C_3H_6O\cdot^+$ ions formed with this relatively high internal energy. To recheck the linearity of the DOF effect, data for 16 homologous 2-alkanones were measured in one time period using a reverse-geometry double-focusing mass spectrometer under computer control (Figure 2).

Experimental Section

Mass spectra, metastable ion (MI) spectra, and collisional activation (CA) spectra were obtained on a modified Hitachi RMU-7 double-focusing mass spectrometer in which the magnetic sector precedes the electrostatic analyzer.[19] Operating conditions were: 70-eV electron energy, 100-μA total emission, 3.9-kV ion accelerating potential, 1.25–1.5-kV multiplier voltage, 1–2 × 10^{-6} Torr source pressure, and an ion source temperature of 225°. Abundances of $C_3H_6O\cdot^+$, $C_2H_3O^+$, $C_3H_7O^+$, and $C_nH_m^+$ (signifying all ions containing only C and H) ions in the normal mass spectra are shown in Figures 3 and 4; an AEI MS-902 was used where necessary to resolve isobaric ions.

For the MI data the pressure in the field-free drift region between the magnet and the electrostatic analyzer was less than 3 × 10^{-7} Torr so contributions from collision-induced metastables were negligible. The mass spectrometer was interfaced with a Digital Equipment Corp. PDP-8 computer to give automated data acquisition and computer control of the electrostatic analyzer (ESA) potential.[20] The relative intensities of $m^*(58\cdot^+ \rightarrow 43^+)$ and m/e $58\cdot^+$ for the DOF plot were determined by scanning the ESA potential alternately over the metastable and precursor ion regions, changing the gain of the dc amplifier manually be a factor of 625 between regions. Ten scans were computer summed to give composite peaks, and the ratio $[m^*(58\cdot^+ \rightarrow 43^+)]/[58\cdot^+]$ was calculated from the maximum intensities and the known gain of the dc amplifier. The shape and peak width of the metastable transition were identical for all the 2-alkanones examined, indicating that the peak heights adequately represent the relative peak intensities.[21] The experimental ratios (Figure 2) were found to be reproducible to within ~5%. MI and CA spectra[22] were obtained for the molecular ions and other high mass oxygen-containing ions as described previously.[19,22] The MI spectrum of 2-dodecanone is shown in Figure 5; other spectra are included in ref 2a.

Synthesis of Compounds

The 2-alkanones $C_{14}H_{28}O$, $C_{15}H_{30}O$, $C_{17}H_{34}O$, $C_{21}H_{42}O$,

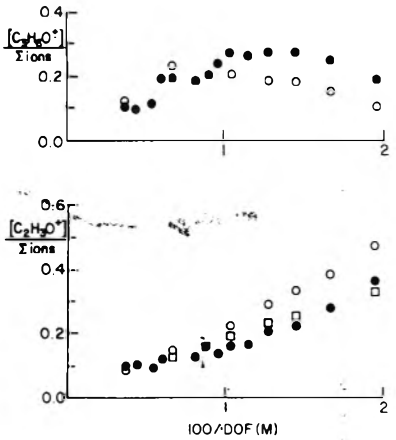

Figure 3. Abundances of $C_3H_6O\cdot^+$ and $C_2H_3O^+$ ions relative to the total ion abundance, in the normal mass spectra of 2-alkanones as a function of the number of molecular degrees of freedom ●, experimental values; O, calculated values; □, calculated for only the direct process, $M\cdot^+ \rightarrow C_2H_3O^+$.

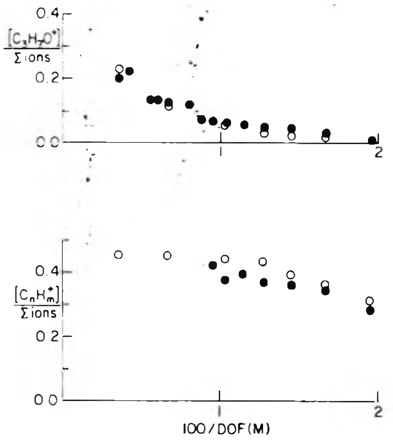

Figure 4. Abundances of $C_3H_7O^+$ and $C_nH_m{}^+$ (species containing only C and H) ions relative to the total ion abundance, in the normal mass spectra of 2-alkanones as a function of the number of molecular degrees of freedom: ●, experimental values; O calculated values.

$C_{23}H_{46}O$, $C_{26}H_{52}O$, and $C_{31}H_{62}O$ were synthesized from the corresponding straight chain carboxylic acids by refluxing the acid with CH_3Li in tetrahydrofuran,[23] with purification by vacuum sublimation. The remaining 2-alkanones were obtained from commercial sources, with purity checked by gas chromatography and mass spectrometry.

Calculations

The ratio $[m^*(C_3H_6O\cdot^+ \rightarrow C_2H_3O^+)]/[C_3H_6O^+]$ was determined from $P(E)_{C_3H_6O\cdot^+}$ based on the factors outlined previously.[8,10] Calculation I considered the effects of dissociations of both low and high energy $M\cdot^+$ ions in competition with the formation of $C_3M_6O\cdot^+$, while calculation II assumed that only high energy pathways were of importance competitively. The energy deposition function for electron impact ionization was obtained from the photoelectron spectrum of the 2-alkanone, using the optical approximation of Meisels;[7] this was convoluted with the thermal energy of the molecule before ionization to obtain $P(E)_{M\cdot^+}$. Rate constants as a function of ion internal energy, $k(E)$, for unimolecular decompositions of $M\cdot^+$ to $C_3H_6O\cdot^+$ ions and to form product ions requiring higher activation energies, E_0, were calculated using RRKM theory.[4-6] For reactions with $E_0 < E_0(M\cdot^+ \rightarrow C_3H_6O\cdot^+)$, $k(E)$ were estimated using the available experimental information from metastable ion spectra, collisional activation spectra, and low electron-energy mass spectra. The probability that a molecular ion of any particular internal energy E will fragment to form a $C_3H_6O\cdot^+$ ion was then calculated from the corresponding $k(M\cdot^+ \rightarrow C_3H_6O\cdot^+)$ and the rate constants at that energy for the competing fragmentations. The internal energy of the $C_3H_6O\cdot^+$ from an $M\cdot^+$ of a particular energy was calculated assuming that the excess internal energy in $M\cdot^+$ is randomized between the $C_3H_6O\cdot^+$ ion and the 1-alkene neutral fragment in porportion to the density of states in each. These results weighted according to $P(E)_{M\cdot^+}$ gave $P(E)_{C_3H_6O\cdot^+}$. For the ratio $[m^*(C_3H_6O\cdot^+ \rightarrow C_2H_3O^+)]/[C_3H_6O\cdot^+]$ the value of $[C_3H_6O\cdot^+]$ was derived from the area of $P(E)_{C_3H_6O\cdot^+}$ below the appearance potential for $C_2H_3O^+$ formation, $A(C_2H_3O^+)$, and the value of $[m^*(C_3H_6O\cdot^+ \rightarrow C_2H_3O^+)]$ from the area of the "metastable window" of energies at $A(C_2H_3O^+)$. Rate constants and energy partitioning were at 0.10-eV intervals; a sample calculation for 2-hexanone at 0.05-eV intervals showed no significant differences in the calculated $[m^*]/[C_3H_6O\cdot^+]$ ratio. Details of these steps are given below. Complete calculations were carried out for $C_6H_{12}O$, $C_7H_{14}O$, $C_8H_{16}O$, $C_9H_{18}O$, $C_{11}H_{22}O$, $C_{17}H_{34}O$, $C_{31}H_{62}O$; results for all but $C_7H_{14}O$ and $C_9H_{18}O$ are shown in Figures 4–8.[24]

Calculation of $P(E)_{M\cdot^+}$. Photoelectron spectra at 21.2 eV were obtained for acetone, 2-butanone, 2-pentanone, and 2-hexanone[25] and for 2-hexanone, 2-heptanone, 2-octanone, and 2-undecanone[26] (Figure 6a–8a).[24] The spectra show a transition at low energy, assigned to ionization from a nonbonding orbital on oxygen, and an unresolved group of transitions at higher energies assumed to arise principally from orbitals belonging to the alkyl chain. The energy difference in onset of the alkyl and carbonyl peaks was found to correlate with the size of the 2-alkanone (Figure 11a); data from the two sets of spectra gave linear correlations with the same slope when the ratio of the areas of these peaks was plotted against the number of carbon atoms in the 2-alkanone (Figure 11b). Photoelectron spectra for the other 2-alkanones (Figures 9a and 10a)[24] were obtained by interpolation and extrapolation of the correlations of Figure 11. Following the treatment of Meisels,[7] the energy deposition function $D(E)$ was obtained from the photoelectron spectrum and the electron energy loss function $F(E_n)$ using the relationship

$$D(E) = \int_{I(M)}^{E_{max}} \chi(E_n, E) F(E_n)\, dE_n$$

where $I(M)$ is the ionization potential of the molecule M and E_{max} is the energy of the ionizing electrons. $\chi(E_n, E)$, the probability that an electron which loses energy E_n will deposit internal energy E in the molecular ion during the ionization process, was obtained from the photoelectron spectrum of M. For E_n less than E_{HeI}, the energy of the helium I resonance line at 21.2 eV, $\chi(E_n, E)$ was set equal to the photoelectron spectrum truncated at $E = E_n$ and normalized to unit area. For $E_n > E_{HeI}$, $\chi(E_n, E)$ was set equal to the HeI photoelectron spectrum normalized to unit area. In calculating the energy loss function from the relation

$$F(E_n) = [\sigma_i(E_n)/E_n] \Big/ \left[\int_{I(M)}^{E_{max}} \sigma_i(E_n)/E_n\, dE_n\right]$$

the relative photoionization cross section, $\sigma_i(E_n)$, for the 2-alkanones was assumed to be equal to that obtained experi-

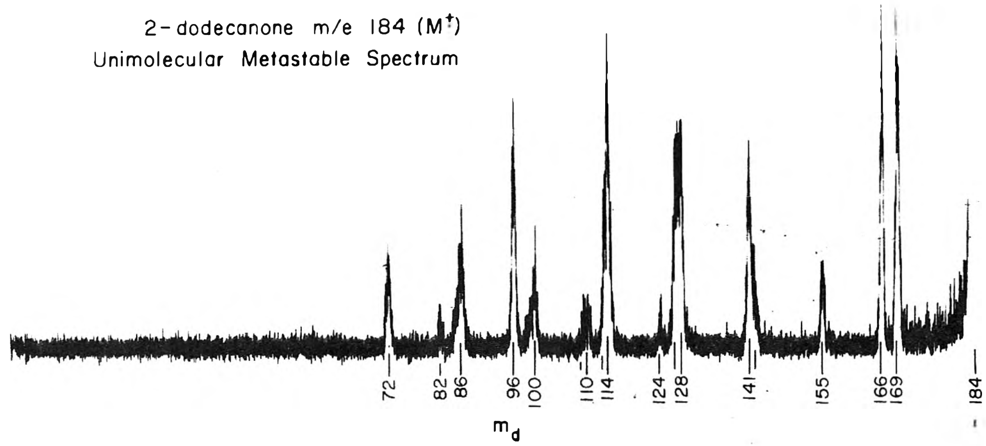

Figure 5. The metastable ion decompositions (MI spectrum) of the molecular ion (*m/e* 184) of 2-dodecanone.

mentally for *n*-butane.[27] Theoretical calculations[28] and the limited experimental data available indicate that the general shape of $\sigma_i(E)$ is the same for most organic molecules. $D(E)$ was convoluted with the thermal energy distribution in the molecules before ionization to obtain the distribution of internal energy in the molecular ion, $P(E)_{M^+}$,[4-7,24] Figures 6b–10b.

Reaction Mechanisms. The $C_3H_6O\cdot^+$ and $C_2H_3O^+$ ions were assumed to be formed from the 2-alkanone molecular ions as shown in reactions 1 and 2,[6,17] with assumed free

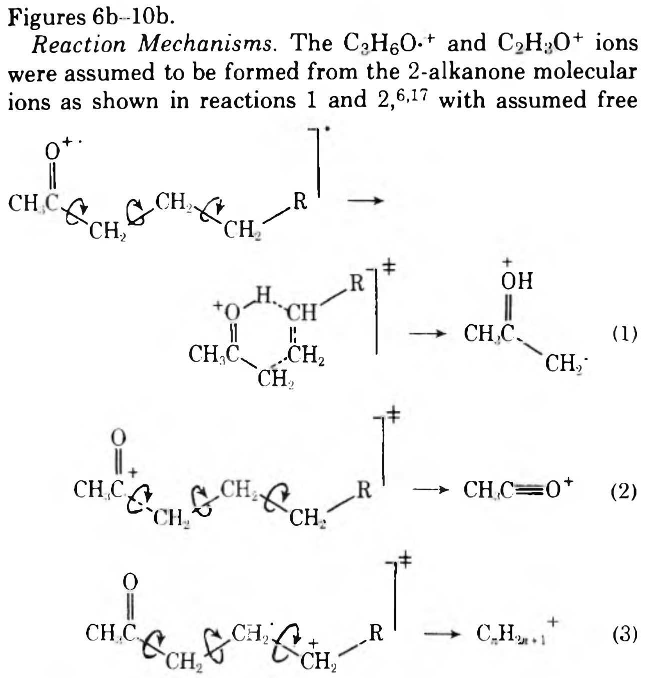

rotations indicated by the circular arrows (vide infra). Collisional activation spectra, as well as metastable ion spectra, of a variety of odd-electron ions in the mass spectra of higher 2-alkanones gave no evidence for the formation of $C_3H_6O\cdot^+$ ions from fragment ions. Substantial evidence has been offered that reaction 1 proceeds through a stepwise mechanism.[6,29] At lowest ion energies transfer of the γ hydrogen has been shown to be substantially faster than the subsequent β cleavage for butanoic acid;[29] at higher internal energies, it would be expected that the tighter-complex rearrangement would be less favored relative to the simple cleavage of this second step. We have assumed that the hydrogen rearrangement is nearly complete in the transition state and that the β bond is partially cleaved; however, the relative results are not changed appreciably if the β bond is assumed to be normal in the activated complex. The most important properties (besides the E_0 values) of the activated complexes for the competing $M\cdot^+$ dissociations are the relative number of free rotors in each, as an additional free rotor causes the sum of energy states to rise more rapidly with increasing energy. All hydrocarbon ions were assumed to originate by direct cleavage of a carbon–carbon bond in the alkyl chain with retention of the charge on the alkyl fragment to form the $C_nH_{2n+1}^+$ ion series (for example, reaction 3), and with subsequent loss of H_2 or CH_4 to form the $C_nH_{2n-1}^+$ ion series.

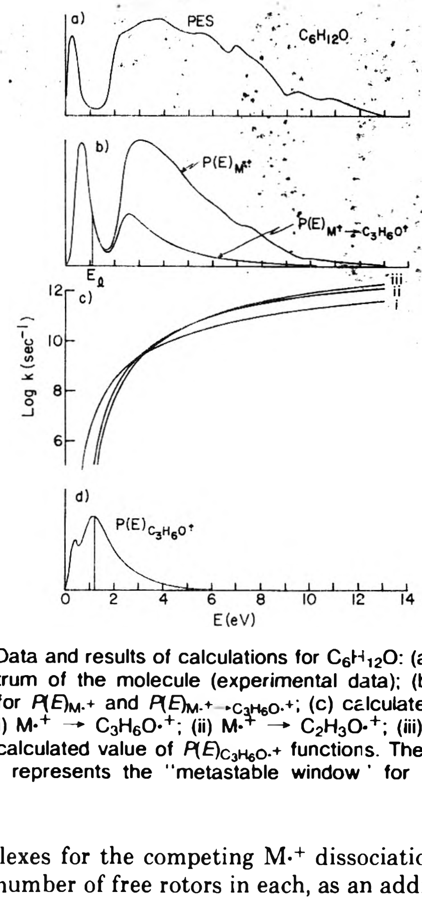

Figure 6. Data and results of calculations for $C_6H_{12}O$: (a) photoelectron spectrum of the molecule (experimental data); (b) calculated functions for $P(E)_{M\cdot^+}$ and $P(E)_{M\cdot^+\to C_3H_6O\cdot^+}$; (c) calculated $k(E)$ functions for (i) $M\cdot^+ \to C_3H_6O\cdot^+$; (ii) $M\cdot^+ \to C_2H_3O^+$; (iii) $M\cdot^+ \to C_nH_m\cdot^+$; (d) calculated value of $P(E)_{C_3H_6O\cdot^+}$ functions. The vertical line at 1.2 eV represents the "metastable window" for $C_3H_6O\cdot^+ \to C_2H_3O^+$.

Activation Energies, E_0. For reaction 1, E_0 was chosen as 0.6 eV in order to give $k_1(E) \simeq 10^6$ sec^{-1} for E = 0.9 eV, in agreement with the difference between the extrapolated 0°K photoionization appearance potential (A) of $C_3H_6O\cdot^+$ and the adiabatic ionization potential (I) of 2-hexanone.[15] The onset of $C_2H_3O^+$ production from 2-hexanone is not clearly defined in measuring A, so that the value of A = 1.7 eV is an upper limit on $E_0(C_6H_{12}O\cdot^+ \to C_2H_3O^+)$ and includes the effects of a kinetic shift and a competitive shift.[5]

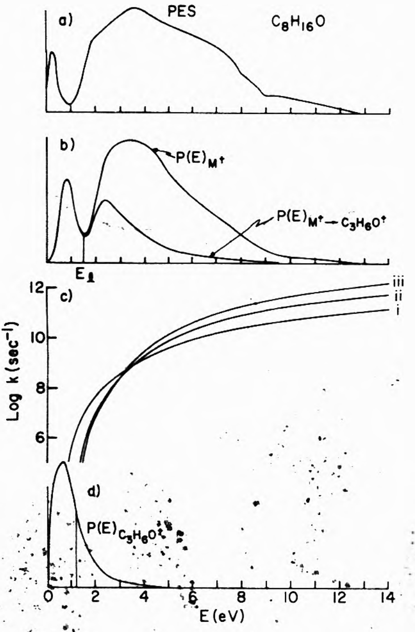

Figure 7. Data and results of calculations for $C_8H_{16}O$: (a) photoelectron spectrum of the molecule (experimental data); (b) calculated functions for $P(E)_{M\cdot +}$ and $P(E)_{M\cdot + \to C_3H_6O\cdot +}$; (c) calculated $k(E)$ functions for (i) $M\cdot^+ \to C_3H_6O\cdot^+$; (ii) $M\cdot^+ \to C_2H_3O\cdot^+$; (iii) $M\cdot^+ \to C_nH_m\cdot^+$; (d) calculated value of $P(E)_{C_3H_6O\cdot +}$ functions. The vertical line at 1.2 eV represents the "metastable window" for $C_3H_6O\cdot^+ \to C_2H_3O^+$.

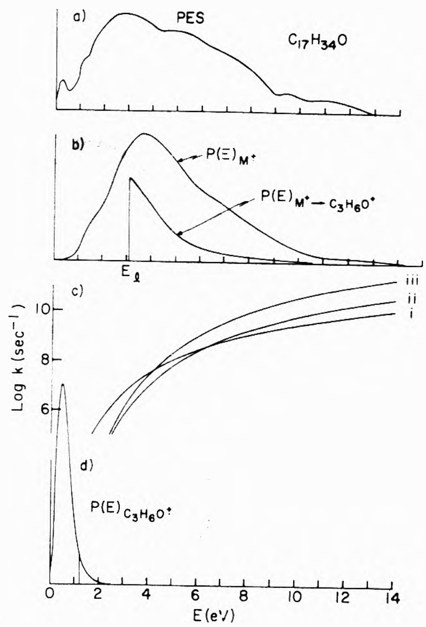

Figure 9. Data and results of calculation for $C_{17}H_{34}O$: (a) photoelectron spectrum of the molecule (extrapolated data): (b) calculated functions for $P(E)_{M\cdot +}$ and $P(E)_{M\cdot + \to C_3H_6O\cdot +}$; (c) calculated $k(E)$ functions for (i) $M\cdot^+ \to C_3H_6O\cdot^+$; (ii) $M\cdot^+ \to C_2H_3O\cdot^+$; (iii) $M\cdot^+ \to C_nH_m\cdot^+$; (d) calculated value of $P(E)_{C_3H_6O\cdot +}$ functions. The vertical line at 1.2 eV represents the "metastable window" for $C_3H_6O\cdot^+ \to C_2H_3O^+$.

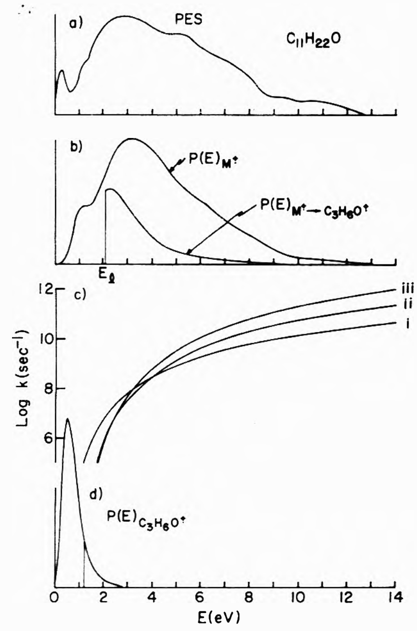

Figure 8. Data and results of calculations for $C_{11}H_{22}O$: (a) photoelectron spectrum of the molecule (experimental data); (b) calculated functions for $P(E)_{M\cdot +}$ and $P(E)_{M\cdot + \to C_3H_6O\cdot +}$; (c) calculated $k(E)$ functions for (i) $M\cdot^+ \to C_3H_6O\cdot^+$; (ii) $M\cdot^+ \to C_2H_3O\cdot^+$; (iii) $M\cdot^+ \to C_nH_m\cdot^+$; (d) calculated value of $P(E)_{C_3H_6O\cdot +}$ functions. The vertical line at 1.2 eV represents the "metastable window" for $C_3H_6O\cdot^+ \to C_2H_3O^+$.

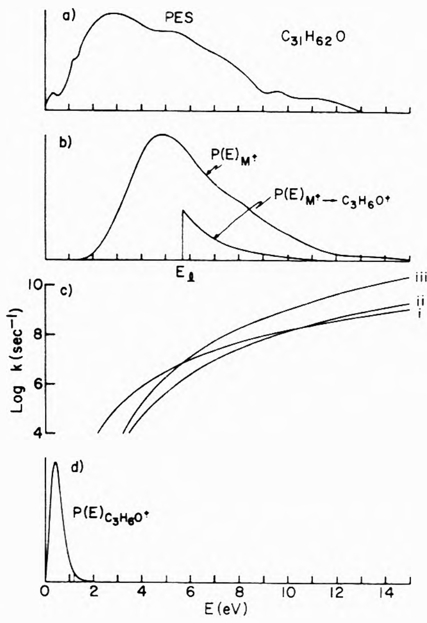

Figure 10. Data and results of calculations for $C_{31}H_{62}O$: (a) photoelectron spectrum of the molecule (extrapolated data); (b) calculated functions for $P(E)_{M\cdot +}$ and $P(E)_{M\cdot + \to C_3H_6O\cdot +}$; (c) calculated $k(E)$ functions for (i) $M\cdot^+ \to C_3H_6O\cdot^+$; (ii) $M\cdot^+ \to C_2H_3O\cdot^+$; (iii) $M\cdot^+ \to C_nH_m\cdot^+$; (d) calculated value of $P(E)_{C_3H_6O\cdot +}$ functions. The vertical line at 1.2 eV represents the "metastable window" for $C_3H_6O\cdot^+ \to C_2H_3O^+$.

E_0 = 1.0 eV was chosen to give agreement with the above results and with the competition between $C_3H_6O\cdot^+$ and $C_2H_3O^+$ formation as measured by charge exchange.[16] E_0 = 1.1 eV was chosen for reactions of type 3 to give agreement with the observed intensity of hydrocarbon ions in the normal mass spectrum of 2-hexanone. The calculated rate curves for these three processes are shown in Figures 6c–10c.

The competition from processes with activation energies lower than 0.6 eV but with activated complexes which are tighter than that for $C_3H_6O\cdot^+$ formation is important for the larger 2-alkanones. The unimolecular metastable spec-

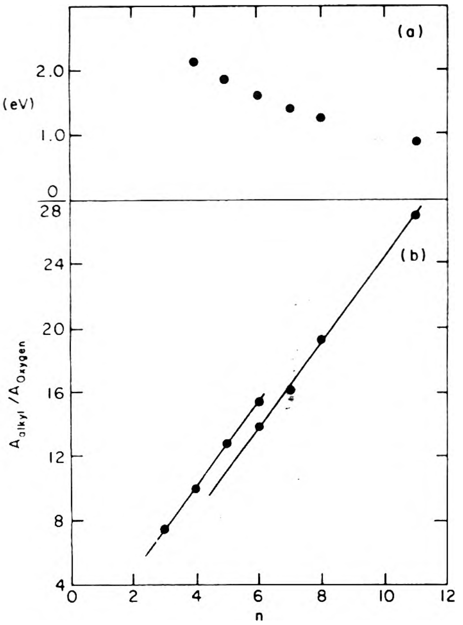

Figure 11. Photoelectron spectra of 2-alkanones: (a) the difference in onset energies (eV) for the alkyl and carbonyl peaks as a function of the number of carbon atoms; (b) the ratio of areas of the alkyl and carbonyl peaks as a function of the number of carbon atoms for spectra from two different sources (see text).

tra of the 2-alkanone molecular ions show many transitions, increasing in number as the 2-alkanone becomes larger (Figure 5); many of the ions resulting from these low energy reactions are of negligible abundance in the normal mass spectrum, as noted previously.[30,31] For 2-alkanones larger than $C_8H_{16}O$, there is no observable metastable transition of the molecular ion to give $C_3H_6O\cdot^+$ despite the fact that this "tight complex" reaction gives a favored product in the normal spectrum. On the other hand, the ions present in the metastable ion spectrum of these $M\cdot^+$ are not common in the normal mass spectrum, indicating that these processes have tighter activated complexes as well as $E_0 < 0.6$ eV. These processes should cause a competitive shift in $A(C_3H_6O\cdot^+)$; for this in calculation I, it was required that the rate constant for formation of $C_3H_6O\cdot^+$ reach $\sim 10^7$ sec^{-1} before the process can be observed. A sharp onset in $P(E)_{M\cdot^+ \to C_3H_6O\cdot^+}$ at this internal energy, E_e, was assumed as shown in Figures 6b–10b. This low energy competition is not important for the lower 2-alkanones; the effect of this assumption was checked in calculation II by assuming a minimum rate constant of 10^6 sec^{-1}. Calculation III neglects competition from both low and high energy processes, and assumes the energy deposition function in producing $M\cdot^+$ to be approximately parabolic, ranging in energy from 0 to 8 eV, similar to the assumptions of Lin and Rabinovitch;[14] however, in contrast, in calculation III, this function is convoluted with the thermal energy calculated for each 2-alkanone.

E_0 for $C_3H_6O^+ \rightarrow C_2H_3O^+$ was estimated to be <1.2 eV from heat of formation data;[18] calculations were made with values of 0.8, 1.0, and 1.2 eV to test the effect of this assumption.

Calculation of $k(E)$. Rate constants for decomposition of the molecular ion via the nth pathway were calculated as a function of internal energy from RRKM theory using the relation

$$k_n(E) = \frac{L_n^{\ddagger} Q_n^{\ddagger} G_n^{\ddagger}(E - E_{0,n})}{h Q_n^* N^*(E)}$$

where $G^{\ddagger}(E - E_0)$ is the sum of states up to energy $E - E_0$ in the activated complex, $N^*(E)$ is the density of states of the molecular ion at energy E, h is Planck's constant, and $L^{\ddagger}$ is the reaction path degeneracy.[4] The ratio of the partition functions for the adiabatic rotations of the activated complex and the molecular ion, $Q_n^{\ddagger}/Q_n^*$, was assumed equal to unity. Vibrational frequencies for the 2-alkanone molecular ions, assumed to be equivalent to those for the corresponding molecules, were obtained by combining the frequencies characteristic of the CH_3COCH_2– group with those of the appropriate alkyl group, $CH_3(CH_2)_n$–. The latter were obtained from the frequencies of the n-alkane $CH_3(CH_2)_{n-1}CH_3$ by removing three frequencies associated with a C–H bond in the CH_3 group and changing the other CH_3 to the corresponding CH_2 frequencies.[24] The frequencies for the CH_3COCH_2– group were obtained from those of acetone in a similar fashion. In addition six new frequencies were added which correspond to the six modes associated with the new C–C bond. In a similar way the frequencies for the 1-alkene molecules were calculated from the frequencies for the n-alkanes and propene.[24] Three free internal rotations were included in the energized $M\cdot^+$, and reduced moments of inertia were calculated from standard bond angles and distances according to the method of Hershbach.[32]

For the activated complex configuration of reaction 1, the three free internal rotations of $M\cdot^+$ were substituted by low frequency torsional modes; earlier studies have shown that the change, not the absolute number of free rotors, is the principal factor in determining $k(E)$.[6] CH_2 deformation frequencies for methylene groups in the ring were increased by a factor of 2, the CH stretching and CH bending frequencies for the hydrogen transferred to the oxygen were reduced by a factor of 2, and the reaction coordinate was taken to be a C–C stretch at 1050 cm^{-1}. The symmetry factor was equal to 2 for this reaction. Reaction 2 was assumed to proceed by a "loose" complex in which the C–C bonds involved in ring formation in reaction 1 were taken as free rotations and a C–C stretch at 1200 cm^{-1} as the reaction coordinate. Other frequencies were assumed to be the same as in the molecule ion, and the symmetry factor was set equal to 1. Reaction 3 was assumed to proceed by a "loose" complex equivalent to that for reaction 2. To account for the fact that alkyl fragment ions or their further decomposition products, are produced by cleavage of any C–C bond in the alkyl chain of the 2-alkanone molecular ion, the symmetry factor L was varied linearly with increasing size of the alkyl chain. L was set equal to 2 for 2-hexanone in order to give agreement with the experimentally observed abundance of hydrocarbon ions in its mass spectrum. This gives a range of L from 2 for $C_6H_{12}O\cdot^+$ to 27 for $C_{31}H_{62}O\cdot^+$. Sums and densities of states for the active molecule–ion and the activated complexes, respectively, were evaluated using the approximations of Whitten and Rabinovitch.[5,24,33]

Energy Partitioning. The excess energy of the molecular ion was assumed to be partitioned statistically between $C_3H_6O\cdot^+$ and the 1-alkene neutral fragment according to the formula given by Vestal:[9]

$$W(E, \epsilon)\, d\epsilon = \left[N_1(\epsilon) N_2(E - \epsilon - E_0)\, d\epsilon \Big/ \int_0^{E-E_0} N_1(\epsilon) N_2(E - \epsilon - E_0) d\epsilon \right]$$

where $W(E, \epsilon)\, d\epsilon$ is the probability of finding energy ϵ to (ϵ

+ dϵ) in the $C_3H_6O\cdot^+$ ion when there is energy E in $M\cdot^+$, and N_1 and N_2 are the densities of states[5,24,32] for the $C_3H_6O\cdot^+$ ion and the neutral fragment, respectively. As noted by Lin and Rabinovitch,[14] the general results of energy partitioning are not sensitive to the details of the vibrational frequencies, and uncertainties in these parameters are outweighed by the uncertainties in $P(E)_{M^+}$ and $P(E)_{M\cdot^+ \to C_3H_6O\cdot^+}$.

$P(E)_{C_3H_6O\cdot^+}$. The internal energy distribution function for the $C_3H_6O\cdot^+$ ion was calculated by integrating $W(E, \epsilon)$ dϵ over all values of E weighted by $P(E)_{M\cdot^+ \to C_3H_6O\cdot^+}$ as follows:

$$P(E)_{C_3H_6O^{\bullet+}} = \int_0^{E_{max}} P(E)_{M^{\bullet+} \to C_3H_6O^{\bullet+}} W(E \quad \epsilon)\, d\epsilon$$

These distributions are shown in Figures 6d–10d. The intensities of the $C_3H_6O\cdot^+$, m*($C_3H_6O\cdot^+ \to C_2H_3O^+$), and the $C_2H_3O^+$ formed from $C_3H_6O\cdot^+$ were calculated from $P(E)_{C_3H_6O\cdot^+}$ using the approximation that ions with internal energy less than E_0 remain as undecomposed $C_3H_6O\cdot^+$ ions while ions with internal energy greater than E_0 will decompose to form $C_2H_3O^+$ ions in the source. Those ions in a narrow energy range (~0.01 eV) about E_0 will appear as metastables; the width of this "metastable window" was arbitrarily chosen so that the calculated and experimental ratios of [m*($C_3H_6O\cdot^+ \to C_2H_3O^+$)]/[$C_3H_6O\cdot^+$] would be equal for 2-hexanone.[14,29] The use of such a "metastable window" in place of a more complicated calculation of the metastable intensity based on the contribution from precursor ions with a range of rate constants for decomposition over the time interval the precursor ion spends in the field free drift region has been shown to be reasonable by Lin and Rabinovitch.[14] Figure 12 shows the relative probabilities that a molecular ion with internal energy E will decompose to give nondecomposing $C_3H_6O\cdot^+$ ions, to give $C_3H_6O\cdot^+$ ions undergoing metastable decomposition, or to give $C_3H_6O\cdot^+$ ions with sufficient energy to produce $C_2H_3O^+$ ions, using calculation I with $E_0(C_3H_6O\cdot^+ \to C_2H_3O^+) = 1.0$ eV. These data combined with $P(E)_{M\cdot^+}$ give the predicted values of [$C_3H_6O\cdot^+$] in the normal mass spectra shown in Figure 3; the calculated values of [$C_2H_3O^+$] combine the production from $C_3H_6O\cdot^+$ and directly from $M\cdot^+$. The value for the total hydrocarbon ions [C_nH_m+] represents the combined products for high energy reactions, and [$C_3H_7O^+$] signifies the total abundance of the doubly-rearranged product plus other low E_0, tight complex reactions as predicted by calculation I.

Discussion

A number of alternative explanations for the DOF effect were first considered and discarded.[2a] It was shown experimentally that the linearity of the DOF correlation is largely independent of molecular ion internal energy and half-life by varying the ionizing electron energy, thermal energy, ion source residence time, and time required to reach the field free drift region.[2a,10] The intensities of $M\cdot^+$, m*($M\cdot^+ \to A^+$), and A^+ relative to the total ion current were plotted as a function of the size of $M\cdot^+$ for a number of homologous series; no consistent trends were observed for any of these. However, all of these series give linear DOF correlations for [m*($A^+ \to D^+$)]/[A^+], and this is also true for certain secondary daughter ions in normal spectra. For example, a reasonably linear correlation with 1/DOF is found for the logarithm of [H_3O^+]/[$C_2H_5O^+$] from 2-alkanols, [$C_2H_5O_2^+$]/[$C_4H_8O_2^+$] from ethyl esters, and [$C_3H_6O\cdot^+$]/[$C_5H_{10}O\cdot^+$] from 4-alkanones,[2a] indicating that the change in [m*($A^+ \to D^*$)]/[A^+] does reflect the change in $P(E)_{A^+}$.

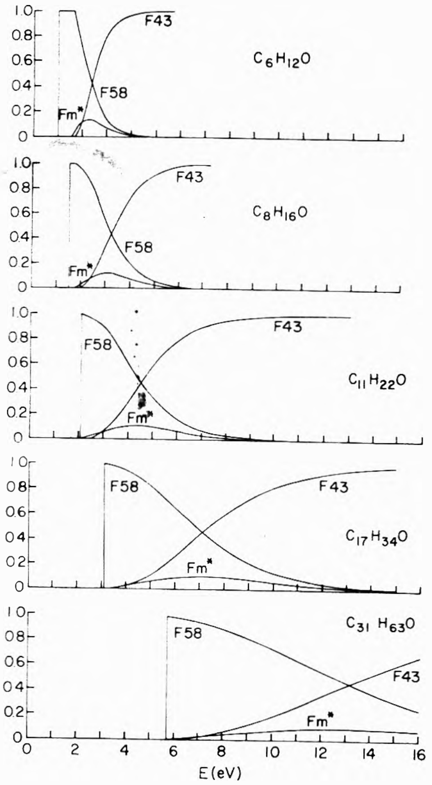

Figure 12. Calculated probabilities as a function of internal energy that $M\cdot^+$ will decompose to give $C_3H_6O\cdot^+$, m*($C_3H_6O\cdot^+ \to C_2H_3O^+$), and $C_2H_3O^+$ from the decomposition of $C_3H_6O\cdot^+$.

Ion Abundances. In general, the abundance values for the major ions in the normal mass spectra (Figures 3 and 4) agree well with those predicted. The error in predicting $C_3H_6O\cdot^+$ abundances for the smaller 2-alkanones may result from errors in the $P(E)_{M\cdot^+}$ distribution, since $C_3H_6O\cdot^+$ is produced from a region of $P(E)_{M\cdot^+}$ which shows a valley for these compounds. The proportion of $M\cdot^+$ ions of these energies could be much greater than that assumed (Figures 6a, 7a) due to autoionization or optically forbidden transitions which occur with finite cross section under electron impact. The calculated values for [$C_3H_6O\cdot^+$] and [$C_2H_3O^+$] would agree with experiment more closely if $E_0(C_3H_6O\cdot^+ \to C_2H_3O^+) > 1.2$ eV, but there is no particular justification for this change. The values of [$C_3H_6O\cdot^+$]/[$C_2H_3O^+$] observed in charge exchange experiments[16] on 2-hexanone (Table I) are consistent with those calculated here in view of the sensitivity of the latter to the value chosen for E_0 ($M\cdot^+ \to C_3H_6O\cdot^+$). Charge exchange experiments[16] on 2-hexanone-*1,1,1,3,3-d*$_5$ indicate that direct cleavage ($M\cdot^+ \to C_2D_3O^+$) predominates at these low energies over indirect acetyl ion formation (as indicated by [$C_2HD_2O^+$]); abundances of these ions in the normal mass spectrum of this labeled compound are also consistent with the values calculated here.[24] Also, ionization efficiency studies using 2-hexanone-*1,1,1,3,3-d*$_5$ indicate that the energy threshold for $C_2HD_2O^+$ formation (indirect pathway) occurs approximately 0.7 eV higher than that for $C_2D_3O^+$ ions, which presumably are produced by the direct process at threshold.[24]

The comparisons for the trends in ion intensities with increasing size of the 2-alkanone and the more detailed comparisons possible for 2-hexanone indicate that the calculations adequately predict the competition between the path-

TABLE I: Decomposition of 2-Hexanone Ions Formed with Specific Internal Energies by Charge Exchange

		$[C_3H_6O\cdot^+]/[C_2H_3O^+]$		
	$E_{C_6H_{12}O\cdot^+}$, eV	1.0	2.1	3.1
Obsd		23	5.8	1.28
Calcd,				
$E_0(M\cdot^+ \longrightarrow C_3H_6O\cdot^+)$	1.1 eV	~10^3	81	2.1
	1.0 eV[a]	99	2.3	0.85
	0.9 eV	8.6	0.61	0.33

[a] Value actually used for other reported results.

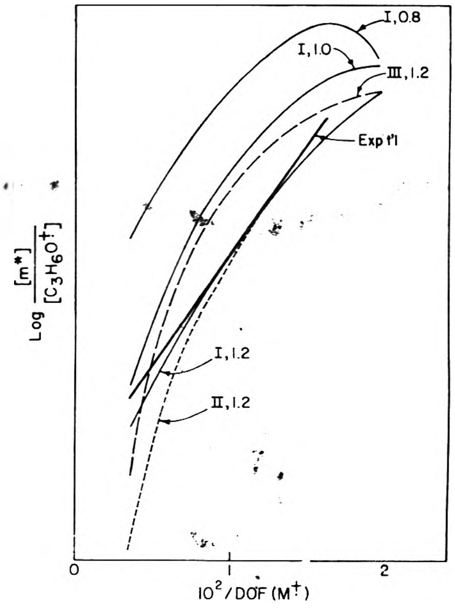

Figure 13. Comparison of results for different models used to calculate the DOF effect. Curves labeled according to type of calculation (I, II, or III, see text) and activation energy (in eV) assumed for the reaction $C_3H_6O\cdot^+ \rightarrow C_2H_3O^+ + CH_3\cdot$.

ways considered, and that the $P(E)_{M\cdot^+}$ functions are valid approximations.

Degrees of Freedom Effect. Figure 2 compares the experimental values of $[m^*(C_3H_6O\cdot^+ \rightarrow C_2H_3O^+)]/[C_3H_6O\cdot^+]$ with those calculated using a threshold value of $k(M\cdot^+ \rightarrow C_3H_6O\cdot^+) = 10^6$ sec^{-1} (calculation II) for $C_6H_{12}O$, $C_7H_{14}O$, and $C_8H_{16}O$, and 10^7 sec^{-1} (calculation I) for the other 2-alkanones, and using $E_0(C_3H_6O\cdot^+ \rightarrow C_2H_3O^+) = 1.2$ eV. The calculated DOF effect shows a remarkably good agreement with the experimental results, duplicating the curvature observed for the smaller members of the series and the linearity in the region from $C_9H_{18}O$ to $C_{31}H_{62}O$, with a slope equal to that observed experimentally. All of these calculations, like those of Lin and Rabinovitch[14] for the 1-alkanol system, correctly predict the general decrease in $[m^*]/[A]$ with increasing molecular ion size. The increasing amount of internal energy carried off by the neutral fragment lowers the average internal energy of A^+, which generally lowers $[m^*]/[A^+]$ (Figures 6–10). An exception can occur for the smallest homolog; if the energy requirement for $m^*(A^+ \rightarrow D^+)$ is less than the energy at which $P(E)_{A^+}$ is a maximum (these energies are equal in Figure 6d), the area of $P(E)_{A^+}$ corresponding to the metastable window will actually increase with increasing molecular ion size. Note (Figure 13) that reducing $E_0(C_3H_6O\cdot^+ \rightarrow C_2H_3O^+)$ to 0.8 ev, a value less than the maximum in $P(E)_{C_3H_6O\cdot^+}$ does cause $[m^*(C_3H_6O\cdot^+ \rightarrow C_2H_3O^+)]/[C_3H_6O\cdot^+]$ to *increase* in going from $C_6H_{12}O$ to $C_7H_{14}O$; the area corresponding to undissociating $C_3H_6O\cdot^+$ does not increase as much as the area corresponding to $m^*(C_3H_6O\cdot^+ \rightarrow C_2H_3O^+)$ with increasing size of the neutral fragment.[24]

The calculations of Lin and Rabinovitch assume that $P(E)_{M\cdot^+}$ is the same for all members of the series; these calculations predict a correlation in which log $([m^*]/[A^+])$ approaches $-\infty$ as 1/DOF approaches zero. This occurs because an increasingly large neutral fragment removes a greater proportion of the internal energy of the molecular ion, resulting in a $P(E)_{A^+}$ which is peaked more and more sharply at lower internal energy, so that the area corresponding to $[m^*]$ approaches zero faster than does that corresponding to $[A^+]$. The results of calculation III generally duplicate this behavior; addition of the thermal energy distribution to the assumed constant energy deposition function produces a $P(E)_{M\cdot^+ \rightarrow C_3H_6O\cdot^+}$ which is weighted slightly to higher internal energies for larger molecules, but still predicts a curved DOF effect in contrast to the experimentally observed linearity. Calculation II, in which the change in the energy deposition function has been approximated from photoelectron spectra, shows an improved, but still curved, DOF effect.

Linearity is nearly achieved in calculation I, in which low energy $M\cdot^+$ fragmentations competitive with the formation of $C_3H_6O\cdot^+$ ions have been included. The proportion of $M\cdot^+$ which should decompose by such processes increases with increasing molecular weight as can be seen from the very slow rise with $M\cdot^+$ internal energy of the calculated $k(E)$ curves for larger species (Figures 9c, 10c); the increasing size of the molecular ion magnifies the effect of the differences in activation energy for two competing reactions. This is also shown by the effect of increasing molecular size on the relative abundances of the $C_3H_6O\cdot^+$ and direct $C_2H_3O^+$ ions (Figure 3).

This also causes the kinetic shift for $C_3H_6O\cdot^+$ formation to increase with the size of $M\cdot^+$; the calculated values show an approximately linear increase. The experimental $(A_{C_3H_6O\cdot^+} - I_{M\cdot^+})$ values for 2-$C_6H_{12}O$ and 2-$C_{17}H_{34}O$ differ by approximately 1.0 eV;[24] from Figures 6c and 9c this would correspond to $k < 10^6$ sec^{-1} for the *onset* for $C_3H_6O\cdot^+$ formation. The minimum rate constant for dominant $C_3H_6O\cdot^+$ formation would of course be substantially higher, but calculation of this value would require information on the $k(E)$ functions for the competing low energy $M\cdot^+$ decompositions. The slopes of these functions must be even more shallow than that for $M\cdot^+ \rightarrow C_3H_6O\cdot^+$; this predicts that the increase of $[C_3H_6O\cdot^+]$/[low energy products] with increasing $M\cdot^+$ energy for higher 2-alkanones will be even more gradual than the increase of $[C_2H_3O^+]/[C_3H_6O\cdot^+]$ with $M\cdot^+$ energy shown in Figures 9c and 10c.

A low energy $M\cdot^+$ decomposition of particular note is the formation of $C_3H_7O^+$ (*m/e* 59).[34] This is an increasingly important process for homologs larger than 2-heptanone and becomes the most intense peak in the mass spectra of 2-alkanones larger than 2-nonadecanone. However, unimolecular metastable transitions to form *m/e* 59 are observed only for $C_7H_{14}O\cdot^+$, $C_8H_{16}O\cdot^+$, and $C_9H_{18}O\cdot^+$.[35]

Collisional activation spectra of the major oxygen-containing ions produced by alkyl fragment loss from the higher 2-alkanones show no detectable formation of *m/e* 59 as well *m/e* 58 ions, indicating that these ions are formed mainly from the molecular ion.[24] The linearity of the DOF effect for the 2-alkanones can thus be explained *without* invoking nonrandomization of energy in the molecular ion fragmentation process. It also appears logical that the linear DOF effects observed for the other systems studied can arise through the same general causes. Lengthening of an alkyl chain for most types of molecular ions should increase the probability of low activation energy, tight complex reactions, which would provide increasing competition to the fragmentation pathway measured for the DOF study. Calculation I (Figure 13) indicates that a change in $E_0(\mathrm{A}^+ \to \mathrm{D}^+)$ from 0.8 to 1.2 eV does not affect the essential linearity of the DOF plot. However, it is obvious that all systems will not necessarily give linear DOF plots, and that this relationship must fail at sufficiently high molecular weights, as both $[\mathrm{A}^+]$ and $[\mathrm{m}^*(\mathrm{A}^+ \to \mathrm{D}^+)]$ must go to zero.

Factors Affecting $P(E)_{\mathrm{A}^+}$. The agreement of the calculated and experimental results support the previous postulate, based on the quasiequilibrium theory,[3] concerning the factors which affect the internal energy distribution of A^+ ions produced from $\mathrm{M}\cdot^+$. The effects of structure (peaks, valleys, general shape) in $P(E)_{\mathrm{M}\cdot^+}$ are discernible in $P(E)_{\mathrm{A}^+}$ for smaller molecules such as 2-hexanone, although the partitioning of energy between A^+ and the neutral lost substantially smooths the distribution. For larger molecules the thermal energy distribution tends to smear out any structure in the photoelectron spectrum, and any remaining structure in $P(E)_{\mathrm{M}\cdot^+}$ is completely removed by the effect of energy partitioning, giving $P(E)_{\mathrm{A}^+}$ distributions which are sharply peaked at low energies.

The calculations confirm that competition from reactions with higher activation energies and looser complexes will reduce the higher energy portion of $P(E)_{\mathrm{A}^+}$, as expected. The increasing number of reaction pathways operative in the larger molecules ($\mathrm{C}_n\mathrm{H}_m{}^+$ formation) approximately compensates for their slower rise of $k(E)$, so that the effect of high energy competition on $P(E)_{\mathrm{M}\cdot^+\to\mathrm{A}^+}$ does not vary greatly over the series. The thermal energy distribution in the larger molecules shifts $P(E)_{\mathrm{M}\cdot^+\to\mathrm{A}}$ to higher internal energies. The dramatic effect of low energy competition has been discussed above. Because the rate constants, $k(E)$, are very sensitive to changes in activation energy, variations in these parameters will be reflected in variations in the competition between different pathways and can cause substantial changes in $P(E)_{\mathrm{M}\cdot^+\to\mathrm{A}^+}$.

Energy partitioning between the ion and the neutral determines how $P(E)_{\mathrm{A}^+}$ is obtained from $P(E)_{\mathrm{M}\cdot^+\to\mathrm{A}^+}$. The calculations confirm that increasing the size of the neutral lost can produce a dramatic shift of $P(E)_{\mathrm{A}^+}$ to lower energies with a corresponding sharpening of the energy distribution. The energy partitioning is sensitive to the relative sizes of the neutral fragment and the A^+ ion, but not to the details of the models chosen to represent them.

Acknowledgment. The authors are indebted to the National Institutes of Health (Grant GM-16609) for generous financial support.

References and Notes

(1) Metastable Ion Characteristics, XXXII. Part XXXI, F. W. McLafferty and J. Winkler, *J. Amer. Chem. Soc.*, **96**, 5182 (1974).

(2) (a) Taken from the Ph.D. theses of PFB, 1974, and DJM, 1971, Cornell University. (b) E. I. du Pont de Nemours and Co., Wilmington, Del. 19898. (c) Marine Biomedical Institute, University of Texas Medical Center, Galveston, Tex. 77550. (d) Vising scientist from the Department of Physical Chemistry, The Hebrew University, Jerusalem.

(3) H. M. Rosenstock, M. B. Wallenstein, A. L. Wahrhaftig, and H. Eyring, *Proc. Natl. Acad. Sci. U.S.*, **38**, 667 (1952).

(4) M. L. Vestal in "Fundamental Processes in Radiation Chemistry", P. Ausloos, Ed., Wiley-Interscience, New York, N.Y., 1968.

(5) P. J. Robinson and K. A. Holbrook, "Unimolecular Reactions", Wiley-Interscience, New York, N.Y., 1972.

(6) F. W. McLafferty, T. Wachs, C. Lifshitz, G. Innorta, and P. Irving, *J. Am. Chem. Soc.*, **92**, 6867 (1970); F. W. McLafferty, "Interpretation of Mass Spectra", 2nd ed, Benjamin-Addison-Wesley, Reading, Mass., 1973, Chapter 8.

(7) G. G. Meisels, C. T. Chen, B. G. Giessner, and R. H. Emmel, *J. Chem. Phys.*, **56**, 793 (1972), and references cited therein.

(8) A. Kropf, E. M. Eyring, A. L. Wahrhaftig, and H. Eyring, *J. Chem. Phys.*, **32**, 149 (1960).

(9) M. L. Vestal, *J. Chem. Phys.*, **43**, 1356 (1965).

(10) D. J. McAdoo, P. F. Bente, III, M. L. Gross, and F. W. McLafferty, *Org. Mass Spectrom.*, **9**, 525 (1974).

(11) F. W. McLafferty and W. T. Pike, *J. Am. Chem. Soc.*, **89**, 5951 (1967).

(12) F. W. McLafferty, T. Wachs, and W. T. Pike, *Adv. Mass Spectrom.*, **4**, 153 (1968).

(13) R. G. Cooks, J. H. Beynon, R. M. Caprioli, and G. R. Lester, "Metastable Ions", Elsevier, Amsterdam, 1973.

(14) Y. N. Lin and B. S. Rabinovitch, *J. Phys. Chem.*, **74**, 1769 (1970).

(15) E. Murad and M. G. Inghram, *J. Chem. Phys.*, **40**, 3263 (1964).

(16) T. O. Tiernan and C. Lifshitz, *J. Chem. Phys.*, **57**, 1515 (1972).

(17) F. W. McLafferty, D. J. McAdoo, J. S. Smith, and R. Kornfeld, *J. Am. Chem. Soc.*, **93**, 3720 (1971).

(18) J. L. Franklin, J. G. Dillard, H. M. Rosenstock, J. T. Herron, K. Draxl, and F. H. Field, *Natl. Stand. Ref. Data Ser., Natl. Bur. Stand.*, **No. 26** (1969).

(19) T. Wachs, P. F. Bente, III, and F. W. McLafferty, *Int. J. Mass Spectrom. Ion Phys.*, **9**, 12 (1972).

(20) T. Wachs and F. W. McLafferty, to be submitted for publication.

(21) M. A. Baldwin and F. W. McLafferty, *Int. J. Mass Spectrom. Ion Phys.*, **12**, 86 (1973).

(22) F. W. McLafferty, P. F. Bente, III, R. Kornfeld, S.-C. Tsai, and I. Howe, *J. Am. Chem. Soc.*, **95**, 2120 (1973); F. W. McLafferty, R. Kornfeld, W. F. Haddon, K. Levsen, I. Sakai, P. F. Bente, III, S.-C. Tsai, and H. D. R. Schuddemage, *ibid.*, **95**, 3886 (1973).

(23) C. Tegner, *Acta Chim. Scand.*, **6**, 782 (1952).

(24) For further details see the thesis of PFB.[2a]

(25) We are indebted to Dr. Neil Ridyard, Perkin-Elmer, Ltd., for these spectra.

(26) We are indebted to Professor R. E. Kirby, Queens College, CUNY, for these spectra.

(27) R. I. Schoen, *J. Chem. Phys.*, **37**, 2032 (1962).

(28) L. I. Lohr and M. B. Robin, *J. Am. Chem. Soc.*, **92**, 7241 (1970).

(29) J. S. Smith and F. W. McLafferty, *Org. Mass. Spectrum.*, **5**, 483 (1971).

(30) F. W. McLafferty, D. J. McAdoo, and J. S. Smith, *J. Am. Chem. Soc.* **91**, 5400 (1969).

(31) K. R. Jennings in "Mass Spectrometry: Techniques and Applications", G. W. A. Milne, Ed., Wiley-Interscience, New York, N.Y., 1971, p 419.

(32) D. R. Hershbach, H. R. Johnston, K. S. Pitzer, and R. E. Powell, *J. Chem. Phys.*, **25**, 736 (1956).

(33) G. E. Whitten and B. S. Rabinovitch, *J. Chem. Phys.*, **41**, 1883 (1965); D. C. Tardy, B. S. Rabinovitch, and G. Z. Whitten, *ibid.*, **48**, 1427 (1968); W. Forst, *Chem. Rev.*, **71**, 339 (1971).

(34) M. Kraft and G. Spiteller, *Justus Liebigs Ann. Chem.*, **712**, 28 (1968).

(35) In a number of previous cases increasing the alkyl chain length has also been noted to increase the ratio of peaks from double- vs. single-hydrogen rearrangement; a recent detailed study[36] of the reasons for this phenomenon did not consider, however, the effects of increasing molecular size on $P(E)_{\mathrm{M}\cdot^+}$ and lower energy processes.

(36) M. A. Winnik, C. K. Lee, and P. T. Y. Kwong, *J. Am. Chem. Soc.*, **96**, 2901 (1974).

Mass Spectrometric Study of the Vaporization of Cesium and Sodium Molybdates

Irving Johnson

Chemical Engineering Division, Argonne National Laboratory, Argonne, Illinois 60439

(Received September 18, 1974)

Publication costs assisted by Argonne National Laboratory

A mass spectrometric examination was made of the vapor over solid and liquid Cs_2MoO_4 and liquid Na_2MoO_4. For both compounds, gaseous monomolybdate molecules are the major constituents of the equilibrium vapor. The partial pressure of Cs_2MoO_4 molecules over the solid compound is given by the equation: $\ln p(\mathrm{atm}) = 15.14 - 3.22 \times 10^4/T$ for T from 1070 to 1170 K. The enthalpy of vaporization of solid Cs_2MoO_4 is 64.1 ± 2.7 kcal/mol and of liquid Na_2MoO_4 is 73.4 ± 4.7 kcal/mol.

Introduction

Cesium and molybdenum are formed in high yields in the nuclear fission of uranium and plutonium, and therefore the possible formation of cesium molybdate in urania–plutonia reactor fuels must be considered. In the typical power reactor, the nuclear fuel is in the form of cylindical rods of the oxide contained within metallic tubes. During the operation of the reactor, the large difference in temperature that exists between the center and the outer surface of the oxide rod can lead to the transport of volatile compounds from the center of the rod to the interface between the oxide and the metallic cladding. The present study was undertaken to determine the composition of the vapor phase in equilibrium with solid and liquid cesium molybdate.

Indirect evidence for the existence of alkali metal molybdates in the vapor over the liquid phase was reported by Spitsyn and Kuleshov,[1] who calcined samples of the molybdates in open platinum crucibles. Mass spectrometric studies[2,3] of the evaporation of alkaline earth metal molybdates indicated the existence of gaseous molybdates. Studies[4] of the vapor phase over liquid lithium and sodium molybdates showed the presence of gaseous Li_2MoO_4 molecules; however, gaseous Na_2MoO_4 molecules were not found. In our mass spectrometric study, the existence of gaseous Cs_2MoO_4 molecules in the vapor over solid and liquid cesium molybdate was demonstrated, and the partial pressure of cesium molybdate was measured as a function of temperature. A reexamination of the vapor phase over liquid sodium molybdate showed that gaseous Na_2MoO_4 molecules were present.

Experimental Section

In this study the composition of the vapor of the compound under study was determined using a Knudsen cell and a mass spectrometer. The Knudsen cell was heated inductively. The temperature was maintained constant by automatically controlling the power to the induction coil. The vapor effusing from the cell was mass analyzed using a quadrupole mass spectrometer. The cell was separated from the quadrupole assembly by a water-cooled copper plate with a ⅛-in. diameter hole to collimate the molecular beam. The beam entered the electron impact ionization chamber at 90° to the axis of the quadrupole mass analyzer. The intensity of the positive ion beam selected by the mass analyzer was measured using an electron multiplier, the output of which, after amplification, was measured either with a potentiometric recorder or a digital voltmeter equipped with a high-speed paper-tape printer. Peak heights were measured with a precision of ±1%. Appearance potentials were estimated by extrapolation of the linear portion of the ionization efficiency curves using the H_2O^+ peak as an internal standard. During the measurements, the pressure in the system was maintained below 10^{-7} Torr by means of an ion pump.

The temperature of the cell was measured with a disappearing-filament optical pyrometer. The precision of the temperature measurements was ±0.5°. The pyrometer, prism, and vacuum-chamber window were calibrated together using a standard strip lamp.

Cesium molybdate from two sources was used. The data reported for the temperature variation of the ion current for Cs_2MoO_4 over the solid were obtained with a high-purity sample of cesium molybdate from the same batch that had been prepared for calorimetric studies[5] in this laboratory. All the other studies were done with a sample from a commerical source (Rocky Mountain Research); this material was found to contain 99 mol % Cs_2MoO_4. The major impurity was probably the dimolybdate. The molybdenum content was 22.71 wt % (the theoretical value for Cs_2MoO_4 is 22.53 wt % Mo).

The initial experiments were done using a tungsten effusion cell with an inner liner of iridium. It was found that cesium molybdate reacted with the iridium liner. The reaction was most extensive when the sample was liquid. The reaction with the container was eliminated by replacing the iridium liner with a gold liner. However, when the sample was melted, the liquid tended to creep out of the orifice in the gold liner and would spread over the top of the cell. This led to nonreproducible ion-current data. This creeping tendency was eliminated by placing the sample in a high-purity alumina crucible inside the gold-lined effusion cell. The molten cesium molybdate did not appear to react with or wet the alumina crucible. All of the solidified residue after melting fell freely from the alumina crucible. No significant gain or loss in weight of the cell components was found when the alumina crucible and gold liner were used. The outer part of the effusion cell was made of molybdenum.

A commericial sample (Baker Analyzed Reagent) of $Na_2MoO_4 \cdot 2H_2O$ was dehydrated by heating at 150° and used without further purification. The material was found to contain 46.61 wt % Mo (the theoretical value for Na_2MoO_4 is 46.59 wt % Mo). The gold-lined molybdenum effusion cell with the alumina inner crucible used for the

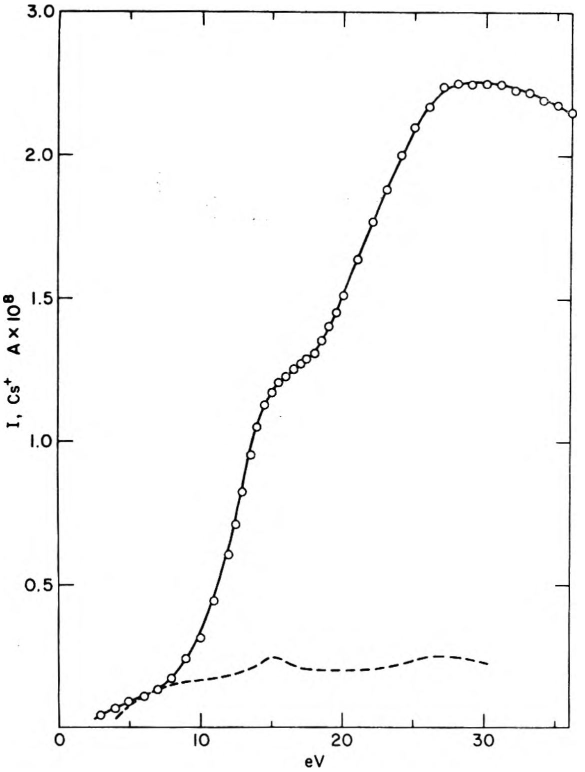

Figure 1. Ionization efficiency curves for Cs^+: (O) observed over solid Cs_2MoO_4; (- - - -) computed for atomic cesium from data of Tate and Smith.[7]

cesium molybdate studies was also used for the study of the vaporization of sodium molybdate.

Results and Discussion

1. Cesium Molybdate. Mass analysis of the positive ions produced by the electron impact ionization of the vapor phase over solid cesium molybdate at 900° indicated the presence of Cs^+, Cs_2^+, Cs_2O^+, $Cs_2MoO_3^+$, and $Cs_2MoO_4^+$. The major peaks were those due to Cs^+ and $Cs_2MoO_4^+$.

An ionization efficiency curve typical in form to that reported for simple ionization was observed for the $Cs_2MoO_4^+$ ion. An appearance potential of 7 eV was obtained by extrapolation of the linear part of the curve. The curve reached a maximum at about 24 eV. The ion-current temperature data were obtained at 22 eV. No ions between $Cs_2MoO_4^+$ and the limit of the mass spectrometer at about 800 mass units, such as fragmentation products of the dimer, $Cs_4Mo_2O_8$, were observed, and hence it is assumed that the $Cs_2MoO_4^+$ ion observed was produced from the parent molecule in the vapor. After verification that the correct number of peaks was obtained for the $Cs_2MoO_4^+$ ion in accordance with the isotopic abundance data for cesium and molybdenum, the resolution of the instrument was decreased to give a single composite peak for this ion. This procedure greatly increased the sensitivity of the instrument. The background signal at the composite peak was insignificant.

The ionization efficiency curve for Cs^+ ion was complex, as shown in Figure 1. The data reported by Tate and Smith[7] were used to construct a curve for the simple ionization of cesium atoms. The scale factor for this latter curve was selected so that the two curves were approximately coincident below about 7 eV. The deviation of the observed curve from the curve derived from the data of Tate and Smith indicates that one or more sources, in addition to simple ionization of cesium atoms, are involved in the production of Cs^+. A likely reaction for the production of cesium ions is

$$Cs_2MoO_4 + e^- = Cs^+ + CsMoO_4 + 2e^- \qquad (1)$$

The appearance potential for this reaction was estimated by assuming that the energy required to remove a cesium atom from the Cs_2MoO_4 molecule is equal to the average of the energies required to remove cesium atoms from Cs_2O and CsO molecules; this energy is 1.6 eV.[8] When the ionization energy for the cesium atom is added, the appearance potential for reaction 1 is 5.6 eV. The deviation of the observed curve for Cs^+ from the predicted curve for the simple ionization of cesium atoms just above ~7 eV is consistent with this reaction. Because the estimated appearance potential of reaction 1 is so near the observed appearance potential for the $Cs_2MoO_4^+$ ion, the two processes would be expected to be competitive. Reaction 1 most likely has a higher probability than the reaction to produce $Cs_2MoO_4^+$ ions. The shoulder on the observed curve for Cs^+ ion indicates the onset of a second fragmentation reaction, which probably also involves the Cs_2MoO_4 molecule. The ion-current temperature data for the Cs^+ ion were obtained at 8 eV. The hydrocarbon background at the mass of the Cs^+ ion was insignificant; however, the Cs^+ ion background gradually increased as the study progressed. To correct for the Cs^+ ion background, traces were taken with the shutter closed before and after each set of measurements at the Cs^+ ion peak.

The observed appearance potentials for Cs_2^+ and Cs_2O^+ of about 16 and 12 eV, respectively, indicate that these ions are produced by fragmentation because the appearance potentials for both ions, if produced by simple ionization of parent molecules, would be expected to be about 4.5 eV.[6] Possible reactions for the formation of these two ions are

$$CsMoO_4 + e^- = Cs_2^+ + MoO_3 + 2e^- \qquad (2)$$

$$Cs_2MoO_4 + e^- = Cs_2O^+ + MoO_3 + 2e^- \qquad (3)$$

for which appearance potentials of 17.4 and 12.7 eV, respectively, were estimated.

The observed appearance potential for the $Cs_2MoO_3^+$ ion was about 12 eV; it is most likely a fragment from a reaction involving Cs_2MoO_4.

The product of the ion current for $Cs_2MoO_4^+$ and the absolute temperature is proportional to the partial pressure of Cs_2MoO_4; the logarithm of the product is shown plotted against the reciprocal of the absolute temperature for two experiments in Figure 2. The change in slope at about 930° of the two lines obtained with 99 mol % cesium molybdate is attributed to the melting of the sample. The difference in the slopes of the two lines is 10.3 ± 6.4 kcal/mol. This difference is equal to $\Delta\bar{H} + \Delta H(\text{fusion})$, where $\Delta\bar{H}$ is the partial molar enthalpy of Cs_2MoO_4 in the melt and $\Delta H(\text{fusion})$ is the heat of fusion of Cs_2MoO_4. Since the liquid phase was nearly pure Cs_2MoO_4, the partial enthalpy should be approximately zero, and the difference in slopes should therefore be equal to the heat of fusion. Fredrickson[9] has obtained a value of approximately 10.5 kcal/mol for the heat of fusion from preliminary drop calorimetry data. The very large uncertainty in the difference in slopes is mostly due to the large scatter of the ion-current data for the temperature region of the solid. This scatter is believed to be due in part to the marked decrease in surface area of the sample that occurred after a molten sample had been frozen.

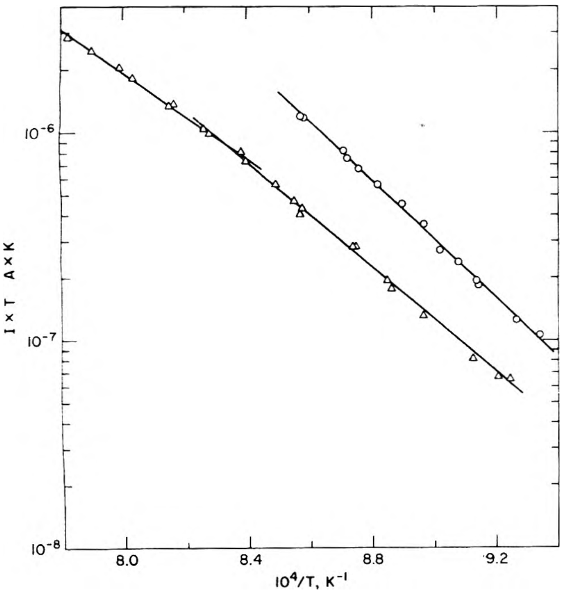

Figure 2. Temperature dependence of $Cs_2MoO_4^+$ over cesium molybdate, at 22 eV: (O) high-purity sample, solid temperature range only; (Δ) 99 mol % sample.

The data for the upper line in Figure 2 were obtained using the high-purity sample of cesium molybdate and with the temperature limited to the solid range of the compound. In this experiment, the precision of the measurements of the ion currents was 0.3% and of the temperature, 0.5°. The data given in Table I may be represented by the equation

$$\ln (IT) = (14.03 \pm 0.33) - (3.22 \pm 0.14) \times 10^4/T \tag{4}$$

with a standard deviation of 3%. The enthalpy of sublimation of solid cesium molybdate computed from the slope is equal to 64.1 ± 2.7 kcal/mol.

The composition of the vapor was computed from measurements of the change in the composition of the solid after long periods of vaporization at a constant temperature. Three experiments were done using the 99 mol % sample of cesium molybdate. The molybdenum content of the sample before and after vaporization was determined using the gravimetric silver molybdate method. The results of the three experiments are summarized in Table II. It is seen that the millimoles of Cs_2MoO_4 in the vapor computed on the assumption that all the weight loss occurred as Cs_2MoO_4 is equal, within the experimental uncertainty, to the millimoles computed from the change in the molybdenum content of the sample. If it is assumed that the samples were mixtures of Cs_2MoO_4 and $Cs_2Mo_2O_7$, the apparent loss of Cs_2O can be computed; the equivalent Cs_2MoO_4 loss computed on this basis is given in the fourth column of Table II. These results indicate that the weight loss and composition changes during vaporization into a vacuum are consistent with a vapor whose composition is that of Cs_2MoO_4. It is concluded that only Cs_2MoO_4 molecules are vaporized from solid cesium molybdate.

The absolute vapor pressure of Cs_2MoO_4 was determined using the Knudsen effusion method. To take into account the weight loss during the heat-up and cool-down periods, as well as variations in the rate of effusion due to temperature changes during the constant temperature period, the following form of the Knudsen equation was used:

TABLE I: $Cs_2MoO_4^+$ Ion-Current Temperature Product vs. Temperature[a]

Temp, K	$I(Cs_2MoO_4^+)T$, A K	Temp, K	$I(Cs_2MoO_4^+)T$, A K
1148.6	8.086×10^{-7}	1145.5	7.482×10^{-7}
1125.8	4.559×10^{-7}	1167.2	1.200×10^{-6}
1091.8	1.871×10^{-7}	1101.8	2.392×10^{-7}
1090.5	1.771×10^{-7}	1079.4	1.253×10^{-7}
1107.7	2.701×10^{-7}	1115.7	3.621×10^{-7}
1070.6	1.070×10^{-7}	1142.3	6.772×10^{-7}
1132.3	5.616×10^{-7}	1165.6	1.193×10^{-6}

[a] Data in chronological order.

TABLE II: Composition of the Vapor Phase over Solid Cesium Molybdate Obtained from Weight Loss and Change in Composition after Evaporation

	Millimoles of Cs_2MoO_4 in vapor		
No.	From total wt. loss (±0.001)[a]	From change in Mo content (±0.002)	From change in Cs content (±0.003)
10	0.144	0.145	0.144
12	0.190	0.187	0.192
15	0.174	0.174	0.174

[a] Estimated uncertainty.

$$\Delta w = 44.33KA\sqrt{M}p_0\left[\int_0^t \frac{\exp B(1/T_0 - 1/T)}{T}\, dt\right] \tag{5}$$

where Δw is the total weight loss observed; K, the Clausing correction factor; A, the orifice area; M, the molecular weight of the effusing species (425.75 for Cs_2MoO_4); p_0, the vapor pressure (in atm) at the temperature T_0 (the average temperature during the constant temperature period); B, the temperature coefficient of the vapor pressure (3.22×10^4, eq 3); and T, the temperature at time t. The integral in eq 5 was evaluated over the period that the cell was at or above 750°; the evaluation was done in a stepwise fashion using the average temperature during each interval. The heat-up and cool-down periods contributed about 2 and 0.1%, respectively, to the value of the integral. The results of three Knudsen effusion experiments are given in Table III. The pressure derived at each temperature was used to compute the value for the intercept, A, of an equation with the same form and slope as eq 4. The vapor pressure of cesium molybdate is given by the equation

$$\ln p(\text{atm}) = (15.14 \pm 0.05) - (3.22 \pm 0.14) \times 10^4/T \tag{6}$$

with a standard deviation of about 5% for the pressure.

The standard free energy of formation of gaseous cesium molybdate may be calculated from the equation

$$\Delta G_f°(Cs_2MoO_4, g) = \Delta G_f°(Cs_2MoO_4, c, \beta) - RT \ln p(Cs_2MoO_4) \tag{7}$$

where $\Delta G_f°(Cs_2MoO_4,c,\beta)$ is the standard free energy of formation of the high-temperature β form of solid cesium molybdate, which is the equilibrium form over the temperature range from 845 K to the melting point at about 1213 K.[10] An equation for the temperature dependence of

TABLE III: Knudsen Pressure Determination of Cesium Molybdate[a]

No.	$44.33 \cdot KA \cdot \sqrt{M}$	T_0, K	Δw, g	Integral eq 5	p_0, atm	Intercept A
10-II	7.71_9	1166.6	0.0197_9	12.72	3.36×10^{-6}	15.03_9
15-I	7.43_6	1183.0	0.0351_5	13.35	5.90×10^{-6}	15.22_0
15-II	7.43_6	1185.7	0.0386_1	14.69	5.89×10^{-6}	15.15_5

[a] Orifice radius, ~0.11 cm; Effusion times, ~500 min.

$\Delta G_f°(Cs_2MoO_4,c,\beta)$ was derived from the enthalpy of formation at 25°,[5] the calorimetric entropy,[11] the preliminary high-temperature enthalpy data obtained by Fredrickson[9] for Cs_2MoO_4, the enthalpy data for liquid and gaseous cesium selected for the JANAF tables,[8] and the equations for gaseous oxygen and solid molybdenum given by Kelley.[12] The equation derived is

$$\Delta G_f°(Cs_2MoO_4, c, \beta) = -393{,}126 + 86.7T + 6.114T \ln T - 1.075 \times 10^{-2}T^2 - 4 \times 10^4/T \quad (8)$$

which, when combined with eq 6 and 7, gives the following equation for the standard free energy of formation of gaseous Cs_2MoO_4 from gaseous Cs:

$$\Delta G_f°(Cs_2MoO_4, g) = -329{,}044 + 56.61T + 6.114T \ln T - 1.075 \times 10^{-2}T^2 - 4 \times 10^4/T \quad (9)$$

The temperature coefficients obtained from ln $(I_{Cs}T)$ *vs.* $1/T$ plots were 6–10% more negative than those observed for the $Cs_2MoO_4^+$ ion. This indicated that a reaction with a more negative temperature coefficient than the fragmentation reaction, eq 1, was making a contribution to the Cs^+ ion current because the fragmentation reaction would be expected to have the same temperature coefficients as the $Cs_2MoO_4^+$ ion. The most likely explanation is a reaction that produces cesium atoms in the gas phase independent of the fragmentation reaction. Several reactions in which cesium atoms may be produced were considered.

Reaction of the cesium molybdate with the outer molybdenum cell, i.e.

$$Cs_2MoO_4 + Mo = 2Cs(g) + 2MoO_2 \quad (10)$$

was rejected because the calculated temperature coefficient is -3×10^4, which is more positive than that observed for the $Cs_2MoO_4^+$ ion. The calculated equilibrium cesium pressure is about 2×10^{-8} atm at 1050 K for reaction 10. A reaction similar to this may have been responsible for the reaction of liquid cesium molybdate with the iridium liner prior to the use of the gold liner.

A more plausible reaction to account for a very small pressure of cesium atoms in the gas phase is the reaction of cesium molybdate to form the dimolybdate:

$$2Cs_2MoO_4 = Cs_2Mo_2O_7 + 2Cs(g) + \tfrac{1}{2}O_2 \quad (11)$$

However, the observed change in composition of cesium molybdate after extensive vaporization (Table II) would indicate that this reaction must play a very minor role in the vaporization process. Noting that the equilibrium cesium pressure would be four times the oxygen pressure, one may compute the cesium pressure from the equation:

$$(5/2)RT \ln p_{Cs} = \Delta G° + 2RT \ln a(Cs_2MoO_4) - RT \ln a(Cs_2Mo_2O_7) \quad (12)$$

where

$$\Delta G° = 2\Delta G_f°(Cs_2MoO_4) - \Delta G_f°(Cs_2Mo_2O_7) - 2\Delta G_f°(Cs, g) \quad (13)$$

The activity terms in eq 12 must be considered because the low-melting $Cs_2Mo_2O_7$ (mp 464°)[10] will form a liquid solution on the surface of the solid Cs_2MoO_4. This liquid layer would have approximately the composition of the liquidus of the Cs_2MoO_4–$Cs_2Mo_2O_7$ system which at 800° contains about 60 mol % $Cs_2Mo_2O_7$. The concentration of the dimolybdate would decrease as the temperature is increased. Since the liquid would be in equilibrium with solid Cs_2MoO_4, the activity of Cs_2MoO_4 would be unity under the choice of reference states implicit in eq 12. The standard free energy change may be computed from the data given above for Cs_2MoO_4 and Cs, the enthalpy of formation of $Cs_2Mo_2O_7$ measured by O'Hare,[13] and an estimate of the entropy of $Cs_2Mo_2O_7$;[14] it is found to be

$$\Delta G° = -208{,}092 + 64.16T \quad (14)$$

If the activity term for $Cs_2Mo_2O_7$ is neglected, the cesium pressure is found to be 1.9×10^{-12} and 6.2×10^{-11} at 1050 and 1150 K, respectively. The temperature coefficient of reaction 11 is -4.2×10^4, if the contribution of the partial molar enthalpy of $Cs_2Mo_2O_7$ is not included. This latter term would be expected to be relatively small, but would have to be taken into account if a quantitative treatment of the Cs^+ ion data was to be made. Therefore, if the observed Cs^+ ion current is a combination of contributions from the fragmentation reaction, eq 1, and the decomposition reaction, eq 11, a temperature coefficient more negative than that found for $Cs_2MoO_4^+$ ion would be expected, as was observed.

2. *Sodium Molybdate.* The mass analysis of the positive ions produced by electron impact ionization of the vapor over liquid sodium molybdate in the temperature range from 870 to 1015° indicated the presence of Na^+, NaO^+, Au^+, $Na_2MoO_4^+$, and $AuNa^+$. The gold-containing ions originated from the interaction of sodium with the gold liner of the effusion cell. The observed appearance potentials for Au^+ and $AuNa^+$ were 7.8 and 6.2 eV, respectively. The appearance potential of Au^+ when formed by the simple ionization of gold atoms is 9.18 eV,[15] and therefore the Au^+ ion observed in this study probably originated from a fragmentation reaction involving the AuNa molecule. The observed appearance potential for the $Na_2MoO_4^+$ ion was 7.2 eV. The ionization efficiency curve for $Na_2MoO_4^+$ reached a maximum at about 25 eV. A detailed study of the mass spectra was not made because our principal objective was to determine whether Na_2MoO_4 gaseous molecules were a constituent of the vapor phase over liquid sodium molybdate.

The ion currents for the Na^+ and $Na_2MoO_4^+$ ions were measured as a function of temperature, using an electron energy of 22 eV. The results are shown in Figure 3. The enthalpy of vaporization of Na_2MoO_4 is 73.4 ± 4.7 kcal/mol, whereas the enthalpy of the process for the production of Na^+ is 62.7 ± 6.2 kcal/mol. The latter enthalpy is smaller than reported by Yamdagni et al.,[4] who determined it to be 72 ± 5 kcal/mol in their study of the vaporization of liquid sodium molybdate from a molybdenum cell over a temperature range from about 1000 to 1130°. They suggested a reaction analogous to reaction 10 to account for the observed Na^+ ion current. In our study the liquid sodium molybdate did not contact the molybdenum outer cell and hence a different series of reactions was responsible for the

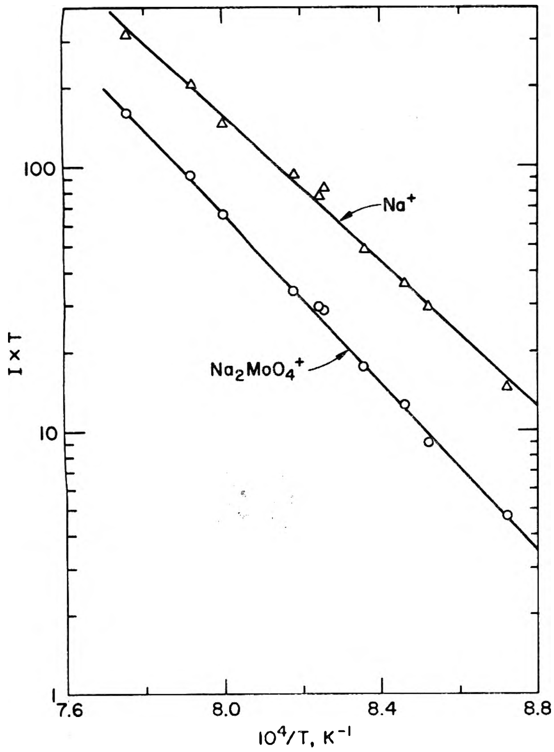

Figure 3. Temperature dependence of Na$^+$ and Na$_2$MoO$_4$$^+$ over liquid sodium molybdate at 22 eV: (O) Na$_2$MoO$_4$$^+$, ordinate scale factor 10^9; (Δ) Na$^+$, ordinate scale factor 10^8. I in amperes.

formation of the Na$^+$ ion. In view of the complication introduced by the reaction with the gold liner in the present study, the results of the two studies cannot be readily compared.

The molybdenum content of the residue from the effusion study was determined and compared with the value for the starting material. From the weight loss and the change in molybdenum content the ratio of Na$_2$O to MoO$_3$ in the vapor was estimated to be 1.03. This indicates that significant decomposition occurred, in addition to the vaporization as Na$_2$MoO$_4$ molecules.

Acknowledgments. The author wishes to thank Dr. P.A. G. O'Hare for the sample of high-purity cesium molybdate used in this study and for his measurement of the enthalpy of formation of cesium dimolybdate. The helpful discussions with Professor Scott Wood of the Illinois Institute of Technology are also gratefully acknowledged. This study was done under the auspices of the U.S. Atomic Energy Commission.

References and Notes

(1) V. I. Spitsyn and I. M. Kuleshov, *J. Gen. Chem. USSR*, **21**, 445 (1950).
(2) C. Pupp, R. Yamdagni, and R. F. Porter, *J. Inorg. Nucl. Chem.*, **31**, 2021 (1969).
(3) G. Verhaegen, R. Colin, G. Exsteen, and J. Drowart, *Trans. Faraday Soc.*, **61**, 1372 (1965).
(4) R. Yamdagni, C. Pupp, and R. F. Porter, *J. Inorg. Nucl. Chem.*, **32**, 3509 (1970).
(5) P. A. G. O'Hare and H. R. Hoekstra, *J. Chem. Thermodyn.*, **5**, 851 (1973).
(6) A. V. Gusarov, L. N. Gorokhov, and A. G. Efimova, *High Temp.*, **5**, 524 (1967).
(7) J. T. Tate and P. T. Smith, *Phys. Rev.*, **46**, 773 (1934).
(8) D. R. Stull and H. Prophet, *Natl. Stand. Ref. Data Ser., Natl. Bur. Stand., No.*, **37** (1971).
(9) D. Fredrickson, personal communication.
(10) H. R. Hoekstra, *J. Inorg. Nucl. Lett.*, **9**, 1291 (1973).
(11) D. W. Osborne, H. E. Flotow, and H. R. Hoekstra, *J. Chem. Thermodyn.*, **6**, 179 (1974).
(12) K. K. Kelley, *Bur. Mines Bull.*, 584 (1960).
(13) P. A. G. O'Hare, personal communication.
(14) The entropy of Cs$_2$Mo$_2$O$_7$ was estimated to be 81.1 cal/deg mol by comparison of the entropies of Na$_2$MoO$_4$, Na$_2$Mo$_2$O$_7$, and Cs$_2$MoO$_4$.
(15) "Handbook of Chemistry and Physics", Chemical Rubber Publishing Co., Cleveland, Ohio, 1966.

The Uranium–Hydrogen System[1]

C. J. M. Northrup, Jr.

Chemical Technology Division 5824, Sandia Laboratories, Albuquerque, New Mexico 87115

(Received September 13, 1974)

Publication costs assisted by Sandia Laboratories

Pressure–composition isotherms have been extended to 680 atm for the uranium–hydrogen system. The present investigation indicates that in contrast to the work of Chevallier, Spitz, and Blum the uranium–hydrogen system retains broad, two-phase plateaus on the pressure–composition isotherms at temperatures as high as 846°. The phase diagram for this system and the calculated thermodynamic potentials are discussed and compared with previous investigations.

Introduction

The uranium–hydrogen system has been studied extensively at lower temperatures (below 450°) where the dissociation pressure is near or below 1 atm.[2-7] More recently, investigators have extended the temperature and pressure range using high-pressure equipment. Pressure–temperature isochores have been used to define the phase boundaries and thermodynamic potentials for the uranium–hydrogen system.[8-12] It was the purpose of this investigation to study the uranium–hydrogen system over the pressure

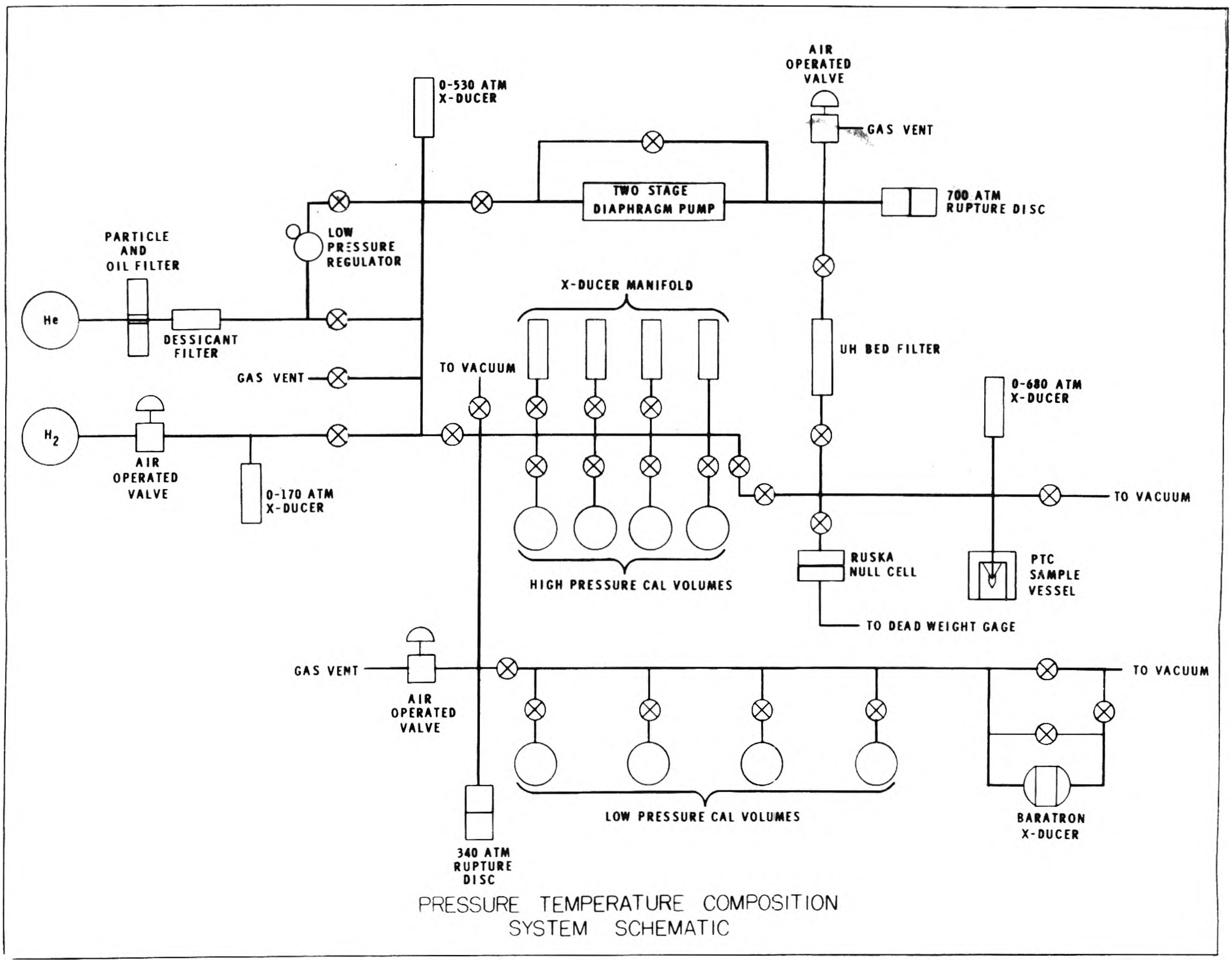

Figure 1. The apparatus used to study the high-pressure high-temperature behavior of the uranium–hydrogen system.

range from 0.1 to 680 atm of hydrogen at temperatures from 596 to 846°. The results of these measurements will be compared with previous data and shown to disagree with the work of Chevallier, Spitz, and Blum.

Experimental Section

Apparatus. The apparatus shown schematically in Figure 1 consisted of a sample vessel, furnace, temperature measurement and control systems, low-pressure glass and high-pressure stainless steel volume calibration systems, pressure measuring systems, and a high-pressure gas pump with a purification train. The high-pressure tubing used throughout the system was made of 316 stainless steel with coned and threaded connections. The valves were standard 30,000 psi valves (Autoclave Engineers, Inc.) with bodies of 316 stainless steel and gaskets of teflon. Gold wires or gold-plated stainless steel rods were placed where needed in the high-pressure tubing to minimize the free gas volume.

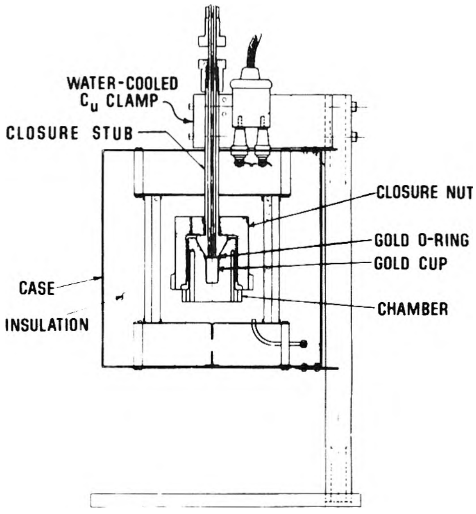

Figure 2. The Udimet 700 high-pressure sample vessel.

The sample vessel (Figure 2) was machined from a single bar of Udimet 700. In some cases, this nickel-based alloy can undergo stress crack corrosion when exposed to hydrogen and therefore the vessel was designed for a minimum yield at 6800 atm at 900°. To minimize permeation, the interior of the vessel was lined with a continuous gold bladder (1 mm wall). Gold capillary tubing was extended from the sample chamber to the high-pressure system beyond the chill block and was electron-beam welded to the end of the nipple cone. The sample vessel was sealed by crushing a gold O ring. To keep the uranium sample from reacting with the gold, the sample was placed inside a thin pure alumina (AL 995, Western Gold and Platinum, Inc.) crucible and cover. A small stainless steel frit was attached to the front of the closure stub of the sample vessel to minimize gas surges and particulate motion.

The furnace, a clam shell type, was powered by a Leeds and Northrup (L&N) zero-voltage-firing silicon-controlled-rectifier power supply that was regulated by a current adjusting controller (L&N, Electromax III). The temperature controller maintained the sample temperature on a given isotherm to a precision of ±0.5°.

The temperature of the reaction vessel was sensed by chromel–alumel thermocouples attached to its outer surface. In addition, there were two sample temperature probes inserted in thermowells drilled into the vessel and positioned adjacent to the sample. These probes consisted of a sheathed, tip sensitive, chromel–alumel thermocouple (Control Products Corp.) and a four-lead platinum resistance temperature sensor (Rosemont 104MD). The temperatures were monitored by a digital indicator (L&N, Numatron). The temperature difference between the sample probes was a constant value for a given isotherm (less than 0.5°) while the temperature distribution on the outer surface of the sample vessel was found to range from 3° at 596° to 10° at 846°.

The temperatures of all tubing and calibrated volumes external to the sample vessel were stabilized in a circulating air bath. These temperatures were sensed with individual platinum resistance temperature sensors (Rosemont, 104ME).

The temperature sensing equipment was calibrated in two different ways. For temperatures below 180°, the probes were clamped to a copper heat sink maintained in a constant temperature oil bath and compared against a platinum resistance standard of known accuracy. In this temperature range, the total uncertainty in temperature was less than ±0.2°. From 450 to 850°, the probes were clamped in an Inconel heat sink which was placed in a tube furnace and surrounded with Fiber Frax felt (Carborundum Corp.). A Pt–Pt—10% Rh thermocouple of known calibration was used to determine the response of the sample probes. The temperature uncertainty of sample probes was less than ±0.7°.

The hydrogen pressure over the sample was monitored with a 680-atm pressure transducer (Teledyne Taber Corp.) and a dead weight gage (Ruska Corp., Model 2400) operated on oil and interfaced to the hydrogen through a pressure null cell (Ruska, Model 2417). The pressure transducer had an uncertainty of ±0.7 atm; however, the dead weight gage had an uncertainty of only 0.01% of each pressure reading or 0.003 atm, whichever was greater.[13] The pressure null cell was machined from a single bar of A-286 stainless steel. The sensitivity of the cell was particularly useful in determining when pressure equilibrium had been reached. Its sensitivity allowed detection of pressure differences on the order of 5×10^{-4} to 1×10^{-5} atm differential pressure per meter division.

The gas pressures in the calibrated volume sections were measured with five separate pressure sensors in a manifold: an MKS Baratron (1000 Torr head, uncertainty ±1 Torr), an Ashcroft Digigauge (0–34 atm, uncertainty $\pm 1.4 \times 10^{-3}$ atm), and three Fairchild (Model TF150) pressure transducers (0–6.8, 0–54, 0–540 atm; uncertainty ±0.1% of the full scale reading). All pressure sensors were calibrated against dead weight gages after being attached to the pressure system. The pressure transducer manifold allowed the gas pressure to be read by the one sensor that was operating with the lowest error.

The volumes of the glass vessels were determined by weighing with water to be 27.62 ± 0.01, 25.61 ± 0.01, 105.30 ± 0.02, 492.99 ± 0.02 cm^3 at 25°. The expansion of helium from these volumes was then used to measure the volumes of the high-pressure section which were 50.5 ± 0.1, 264.1 ± 0.1, 1066.4 ± 0.3, 3966.1 ± 0.6 cm^3 at 25° The total free gas volume of the sample vessel containing unhydrided uranium was 10.02 ± 0.01 cm^3. After hydriding the free gas volume was determined to be 9.36 ± 0.01 cm^3. This change in free gas volume agrees with the values expected due to the expansion of the sample on hydriding. This change in sample volume was very significant in determining the hydride compositon at high pressures as will be discussed later. The sample vessel was heated to different temperatures at various pressures and the pressure vs. temperature response was noted. Even though the pressure transducers, high-pressure valves, etc. were maintained at room temperature while the reaction vessel was heated, it was found that for all temperatures and pressures, the free gas volume with the hydrided sample could be separated into a "hot zone" with volume 2.41 ± 0.01 cm^3 and a "cold zone" with volume 6.95 ± 0.01 cm^3. The insensitivity of the "zone" calculations to variations in temperature and pressure was probably a consequence of (1) lining the sample vessel with a material (gold) that has a very low solubility for hydrogen, thus minimizing solubility corrections, (2) overdesigning the vessel so that the dimensional changes are small over this pressure range, and (3) minimizing the free gas volume in the transition region between the hot and cold zones.

Permeation from the sample vessel could be detected at elevated temperatures and pressures and therefore a permeation coefficient and measured for each isotherm. By recording the time of each extraction, the hydrogen lost by permeation could be determined. Losses due to permeation ranged from 1 to 13% of the total hydrogen extracted from the sample over an isotherm, and these corrections were included in the final calculations for sample composition.

The system was pumped to high pressures with a two-stage diaphragm pump (American Instruments Co., 46-14021 SP). The gas was passed through a powdered UH_3 bed and a stainless steel particle filter just prior to entering the sample vessel.

Materials. The uranium metal used was high-purity, depleted uranium slabs furnished by the Atomic Energy Commission. The analysis of the sample is shown in Table I. X-Ray analysis showed only single phase α (orthorhombic) uranium patterns. The sample was cleaned successively in warm 1:1 HNO_3, distilled water, and ethanol, and then weighed (18.7193 ± 0.0001 g). It was loaded into the vacuum baked (1000°, 10^{-7} Torr) alumina crucible which was transferred to the sample vessel. The seal of the sample vessel was torqued closed and the vessel attached to the pressure system and evacuated.

The hydrogen used in these experiments was Matheson Gold Seal (99.999% min) gas that was passed through a powdered UH_3 column located adjacent to the sample vessel. The UH_3 in the column was made in situ from the same grade of uranium as the sample. Prior to the entry of hydrogen, the system was evacuated (gage pressure, 10^{-3} Torr) and flushed with purified helium several times. Due to the capillary tubing in the closure stub, etc. all the system was not at as low a pressure as the gage reading but contamination was minimized by the flushing operation. It was then pressure checked with purified helium to 680 atm and evacuated again. Finally the hydrogen was allowed to

TABLE I: Impurity Analysis of Uranium Samples[a]

Element	ppm	Element	ppm
Cu	3	As	ND
Fe	12	Ge	ND
Pb	3	Bi	ND
B	8	Cd	ND
Mg	12	Mn	ND
Si	35	Ni	ND
P	ND	Ti	ND
Zn	ND	Tl	ND
V	ND	In	ND
Co	ND	Ba	ND
Mn	3	Li	ND
Sb	ND	Be	ND
Sn	ND	Cr	ND
O	26	Al	12
N	9		

[a] The elemental analysis was obtained by emission spectroscopy (D. Wanner), spark source mass spectroscopy (F. Oswalt), and vacuum fusion (W. Andrzejewski), al. of Sandia Laboratories. ND, not detectable.

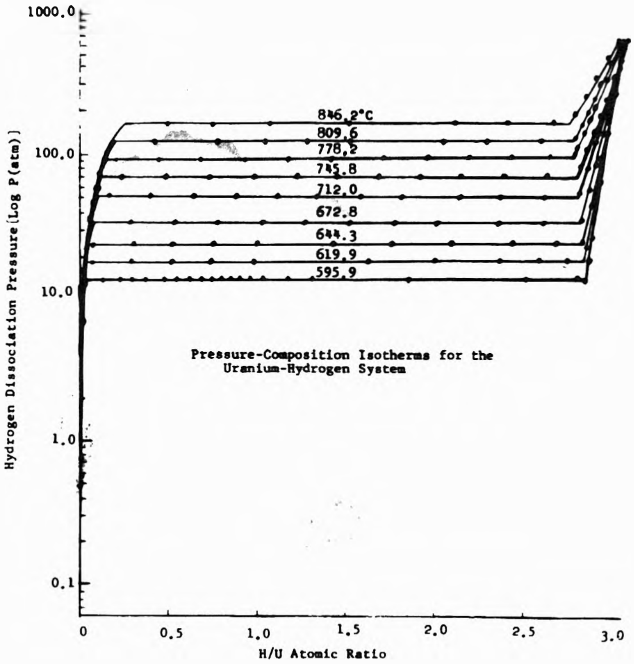

Figure 3. Pressure–composition isotherms for the hydrogen–uranium system.

flow through. After several minutes, the system was sealed and pumped to approximately 600 atm. The temperature was cycled from room temperature to 600°. By cycling the temperature and pressure four or five times, the sample was made very reactive and desorption measurements showed that it could be fully and reproducibly hydrided.

Experimental Procedure. In a typical run, the sample was pressurized at room temperature to approximately 600 atm of hydrogen and left overnight. The next morning, the sample temperature was raised to the desired temperature and allowed to equilibrate. The pressure was then monitored for a length of time to determine the permeation coefficient for that temperature and pressure. Then an aliquote of hydrogen was transferred to the high-pressure calibration system. When the system reached an equilibrium (i.e., the change in pressure was either dominated by the loss of gas by permeation or was less than 0.1% of the overpressure per hour, whichever was greater) the pressure was recorded. By successive measurements, pressure-composition isotherms were obtained for nine temperatures between 596 and 846°. The change in composition of the sample was obtained by determining the quantity of hydrogen transferred to the calibration volumes and subtracting from it the quantity of gas lost from the free gas volume of the sample vessel. In these calculations, the free gas volume of the hot zone was assumed to vary from 2.41 to 3.07 cm^3 according to the law of mixtures as the desorption from the sample continued across the two-phase plateau. The change in sample volume was found to be particularly important at high pressures. The total composition was calculated by summing the individual extractions from the sample. These calculations were performed on a CDC 6600 computer.

The equation of state for hydrogen as proposed by Roder, McCarty, and Hall was used to determine the density of hydrogen.[14] Since this relation is solved for pressure P (ρ, T), and cannot be solved explicitly for the density (ρ) as a function of pressure and temperature (T), the solution was approximated and then solved iteratively using Newton's method until the deviations in the calculated density produced changes in the pressure that were smaller than the deviations due to the error in the measured pressure (0.01% of the pressure reading or 0.003 atm, whichever was greater). The equation of state for hydrogen has not been measured directly at both high temperatures and pressures and therefore the uncertainty of the gas density is difficult to determine; however, the relation used here is considered to have an uncertainty of 0.8% or less for these pressures and temperatures.[14]

As can be seen in Figure 3, the isotherms have plateaus that are flat with abrupt discontinuities at the phase boundaries. Although the temperature controller maintained the temperature on a given isotherm to ±0.5°, pressure shifts associated with the temperature fluctuations could be detected. The overall accuracy of the pressure–composition isotherms was difficult to determine statistically because so many variables are involved in complex and possibly synergistic ways. An attempt was made to estimate the uncertainty in the composition by varying the input parameters within their measured uncertainties about the measured points. As might be expected, the overall uncertainty changes with the magnitude of the stoichiometry and the isotherm of interest. For example, at 595° and low stoichiometries, the uncertainty in the composition is considered to be ±0.002H/U and is dominated by the uncertainties in the free gas volumes of the sample and calibration vessels. At higher compositions on the plateau, the uncertainty is ±0.008H/U and at very high pressures, it increases to ±0.020H/U. For the 846° isotherm, the overall uncertainty in the composition increased primarily due to the uncertainty in the coefficient for hydrogen permeation from the sample vessel. For this isotherm and low stoichiometries, the uncertainty in the composition is ±0.03H/U and at higher stoichiometries on the plateau, it is ±0.07H/U. At very high pressures, the uncertainty in composition may be as high as ±0.18H/U but is thought to be considerably less.

Results and Discussion

The pressure–composition isotherms obtained in this study (Figure 3) were obtained for each of the three metal

TABLE II: Coefficients of Eq 1 for the Two-Phase Plateau Region (H/U Ratio Equal to 1.5) and the Apparent Thermodynamic Potentials for the Formation of the Hydride from Three Phases of Uranium

	α uranium + βUH_3	β uranium + βUH_3	γ uranium + βUH_3
A	-4225 ± 4	-4110 ± 80	-4200 ± 30
B	6.045 ± 0.004	5.94 ± 0.08	6.02 ± 0.03
${}_a\Delta H$, kcal mol^{-1}	-28.96 ± 0.03	-28.2 ± 0.5	-28.8 ± 0.2
${}_a\Delta S$, cal mol^{-1} °K^{-1}	-41.43 ± 0.03	-40.7 ± 0.6	-41.3 ± 0.2
${}_a\Delta G_{298}$, kcal mol^{-1}	-16.62 ± 0.04	-16.1 ± 0.7	-16.5 ± 0.3

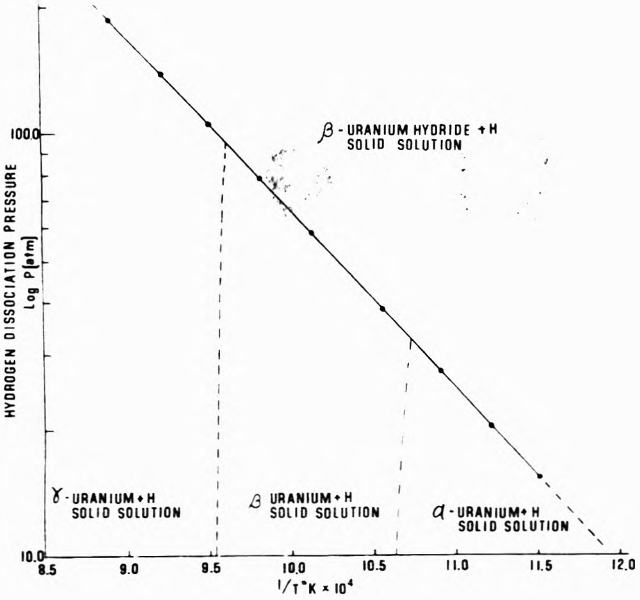

Figure 4. Dissociation pressure vs. reciprocal temperature for U/H ratio of 1.5.

phases of uranium (α, β, γ). For all isotherms, as hydrogen is removed from the solid solution with uranium hydride (β phase UH_3), the pressure drops rapidly until a plateau is reached indicating the existence of two solid phases. As additional gas is removed, the plateau ends abruptly, dropping the pressure rapidly, and indicating the transition to the single phase metal solid solution containing dissolved hydrogen.

For a given composition, the pressures on the two-phase plateau could be fitted to the relation:

$$\log P(\mathrm{atm}) = \frac{A}{T(°\mathrm{K})} + B \tag{1}$$

where the coefficients A and B are given in Table II for the three phases of uranium metal and β-uranium hydride at an atom ratio of H/U equal to 1.5. Between the α, β, and γ-uranium phases, little deviation is found in the least-squares fits for the coefficients A and B (Figure 4) even though there are significant enthalpy and entropy changes between the metal phases. These changes are partially manifested as shifts in the solubility at the phase boundary.

The simple reaction for the uranium–hydrogen reaction may be expressed as

$$U + \frac{r}{2}H_2 \longrightarrow UH_r \tag{2}$$

However, when the reaction is considered in greater detail, eq 2 can be separated into a piece-wise continuous reaction of hydrogen reacting with uranium as a metal, a two-phase material, and finally reacting with the hydride. Equation 2 can be expanded to describe steps of the reaction as shown by[15]

$$\begin{array}{ll} \text{a} & U + \frac{r'}{2}H_2 \longrightarrow UH_{r'} \\ \text{b} & UH_{r'} + \frac{(r'' - r')}{2}H_2 \longrightarrow UH_{r''} \\ \text{c} & UH_{r''} + \frac{x}{2}H_2 \longrightarrow UH_{r''+x} \\ \text{net reaction} & U + \frac{r'' + x}{2}H_2 \longrightarrow UH_{r''+x} \end{array}$$

$$\text{where } r'' + x = r \tag{3}$$

Here r' and r'' are respectively the lower and upper stoichiometries of the tie line between the phase boundaries for the same isotherm and $(r'' + x)$ is the final atom ratio of the hydride. At lower temperatures, where $r' \sim 0$ and $r'' \sim 3.0$ the net reaction in eq 3 has the form:

$$U + \frac{3}{2}H_2 \longrightarrow UH_3 \tag{4}$$

The integrated form of the van't Hoff equation may be expressed in its general form for the pressure plateau region as

$$\ln P(\mathrm{atm}) = \frac{2}{(r'' - r')R}\left(\frac{\Delta H}{T(°K)} - \Delta S\right) \tag{5}$$

from which the enthalpy (ΔH) and entropy (ΔS) for the plateau region may be calculated.[15] In agreement with previous studies, the van't Hoff plots of the plateau pressures (Figure 4) were found to be straight lines.[2,11] Using this observation from previous investigations, the high-temperature data have been extrapolated back to the region where $(r'' - r')$ equals 3.0, thus "apparent" potentials of formation (${}_a\Delta H$, ${}_a\Delta S$) can be obtained from the extrapolated higher temperature data. Correspondingly, the "apparent" free energy (${}_a\Delta G_{298}$) may be determined from standard relations. In Table III, the results of this study are compared with the work of previous investigators.

The "apparent" enthalpy and entropy calculated in the present study are lower than those of previous investigators. These differences are thought to be the result of the purity of the uranium used in the different studies. Particular care was taken to minimize oxygen contamination of the sample in the present work. The excellent agreement between the high-temperature and low-temperature values of ${}_a\Delta H$ indicate that the "apparent" enthalpy is reasonably constant with temperature.

The only other high-pressure data that extends above 650° is that of Chevallier, Spitz, and Blum.[11] Their data are in considerable disagreement with the present results at high temperatures. It is difficult to discern specifically

TABLE III: Comparison of the Plateau Dissociation Pressures (atm) and Thermodynamic Properties

Ref Temp,°C	2a	8	9	10	4,2b,12	5	6	7	11	This work[d]
595.9	16.6	16.7	14.6	15.3	18.0[a]	11.6[a]	15.8[a]	15.7[a]	15	15.19 ± 0.05
619.9	22.9[a]	23.0	20.1	21.0	25.0[a]	15.9[a]	21.7[a]	21.6[a]	21	20.53 ± 0.08
644.3	32.2[a]	31.3	27.4	28.4	34.3[a]	21.5[a]	29.5[a]	29.4[a]	27	27.55 ± 0.09
672.8	43.9[a]	44.0[a]	38.4[a]	39.6[a]	48.6[a]	30.0[a]	41.3[a]	41.2[a]	36	38.72 ± 0.08
712.0	67.9[a]	68.0[a]	59.3[a]	60.7[a]	75.8[a]	46.0[a]	63.6[a]	63.4[a]	51	58.3 ± 0.1
745.8	96.2[a]	96.4[a]	83.9[a]	85.5[a]	108[a]	64.7[a]	89.7[a]	89.6[a]	65	79.3 ± 0.2
778.2	131[a]	131[a]	114[a]	116[a]	149[a]	87.9[a]	122[a]	122[a]	74	106.3 ± 0.9
809.6	175[a]	176[a]	153[a]	154[a]	200[a]	116[a]	163[a]	163[a]	81	138.6 ± 0.9
846.2	239[a]	239[a]	207[a]	209[a]	274[a]	158[a]	220[a]	226[a]	86	185 ± 2
T for a dissc press of 1 atm	430	429	435	432[a]	420[a]	445[a]	430	431[a]	431[a]	425[a]
Thermodynamic Properties for the Formation of β-UH_3 from α-Uranium[c]										
ΔH, kcal mol^{-1}	−30.8	−30.8 ± 0.4	−30.7	−30.3 ± 0.1	−30.08 ± 0.03 (−30.45) (−30.35 ± 0.03)	−29.1 ± 0.3	−30.5 ± 0.7	−30.6	−30.1	−28.96 ± 0.03
ΔS, cal mol^{-1} °K^{-1}	−43.9	−43.9	−43.3	−43.0	−43.6	−42.5	−43.3 ± 0.4	−43.3	−42.7	−41.43 ± 0.03
ΔG_{298}, kcal mol^{-1}	−17.7	−17.7	−17.8	−17.5	−17.4	−16.4	−17.6	−17.7	−17.4	−16.62 ± 0.04
A[b]	−4500	−4500	−4480	−4410	−4600	−4255	−4450	−4460	−4380	−4225 ± 4
B[b]	6.40	6.40	6.32	6.26	−6.55	6.20	6.32	6.33	6.22	6.045 ± 0.004

[a] Indicates the values in the table were extrapolated beyond the temperature range of the original work. [b] These are coefficients in eq 1 for the plateau dissociation pressure vs. temperature. [c] Thermodynamic values not given in the original works were computed from eq 5. [d] Uncertainties in the dissociation pressures are a 1 σ standard deviation corresponding to H/U compositions from 0.5 to 2.5 and therefore define the maximum slope of the plateaus.

why this is the case; however, since in their sample the two-phase region was rapidly disappearing at 710°, and nonexistent above 820°, perhaps their sample reacted with some other material and failed to respond to hydrogen at the higher temperatures.

Acknowledgments. The author wishes to thank Mr. L.P. Baudoin for his expert assistance in the design of the high-pressure system. The valuable discussions with Mr. J.F. Lakner, Dr. H.P. Stephens, and Dr. M.L. Lieberman on thermodynamics and properties of hydrides were particularly helpful to the author and I thank them. A number of the members of the Sandia Laboratories Primary Standards Laboratory assisted with pressure, volume, and temperature calibrations which is greatly appreciated. Finally, R.P. Wemple provided valuable assistance in the construction and operation of the high-pressure system and his aid is highly valued by the author.

References and Notes

(1) This work supported by the U.S. Atomic Energy Commission.

(2) (a) F. H. Spedding, *et al.*, *Nucleonics*, **4**, 4 (1949); (b) H. E. Flotow and B. M. Abraham, USAEC Report No. AECD-3074, Argonne National Laboratory (Jan. 5, 1951).

(3) M. W. Mallett and M. J. Trzeciak, *Trans. Am. Soc. Met.*, **50**, 981 (1958).

(4) H. E. Flotow, H. R. Lohr, B. M. Abraham, and D. W. Osborne, *J. Am. Chem. Soc.*, **81**, 3529 (1959).

(5) M. Destriau and J. Seriot, *C. R. Acad. Sci.*, **254**, 2982 (1962).

(6) E. Wicke and K. Otto, *Z. Phys. Chem.* (*Frankfurt am Main*), **31**, 222 (1962).

(7) J. Besson and J. Chevallier, *C. R. Acad. Sci.*, **258**, 5888 (1964).

(8) T. R. P. Gibb, J. J. McSharry, and H. W. Kruschwitz, *J. Am. Chem. Soc.*, **74**, 6203 (1952).

(9) H. Mogard and G. Cabane, *Rev. Met.* (*Paris*), **51**, 617 (1954).

(10) G. C. Libowitz and T. R. P. Gibb, Jr., *J. Phys. Chem.*, **61**, 793 (1957).

(11) J. Chevallier, J. Spitz, and P. L. Blum, *C. R. Acad. Sci.*, **264**, 93 (1967).

(12) B. M. Abraham and H. E. Flotow, *J. Am. Chem. Soc.*, **77**, 1446 (1955).

(13) The calibration of the dead weight gage was traceable to the National Bureau of Standards, Germantown, Md.

(14) H. M. Roder, R. D. McCarty, and W. J. Hall, *Natl. Bur. Stand. Tech. Note*, **No. 625** (Oct 1972).

(15) W. M. Mueller, J. P. Blackledge, and G. G. Libowitz, "Metal Hydrides," Academic Press, New York, N.Y., 1968.

Gas Solid Chromatographic Measurements of the Change in the Heat Capacity during Adsorption on Graphitized Thermal Carbon Blacks

Claire Vidal-Madjar, Marie-France Gonnord, Michel Goedert, and Georges Guiochon*

Laboratoire de Chimie Analytique Physique, Ecole Polytechnique, 75005 Paris, France *(Received July 26, 1974)*

Publication costs assisted by Ecole Polytechnique

Gas chromatography is widely used to measure the thermodynamic functions of adsorption on the homogeneous surface of graphitized thermal carbon black in the region where Henry's adsorption law is valid. A high-precision instrument with computer data acquisition measures the isosteric heat of adsorption and the change of the heat capacity during adsorption. The method is used to study the adsorption of benzene and *n*-pentane on different graphitized thermal carbon black samples. The data are directly comparable with the values calculated from statistical thermodynamics on graphite since it is shown that adsorbate–adsorbate interactions are negligible and that the behavior of the bulk gas phase is nearly ideal. The results obtained for benzene could be compared with the molar heat capacity of adsorbed benzene measured by calorimetric methods and extrapolated at zero surface coverage. With *n*-pentane, however, the gas solid chromatographic method is unique, as extrapolation of calorimetric measurements is impossible because of strong adsorbate–adsorbate interactions at relatively low surface coverage.

Introduction

Recent theoretical developments in adsorption studies have focused attention on the importance of the heat capacity of the adsorbed molecules. This paper deals with the determination of this thermodynamic function.

The molecular statistical theory of adsorption allows the derivation of the thermodynamic functions of adsorption from the partition function of the adsorbed molecule.[1–4] The principles of this theory[2–6] have been successfully applied to predict the thermodynamic functions of adsorption of various compounds on graphitized thermal carbon black (GTCB) which is the choice absorbent for this type of study because of its homogeneous surface and because its particles are aggregates of small polyhedral particles each face of which is a 001 plane of the graphite lattice.[7]

The theoretical importance of the determination of the heat capacity change during adsorption at very low surface coverage results mainly from the fact that the adsorbate heat capacity is very sensitive to the model proposed for the adsorbed molecule.

The experimental methods of measurement of the adsorbate heat capacity have been reviewed by Pace[8] who outlined the problems encountered in carrying out significant measurements of the heat capacity of the adsorbed gas, especially for coverage ratios smaller than one monolayer.

Berezin and Kiselev[9,10] have measured the heat capacity of organic vapors adsorbed on GTCB, as a function of the surface coverage at 20°. The lowest coverage studied was 1 μmol/m^2 which is approximately equivalent to 30% of a monolayer.

Gas chromatography has been used in many instances to measure the thermodynamic functions of adsorption on numerous adsorbents, especially at very low surface coverage of GTCB,[11–15] but until now no attempt has been made to determine by this method the adsorption change of the heat capacity.

Such a measurement needs a highly accurate instrument in which all experimental parameters (pressures, temperatures, injection characteristics, . . .) are tightly controlled. Also retention times have to be measured very precisely using the mass center of the elution peaks and not their maximum and this can be done only through computer acquisition of the elution chromatogram.

The molecular statistical theory of adsorption can be used to predict the change of the heat capacity during adsorption at very low surface coverage as well as the free energy and the differential heat of adsorption.[5,16]

We present here the principles of the chromatographic measurement of the change of the heat capacity during adsorption and a comparison between the theoretical results and the experimental values obtained for the adsorption of benzene and *n*-pentane on graphitized thermal carbon black.

Theoretical

1. Thermodynamic Functions Calculated from Statistical Thermodynamics. It has been shown that Henry's adsorption equilibrium constant per unit surface area (K_H) can be calculated from statistical mechanics.[3,6] For quasirigid molecules, in the classical approximation, we have

$$K_H = \frac{1}{8\pi^2 ART} \int\cdots\int [\exp(-\phi/RT) - 1] \times \sin\theta \, dx \, dy \, dz \, d\theta \, d\varphi \, d\psi \qquad (1)$$

where ϕ is the potential energy of adsorption; x, y, and z are the coordinates of the mass center of the molecule; θ, φ, and ψ are the Euler angles of orientation to the surface; and A is the surface area of the adsorbent. Equation 1 assumes no lateral interactions in the adsorbed phase and an ideal bulk gas phase.

With Steele's notations[4] the second virial coefficient describing the interaction of the adsorbate with the surface is

$$B_{AS} = \frac{1}{8\pi^2} \int\cdots\int [\exp(-\phi/RT) - 1] \times \sin\theta \, dx \, dy \, dz \, d\theta \, d\varphi \, d\psi \qquad (2)$$

The limiting value for zero pressure of the apparent volume of the gas space or excess volume V_{ex} that the adsorbed

TABLE I: Thermodynamic Functions of Adsorption of Benzene on Graphite Calculated from Statistical Thermodynamics

T, °C	B_{AS}, cm^3/m^2	q_{st}, kcal/mol	ΔC_p, cal/mol °K
0	472.11	9.720	2.60
20	130.77	9.586	2.85
40	43.13	9.447	3.12
60	16.41	9.303	3.41
80	7.03	9.152	3.71
100	3.33	8.995	4.01
120	1.71	8.833	4.29
140	0.95	8.665	4.55
160	0.56	8.492	4.78
180	0.35	8.316	4.96

molecules would occupy if present at a pressure p[17] can be predicted from the B_{AS} value:

$$\lim_{p \to 0} V_{ex} = B_{AS} \tag{3}$$

Barker and Everett[18] have derived an exact expression which takes into account the adsorbate–adsorbate interactions and the nonideality of the gaseous phase in terms of virial coefficients. The thermodynamic functions of adsorption can easily be calculated from the relationship giving the Henry coefficient.[3,6]

From eq 1 we have derived the isosteric heat of adsorption q_{st} and the change in the heat capacity during the adsorption ΔC_p for benzene adsorbed on the basal plane of the graphite surface (cf. Table I) using the classical methods of statistical thermodynamics. The adsorption potential is calculated after the semiempirical Lennard-Jones potential, as suggested by Kiselev and coworkers[19,20]

$$\Phi = \sum_i \Phi_i = \sum_i \left[-C_{i1} \sum_j r_{ij}^{-6} - C_{i2} \sum_j r_{ij}^{-8} + B_i \sum_j r_{ij}^{-12} \right] \tag{4}$$

In this equation r_{ij} is the distance between the ith atom center of the adsorbate molecule and the jth carbon atom center of graphite. The potential energy of the molecule ϕ is taken as the sum of the potential energies of its separate atoms ϕ_i.

The attraction constant is calculated using the Kirkwood–Müller formula[21]

$$C_{i1} = -6mc^2 \left[\alpha_i \alpha_j \Big/ \left(\frac{\alpha_i}{\chi_i} + \frac{\alpha_j}{\chi_j} \right) \right] \tag{5}$$

C_{i2} is given by a similar formula.[20] α_j = 0.937 Å^3 is the polarizability of graphite carbon atoms, their diamagnetic susceptibility is $\chi_j = 1.05 \times 10^{-5}$ Å^3.[22] For carbon atoms in benzene α_i = 0.96 Å^3 and $\chi_i = 1.23 \times 10^{-5}$ Å^3; for the hydrogen atom α_i = 0.43 Å^3 and $\chi_i = 0.37 \times 10^{-5}$ Å^3.[23]

The repulsion constant B_i is calculated for each type of atom in the adsorbate molecule so that the equilibrium distance is the sum of the van der Waals radii of this atom and the graphite carbon atom.

The summations in eq 4 were calculated using a computer for the nearest 10,000 carbon atoms in a semispherical volume of 40 Å radius; the accuracy of this calculation is 10^{-4}. The program principles have been published.[24]

Integration of eq 1 is carried out for all distances z of the molecule above the graphite surface and for all its orientations. As the potential of adsorption does not change when the molecule of benzene moves parallel to the graphite surface, eq 1 is simplified to

$$K_H = \frac{1}{4\pi RT} \int \cdots \int [\exp(-\Phi/RT) - 1] \cdot \sin\theta \, d\theta \, d\psi \, dz \tag{6}$$

The model of adsorption described by eq 6 is that of an ideal bidimensional gas adsorbed on a homogeneous surface.

2. *Thermodynamic Functions Derived from Gas Chromatography.* The adsorption isotherm is obtained by gas chromatography from the change of the net retention volume V_R^0 with the concentration of the compound in the gas phase, according to the relation[14]

$$n_a = \frac{1}{A} \int_0^{n_g} V_R^0 \, dn_g \tag{7}$$

where n_g is the number of molecules of the component in the gas phase per unit volume, n_a the number of adsorbate molecules per unit surface area, and A the total surface area of adsorbent in the column. At zero surface coverage the retention volume per unit surface area V_A is equal to the slope of the adsorption isotherm $n_a = f(n_g)$ at the origin. Steele[25] has shown that the most convenient form of the adsorption isotherm is a virial expression, i.e., a power series of the amount adsorbed

$$\ln \frac{n_a}{p^*} = \ln K_H + 2B_{2D} n_a + \frac{3}{2} C_{2D} n_a^2 + \ldots \tag{8}$$

where p^* is the fugacity of the bulk gas phase.

For a static system and a solute highly diluted in the bulk gas phase under total pressure P, Locke[26] derived a relationship which takes into account the nonideality of the gas phase, neglecting higher order terms

$$\ln \frac{n_a}{n_g} = \ln K_H RT + 2B_{2D} n_a + 2B_{12} \frac{P}{RT} \tag{9}$$

where B_{12} is the second virial coefficient characterizing the interaction between the molecules of the diluent gas and the sample vapor. Equation 9 is valid if the diluent gas is not adsorbed.

Locke has applied eq 9 to gas chromatography using for P the average pressure in the chromatographic column. This is not correct however and Everett,[27] taking into account that the partition coefficient at infinite dilution (n_a/n_g) changes with the pressure, has calculated the exact value of the retention volume in gas liquid chromatography when the gas phase is not ideal. The same treatment can be used in gas solid chromatography[28,29] and gives

$$\ln V_A = \ln K_H RT + 2B_{2D} n_a + 2B_{12} \frac{P_o}{RT} j_3^4 \tag{10}$$

where

$$j_3^4 = \frac{3}{4} \frac{(P_i/P_o)^4 - 1}{(P_i/P_o)^3 - 1} \tag{10a}$$

P_i is the inlet pressure and P_o the outlet pressure.

The corrected retention volume per unit surface area is then

$$\ln V_A^c = \ln K_H RT = \ln V_A - e_1 - e_2 \tag{11}$$

The Henry coefficient per unit surface area can thus be derived from the retention volume per unit surface area according to the above equation. We shall show in the next section that in the experimental conditions used in this work both corrective terms $2B_{2D}n_a$ and $2B_{12}(P_o/RT)j_3^4$

can be neglected. From the value of the Henry adsorbate equilibrium constant given by eq 11 it is possible to derive the isosteric heat of adsorption[11-15]

$$q_{st} = R\frac{d \ln K_H}{d(1/T)} \qquad (12)$$

For practical applications it has always been assumed until now that q_{st} is independent of temperature. If data points which are more or less scattered deviate from linearity, this is usually considered as due to experimental error.[30] For a given coverage ratio however the isosteric heat of adsorption changes with temperature if the heat capacity of the compound in the gas phase is different from that in the adsorbed phase. The change of q_{st} with temperature is given by[8-30]

$$(\partial q_{st}/\partial T)_{n_a} = C_p - C_a = -\Delta C_p \qquad (13)$$

where C_a is the molar heat capacity of the adsorbed compound and C_p is the molar heat capacity of the vapor at constant pressure. The mean value of the change of the heat capacity during adsorption, $\overline{\Delta C_p}$, in the temperature range studied can be derived from eq 13 by integration

$$q_{st} = b - \overline{\Delta C_p}T \qquad (14)$$

This equation is valid if there is no discontinuity or maxima of ΔC_p in the temperature range studied.

A maximum in the value of the molar heat capacity of the adsorbate is to be expected only when a two-dimensional condensation does occur. Such a maximum can only appear at low temperatures and high surface coverages[8] or when adsorbate–adsorbate interactions are large[10] and obviously not in the experimental conditions prevailing in gas chromatography.

If the theoretical model assumed for benzene adsorption is correct, it is seen in Table I that statistical thermodynamics predicts a variation in the value of ΔC_p with temperature. In the temperature range where our experiments are carried out (90–160°), however, this variation is of the same order of magnitude as the errors made on $\overline{\Delta C_p}$ measurements themselves (ca. 10%). From eq 12 and 14 we obtain by integration

$$R \ln K_H = a + \frac{b}{T} + \overline{\Delta C_p} \ln T \qquad (15)$$

and for the corrected retention volume V_A^c

$$R \ln V_A^c = a + R \ln R + \frac{b}{T} + (\overline{\Delta C_p} + R) \ln T \qquad (16)$$

Thus a least-squares fitting of the experimental measurements of V_A^c at various temperatures allows the determination of $\overline{\Delta C_p}$.

3. Measurement of the Heat Capacity Change during Adsorption. The net retention volume is usually derived from the value of the retention time of the compound t_R, the retention time of an unretained compound t_0, and the carrier gas flow rate D_c at the column temperature T_c

$$V_R^0 = j(t_R - t_0)D_c \qquad (17)$$

j is a correction factor which takes into account the effect of gas compressibility

$$j = 1.5\frac{(P_i/P_o)^3 - 1}{(P_i/P_o)^2 - 1} \qquad (18)$$

The flow rate at column temperature is related to the measured flow rate D_A by the relation

$$D_c = D_A\frac{T_c}{T_A}\frac{P_A - P_E}{P_o} \qquad (19)$$

where P_E is the partial pressure of water in the flowmeter, P_A the atmospheric pressure, P_o the outlet pressure of the column during the experiment, and T_A the ambient temperature. These corrections are difficult to make exactly, and the flow rate which is usually measured with a soap bubble flowmeter is never known with a precision much better than 1%, so it is better to measure $\overline{\Delta C_p}$ with a procedure which does not need to measure D_c.

The geometrical volume of the column plus the dead volumes of the instrument is given by

$$V_G = jt_0D_c \qquad (20)$$

Combining eq 17 and 20, we have

$$V_R^0 = \frac{t_R - t_0}{t_0}V_G \qquad (21)$$

as long as inlet and outlet pressures are maintained constant during the entire experiment.

The specific retention volume or retention volume per unit surface area is thus

$$V_A = \frac{t_R - t_0}{t_0}\frac{V_G}{A} \qquad (22)$$

V_R^0 may be compared with the excess volume defined by Steele and Halsey[17] which is measured from static measurements at low vapor pressure of the adsorbate in the initial part of the adsorption isotherm, where Henry's law is valid

$$V_R^0 = K_HRTA = \lim_{p \to 0} V_{ex} \qquad (23)$$

As V_G, which is a geometrical volume, does not change appreciably with temperature, we can write

$$d \ln k'/d(1/T) = d \ln V_A/d(1/T) \qquad (24)$$

with $k' = (t_R - t_0)/t_0$.

If adsorbate–adsorbate interactions are negligible ($e_1 = 0$) and if the gaseous phase is ideal ($e_2 = 0$), we have combining eq 12, 23, and 24

$$q_{st} = R\frac{d \ln k'}{d(1/T)} + RT \qquad (25)$$

The value of the retention volume (eq 16) and k' are derived from

$$R \ln k' = a - \ln\frac{V_G}{A} + R \ln R + \frac{b}{T} + (\overline{\Delta C_p} + R) \ln T \qquad (26)$$

When the corrective terms e_1 and e_2 are not negligible k' is replaced in eq 26 by k'^c, the corrected capacity factor with

$$\ln k'^c = \ln k' - e_1 - e_2 \qquad (27)$$

Using a least-squares fit method, it is possible to determine the constants of eq 26 corrected or not for gas-phase nonideality or adsorbate–adsorbate interactions, as needed. The three constants are

$$\begin{aligned} \alpha &= a - \ln V_G/A + R \ln R \\ \beta &= b \\ \gamma &= \overline{\Delta C_p} + R \end{aligned} \qquad (28)$$

The method is valid as long as all the experimental parameters are controlled with a sufficiently high precision. Using the procedure described above by eliminating the flow rate measurements, we arrive at a much better precision for the

TABLE II: Experimental Data for *n*-Pentane Adsorbed on Graphitized Thermal Carbon Black Sterling MTG

T, °C	t_R, sec	t_m, sec	t_0, sec	log k'	V_A, cm^3/m^2	e_2
120.015	154.699	77.584	77.235	0.0013 ± 0.5 × 10^{-3}	0.34	0.0020
109.987	177.117	77.230	76.848	0.1155 ± 0.5 × 10^{-3}	0.44	0.0020
100.075	208.076	76.832	76.412	0.2363 ± 0.4 × 10^{-3}	0.58	0.0020
90.065	252.453	76.403	75.938	0.3663 ± 0.5 × 10^{-3}	0.78	0.0020
80.075	316.462	75.946	75.428	0.5045 ± 0.5 × 10^{-3}	1.08	0.0020
70.029	411.711	75.515	74.935	0.6526 ± 0.7 × 10^{-3}	1.52	0.0020
60.040	555.646	75.002	74.349	0.8111 ± 0.3 × 10^{-3}	2.18	0.0019
54.980	656.298	74.711	74.015	0.8598 ± 0.6 × 10^{-3}	2.65	0.0019

measurement of the isosteric heat of adsorption.[31] Using our equipment the random errors on k' measurements are smaller than 10^{-3} which is necessary for a significant determination of the mean value of the heat capacity change during adsorption in the temperature range studied.

The derivation of the coefficients α, β, γ for eq 26 or 27 has been carried out following the procedure described by Linnik[32] on a Univac 1108 computer, with double precision calculations. At the same time the random error made on the coefficient estimation is given[32] and the student t factor is chosen in such a way that the coefficients of eq 28 are known at a 95% confidence level.

It has to be noticed that the values of k' reported in Table II for n-pentane adsorbed on GTCB Sterling MTG have to be known with a very high precision but not necessarily the values of the retention volume V_A which is fortunate since the largest sources of error made on V_A measurements come from the determination of the geometrical volume V_G, and the surface area A.

TABLE III: Adsorption of Methane on Graphitized Thermal Carbon Black at 20° [a]

	V_A, cm^3/m^2	q_{st}, kcal/mol
Gas chromatography[b]	0.0064	3.11
From adsorption isotherm[c]	0.0100	2.9
From adsorption isotherm[d]	0.0082	3.03
This work, Sterling MTG	0.0054	3.49 ± 0.02
This work, Sterling FTG H_2 treated	0.0071	3.31 ± 0.01

[a] Comparison between data from the literature extrapolated at 20° and our experimental results. [b] Reference 15. [c] Reference 34. [d] Reference 35.

Experimental Section

1. Chromatographic Equipment. The chromatographic equipment specially designed for high precision measurements has been described previously.[31]

The column is in an oil bath. Its temperature is controlled within 0.01° per day. The flame ionization detector is connected to a buffer gas tank in which the pressure (ca. 1100 mbar) is controlled within 0.3 mbar. This is the column outlet pressure. The inlet pressure is controlled by a Texas Instruments pressure controller, working with reference to the outlet pressure, with fluctuations smaller than ±0.015 mbar.

The gas volumes outside the column have been kept as small as possible by design. The volumes of these tubings, between sampling valve and column, and between column and detector, are estimated to be both about 20 µl.

The columns (i.d. 2 mm) were filled with graphitized thermal carbon black previously sieved (160–200-µ fraction). Sterling MTG (surface area 8.7 m^2/g) and Sterling FTG (surface area 12.7 m^2/g) have been kindly supplied by Dr. W.R. Smith (Cabot. Co, Boston). Sterling FTG, hydrogen treated at 1000° (surface area 12.5 m^2/g), was obtained by courtesy of Dr. F. Bruner (Analytical Chemistry Institute, Rome University). The surface was measured using the BET method.

The Sterling MTG sample and the hydrogen treated Sterling FTG sample were packed in a 2-m long column while the Sterling FTG sample graphitized by Cabot was used to fill a 50-cm long column. The carrier gas was ultrahigh-purity helium purchased from Air Liquide (O_2 < 1 Vpm and H_2O < 2 Vpm). Before entering the column the carrier gas flows through a Molecular Sieve 5 A trap at room temperature. Great care is taken to prevent diffusion of oxygen into the instrument which is carefully purged before heating the column.

A Carlo Erba liquid sampling valve is used to inject a 2-µl gas sample of a mixture of methane and the vapor of the compound studied diluted in helium. The sample size is approximately 0.1 µg. The starting time of the injection is known with an accuracy of 30 msec;[31] its time width has no influence on the component retention time.

The detector signal is recorded on punched tape at the maximum speed of 5 data per second. The data are then handled on a Hewlett-Packard computer which calculates the different moments of the chromatographic elution peak. Retention times are defined as the mass center of the elution peak.

Peaks are fairly symmetrical due to the high homogeneity of the GTCB adsorbent and can be classified in category 1 of Guiochon and Goedert's simulation treatments.[33]

2. Determination of the Retention Time of the Unretained Compound. To determine the gas hold-up time, t_0, i.e., the retention time of an unretained compound, we need a suitable tracer. Methane has been used since it is the least adsorbed gas which gives a signal with the flame ionization detector. Methane time is not however equal to t_0, and a correction is necessary.

Its value can be estimated from different literature data. Static measurements of the adsorption of methane on GTCB have been made.[34,35] The values V_A reported in Table III are extrapolated at 20° from the values of $K_HRT = \lim_{p\to 0} V_{ex}/A$ at different temperatures reported in these papers.

The retention volume per unit surface area of methane has been measured by gas chromatography.[15] The value extrapolated at 20° is also reported Table III. For our calcu-

TABLE IV: Influence of the Corrections on the Thermodynamic Functions Measured for *n*-Pentane Adsorbed on GTCB Sterling MTG

Correction applied	k' at 100°	$\overline{q_{st}}$, kcal/mol	$\overline{\Delta C_p}$, cal/mol °K	Observation	Cor no.
Bulk results no correction	1.712	8.831 ± 0.042	5.79 ± 0.50		0
Correction for methane retention	1.727	8.837 ± 0.046	6.25 ± 0.50		1
Correction 1 + correction for nonideality of the gas phase	1.719	8.838 ± 0.046	6.29 ± 0.50		2
Correction 1 + correction for random temperature fluctuations (±0.01°)	1.727	8.837 ± 0.046	6.25 ± 0.50	Simulation treatment	3
Correction 1 + correction for a +0.1° deviation from the exact temperature	1.732	8.842 ± 0.046	6.26 ± 0.50	Simulation treatment	4
Corrections for $V'_i = V'_d = 20\ \mu l$, $\Delta t = 415$ msec, $\tau = 200$ msec	1.741	8.837 ± 0.046	6.25 ± 0.50	Simulation of correction for instrumental errors on retention times	5
Corrections for $V'_i = V'_d = 100\ \mu l$, $\Delta t = 2072$ msec, $\tau = 200$ msec	1.779	8.837 ± 0.046	6.25 ± 0.50	Simulation of correction for instrumental errors on retention times	6
Corrections for $V'_i = V'_d = 100\ \mu l$, $\Delta t = 2072$ msec, $\tau = 500$ msec	1.786	8.838 ± 0.046	6.25 ± 0.50	Simulation of correction for instrumental errors on retention times	7

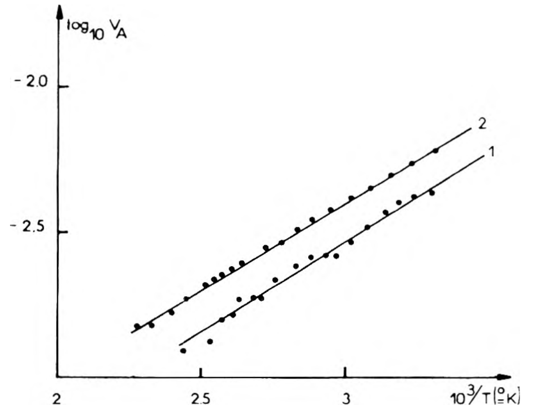

Figure 1. Variation with temperature of the specific retention volume of methane on GTCB (cm^3/m^2): (1) Sterling MTG, $R \ln k_m' = -18.068 + 2885/T$; (2) Sterling FTG, H_2 treated, $R \ln k_m' = -13.091 + 2727/T$.

lations, however, we need not only the retention time of methane, t_m, but also its ratio to the time of an unretained compound t_0 and literature data can only give an estimation of this ratio. To carry out this measurement, the flame ionization detector is changed for a catharometer detector and hydrogen is used as carrier gas. Helium is not retained on graphite at the temperature of the experiments as shown by Steele's statistical thermodynamic calculations.[4] Our experimental results are also reported in Table III. They are in excellent agreement with the data derived from the literature.

Figure 1 shows for each column the variation of the specific retention volume of methane, V_A, with temperature. V_A is proportional to the capacity factor for methane k_m'.

The differential energy of adsorption is calculated by a least-squares fit of the experimental data ($\ln k_m'$ vs. $1/T$) to a linear equation. The isosteric heat of adsorption reported in Table III is derived.

This regression analysis shows that the relative random error made on k_m' estimation at the 95% confidence level calculated from the relative standard deviation is 0.5% on the Sterling FTG H_2 treated sample and 2% on the Sterling MTG sample, because the difference ($t_m - t_0$) is 2.2 sec at 100° with the first sample of larger area and only 0.2 sec with the second one. A computer simulation treatment shows that the resulting absolute errors on $\overline{\Delta C_p}$ at a 95% confidence level, occurring from the errors on k_m' are ±0.03 cal/mol for the Sterling MTG sample and for the hydrogen treated Sterling FTG sample. With the untreated Sterling FTG GTCB sample the value of methane correction has been extrapolated from the value measured on the H_2 treated sample. The question arises of the validity of methane retention measurement with hydrogen carrier gas. At 20°, using the method described by Steele[4] the value of the specific retention volume calculated for hydrogen on graphite, $V_A = B_{AS}/A$, is 4×10^{-4} cm^3/m^2, only a factor of 10 lower than the specific retention volume of methane at the same temperature.

TABLE V: Thermodynamic Functions of Adsorption of Benzene and *n*-Pentane on Graphitized Thermal Carbon Black

Adsorbate	GTCB sample	$\overline{q_{st}}$, kcal/mol	b, kcal/mol	$\overline{\Delta C_p}$, cal/mol °K
Benzene	Sterling MTG	9.78 ± 0.07	12.9 ± 0.1	8.1 ± 0.3
	Sterling FTG	9.98 ± 0.05	12.3 ± 0.1	5.8 ± 0.2
	H_2 treated Sterling FTG	9.83 ± 0.05	12.2 ± 0.2	6.0 ± 0.6
n-Pentane	Sterling MTG	8.84 ± 0.03	11.1 ± 0.2	6.2 ± 0.5
	Sterling FTG	8.88 ± 0.04	10.8 ± 0.2	5.2 ± 0.7
	H_2 treated Sterling FTG	8.83 ± 0.06	11.5 ± 0.2	7.2 ± 0.6

With an average absolute pressure of 2 atm in the gas chromatographic column, 2.6×10^{-7} mol/m^2 of hydrogen are adsorbed.

Assuming the hydrogen molecule occupies an area of 12 Å^2, the reduction of the total surface area available because of hydrogen adsorption is 2% at 20° and approximately 1% at 100°. This results in the same reduction of the experimental k_m' value compared to the theoretical one. This change is of the same order of magnitude as the relative error made in k_m' measurements, so that hydrogen adsorption is negligible here.

When the flame ionization detector is used, the retention time of the unretained compound is calculated from the methane retention time by

$$t_0 = \frac{t_m}{1 + k_m'} \tag{29}$$

At each temperature k_m' is derived from the equation given in Figure 1, previously established for the corresponding column. The data in Table IV shows that the correction made for the retention of methane on graphitized thermal carbon black is significant. For instance, bulk results give $\overline{\Delta C_p}$ = 5.79 cal/mol °K for *n*-pentane on Sterling MTG while the corrected value is $\overline{\Delta C_p}$ = 6.25 cal/mol °K.

3. Instrumental Errors. The question of instrumental errors has already been discussed at length by Goedert and Guiochon.[31] We deal only with its influence on the measurements of $\overline{\Delta C_p}$ and of the isosteric heat of adsorption.

Goedert and Guiochon[36] have shown that a temperature gradient of ±0.01° introduces a relative error of about 10^{-5} on the determination of k' for a coiled column 2-m long with a 10-cm coil diameter. This error is smaller by a factor of 50 than the average error made on k' measurements themselves. The influence of average fluctuations of ±0.01° on $\overline{\Delta C_p}$ and $\overline{q_{st}}$ measurements are reported in Table IV and are insignificant. These values have been obtained from a simulation test reproducing the temperature fluctuations which have been introduced into the program of determination of the coefficients of eq 26.

Another simulation test reported in Table IV shows that the corrected $\overline{\Delta C_p}$ values are influenced very little by the lack of accuracy of the temperature measurements. Periodic calibration by the Conservatoire National des Arts et Métiers, Paris, shows that they are accurate within 0.05°. Table V shows that a systematic error of +0.1° changes $\overline{\Delta C_p}$ by only 0.5%, much less than the average error of the measurement.

Two systematic errors appear during the measurement of the retention time: the time constant τ of the electronic system and the time spent in the dead volume of the instrument, Δt. The corrections should be applied only to the denominator term of k', as they cancel by difference in the numerator term $(t_R - t_0)$.

The dead volumes of the instrument are the volumes between the sampling valve and the column inlet, V_i, and between the column outlet and the detector, V_d.[31] Both volumes have been designed to be as small as possible; they are estimated at about 20 µl from geometrical considerations. The corresponding correction is

$$\Delta t = \frac{1}{D_c}\left(\frac{P_i}{P_o}V_i + V_d\right) \tag{30}$$

where D_c is the flow rate at column outlet pressure.

Combining eq 20 and 30, we have

$$\Delta t = \frac{jt_0}{V_G}\left(\frac{P_i}{P_o}V_i + V_d\right) \tag{31}$$

V_G is measured once for each column from flow rates and unretained retention times measurements using eq 20.

Whenever the retention time is measured from the peak first moment, the correction for the detector time constant is to substract this time constant. A larger time constant results in a larger signal-to-noise ratio and a more precise time measurement, but, on the other hand, the time constant cannot be accurately measured and even the concept of time constant for real detectors and amplifiers is an oversimplification.[31,33] A compromise is thus necessary and a value of 200 msec has been selected.

In Table IV it is seen that these corrections for systematic instrumental errors do not result in any appreciable change of either the $\overline{\Delta C_p}$ value or the mean value of the isosteric heat of adsorption. Different simulation tests have been carried out using corrections corresponding to highly improbable values, such as, V_i = V_o = 100 µl and a time constant of 500 msec. q_{st} remains unchanged while the increase in $\overline{\Delta C_p}$ is less than 1%. The reason is that these corrections merely result in a proportional change of k', thus shifting the ln k' vs. $1/T$ graph without modifying the temperature dependence.

Consequently, even at the level of accuracy presently obtained, only the correction for methane retention, which is temperature dependent, is meaningful as far as $\overline{\Delta C_p}$ measurements are concerned.

Results

Table II lists the experimental results of the measurements of retention times of *n*-pentane on the GTCB Sterling MTG sample. At each of the eight different experimental temperatures, six injections of the same mixture of adsorbate vapor and methane were made. The mean value of k' at each temperature is listed and used in further treatment. A total of 48 experimental data is thus used for each system. The successive measurements of each series were carried out by decreasing the temperature. A final measurement was then made at the highest temperature to

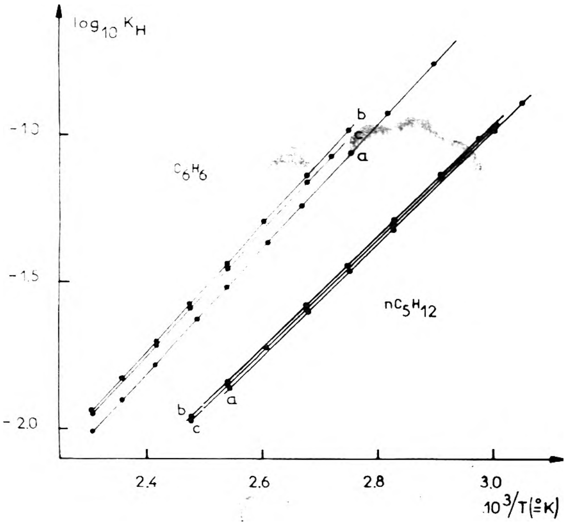

Figure 2. Variation with temperature of the Henry adsorption coefficient (μmol/m² mmHg) of *n*-pentane and benzene adsorbed on GTCB: (a) Sterling MTG; (b) Sterling FTG; (c) Sterling FTG H_2 treated.

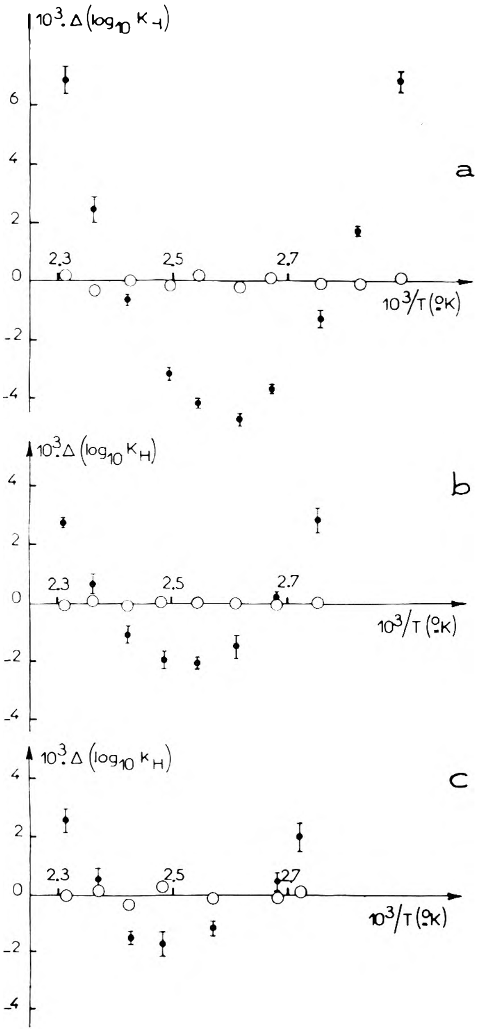

Figure 3. Deviation of the experimental values of log K_H for benzene from linear dependence on the reverse of the temperature (solid points) and from a fit on eq 15 (open circles): (a) Sterling MTG; (b) Sterling FTG; (c) Sterling FTG H_2 treated. The vertical line represents the relative standard deviation interval for each temperature. It is the same for the solid points or the open circles.

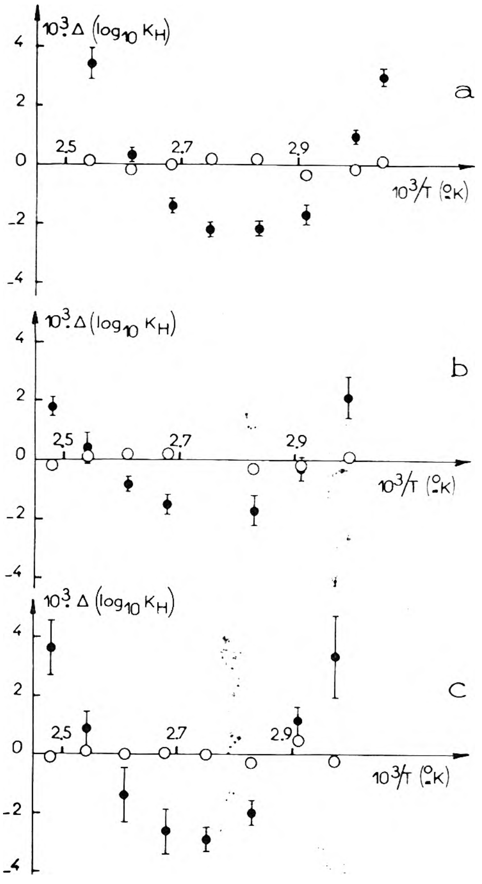

Figure 4. Same as Figure 3 except for *n*-pentane.

check that the k' value has not changed during the whole thermal treatment. The standard deviation of the measurement of log k' is between 2 and 5 × 10^{-4} (cf. Figures 3 and 4).

Figure 2 shows the variation of the Henry adsorption coefficient per unit surface area with the temperature, adsorbed on the three GTCB samples for benzene and *n*-pentane. At first glance it seems that the graph log K_H vs. $1/T$ could be well fitted by a straight line. The importance of the systematic deviations $\Delta(\log K_H)$ between the experimental data and the result of a straight line fit is demonstrated in Figure 3 for benzene and Figure 4 for *n*-pentane (solid points). They are much larger than the relative standard deviation reported on these graphs for each experimental point. The deviations between experimental data and the result of a least-squares fit on eq 15 (circles in Figures 3 and 4) are smaller than the errors and scattered around zero.

The values of the coefficients derived from the least-squares fit of the experimental results in eq 15 are given in Table V. The larger random errors made on the measurements of log k' with the Sterling FTG H_2 treated sample explain the larger error made on the mean value of the heat capacity change during adsorption, $\overline{\Delta C_p}$ (cf. Table V). The random errors made on $\overline{\Delta C_p}$ measurements are usually about 5–10% but when experimental conditions are favorable as with benzene on the Sterling MTG or Sterling FTG samples, the precision of the $\overline{\Delta C_p}$ measurement is very good (2.5%). In Table V is also reported the mean value of the isosteric heat of adsorption q_{st} in the range of temperature studied, for the sake of comparison with measurements previously published. This value is obtained by fit-

TABLE VI: Influence of Sample Size on the Retention of Benzene and *n*-Pentane on Graphitized Thermal Carbon Black

Adsorbent	Adsorbate	Amount injected, μg	k'	rsd
Sterling MTG	n-Pentane	0.360	1.001	1.1×10^{-3}
	120.07°	0.150	1.001	1.1×10^{-3}
		0.030	0.993	1.9×10^{-3}
	Benzene	0.250	0.855	0.4×10^{-3}
	160.03°	0.200	0.860	0.6×10^{-3}
		0.060	0.860	7×10^{-3}
H_2 treated Sterling FTG	n-Pentane	0.240	5.773	1.3×10^{-3}
	129.7°	0.100	5.775	1.0×10^{-3}
		0.030	5.792	2.3×10^{-3}
	Benzene	0.0100	6.342	1.0×10^{-3}
	160.05°	0.065	6.345	1.5×10^{-3}
		0.015	6.391	5.0×10^{-3}

ting a straight line through the experimental points. For each temperature the isosteric heat of adsorption can be calculated from b and $\overline{\Delta C_p}$ values using eq 14.

a. Influence of the Adsorption Isotherm Curvature. Table VI shows the influence of sample size on k' value and therefore on the retention volume V_A which is directly proportional to k'. The effect of sample size is negligible as the variations in k' are of the same magnitude than the errors of measurements. It can be assumed that the adsorption isotherm is linear for the compounds studied in the temperature range of the experiment. During all this work, the amount injected in the column was approximately 0.1 μg. We shall estimate the corresponding surface coverage for benzene on the graphitized thermal carbon black sample.

The maximum concentration in the gas phase at the column outlet is given by the following eq[16]

$$n_g^M = m\sqrt{N}/V_R\sqrt{2\pi} \tag{32}$$

where m is the amount injected, N the number of theoretical plates, and V_R the retention volume. The maximum surface concentration n_a^M in the adsorbed phase is thus

$$n_a^M = n_g^M k' V_R / A(1 + k') \tag{33}$$

Therefore the maximum surface concentration at column outlet is directly related to the amount injected in the column by the relation

$$n_a^M = m\sqrt{N}k'/A\sqrt{2\pi}(1 + k') \tag{34}$$

With the 2-m long column of Sterling MTG at 160° the maximum density of benzene molecules adsorbed at the column outlet is thus $n_a^M = 0.3 \times 10^{-3}$ μmol/m^2 which corresponds to 10^{-4} of a monolayer. For Sterling FTG, we have $n_a^M = 0.1 \times 10^{-3}$ μmol/m^2 (ca. 3×10^{-5} of a monolayer).

Near the inlet, these values are larger but at 2 cm from the column inlet, they are only a factor of 10 larger. Equation 32 shows that n_a^M is inversely proportional to the square root of the column length.[12]

This shows that in our gas chromatographic experiments the adsorption phenomenon is studied in a range of surface coverage 100 times lower than the lowest coverage attainable in static experiments.

The adsorbate–adsorbate interactions are characterized by the value of the two-dimensional second virial coefficient B_{2D} of eq 10. The value of B_{2D} can be calculated from the experimental data of Ross and Olivier[37] for benzene adsorbed on graphitized thermal carbon black. The value of B_{2D} (-4.5×10^4 m^2/mol) is easily derived from the model they adopted for the two-dimensional equation of state and the isotherm at low surface coverage.

The corrective term of eq 11 expressing the influence of adsorbate–adsorbate interactions is thus $2B_{2D}n_a = -2.7 \times 10^{-5}$ for the Sterling MTG column and $2B_{2D}n_a = -0.9 \times 10^{-5}$ for the H_2 treated Sterling FTG column.

Adsorbate–adsorbate interactions are thus completely negligible in our gas chromatographic experiments. Blu, Jacob, and Guiochon[29] arrived at the same conclusion for the system n-heptane–graphitized carbon black.

We shall notice here the very good agreement between the static measurements of Ross and Olivier[37] and the chromatographic data for benzene adsorbed on graphitized thermal carbon black (cf. Table VII). At 49.6° the value of the Henry constant derived from Ross and Olivier's experimental results is 0.52 μmol/(m^2 mmHg). The values of the Henry constant extrapolated at this temperature from gas chromatographic retention data are 0.58 and 0.49 μmol/(m^2 mmHg) on the Sterling FTG and Sterling MTG samples, respectively.

b. Contribution of the Gas-Phase Nonideality to the Measurements. We have already shown that helium which is used as carrier gas is not adsorbed on graphitized thermal carbon black. The only possible influence of the carrier gas on the retention is thus the nonideal behavior of the gas phase, accounted for by the last term of eq 10.

The second virial coefficient, B_{12}, for the interactions between the solute vapor and helium has been calculated using the method described by Hirschfelder, Curtiss, and Bird.[39] At 100° B_{12} is 31.0 cm^3/mol for the system n-pentane–helium and 22.0 cm^3/mol for the system benzene–helium. The corrective term of eq 10, $(2B_{12}P_o/RT)j_3{}^4$, is thus about 2×10^{-3} under the present experimental conditions.

The corrective term e_2 in eq 11 is significant when applied to the capacity factor k' which is determined with a relative precision of 0.5×10^{-3} (cf. Table II) but it is not so for the absolute values of the specific retention volume V_A, because the largest sources of errors made in this case originates in the measurements of the geometric gas volume V_G, and of the surface areas.

As regards to the determination of the adsorption change of the heat capacity, however, it is only the variation of the corrective term with temperature which is important. In the temperature range of measurements, 90–160° for benzene and 60–130° for n-pentane, the variation of the corrective term with temperature is at least a factor of 5 smaller than the measurement errors on ln k'. The value of $\overline{\Delta C_p}$ is only 0.5% larger when the correction for gas-phase nonideality is made. The gas phase can thus be considered as ideal.

Discussion

Gas chromatography has been made accurate enough to permit the measurement of the temperature dependence of the thermodynamic functions of adsorption at zero surface coverage. Furthermore we have shown that the corrections for nonideal behavior of the molecule in both the adsorbed and gas phases are negligible.

The isosteric heat of adsorption and the Henry adsorption coefficients extrapolated at 20 and 49.5° from our gas chromatographic experiments are reported in Table VII. These data are compared with those available in the litera-

TABLE VII: Comparison between the Results of the Gas Chromatographic and Static Methods (Benzene Adsorption on Graphitized Thermal Carbon Black)

	T, °C	K_H, μmol/m²·mmHg	q_{st}, kcal/mol
Sterling MTG	100	0.060	9.9
(this work)	49.6[a]	0.49	10.3
	20[a]	2.57	10.5
Sterling FTG	100	0.073	10.1
(this work)	49.6[a]	0.62	10.4
	20[a]	3.30	10.6
Sterling FTG	100	0.070	10.0
H_2 treated	49.6[a]	0.58	10.3
(this work)	20[a]	3.01	10.4
Ref 37[b]	49.6	0.52	9.25[b]
Ref 38[b]	20	3.59	10.2[b]

[a] Experimental data extrapolated at lower temperature. [b] Experimental data extrapolated for zero surface coverage.

ture and obtained from the static adsorption measurements extrapolated to zero surface coverage.

The isosteric heat of adsorption measured by gas chromatography agree well with the experimental results of Isirikyan and Kiselev[38] and also with the isosteric heat of adsorption (10.0 kcal/mol) measured by Pierotti and Smallwood[40] for benzene adsorbed on GTCB Sterling FT. This last value is also extrapolated to zero surface coverage from static adsorption isotherm experiments. All the above experiments are in disagreement with Ross and Olivier's value of 9.25 kcal/mol.[37]

For the adsorption Henry coefficient K_H our results on Sterling MTG are much lower than on Sterling FTG, but in better agreement with the experiments of Ross and Olivier. The adsorption coefficient on the Sterling FTG sample is closed to that measured on the Sterling FTG H_2 treated sample. The difference may be explained from measurement errors in the surface area of both sample using the BET method.

Good agreement is observed between our results on the Sterling FTG sample and those of Isirikyan and Kiselev obtained on different samples of graphitized thermal carbon black. It is thus significant to compare our measurement of the heat capacity change during adsorption of benzene on GTCB with that obtained from calorimetric measurements by Berezin and Kiselev.[9,10]

These authors have measured the average molar heat capacity, C_a, of benzene adsorbed on thermal graphitized carbon black for surface coverages between 1 and 15 μmol/m². At the lowest surface coverage the error made on C_a is 11%.[41] The lowest surface coverage attainable in the calorimetric measurement is thus more than a factor of 10^3 larger than the one at which the gas chromatographic measurement is carried out. The value extrapolated at zero surface coverage is C_a = 24 cal/mol °K.

This extrapolation is valid as long as adsorbate–adsorbate interactions are weak, as demonstrated by Berezin and Kiselev.[10] This is in agreement with a previous result by Pierce and Ewing.[42] The adsorption isotherms of benzene are concave to the pressure axis at low coverage; the heat of adsorption does not increase with increasing surface coverage as expected when lateral interactions take place in the first layer of molecules as with most other adsorbates such as *n*-pentane.

The limiting value of the molar heat capacity of benzene vapor at zero pressure, C_p = 18.37 cal/mol °K is calculated from the molar heat capacity of benzene under atmospheric pressure $C_p^{1\,\text{atm}}$ = 19.25 cal/mol °K,[43] according to the following equation[44]

$$C_p = C_p^{1\,\text{atm}} + TP\frac{d^2B}{dT^2} \tag{35}$$

The second derivative of the benzene virial coefficient B with respect to the temperature was calculated from the experimental data compiled in ref 45.

The adsorption change in the heat capacity of benzene at 20°, ΔC_p, obtained from calorimetric measurements on a GTCB of high surface area (S = 29 m²/g) is thus 5.6 ± 2 cal/mol °K. This value is in good agreement with that measured in this work on the Sterling FTG samples. It is also very close that calculated by Pierotti and Smallwood[40] from the adsorption isotherms of benzene adsorbed on Sterling FTG (2700°). As expected, $\overline{\Delta C_p}$ did not change with surface coverage and was found to be 5.5 ± 0.5 cal/mol °K.

On the Sterling MTG sample the heat capacity change measured is higher than on the Sterling FTG samples ($\overline{\Delta C_p}$ = 8.1 ± 0.3 cal/mol °K) and the mean value of the isosteric heat of adsorption lower (Table V). Table VII shows also that the adsorption Henry coefficient is much smaller than the one on the Sterling FTG samples. This may indicate that this GTCB of lower surface area possesses a different surface structure. Within the limits of errors the heat capacity change during adsorption $\overline{\Delta C_p}$ measured for *n*-pentane is the same on the two untreated Sterling samples. It is higher with the hydrogen treated Sterling FTG. The mean values of the isosteric heat of adsorption of *n*-pentane are however very close for the three samples studied (Table V).

The values of the heat capacity change during adsorption for *n*-pentane on GTCB at zero surface coverage are unique. They cannot be obtained using the conventional methods of measurements. When adsorbate–adsorbate interactions cannot be neglected even at moderate surface coverages, which is the case for most organic compounds on graphitized thermal carbon black,[42] the molar heat capacity cannot be extrapolated to zero surface coverage. This is true for *n*-pentane whose adsorption isotherm has the normal convex shape in the low-pressure region[6] indicating that lateral interactions increase with increasing surface coverage.

High-precision gas chromatography thus allows the study of the adsorption change of the heat capacity at zero surface coverage and the comparison with the value derived from statistical thermodynamics.

The mean value of the heat capacity change during adsorption of benzene on graphite calculated with the model of eq 1 is 4.4 cal/mol °K in the temperature range investigated (cf. Table I). This is 1 cal/mol °K lower than the value found in our experiments (Table V) which shows that the model used to calculate the adsorption potential has to be refined. In fact, as we have shown earlier, when using the adsorption potential given by eq 4 it is not possible to predict correctly the relative retentions of phenanthrene and anthracene[5] or that of *cis*-2-butene and *trans*-2-butene.[16]

However, the very close values of $\overline{\Delta C_p}$ obtained for benzene and n-pentane on GTCB Sterling FTG proves that the adsorption behavior of both molecules on the homogeneous surface of graphitized thermal carbon black is very similar when adsorbate–adsorbate interactions are negligible.

Accurate gas chromatography opens a new field of studies in adsorption.

Acknowledgment. The authors gratefully acknowledge Mr. Jean-Pierre Olivo for his technical assistance in this work.

References and Notes

(1) T. L. Hill, *J. Chem. Phys.*, **14**, 441 (1946).
(2) A. V. Kiselev and D. P. Poshkus, *Trans. Faraday Soc.*, **59**, 176, 428, 1438 (1963).
(3) D. P. Poshkus, *Discuss. Faraday Soc.*, **40**, 195 (1965).
(4) W. A. Steele, "The Solid Gas Interface," E. A. Flood, Ed., Marcel Dekker, New York, N.Y., 1967, Chapter 10.
(5) C. Vidal-Madjar and G. Guiochon, *Bull. Soc. Chim. Fr.*, 3110 (1971).
(6) N. N. Avgul and A. V. Kiselev, "Chemistry and Physics of Carbon," Vol. 6, P. L. Walker, Ed., New York, N.Y., 1970, p 1.
(7) W. R. Smith, "Encyclopedia of Chemical Technology," Vol. 4, 2nd ed, Interscience, New York, N.Y., 1964, pp 243–278.
(8) E. L. Pace, "The Solid Gas Interface," Vol. 1, E. A. Flood, Ed., Marcel Dekker, New York, N.Y. 1967, Chapter 4.
(9) G. I. Berezin and A. V. Kiselev, *J. Colloid Interface Sci.*, **22**, 161 (1966).
(10) G. I. Berezin, A. V. Kiselev, R. T. Sagatelyan, and V. A. Sinitsyn, *J. Colloid Interface Sci.*, **38**, 335 (1972).
(11) S. Ross, J. K. Saelens, and J. P. Olivier, *J. Phys. Chem.*, **66**, 696 (1962).
(12) R. L. Gale and R. A. Beebe, *J. Phys. Chem.*, **68**, 555 (1964).
(13) P. A. Elkington and G. Curthoys, *J. Phys. Chem.*, **73**, 2321 (1969).
(14) A. V. Kiselev, "La chromatographie gaz-solide," Masson et Cie, Paris, 1969.
(15) E. V. Kalaschnikova, A. V. Kiselev, R. S. Petrova, and K. D. Shcherbakova, *Chromatographia*, **4**, 495 (1971).
(16) M. F. Gonnord, C. Vidal-Madjar, and G. Guiochon, *J. Colloid Interface Sci.*, to be published.
(17) W. A. Steele and G. D. Halsey, *J. Phys. Chem.*, **59**, 57 (1955); *J. Chem. Phys.*, **22**, 979 (1954).
(18) J. A. Barker and D. H. Everett, *Trans. Faraday Soc.*, **58**, 1608 (1962).
(19) N. N. Avgul, A. V. Kiselev, I. A. Lygina, and D. P. Poshkus, *Dokl. Akad Nauk SSSR, Otd. Khim. Nauk*, 1196 (1959).
(20) N. N. Avgul, A. A. Isirikyan, A. V. Kiselev, I. A. Lygina, and D. P. Poshkus, *Dokl. Akad. Nauk SSSR, Otd. Khim. Nauk*, 1314 (1957).
(21) D. M. Young and A. D. Crowell, "Physical Adsorption of Gases," Butterworths, London, 1962.
(22) R. M. Barrer, *Proc. Roy. Soc.*, **161**, 476 (1937).
(23) A. V. Kiselev, D. P. Poshkus, and A. Y. Afreimovich, *Russ. J. Phys. Chem.*, **42**, 1345 (1968).
(24) C. Vidal-Madjar, L. Jacob, and G. Guiochon, *Bull. Soc. Chim. Fr.*, 3105 (1971).
(25) W. A. Steele, *Surface Sci.*, **39**, 149 (1973).
(26) D. C. Locke, *J. Phys. Chem.*, **69**, 3768 (1965).
(27) D. H. Everett, *Trans. Faraday Soc.*, **61**, 1637 (1965).
(28) G. Blu, G. Guiochon, and L. Jacob, *Bull. Centre Rech. Pau, SNPA*, **4**, 485 (1970).
(29) G. Blu, L. Jacob, and G. Guiochon, *J. Chromatogr.*, **61**, 207 (1971).
(30) Y. Y. Huang, *J. Catal.*, **25**, 131 (1972).
(31) M. Goedert and G. Guiochon, *Anal. Chem.*, **45**, 1188 (1973).
(32) Y. V. Linnik, "Méthode des moindres carrés," Dunod, Paris, **1963**, p 170.
(33) M. Goedert and G. Guiochon, *Chromatographia*, **6**, 116 (1973).
(34) N. N. Avgul, A. G. Bezus, E. S. Dobrova, and A. V. Kiselev, *J. Colloid Interface Sci.*, **42**, 486 (1973).
(35) G. Constabaris, J. R. Sams, and G. D. Halsey, *J. Phys. Chem.*, **65**, 367 (1961).
(36) M. Goedert and G. Guiochon, *Anal. Chem.*, **45**, 1180 (1973).
(37) S. Ross and J. P. Olivier, "On Physical Adsorption," Interscience, New York, N.Y., 1964, p 239.
(38) A. A. Isirikyan and A. V. Kiselev, *J. Phys. Chem.*, **65**, 601 (1961).
(39) J. O. Hirschfelder, C. F. Curtiss, and R. B. Bird, "Molecular Theory of Gases and Liquids," Wiley, New York, N.Y., 1954.
(40) R. A. Pierotti and R. E. Smallwood, *J. Colloid Interface Sci.*, **22**, 469 (1966).
(41) A. V. Kiselev and V. P. Dreving, "Experimental Methods of Adsorption and Chromatography," Moscow, 1973, p 186, in Russian.
(42) C. Pierce and B. Ewing, *J. Phys. Chem.*, **71**, 3408 (1967).
(43) G. W. C. Kaye and T. H. Laby, "Tables of Physical and Chemical Constants," 11th ed, Longmans Green and Co. London, 1956.
(44) E. A. Guggenheim, "Thermodynamics," North Holland Publishing Co, Amsterdam, 1957, p 113.
(45) J. H. Dymond and E. B. Smith, "The Virial Coefficient of Gases," Clarendon Press, Oxford, 1969.

A New Example of Formal Non-Steady-State Kinetics. A Model of Heterogeneous Atom Recombination

W. Brennen* and M. E. Shuman

Department of Chemistry and Laboratory for Research on the Structure of Matter, University of Pennsylvania, Philadelphia, Pennsylvania 19174 *(Received August 19, 1974)*

Publication costs assisted by the National Science Foundation

Solutions to the rate equations governing the kinetics of a simple adsorption–abstraction mechanism for the heterogeneous recombination of atoms are examined in detail and compared to a description of the same mechanism based on the steady state hypothesis.

Introduction

Textbook illustrations of the phenomenological description of the time history of reactants, intermediates, and products in "complex," i.e., two or more step, reactions are ordinarily confined to Harcourt and Esson's classic, sequential first-order reaction scheme, A → B → C,[1] or to one or another of its close relatives which include more first-order steps and/or one or more of the reverse processes.[2-7] All other mechanisms are dealt with using the steady state hypothesis. The reason for this is that even two-step mechanisms in which one or both steps are second-order reactions usually lead to unwieldy solutions expressed in terms of higher functions, if explicit solutions may be had at all.[8-10]

In conjunction with an experimental investigation of the surface recombination of nitrogen atoms, we have been led to explore the behavior of a two-step mechanism which is at once conceptually transparent and mathematically manageable. We believe that a close scrutiny of this example will prove rewarding to any student of chemical kinetics, and we are confident that the insights afforded by this simple model will prove useful in the analysis of surface kinetics experiments.

Results and Discussion

Mechanism and Rate Equations. The physical picture is closely related to the Langmuir–Rideal mechanism for the recombination of atoms at active surface sites.[11,12] Suppose, ad arguendo, that the active sites are initially empty. An atom, N, approaching the surface from the gas phase may strike an empty site, E, and stick, creating a filled site, F. Subsequently, another atom may strike the filled site, combine with the atom adsorbed there to form the molecule N_2, which departs, regenerating an empty site. This mechanism may be written as follows:

$$\mathrm{N} + \mathrm{E} \xrightarrow{k_1} \mathrm{F} \tag{1}$$

$$\mathrm{N} + \mathrm{F} \xrightarrow{k_2} \mathrm{N_2} + \mathrm{E} \tag{2}$$

We wish to draw attention to the absence of the reverse of reaction 1. This is an important simplification, without which our method of dealing with the mechanism would fail. Physically, this omission amounts to assuming a long adsorption lifetime compared to $(k_2N)^{-1}$, the pseudo-first-order lifetime of a filled site with respect to abstraction.

It is convenient to define the following quantities: let S be the total concentration of active sites, empty plus filled, i.e., $S = E + F$; let $\rho = k_2/k_1$, and $R = S/N_0$, where N_0 is the initial concentration of atoms. The dimensional awkwardness of dealing with atom concentrations in units cm^{-3} and surface active site concentrations in units cm^{-2} may be side-stepped by taking the surface-to-volume ratio to be unity and simply speaking of the *numbers* of atoms and sites.

The differential equations governing the kinetics of our mechanism are

$$-\mathrm{d}N/\mathrm{d}t = k_1NE + k_2NF = (k_1 - k_2)NE + k_2NS \tag{3}$$

$$-\mathrm{d}E/\mathrm{d}t = k_1NE - k_2NF = (k_1 + k_2)NE - k_2NS \tag{4}$$

Introducing the reduced variables, $\hat{N} = N/N_0$, $\hat{E} = E/S$, $\theta = k_1N_0t$, and the parameters R and ρ defined above, eq 3 and 4 become

$$-\frac{1}{R}\frac{\mathrm{d}\hat{N}}{\mathrm{d}\theta} = (1 - \rho)\hat{N}\hat{E} + \rho\hat{N} \tag{5}$$

$$-\frac{\mathrm{d}\hat{E}}{\mathrm{d}\theta} = (1 + \rho)\hat{N}\hat{E} - \rho\hat{N} \tag{6}$$

Since $\hat{N}$ appears in both terms on the right side of both equations, we may proceed in the following way. Let $Z = \int_0^\theta \hat{N}\,\mathrm{d}\theta$, so that $\mathrm{d}Z/\mathrm{d}\theta = \hat{N}$ or $\mathrm{d}Z = \hat{N}\,\mathrm{d}\theta$. Then eq 5 and 6 become

$$-\frac{1}{R}\frac{\mathrm{d}\hat{N}}{\mathrm{d}Z} = (1 - \rho)\hat{E} + \rho \tag{7}$$

$$-\frac{\mathrm{d}\hat{E}}{\mathrm{d}Z} = (1 + \rho)\hat{E} - \rho \tag{8}$$

Equation 8 may be readily integrated, assuming $\hat{E} = 1$ at $\theta = 0$, to give the following expression describing the evolution of the relative number of empty sites:

$$\hat{E} = \frac{\rho}{1 + \rho} + \left(\frac{1}{1 + \rho}\right)e^{-(1+\rho)Z} \tag{9}$$

Putting this result into eq 7 and integrating yields an expression describing the decay of the relative number of atoms:

$$\hat{N} = 1 - \left(\frac{2\rho R}{1 + \rho}\right)Z - \frac{R(1 - \rho)}{(1 + \rho)^2}[1 - e^{-(1+\rho)Z}] \tag{10}$$

Equations 9 and 10 govern the kinetics in the event that the surface sites are initially empty, clearly a special case, which applies only to the first experiment with a virgin surface. For an arbitrary initial relative number of empty sites, $\hat{E}_0$, it is easy to show that eq 9 and 10 must be replaced by

$$\hat{E} = \frac{\rho}{1 + \rho} + \left[\hat{E}_0 - \frac{\rho}{(1 + \rho)}\right]e^{-(1+\rho)Z} \tag{11}$$

and

$$\hat{N} = 1 - \left(\frac{2\rho R}{1 + \rho}\right)Z - \frac{R(1 - \rho)}{(1 + \rho)}\left[\hat{E}_0 - \frac{\rho}{1 + \rho}\right][1 - e^{-(1+\rho)Z}] \tag{12}$$

Equations 10 and 12 express $\hat{N}(\theta)$ as a function of the quantity $\int_0^\theta \hat{N}(\theta)\,\mathrm{d}\theta$; that is, the value of $\hat{N}$ at any particular epoch, θ, depends in a complicated way on its entire previous history. Likewise, according to eq 9 and 11, the instantaneous value of $\hat{E}$ depends on the prior history of the relative number of atoms. These may not at first sight appear to be particularly illuminating results because we naturally wish to study the histories $\hat{N}(\theta)$ and $\hat{E}(\theta)$ themselves, and these are contained in the equations in highly implicit form. Fortunately, certain features of the problem may be discussed without having the actual time histories in hand, the histories may be obtained in explicit analytical form in special cases, and a simple numerical procedure can be devised to generate the time dependence of $\hat{E}$ and $\hat{N}$ for any case.

Steady-State Hypothesis. In the mechanism under discussion the role of intermediate may be assigned to the empty sites, which are destroyed in reaction 1 and formed in reaction 2. Accordingly, the canonical steady-state approach requires setting the derivative, $\mathrm{d}\hat{E}/\mathrm{d}\theta$, equal to zero in eq 6 and solving for the steady-state value of the relative number of empty sites thus

$$\hat{E}_s = \rho/(1 + \rho) \tag{13}$$

This result may then be substituted in eq 5 which, upon integration, gives the time dependence of $\hat{N}$ under steady-state conditions. The result is

$$\hat{N}_s = \exp[-2\rho R\theta/(1 + \rho)] \tag{14}$$

In the steady state the relative number of atoms declines exponentially with a pseudo-first-order rate constant equal to $2k_1S\rho/(1 + \rho)$.

It is natural to wonder about the circumstances, if any, in which an actual atom decay is correctly described by the results of the steady-state treatment or, more generally, what relation any actual decay history has to the steady-state result. A glance at eq 13 and 11 reveals that when $\hat{E}_0$, the initial number of empty sites, is exactly equal to the steady-state value, $\hat{E}$ remains constant at that value throughout the decay and eq 14 correctly describes the decay of atoms. For any other circumstances in general, $\hat{E}$ differs from the steady-state value throughout the decay, although it approaches nearer to $\hat{E}_s$ as the decay progresses, Z grows, and the second term in eq 11 declines in absolute magnitude. Note, however, that $\hat{E}$ is not asymptotic to $\hat{E}_s$ in a single decay because Z is not asymptotic to infinity. In general, the fraction of sites empty at the end of a decay will be different from $\hat{E}_s$, although for certain combinations of parameters the difference will be insignificantly small not only at the end of a decay but also for most of its duration. The fact that the value of $\hat{E}$ draws closer to $\hat{E}_s$ during a decay, regardless of its initial value, clearly implies that if a sufficiently long sequence of experiments is conducted, starting the first experiment with a surface on which all the active sites are initially empty, sooner or later the behavior of subsequent decays will be indistinguishable from that expressed by eq 13 and 14.

Initial and Final Rates. From the certain knowledge that both θ and Z are zero at the beginning of a decay, the relation d ln $\hat{N}/\mathrm{d}\theta = \mathrm{d}\hat{N}/\mathrm{d}Z$, and eq 12, we find

$$[\mathrm{d}\ln\hat{N}/\mathrm{d}\theta]_{\theta=0} = -R[\rho + \hat{E}_0(1-\rho)] \qquad (15)$$

This expression for the initial logarithmic decay slope will later prove to be useful for initiating the numerical procedure for computing decay histories. By setting $\hat{E}_0$ in eq 15 equal to $\rho/(1+\rho)$, the steady-state value, agreement with eq 14 may be readily confirmed. The logarithmic decay slope at any time, θ, is given by eq 15 if $\hat{E}_0$ is replaced by $\hat{E}(\theta)$.

In order to learn about the behavior of a general decay in its final stages it is necessary to ascertain the asymptote approached by the quantity Z at $t = \infty$, call it Z_∞. An equation for this quantity may be obtained simply by setting eq 12 equal to zero, for we may be quite sure that $\hat{N} = 0$ at $\theta = \infty$. Regrettably, except for special cases, the resulting equation for Z_∞ is transcendental and must be solved numerically for specified values of ρ, $\hat{E}_0$, and R. The general behavior of an arbitrary decay may be summarized by saying that it starts out exponentially with a logarithmic slope given by eq 15 and finishes exponentially with a different logarithmic slope which may be either larger or smaller than the initial value.

The Special Case $\rho = 1$. When $\rho = 1$, eq 7 becomes

$$-\frac{1}{R}\frac{\mathrm{d}\hat{N}}{\mathrm{d}Z} = -\frac{1}{R}\frac{\mathrm{d}(\ln\hat{N})}{\mathrm{d}\theta} = 1 \qquad (16)$$

which may be integrated straightaway to give

$$\hat{N} = e^{-R\theta} = e^{-k_1 S t} \qquad (\rho = 1) \qquad (17)$$

It follows from eq 17 and the definition of Z that

$$Z = \int_0^\theta \hat{N}\,\mathrm{d}\theta = \frac{1}{R}(1 - e^{-R\theta}) \qquad (\rho = 1) \qquad (18)$$

This expression for Z may be put into eq 11 to obtain the explicit time dependence of $\hat{E}$

$$\hat{E} = \frac{1}{2} + \left(\hat{E}_0 - \frac{1}{2}\right)\exp\left[-\frac{2}{R}(1 - e^{-R\theta})\right] \qquad (\rho = 1) \qquad (19)$$

Equations 17, 18, and 19 completely specify the behavior of the system in this special case.

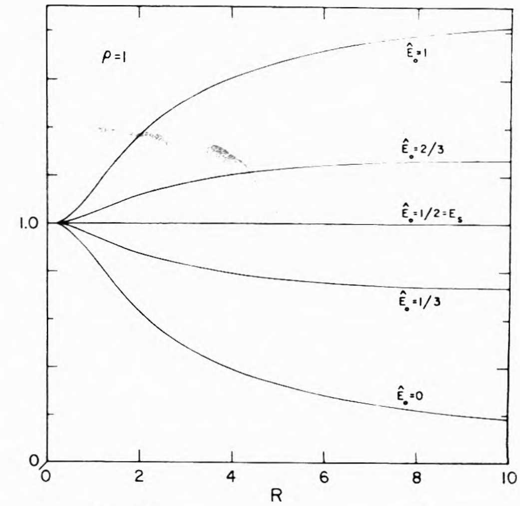

Figure 1. Graph of $\hat{E}_\infty/\hat{E}_s$ vs. R for selected values of $\hat{E}_0$ for the special case $\rho = 1$.

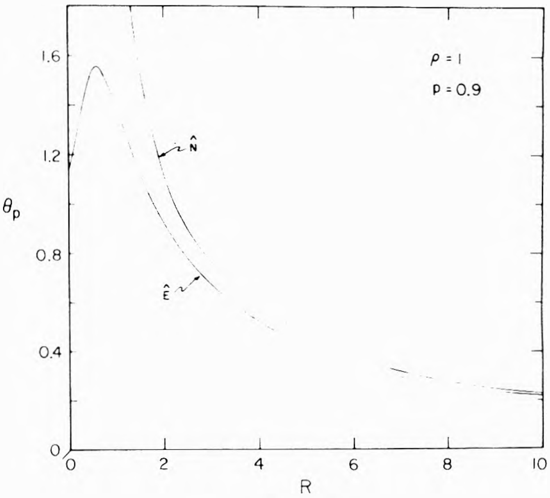

Figure 2. Graph of $\theta_{0.9}$ vs. R for $\hat{E}$ and $\hat{N}$ for the special case $\rho = 1$.

We have seen in eq 14 that the decay of atoms is a simple exponential whenever $\hat{E}_0 = \hat{E}_s$. Now we see in eq 17 that the decay of $\hat{N}$ is also a simple exponential when $\rho = 1$, regardless of the initial value of the fraction of empty sites. The physical reason for this is that when $\rho = 1$, i.e., $k_1 = k_2$, an atom is just as likely to be removed when the site is empty as when it is already occupied. The removal of atoms proceeds as though there were only one kind of site, the kinetic distinction between empty and filled sites having been eliminated. Since the total number of sites, S, is constant, the decay of atoms is pseudo-first order with an effective rate constant $k_1 S$, just as eq 17 indicates.

As time advances, the quantity Z increases from zero and asymptotically approaches the value $Z_\infty = 1/R$. Likewise, it may be seen from eq 19 that $\hat{E}$ approaches an asymptote, $\hat{E}_\infty$, as θ increases without limit. It is instructive to consider the ratio of this asymptote to the steady-state value, the latter being equal to 0.5 in this special case

$$\hat{E}_\infty/\hat{E}_s = 1 + (2\hat{E}_0 - 1)e^{-(2/R)} \qquad (20)$$

Graphs of this ratio as a function of R are shown for a few values of $\hat{E}_0$ in Figure 1. When the number of surface sites is sufficiently small compared to the initial number of atoms, that is, when R is small enough, the fraction of empty sites at infinite time is always close to the steady-state value. When R is small, each surface site must be used many times on the average for all the atoms to be processed; consequently, ample opportunity for establishing a steady-state exists. On the other hand, when R is very

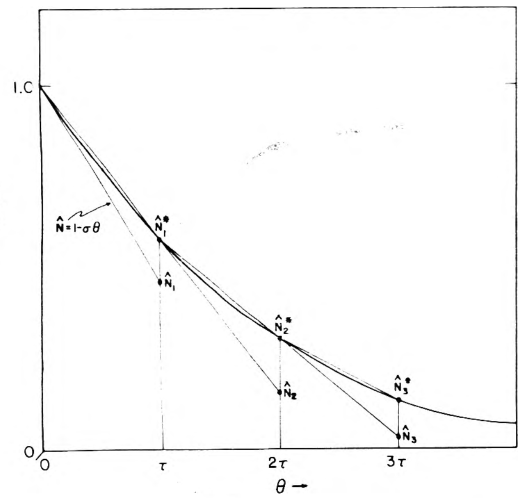

Figure 3. Schematic graph of $\hat{N}$ vs. θ to illustrate the numerical computation of decay histories.

large, most sites do not interact with an atom at all, and those that do interact, rarely do so more than once; consequently, if all sites are covered to start with ($\hat{E}_0 = 0$), the decay is accomplished mainly by the removal of adsorbed atoms, and if all sites are empty to start with ($\hat{E}_0 = 1$), the decay is accomplished mainly by adsorption.

It is also of interest to inquire about the rate at which $\hat{E}$ approaches its asymptotic value, compared to the rate at which atoms disappear. For this purpose consider the quantity $(\hat{E}_0 - \hat{E})/(\hat{E}_0 - \hat{E}_\infty)$ which varies from 0 at the beginning of a decay to 1 at the end; and for comparison consider also the quantity $(1 - \hat{N})$, which also varies from 0 to 1 throughout the decay. With a little algebra one may solve for the time, θ_p, required for each of these quantities to achieve some arbitrary fraction, p, of its final value. The results of such calculations for $p = 0.9$ are shown in Figure 2. For the disappearance of atoms, θ_p is of course just proportional to $1/R$, the reduced exponential lifetime (see eq 17). The surface coverage never approaches its asymptote more slowly than $\hat{N}$ does, and when R is small, it does so much more quickly. Curiously enough, θ_p for the change in $\hat{E}$ has a maximum at $R = 0.59$, approaches that for $\hat{N}$ at large R, and approaches the value $\ln (1 - p)^{-1/2}$ as R approaches zero. The position of the maximum is fairly insensitive to the choice of p. For any p greater than 0.5, the maximum lies at some value of R between 0.46 and 0.59. Finally, it may be noted that θ_p for the change in $\hat{E}$ is independent of $\hat{E}_0$ in this special case, $\rho = 1$.

Numerical Procedure and Some Results for $\rho \neq 1$. Our procedure for generating solutions to the basic differential eq 7 and 8 in the event that $\rho \neq 1$ may most easily be followed by reference to Figure 3 in which the curve schematically represents the time history of $\hat{N}$ we wish to compute. According to eq 15, for sufficiently short times we may write

$$\hat{N} = e^{-\sigma\theta} \cong 1 - \sigma\theta \tag{21}$$

where $\sigma = R[\rho + \hat{E}_0(1 - \rho)]$. Let us divide the θ axis into equal intervals of length τ. The success of our procedure clearly depends on selecting a judiciously small value for τ in any particular computation. Assuming that $\hat{N}$ follows the approximate straight line in eq 21 throughout the first time interval, we may compute its value, $\hat{N}_1$, at the end of that interval by substituting τ for θ in that equation. The trapezoidal area under that initial line segment is an approximation to the value of Z at the time τ, which we may denote by Z_1. Thus

$$Z_1 = \int_0^\tau (1 - \sigma\theta)\, d\theta = \tau\left(1 - \frac{1}{2}\sigma\tau\right) \tag{22}$$

We may put this value of Z_1 into eq 12 to obtain a refined estimate of $\hat{N}$ at the time τ, shown optimistically on the curve as $\hat{N}_1{}^*$ in Figure 3. Likewise, the area beneath the line segment joining the points (0, 1) and (τ, $\hat{N}_1{}^*$) may be taken to be a refined value of Z_1, which we may call $Z_1{}^*$. The line joining (0, 1) to (τ, $\hat{N}_1{}^*$) is extrapolated to the time 2τ to establish the point (2τ, $\hat{N}_2$). The value for Z_2 is then taken as the sum of $Z_1{}^*$ plus the area beneath the line segment joining (τ, $\hat{N}_1{}^*$) and (2τ, $\hat{N}_2$). The value of Z_2 thus obtained is put into eq 12 to compute $\hat{N}_2{}^*$. The value of $\hat{N}_2{}^*$ may then be used to calculate $Z_2{}^*$, a refined value for Z_2, by adding to $Z_1{}^*$ the area beneath the segment joining (τ, $\hat{N}_1{}^*$) to (2τ, $\hat{N}_2{}^*$), which segment is then extrapolated to obtain $\hat{N}_3$, and so on. The sequence of $\hat{N}_i{}^*$ values together with $\hat{E}$ values obtained by substitution of the $\hat{Z}_i{}^*$ into eq 11 are the desired solutions to eq 7 and 8. The procedure just sketched may readily be programmed for digital computation. Selecting a value of τ too large for the case in hand leads to oscillations of the $\hat{N}_i{}^*$ about the solution, which range from mild to bizarre.

Each decay is uniquely determined by the parameter trio (ρ, $\hat{E}_0$, R). Close examination of eq 11 and 12 reveals that computational effort devoted to exploring parameter space may be reduced as a result of simple relationships between certain pairs of decays which we call *complimentary*. The decay (ρ_1, $\hat{E}_{01}$, R) and the decay (ρ_2, $\hat{E}_{02}$, R) = ($\rho_1{}^{-1}$, $1 - \hat{E}_{01}$, R) are complimentary. For such a pair

$$\hat{N}_1(\theta) = \hat{N}_2(\rho_1\theta) \tag{23}$$

$$\hat{E}_1(\theta) + \hat{E}_2(\rho_1\theta) = 1 \tag{24}$$

Thus, for example, a single computation yields histories for the complimentary decays (5, 0.6, 1) and (0.2, 0.4, 1). Furthermore, curves such as those in Figure 2 are superimposable for complimentary decays providing that the ordinate pertaining to the second member of the complimentary pair is multiplied by a factor of ρ_1.

Speaking somewhat loosely, the *shapes* of $\hat{N}(\theta)$ vs. θ graphs are mainly affected by the parameters ρ and $\hat{E}_0$, whereas the *rates* at which $\hat{N}$ and $\hat{E}$ approach their respective asymptotes are mainly affected by the parameter R. In Figure 4 we have illustrated the variety of decay curve shapes arising from various choices for ρ and $\hat{E}_0$ in the event that $R = 1$. For reference, the special case $\rho = 1$, which is governed by eq 17, has been included in Figure 4.

Figure 5, computed for $\rho = 5$, is the analog of Figure 1. The results in Figure 5 together with eq 13 and 24 may be used to generate corresponding graphs for decays with $\rho = 0.2$.

Finally, Figures 6 and 7, showing results computed for $\rho = 5$, $p = 0.9$, and the extreme possibilities for $\hat{E}_0$, are analogous to Figure 2.

Epilogue

Any practitioner of experimental gas–surface kinetics is painfully aware of the difficulties involved in effecting a separation of the inherent characteristics of the surface processes from the supererogatory kinetic properties of the

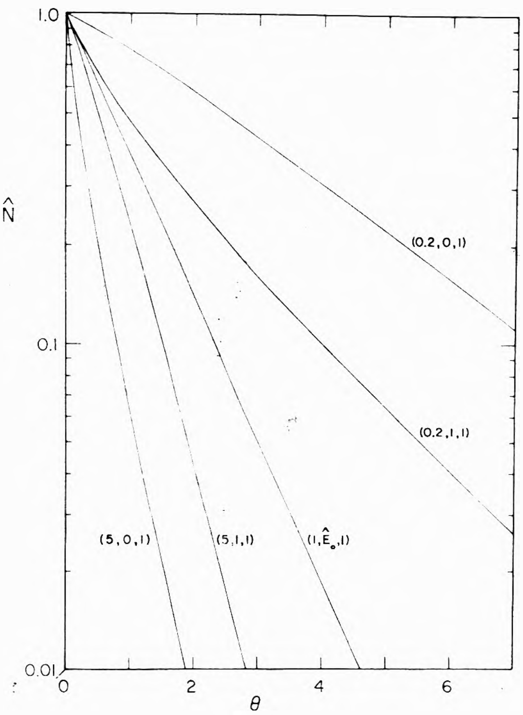

Figure 4. Computed graphs of $\hat{N}$ vs. θ for selected parameter trios. The special case $\rho = 1$, for which the decay graph is a simple exponential, is included for comparison.

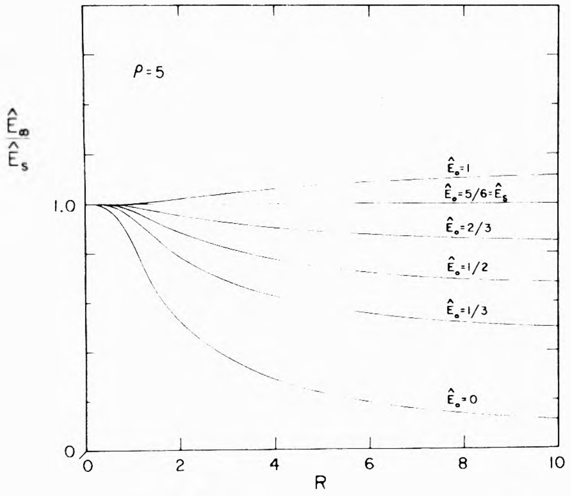

Figure 5. Graph of $\hat{E}_\infty/\hat{E}_s$ vs. R for selected values of $\hat{E}_0$ for the case $\rho = 5$.

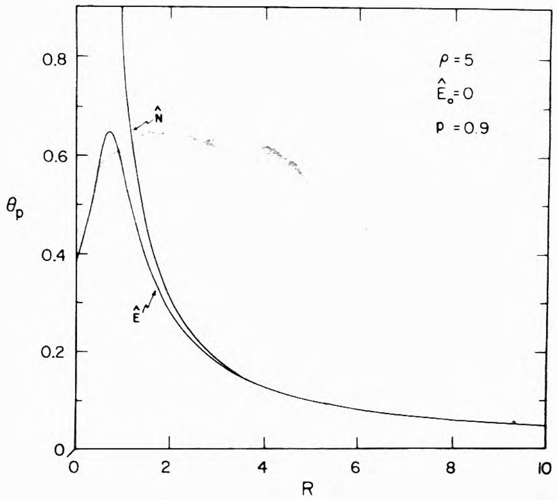

Figure 6. Graph of $\theta_{0.9}$ vs. R for $\hat{E}$ and $\hat{N}$ for the case $\rho = 5$, $\hat{E}_0 = 0$.

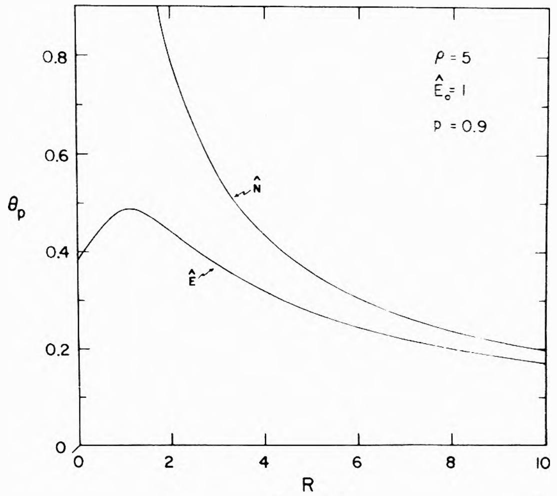

Figure 7. Graph of $\theta_{0.9}$ vs. R for $\hat{E}$ and $\hat{N}$ for the case $\rho = 5$, $\hat{E}_0 = 1$.

system which arise from gaseous atoms having to overcome impediments to their arrival at the surface. In presenting our formal mechanism we have purposely avoided mentioning diffusion and flow problems in order to focus attention on the kinetics of the surface process itself. In discussions of surface recombination which deal in detail with the complications introduced by diffusion and flow in actual experimental arrangements it has been the custom to treat the surface formally as a featureless sink for atoms, and it is usual to define for this purpose a quantity γ, which is the probability that an atom will be permanently removed from the gaseous sample upon making a single gas-kinetic encounter with the surface. The analysis of experimental results is bent toward the determination of a value of γ thought to be characteristic of the material from which the surface is made, and its temperature. The possibilities that γ might depend on the time in a given experiment or on the prior history of the surface have usually, though not always,[14] been ignored. For many years it was usual to write the rate law for the disappearance of atoms in heterogeneous recombination as first order in atomic concentration. In recent times this rate law has occasionally proved to be inadequate and experimental results have been treated using an ad hoc rate law composed of a sum of first-order and second-order terms. It has even been claimed in some work that the rate law is strictly second order in atomic concentration. The mechanistic justification for one or another of these forms of the rate law has always been somewhat vague and tailored to current exigencies. The simple mechanism discussed here obeys a rate law which cannot be generally described in terms of order numbers; however, it can in various circumstances masquerade as a first- or second-order reaction or a linear combination of the two, and it may therefore be flexible enough to accomodate the apparent inconsistencies of results regarding the form of the rate law for heterogeneous recombination of atoms. The results we have presented suggest how a "complex" mechanism of surface recombination might manifest itself in the shape of an atom decay history at short times when surface coverage is approaching its asymtotic value. It is clearly desirable that suitable experiments be undertaken to establish the time scale of prestationary state processes in surface recombination of atoms in order that we may develop a more detailed view of surface reaction mechanisms than a single parameter can give.

Acknowledgments. We are grateful to Professor J.V. Michael for a stimulating discussion of the details of his atomic hydrogen recombination experiments, and we thank Professors John Miller and Knut Krieger for their interest in this work.

This work was supported by the National Science Foundation under Grant No. NSF-GH-33633.

References and Notes

(1) A. V. Harcourt and W. Esson, *Proc. Roy. Soc., Ser. A*, **14**, 470 (1865); *Phil. Trans. Roy. Soc.* **156**, 193 (1866); *ibid.*, **157**, 117 (1867).
(2) P. V. Bevan, *Phil. Trans. Roy. Soc., Ser. A*, **202**, 71 (1904).
(3) A. Rakowski, *Z. Phys. Chem.*, **57**, 321 (1907).
(4) T. M. Lowry and W. T. John, *J. Chem. Soc.*, **97**, 2634 (1910).
(5) B. Zwolinski and H. Eyring *J. Am. Chem. Soc.*, **69**, 2702 (1947).
(6) F. A. Matsen and J. L. Franklin, *J. Am. Chem. Soc.*, **72**, 3337 (1950).
(7) N. M. Rodiguin and E. N. Rodiguina, "Consecutive Chemical Reactions", Van Nostrand, Princeton, N.J., 1964.
(8) E. Abel, *Z. Phys. Chem.*, **56**, 558 (1906).
(9) J. Chien, *J. Am. Chem. Soc.*, **70**, 2256 (1948).
(10) E. I. Adirovich, *Dokl. Akad. Nauk SSSR*, **61**, 467 (1948).
(11) I. Langmuir, *Trans. Faraday Soc.*, **17**, 621 (1921).
(12) E. K. Rideal, *Proc. Camb. Phil. Soc.*, **35**, 130 (1939).
(13) H. Wise and B. J. Wood in "Advances in Atomic and Molecular Physics," Vol. 3, Academic Press, New York, N.Y., 1967, pp 291–353, and references cited therein.
(14) J. J. Ahumada and J. V. Michael, *J. Phys. Chem.*, **78**, 465 (1974).

Aggregation of 1,1′-Diethyl-2,2′-cyanine Chloride as Studied by Nuclear Magnetic Resonance

R. E. Graves* and P. I. Rose

Research Laboratories, Eastman Kodak Company, Rochester, New York 14650

(Received August 8, 1974)

Publication costs assisted by Eastman Kodak Company

The dye, 1,1′-diethyl-2,2′-cyanine chloride, was studied in aqueous solution using Fourier transform proton magnetic resonance. The concentration dependencies of the chemical shifts for several different dye protons were determined over a concentration range of 2×10^{-2} to 3×10^{-5} M. All resonances shifted to higher applied field as dye concentration increased, establishing an aggregate structure in which dye molecules stack face to face with considerable overlap of the quinolinium ring system. In dilute solutions where only a monomer $\rightleftarrows$ dimer equilibrium occurs, the nmr data are interpreted in terms of "ring-current" theory and a dimer model that leads to $K_D \sim 1 \times 10^3$ M^{-1}. At higher concentrations, greater degrees of aggregation occur, which, by 2×10^{-2} M, shift dye aromatic protons −0.36 ppm compared with the monomer values. This shift change is interpreted in terms of a polymer composed of units similar to the dimer. Little specific evidence for any *unique* J-aggregate structure could be obtained. In D_2O solutions, the methinyl proton was replaced slowly by deuterium and the rate was studied from pD 7 to 10.6. A rate constant for the acid-catalyzed process of 5×10^2 M^{-1} sec^{-1} was found for dye solutions at zero ionic strength.

Introduction

Dyes with the general formula

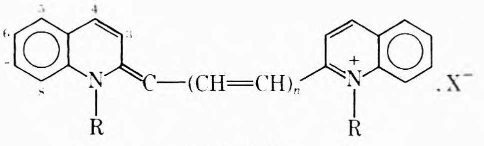

$n = 0, 1, 2, \ldots$
R = alkyl

have been particularly interesting to spectroscopists and photochemists since the early part of this century. Generally, aqueous solutions of these dyes have a visible absorption spectrum that depends strongly upon dye concentration. Increasing dye concentration produces at least one, and often several, new absorption bands that are shifted by as much as 1000 Å to shorter or longer wavelengths compared to the dilute-solution spectrum. For sufficiently dilute solutions, most of these dyes can be shown to produce the spectrum of the unassociated dye molecule. The spectral changes observed upon increasing concentration have been attributed to dye association.[1] The first new band that appears at shorter wavelength is usually ascribed to a dimer. For many cyanines dimerization is followed by a generally unspecified degree of aggregation, which results in further shifts in the main band to even shorter wavelengths. At higher concentrations, certain of the cyanine dyes exhibit an intense and unusually sharp absorption at longer wavelengths ("J" band).[2,3] The most well-known example of "J" band formation is aqueous 1,1′-diethyl-2,2′-cyanine chloride, which has $n = 0$ in the series shown above and is the subject of this paper.

While much speculation has taken place concerning the nature of the dye–dye interactions, little evidence seems to exist regarding important details of the structure of the associated dye species. The extent of aromatic ring overlap is not known, even though this is a critical parameter in theories that have been proposed to account for the spectral shifts.[4,5]

Our experiments represent an effort to obtain nmr data which can be understood in terms of a consistent picture of the complex equilibria that lead eventually to the so-called "J" aggregate.

During the course of this investigation, a hydrogen exchange reaction was observed for the dye in water and in methanol solutions. The kinetics of this process in aqueous solution are also reported.

Experimental Section

The dye used in these experiments was obtained from Eastman Organic Chemicals. It was recrystallized from ethanol and then dried in a vacuum oven at 80° for 4 hr. No further purification was attempted. All but the most concentrated samples were prepared with 100.0 at. % D_2O supplied by Diaprep, Inc. Otherwise, 99.7 at. % D_2O obtained from Merck Sharp and Dohme was used. The methanol solutions were prepared with methanol-d_4, also obtained from Merck Sharp and Dohme.

Absorption spectra were obtained on a Cary Model 14 spectrometer at room temperature. Portions of the dye were weighed on a microbalance, dissolved in distilled water, and stored in the dark. The samples were shaken intermittently and sonicated over 24 hr to ensure complete dissolution of dye.

Typically, sodium 3-trimethylsilylpropionate-2,2,3,3-d_4 (TSP) would be added to aqueous samples for use as an nmr internal reference. However, we found that salts such as this are not sufficiently inert with respect to the equilibria under study and thus, they were omitted. The chemical-shift scale was established by measuring the shift of the HDO resonance of the solvent relative to TSP ($\delta = -4.64$ at our probe temperature) and then measuring the position of lines in the dye spectra relative to the HDO line. This method was checked for each sample to ensure that the probe temperature and sample pD were constant, because of the sensitivity of the HDO resonance position to temperature and pD. The chemical shifts in this work are reported relative to TSP.

Since salts must be avoided in the aqueous dye samples; no buffers were used. If the pD fell below 6.4, protonation (deuterionation) of the dye could be detected by the appearance of new resonances in the spectra.[6] Determinations of the pD of dye solutions established that it remained at 7.0 ± 0.1.

Degradation of the dye solutions due to exposure to light and air is possible. No degradation was detected by nmr in samples as much as two weeks old.

The europium(III) tris(1,1,1,2,2,3,3-heptafluoro-7,7-dimethyl-4,6-octanedione), Eu(fod)$_3$, used as a shift reagent, was obtained from Norell Chemical, Inc. It was kept in a drybox under nitrogen until use. The reagent was added to 3×10^{-3} M deuteriochloroform solutions of the dye.

The pD of samples used in the study of the rate of H–D exchange was adjusted by adding small quantities of dilute DCl or NaOD while observing the change on a Radiometer Model 26 pH meter. Sufficient sample was prepared so that any possible change in the pD of a sample could be followed independently of the nmr experiments.

The nmr spectra were obtained on a Varian Model HA-100 spectrometer at a probe temperature of 36°. The instrument had been modified for Fourier transform (FT) mode operation.[7] All spectra were obtained by signal averaging in the FT mode since many of the solutions were of such low concentrations as to make signal averaging in the "slow-sweep" mode impractical. The time used for accumulation ranged from several minutes to 3 days depending upon the concentration of the solution and the signal-to-noise ratio (S/N) desired in the resultant spectrum. For the most dilute solution, 260,000 "impulse responses" with a duration of 1.0 sec were averaged.

The data used in the rate study were also obtained in the FT mode. In this case, data were accumulated for 20 min, stored on magnetic tape, and another accumulation was started. We were able to take data without long interruptions since the process of storing data on tape required less than 1 min.

Field-frequency lock for the spectrometer was maintained using the signal from the residual HDO of the aqueous solvent. An offset mode of FT operation was developed such that all resonances appear in the usual manner even though the lock line is near the center of the spectrum.[7] Without this modification, the "normal" mode of FT operation results in a serious complication of the spectrum by producing overlap of the methyl and aromatic signals.

Spectral simulation was done on a Varian Model 620/i computer interfaced with the FT nmr apparatus. The program used was supplied by Varian.

Results

Absorption Spectra. The general features of the visible absorption spectra of the dye were found to be in agreement with previously published spectra.[1,8,9] At the lowest concentration examined, 1×10^{-5} M, the absorption maximum is at 525 nm with a strong secondary absorption at 490 nm, which is attributed to the first vibronic level of the monomer. No spectral changes occur until the concentration of dye exceeds $\sim 5 \times 10^{-5}$ M. As the concentration increases to 1×10^{-3} M, a new absorption maximum is formed at 484 nm with a loss of extinction at 525. An isosbestic point was detected at 496 nm. Since the band at 484 nm has been attributed to a dimer, the presence of the isosbestic point is evidence that only a monomer $\rightleftharpoons$ dimer equilibrium is significant for dye concentrations up to 10^{-3} M.

At higher concentrations, several competing equilibria appear to exist with new bands appearing at both shorter and longer wavelengths.[1,2]

Nmr Spectral Analysis. The spectrum of a solution of 1,1′-diethyl-2,2′-cyanine chloride in D_2O at a concentration of 6.7×10^{-3} M is shown in Figure 1. The spectrum is composed of three distinct bands centered about the solvent signal. A triplet at 1.55 ppm and a quartet at 4.41 ppm result from the methyl and methylene protons of the ethyl groups. The complex pattern below 7 ppm is composed of the lines due to the 12 aromatic ring protons. The resonance for the methine proton, H_9, is not always observed. It was found that this was due to exchange with deuterium of the solvent, which is discussed in a later section. In freshly prepared solutions, the methine signal appears at 5.1 ppm.

Changes in the various aromatic proton chemical shifts should be the most sensitive nmr measure of the aggregation phenomena. However, since the region is complicated by large second-order spin–spin interactions, this information was not fully usable. An analysis was attempted of the aromatic (ABCDEF) spin system in an effort to assign as

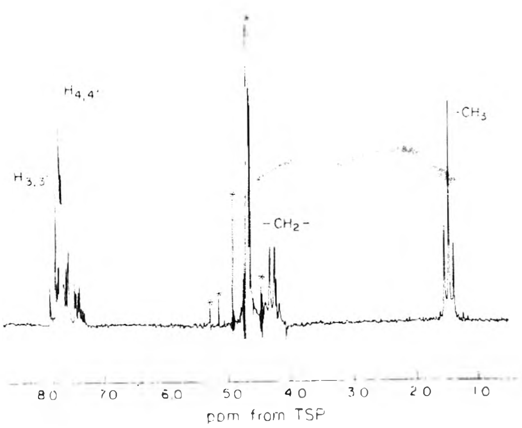

Figure 1. Nmr spectrum of a 6.7 × 10^{-3} *M* solution of 1,1′-diethyl-2,2′-cyanine chloride in D_2O. (Marked lines are solvent or instrumental.)

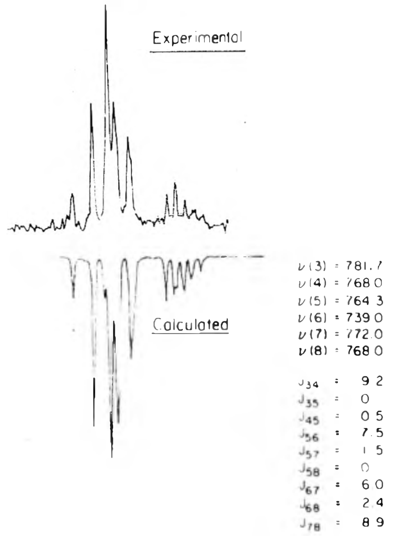

Figure 2. Comparison of calculated and experimental nmr spectra for the aromatic region of a 1 × 10^{-3} *M* solution of 1,1′-diethyl-2,2′-cyanine chloride in D_2O.

many chemical-shift values as possible. Figure 2 shows a comparison of the calculated and experimental spectrum for a dye concentration of 1 × 10^{-3} *M*. The parameters used to give this result are listed in the figure and are in reasonable agreement with published values for analogous compounds.[8] (The values of the coupling constants for the aromatic protons were obtained by use of a europium shift reagent.[9])

Only three of the six aromatic protons could be assigned to distinct features of the spectrum (Figure 1). Two pairs of lines, assigned to $H_{3,3'}$ and $H_{4,4'}$, form an "AB" pattern. Assignment of the low-field part to $H_{3,3'}$ is based upon the proximity of these protons to the opposite quinolinium ring. The lines assigned to $H_{4,4'}$ are partially obscured by other signals. The group of lines at ~7.30 ppm is assigned to protons 6 and 6′. The high-field position of these relative to the other aromatic protons is consistent with assignments in analogous compounds.[8]

Concentration and Temperature Effects. The effect of aggregation upon the spectrum of the dye was observed in a series of solutions whose concentrations ranged from 3 × 10^{-5} to 2 × 10^{-2} *M*. The chemical-shift values for the methyl and the 3,3′ protons are plotted as a function of concentration in Figure 3. From the data in Figure 3, one can extrapolate to a chemical shift in water at "infinite" dilution of 7.96 ± 0.01 ppm for protons 3,3′ and 1.65 ppm for the methyl protons. These values are believed to characterize the dye monomer and should be compared to the chemical-shift values obtained for the dye in methanol, where the dye has been established[10] to be in the monomeric state. In methanol solutions, a shift of 7.97 ppm was found for the 3,3′ protons and a shift of 1.65 ppm for the methyl protons. This agreement, despite the difference in solvent, allows one to conclude that the dye is essentially monomeric in D_2O solution at 1 × 10^{-5} *M*.

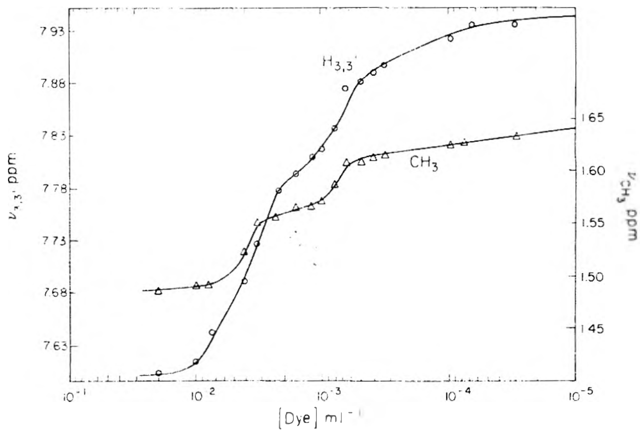

Figure 3. A plot of the chemical shift of $H_{3,3'}$ and the methyl group of 1,1′-diethyl-2,2′-cyanine chloride in D_2O as a function of concentration.

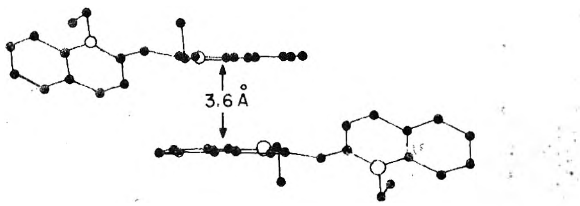

Figure 4. The model of the dimer of the dye arrived at by analysis of the nmr data.

From Figure 3 one can obtain a total "dilution shift" of −0.36 ppm for $H_{3,3'}$ and −0.165 ppm for the methyl protons.

One can interpret the data from the dilution study in terms of a model for dye–dye interaction which is consistent with both the molecular and crystal structures.[11,12] The molecular structure imposes restrictions on dye association because of the ~54° "twist" between the planes of the two quinolinium moieties. The crystal structure also shows that for pairs of dye molecules with close nonbonded interactions (~3.3–3.6 Å between adjacent quinolinium planes), the *N*-ethyl groups point *away* from each other. This situation also seems reasonable from electrostatic and steric considerations for the association of the dye molecules in solution.

The twist requires one to regard the dye as a mixture of enantiomers, i.e., of "right-" and "left-handed" structures which may be termed, for convenience, "d" and "l." The crystal structure shows that the dye molecules that "pair" as described above are centrosymmetrically related, i.e., the *alternation* ... dldl ... exists. The resulting aggregate would then not possess any helical sense.

The arrangement shown in Figure 4 depicts our model for the basic unit of the dye aggregate (dimer). As implied

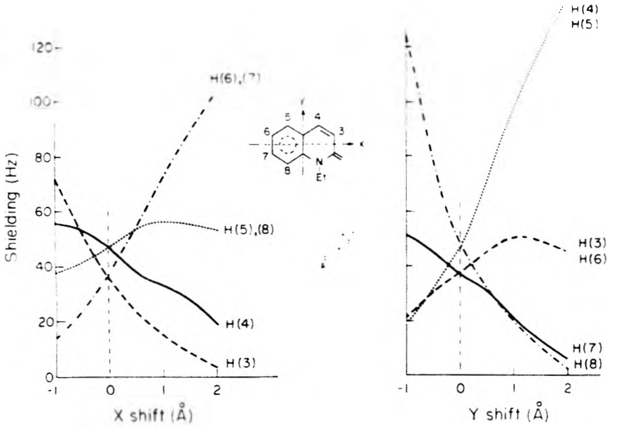

Figure 5. The effect on the chemical shift of the various aromatic ring protons as a function of the position of the overlapping ring system.

above, it resembles the juxtaposition of two dye molecules in the crystal.

For this model we determined the set of perpendicular and radial distances of each proton, H_i, from each of the condensed rings of the nearest nonbonded quinolinium system (i.e., on an adjacent dye molecule). This gave a basis[13] for calculating the chemical-shift change experienced due to "ring currents" when the state of the dye changes from monomer to dimer, trimer, etc.

It is important that under no conditions was more than a single, averaged spectrum observed for the dye. This means that exchange of a dye molecule between monomer and the various n-mers is rapid on the nmr time scale.[14] For the same reason, although there will be more than one environment for each proton, H_i, in any n-mer, only a single average resonance is observed.

The chemical shift of a dye proton, H_i, for a solution of dye aggregate(s) undergoing fast exchange is given by

$$\delta_i^{(n)} = \frac{N_E\delta_{i,E} + N_0\delta_{i,0}}{N_E + N_0} \tag{1}$$

where N_E represents the number of H_i protons on end or "external" groups of n-mers and $\delta_{i,E}$ is the chemical shift characteristic of that environment; N_0 and $\delta_{i,0}$ represent similar parameters for H_i when found in internal (overlapped) portions of the n-mer. For a dimer one has

$$\delta_i^{(2)} = (\delta_{i,E} + \delta_{i,0})/2 \tag{1a}$$

If one makes the chemical shifts relative to the infinite dilution value (monomer) and assumes that

$$\delta_{i,E} \approx \delta^{(1)} \equiv 0 \tag{2}$$

eq 1 can be rewritten as

$$\begin{aligned}\Delta_i^{(n)} &= N_0\Delta_{i,0}/(N_E + N_0)\\ &= (n - 1)\Delta_{i,0}/n\end{aligned} \tag{3}$$

It is seen that $\Delta_{i,0}$ becomes the characteristic shift change upon formation of the "infinite" (e.g., $n \gtrsim 15$) aggregate.

In Figure 5, the aggregation-induced shift was calculated as a function of displacement of the aromatic plane of one dye with respect to its nearest neighbor. Clearly, the "ring current" theory predicts that only ~100% overlap would result in the small differences observed for Δ_0 among the various aromatic proton positions. The predicted Δ_0 is -0.40 ± 0.05 ppm, in good agreement with the experimental $H_{3,3'}$ value of -0.36 ppm.

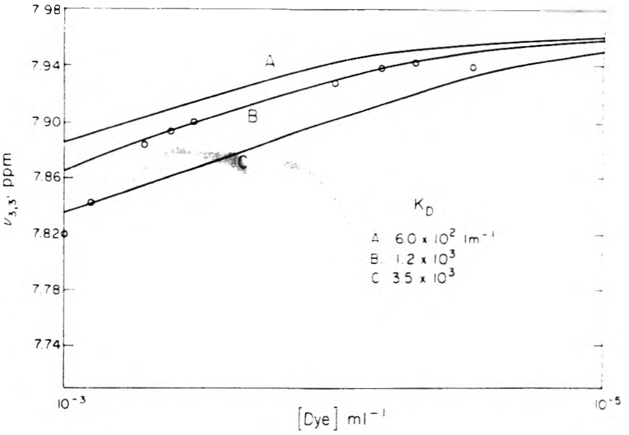

Figure 6. Theoretical curves showing the effect of the dimerization constant (K_D) on the chemical shift of $H_{3,3'}$ as a function of concentration. The dots (O) indicate experimentally determined chemical-shift values.

Both the electronic absorption and nmr data obtained for an aqueous solution of the dye are difficult to interpret quantitatively at high concentrations since several aggregate species coexist. From 10^{-5} to $\sim 10^{-3}$ M, however, the electronic spectra indicate that only a monomer–dimer equilibrium takes place.[10] For the equilibrium

$$2\text{M} \rightleftarrows \text{D} \tag{4}$$

with

$$K_D = [\text{D}]/[\text{M}]^2 \tag{5}$$

one can derive an expression for the dimerization constant, K_D, in terms of the observed chemical shift change, Δ(obsd), the dimer chemical shift, $\Delta^{(2)}$, and the dye concentration, C.

Equation 6 was derived with the usual assumptions regarding the material balance and a dimer chemical shift given by eq 3. In Figure 6, three chemical-shift vs. concentration curves are shown, which were calculated using eq 6. Also shown are the experimental chemical-shift values that permit an estimate of $K_D = \sim 1 \times 10^3\ M^{-1}$.

Nmr spectra of a 2×10^{-2} M solution of the dye in D_2O at various temperatures between 0 and 35° were obtained. Even though the electronic spectrum for a solution at this concentration gains considerable J-band intensity with decreasing temperature,[10] only small changes in the chemical shifts to *lower* field were observed. Also observed were *relative* changes in the chemical shifts of certain aromatic protons. For example, the chemical shift difference between $H_{3,3'}$ and $H_{4,4'}$ is gradually reduced from 13.6 to 6.6 Hz in going from 35 to 0°. This results primarily from a larger deshielding of the $H_{4,4'}$ proton than of $H_{3,3'}$. Heating from 35 to 60° produced no significant effect upon the $H_{3,3'}$–$H_{4,4'}$ separation but resulted in a spectrum that was essentially identical with one obtained at 35° for a concentration of $\sim 5 \times 10^{-3}$ M. Previous studies of this dye demonstrate that heating a 2×10^{-2} M solution to 60° completely eliminates the J band and results in an electronic absorption spectrum that closely resembles that of a 5×10^{-3} M solution at room temperature.[10]

Hydrogen–Deuterium Exchange. A transient feature of the dye nmr spectrum is the signal due to the methine proton (H_9). We were unable, at first, to observe this signal in D_2O solution, although it appeared in spectra of the dye in methanol (5.1 ppm). The H_9 resonance was observed for D_2O solution only by taking the spectrum soon after the

TABLE I: Observed Pseudo-First-Order Rate Constants for Deuteration of 1,1′-Diethyl-2,2′-cyanine[a]

pD	$10^5 k_p$[b]	pD	$10^5 k_p$[b]
7.08	8.1	9.08	2.7
7.15	4.7	10.05	2.7
8.04	3.2	10.65	2.3

[a] [dye] = 3 × 10^{-3} *M*. [b] Reaction was observed at 36° and pD was measured at ~25°.

sample had been prepared. Even in methanol-d_4, the H_9 resonance disappeared after several days at room temperature.

The change in H_9 signal intensity was followed as a function of both time and pD. Each data point was obtained by averaging the signal for ~20 min and is assumed to represent the intensity at a "time" defined as the middle of the accumulation period. The assumption loses validity only if the averaging period approaches the reaction half-life.

Representative kinetic data are shown in Figure 7. A pseudo-first-order process is established by the generally good fit to the semilog plots by least-squares lines. The resulting pseudo-first-order rate constants, k_p, are given in Table I. Rate constants were calculated from the data in Table I by assuming the following equation:

$$K_D = C\Delta(\text{obsd})/2\Delta^{(2)}\left[C\left(1 - \frac{\Delta(\text{obsd})}{\Delta^{(2)}}\right)\right]^2 \qquad (6)$$

$$\text{rate}_{\text{obsd}} = (k_0 + k_{D^+}[D^+] + K_{OD^-}[OD^-])[\text{dye}] \qquad (7)$$

in which k_0, k_{D^+}, and k_{OD^-} are the respective constants for the possible uncatalyzed, acid-catalyzed, and base-catalyzed reactions leading to exchange. The best fit to the data results from $k_0 = 2.5 \times 10^{-5}$ sec^{-1}, $k_{D^+} = 5 \times 10^2$ M^{-1} sec^{-1}, $k_{OD^-} \approx 0$. The rate curve calculated using these values is shown in Figure 8 along with the experimental pseudo-first-order rate constants.

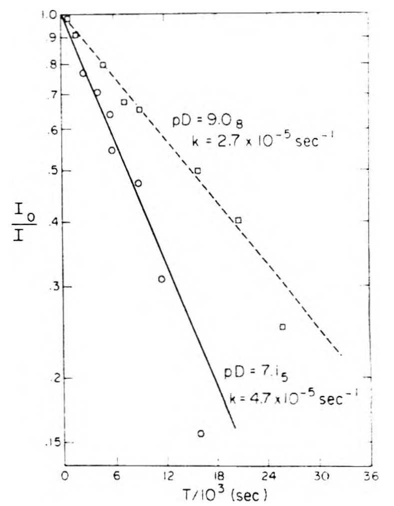

Figure 7. Plot of the intensity (area) of the methine proton signal (H_9) as a function of time for pD 9.0_8 and 7.1_3.

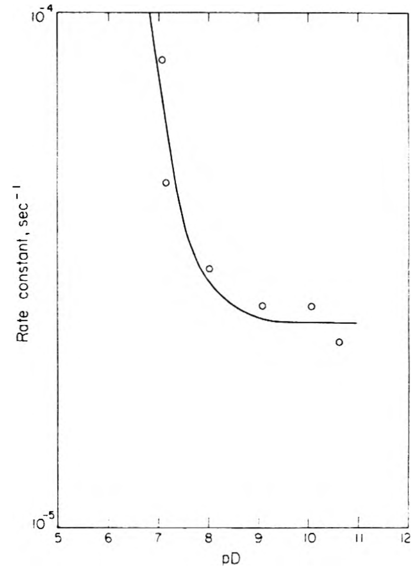

Figure 8. Plot of the data in Table I (O) showing the theoretical curve obtained from the analysis of the rate data.

Discussion

It is evident from this study that the nmr chemical shifts are sensitive to the association of 1,1′-diethyl-2,2′-cyanine. Of immediate significance is the *increased shielding* that is observed for all the dye protons with increasing degree of association (concentration). This aspect of these results establishes that the various dye states in solution involve an overlapping (face-to-face) arrangement of the aromatic planes. The presence of "in-plane" interactions is not supported by this datum. Also, the magnitude of the nmr chemical shift changes are much larger than could be expected to result from a dye–counterion interaction.[15] The data, thus, support Padday's[16] conclusion that dye association rather than ion pairing[17] is responsible for the changes in the visible absorption spectrum of the dye.

The "ring-current" effect, which is widely employed to explain chemical-shift changes produced (through space) by aromatic rings, clearly predicts that a proton that approaches the edge of an aromatic ring will be deshielded. A nucleus that is above the ring system can experience a large shielding, which is observed in this study for all the proton resonances of the dye as the concentration is increased.

Since the interpretation of our data involves the classical Johnson and Bovey "ring-current" theory,[13] the question can be raised concerning its suitability. There is evidence that the theory underestimates the deshielding produced *in* the aromatic plane;[18] however, we believe that sufficient evidence exists showing substantial accuracy of this theory for predicting the above-the-plane shieldings.[18,19] Furthermore, evidence has been given that places the aromatic ring current of nitrogen heterocycles at nearly 100% of the value for the hydrocarbon analogs.[20]

Further information is obtained by comparing the dilution shifts experienced by the various aromatic ring hydrogens. We have shown that only very small relative shifts are found. For a given interplanar separation, a search was made for conformations of "associated" quinolinium rings that would result in nearly identical ring-current shifts, Δ_0, on *all* of the six aromatic hydrogens as this datum requires. We can propose only one reasonable conformation which meets this requirement, namely, that which involves nearly complete overlap of the heterocyclic nuclei of adjacent dye molecules. Figure 5 shows values of Δ_0 for each ring proton which are calculated for varying amounts of relative ring displacements in the x and y directions. It is evident that the similarity in Δ_0 required by the data for all protons is approached only for zero displacement. We estimate that the relative shifts would be particularly sensitive to ring displacements along the "major" axis (labeled x in the diagram). The shift data for the dye between 10^{-5} and 2×10^{-2} M at 35° would limit the possibility of this sort of aggregate stagger to less than 1 Å. Displacements in the orthogonal direction (y axis) are nearly as effective in producing large relative shifts, and, again, values of ~1 Å would have been detectable.

The structure of the dye aggregate proposed by Scheibe[21] and coworkers, in which the dye molecules are arranged in a parallel "card pack" structure, fails to give even reasonable agreement with our nmr results. From his model we calculate the following chemical shift changes (in Hertz) for the various aromatic protons in the fully aggregated dye: $\Delta_0(H_3) = 148$, $\Delta_0(H_4) = 134$, and $\Delta_0(H_5) = 67$. As can be seen, not only is there a large discrepancy between the measured and calculated shifts but also a large relative shift between the protons.

The nmr spectral effects found upon cooling a 2×10^{-2} M solution from 35 to 0° provides, on the basis of the above discussion, some insight concerning the J-aggregate structure. It is known from the visible absorption data that the J state does not involve a large fraction of the total available dye until the temperature of nearly saturated solutions is reduced to ~5°.[10] This implies that changes in the nmr spectrum by cooling result from increased amounts of dye in the J-aggregated state. The principal effect that was observed by nmr was the change in the relative chemical shift of the aromatic protons.

These effects are interpreted as evidence for distinctly altered and *reduced* overlap of the associated aromatic moieties in the J species. This would also reduce the angle θ, which is measured between the direction of the principal transition moment (along the major molecular axis) and the line that defines the aggregate axis. Molecular exciton theories[4] have been developed that require that θ be above or below a certain critical value in order for aggregation to result in short- or long-wavelength displacements of the electronic absorption bands of the dye. The most recent theory[5] indicates a critical angle that varies somewhat depending upon the dye considered but has a value <35°. Our model of the 1,1'-diethyl-2,2'-cyanine dimer has $\theta \sim 29°$, while the J aggregate would have a smaller, though presently indeterminate value. (In our dldldl . . . model, the meaning of the angle θ is not as straightforward a matter as for planar dyes.) We furthermore interpret our results to indicate no *major* change in the aggregate structure upon passing from dimer to H to J states.

From the dimerization constant of $\sim 1 \times 10^3$ M^{-1}, the 2,2'-cyanine dye has less tendency to dimerize compared with several thiacyanine and thiacarbocyanine dyes that have constants of $\sim 1 \times 10^4$ to 3×10^5 M^{-1}.[22] This situation is not unexpected based upon a comparison of the absorption spectra for these (planar) dyes at similar concentrations.

There is considerable uncertainty in our value of K_D since it is evident that dimer formation is not extensive in the limited concentration range over which the dimer equilibrium is dominant. We know of no other published value of K_D for this dye with which to compare the nmr determined value. However, the earlier work of Scheibe[23] presents data that indicate a dimerization constant $\sim 0.2 \times 10^3$ M^{-1}.

If we suppose that deuteration of the cyanine results from the following sequence which involves protonation:

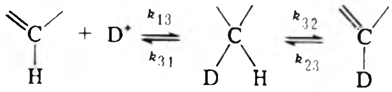

(8)

$$\text{C(H)} + D^+ \underset{k_{31}}{\overset{k_{13}}{\rightleftharpoons}} \text{C(D)(H)} \underset{k_{23}}{\overset{k_{32}}{\rightleftharpoons}} \text{C(D)} + H^+ \qquad (8)$$

we can write the following expression for the replacement of the methine proton:

$$\text{rate} = -\left(k_{13} - \frac{k_{31}}{k_a} + \frac{k_{32}}{k_a}\right)[D^+][\text{dye}] \qquad (9)$$

where[22]

$$k_a = [\text{dye}][D^+]/[\text{dye H}^+] \sim 1 \times 10^{-4}$$

From the values of the protonation and deprotonation rate constants determined recently by Dynes and coworkers,[24] we estimate a value for the overall rate in eq 9 of $\sim 3 \times 10^3$ M^{-1} sec^{-1}. This value is approximately a factor of 6 larger than our experimental result; however, we note that the data[24] that were used to arrive at the estimate for the (acid-catalyzed) second-order rate constant pertain to experiments done using 0.2 M KNO_3 and with much more dilute (1×10^{-5} M) dye solutions than used in the present work. In the absence of a more suitable mechanism, we presently attribute the slower rate observed by us to a combination of these factors. Dynes and coworkers[24] have already shown their equilibria to be sensitive to ionic strength, and it is possible that it is sensitive to the dye concentration as well.

With appropriate choice of cyanine pK_a, it would be possible to "tag" dye molecules with tritium at some low pH so that exchange out would be negligible at the pH range of interest. It appears that dyes with pK_a values around 1.0 would be suitable.

Acknowledgments. The authors thank Drs. A.H. Herz, W. West, and W. Cooper for helpful suggestions. Absorption spectra were obtained through the kind efforts of Mr. M. Scozzafava.

References and Notes

(1) W. West in "Theory of The Photographic Process," 2nd ed, C. E. K. Mees and T. H. James, Ed., Macmillan, New York, N.Y., 1966.
(2) E. E. Jelley, *Nature (London)*, **138**, 1009 (1936).
(3) G. Scheibe, *Z. Angew. Chem.*, **49**, 563 (1936).
(4) E. G. McRae and M. Kasha, *J. Chem. Phys.*, **28**, 721 (1958).
(5) K. Norland, A. Ames, and T. Taylor, *Photogr. Sci. Eng.*, **14**, 295 (1970).
(6) L. H. Feldman, A. H. Herz, and T. H. Regan, *J. Phys. Chem.*, **72**, 2008 (1968).
(7) R. E. Graves, unpublished work.
(8) (a) O. Sciacovelli and W. von Philipsborn, *Org. Magn. Resonance*, **3**, 339 (1971); (b) T. Schaefer, *Can. J. Chem.*, **39**, 1864 (1961).
(9) R. E. Graves and P. I. Rose, *J. Chem. Soc., Chem. Commun.*, 630 (1973).
(10) H. Ecker, *Kolloid Z.*, **3**, 92 (1940).
(11) H. Yoshioka and K. Nakatsu, *Chem. Phys. Lett.*, **11**, 255 (1971).
(12) B. Dammier and W. Hoppe, *Acta Crystallogr., Sect. B*, **27**, 2364 (1971).
(13) C. E. Johnson and F. A. Bovey, *J. Chem. Phys.*, **29**, 1012 (1958).
(14) J. W. Emsley, J. Feeney, and L. H. Sutcliffe, "High Resolution Nuclear Magnetic Resonance," Vol. 1, Pergamon Press, Oxford, 1965, pp 481–487.
(15) D. J. Blears and S. S. Danyluk, *J. Amer. Chem. Soc.*, **89**, 21 (1967).
(16) J. F. Padday, *J. Phys. Chem.*, **71**, 3488 (1967).
(17) R. B. McKay and P. J. Hillson, *Trans. Faraday Soc.*, **61**, 1800 (1965).
(18) C. W. Haigh and R. B. Mallion, *Org. Magn. Resonance*, **4**, 203 (1972).
(19) P. I. Rose, *Org. Magn. Resonance*, **5**, 187 (1973).
(20) N. Jonathan, S. Gordon, and B. P. Dailey, *J. Chem. Phys.*, **36**, 2443 (1962).
(21) G. Scheibe, F. Haimerl, and W. Hoppe, *Tetrahedron Lett.*, **35**, 3067 (1970).
(22) W. West and S. Pearce, *J. Phys. Chem.*, **69**, 1894 (1965).
(23) G. Scheibe, *Kolloid Z.*, **82**, 1 (1938).
(24) P. J. Dynes, G. S. Chapman, E. Kebede, and F. W. Schneider, *J. Amer. Chem. Soc.*, **94**, 6356 (1972).

An *Electron* Spin Resonance Study of SO_2^- Radicals on Synthetic Zeolites

Yoshio Ono,* Hiroji Tokunaga, and Tominaga Keii

Department of Chemical Engineering, Tokyo Institute of Technology, Ookayama, Meguro-ku, Tokyo, 152, Japan

(Received August 26, 1974)

Publication costs assisted by the Tokyo Institute of Technology

Formation of SO_2^- radicals over various zeolites and alumina has been confirmed using an esr technique. In the case of NH_4Y, the number of radicals is maximum at the adsorption temperature of 200°, and two types of SO_2^- radicals are observed. One gives an esr signal with $g_\parallel = 2.008$ and $g_\perp = 2.002$, is unstable over 300°, undergoes a collisional broadening in the presence of oxygen at room temperature, and reacts with oxygen at 200°. The other gives an esr signal with $g_\parallel = 2.010$ and $g_\perp$ = 2.0[illegible]2, is stable up to 500°, and does not interact with oxygen. It is concluded that the adsorption sites for the former are located in the supercage and that those for the latter are located in the sodalite unit. The effect of the calcination temperature on radical formation indicates that adsorption sites for SO_2^- radicals are formed as a result of deamination and dehydroxylation of NH_4Y. The presence of preadsorbed SO_2^- radicals enhances the formation of O_2^- radicals on decationated zeolites.

Introduction

Zeolites have been known to possess redox properties capable of converting certain adsorbed molecules into the corresponding radical cations and anions.

Stamires and Turkevich[1] have demonstrated that triphenylamine forms cation radicals over decationated zeolites. Since then, many works have been reported on the formation of various cation radicals over zeolites.[2-7] On the other hand, the formation of anion radicals over zeolites has been scarcely reported. Turkevich and Ono[8] reported the formation of trinitrobenzene anions over decationated Y zeolites. Flockhart et al.[9] studied the conditions of the formation of anion radicals of trinitrobenzene and tetracyanoethylene on decationated Y zeolites in some detail.

Stabilization of anion radicals of simple inorganic substances such as oxygen[7-15] or carbon dioxide[16] on zeolite surfaces has been also reported, but anion formation has been always assisted by uv or γ irradiation except for a few cases.[14,15]

We have previously reported that sulfur dioxide, when adsorbed on synthetic mordenite, formed its anion radicals.[7] The present study deals with the formation of sulfur dioxide anions mainly over Y zeolites. The conditions and the mechanism of the formation of anions, their thermal stability, and their interaction with oxygen have been studied.

Experimental Section

Materials. The ammonium form of Y-type zeolite (NH_4Y) was prepared by exchanging the sodium from a Linde type Y zeolite with NH_4^+ cations from an ammonium nitrate solution. The per cent exchange was determined to be 90.5% by flame photometry of the eluted sodium cations. The ammonium form of L-type zeolite (NH_4L) was prepared in the same manner from a type L zeolite obtained from Strem Chemical Inc. The degree of exchange was 45.5%.

Hydrogen mordenite (HM) was obtained from Strem Chemical Inc.

Alumina was prepared by adding aqueous ammonia to aluminum nitrate solution. The precipitate was dried at 90° for 15 hr and then calcined at 500° for 2 hr.

Silica gel was obtained from Mizusawa Chemical Industry. Sulfur dioxide was obtained from Matheson.

Apparatus and Procedure. Adsorption of gases was carried out with a conventional static vacuum system. The standard method for samples preparation was as follows: 50 mg of NH_4Y was placed in an esr sample tube with an inner diameter of 3 mm and evacuated at 200° for 1 hr and then at 600° for 5 hr. The sample was kept under vacuum and showed a small peak at $g = 2.00$, but the intensity was negligibly small in comparison with that of sulfur dioxide anions. Then, the sample was exposed to sulfur dioxide vapor of 13 mmHg at 200° for 2.5 hr. The esr measurements were carried out with a JEOL-PE-1X spectrometer with a 100-kHz field modulation. Radical concentrations were estimated by comparison of the areas obtained by double integration of the first derivative curves for the sample and the standard solution of 1,1-diphenyl-2-picrylhydrazyl.

Results and Discussion

Formation of SO_2^- and Its Thermal Stability. When NH_4Y evacuated at 600° for 5 hr was exposed to sulfur dioxide vapor of 13 mmHg for 2.5 hr at 200°, an esr signal with anisotropic g values of $g_\parallel = 2.008$ and $g_\perp = 2.002$ was observed at room temperature as shown in Figure 1a. The signal was a little broader at −196°. The comparison of these g values with those of SO_2^- in literatures[17-20] indicates that sulfur dioxide forms its anion radical on the zeolite. The intensity and the line shape does not change at all within 24 hr at room temperature.

Then, the thermal stability of SO_2^- was examined by evacuating the system at various temperatures. At room temperature, the radicals were entirely stable for 7 hr and, at 200°, they were still quite stable and the esr intensity decreased only 10% in 4 hr. At these temperatures, the line shapes of the spectra did not change with time; the esr signal with $g_\parallel = 2.008$ was observed all the time. At the evacuation temperature of 300°, the esr intensity decreased considerably in the first 15 min and continued to decrease until it reached 15% of the original intensity after about 1 hr and then remained constant. The decrease in the inten-

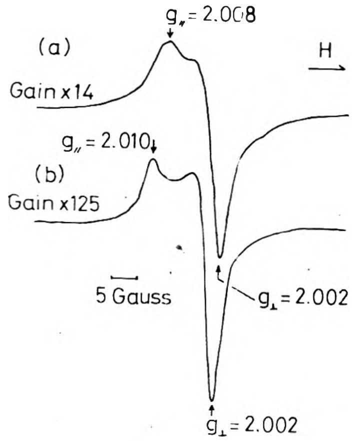

Figure 1. Esr spectra of SO_2^- radicals on decationated Y: (a) SO_2^- formed at 200°, (b) after evacuation at 300°.

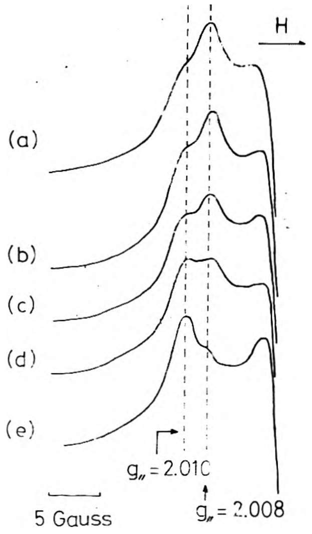

Figure 2. Change in the line shape of SO_2^- signal with adsorption time at 400°: adsorption time (a) 4 min, (b) 15 min, (c) 60 min, (d) 230 min, (e) after evacuation for 45 min.

sity was accompanied by a change in the line shape. The sample evacuated at 300° for 4 hr showed esr signals of $g_\parallel = 2.010$ and $g_\perp = 2.002$, as shown in Figure 1b. When this sample was further evacuated at 500° for 2 hr, the esr intensity decreased only slightly, but the line shape did not change any longer. Then, the sample was again exposed to sulfur dioxide at 200°, and it was found that the esr intensity and the line shape returned to those of the sample before evacuation treatments. This indicates that the decrease in the esr intensity over 300° is caused by the desorption of sulfur dioxide, not by the destruction of the adsorption sites for SO_2^-. It is suggested that there are two types of adsorption sites for SO_2^-; one gives the SO_2^- radicals which show esr signals with $g_\parallel = 2.008$ and $g_\perp = 2.002$, and are unstable over 300°, while the other gives SO_2^- radicals which show the esr signal with $g_\parallel = 2.010$ and $g_\perp = 2.002$ and are stable up to 500°. We will designate the former site A and the latter site B for further discussions.

Effect of Adsorption Temperature on SO_2^- Formation. After NH_4Y was evacuated at 600° for 5 hr, it was exposed to sulfur dioxide vapor at 200° and the change in the esr intensity of SO_2^- was followed with time. The esr intensity increased for first 2.5 hr and then remained constant. The final amount of radicals was 1.4×10^{18} spins/g.

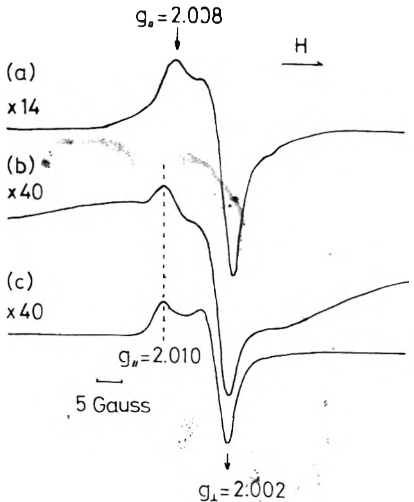

Figure 3. Change in the line shape with oxygen pressure: (a) 0 mmHg, (b) 33 mmHg, (c) 145 mmHg.

The NH_4Y samples treated at 600° for 5 hr were exposed to sulfur dioxide vapor of 13 mmHg for 3.5 hr at various temperatures. Below 200°, the intensity increases with adsorption temperature, suggesting that the formation of SO_2^- needs activation energy. If the adsorption is carried out at room temperature, the esr intensity is only about 4% of the sample of adsorption temperature of 200° even after 15 hr. The intensity is maximum at 200°. Above 300°, the intensity decreases with adsorption temperature, showing that SO_2^- radicals are unstable in this temperature region in accord with the results described in the previous section. Actually, at the adsorption temperature of 400°, the esr intensity decreased with time, and at the same time, the line shape changed (Figure 2). At 2 min, both of the signals with $g_\parallel = 2.008$ and $g_\parallel = 2.010$ were observed, but the relative intensity of the former decreased as the adsorption time increased. When the sample was evacuated at 400° for 45 min, the spectrum showed SO_2^- radicals were present only on site B (Figure 2e). This shows that SO_2^- radicals are formed both at site A and site B initially, but the SO_2^- radicals at site A decays with prolonged heating at 400°.

Interaction of Oxygen with SO_2^- Radicals. The NH_4Y exposed to sulfur dioxide at 200° for 2.5 hr and evacuated at room temperature showed esr signal with a $g_\parallel$ value of 2.008 as shown in Figure 3a. To this system, gaseous oxygen of various pressures was admitted. On admission of 33 mmHg of oxygen, the signal suddenly broadened as shown in Figure 3b. When 145 mmHg of oxygen was added, the spectrum showed a signal of $g_\parallel = 2.010$ (SO_2^- on site B) without any sign of broadening, instead of the signal of $g_\parallel = 2.008$ (SO_2^- on site A) as shown in Figure 3c. Further increase of oxygen pressure did not change the line shape of the spectrum. Evacuation of oxygen at room temperature led to the recovery of both the intensity and the line shape of the esr spectrum to those of the spectrum before oxygen adsorption. Thus, the loss of esr intensity on admission of oxygen is not caused by an irreversible reaction of SO_2^- with oxygen, but by a physical interaction, namely, by a collisional broadening of the esr signal. The above results indicate that only the SO_2^- radicals adsorbed on site A interact with oxygen and that their esr signals are completely washed out as a result of collisional broadening. By contrast, the SO_2^- radicals adsorbed on site B do not undergo the broadening. The difference in the behavior of the SO_2^-

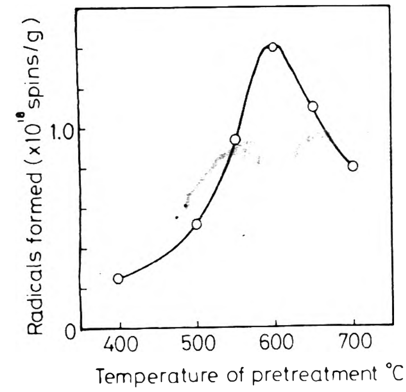

Figure 4. Effect of calcination temperature on the formation of SO_2^- radicals on decationated Y.

adsorbed on site A and those on site B toward oxygen is probably due to the difference in the accessibility of oxygen to the sites: site A may be located in the supercage to which oxygen is easily accessible, while site B may be located in the sodalite unit (most probably site I′) and the entrance of oxygen molecules into the sodalite cage may be blocked at the window of the sodalite cage by the preadsorbed sulfur dioxide at site II or site II′. This also explains the slow desorption of SO_2^- radicals from site B. A similar phenomenon due to the difference in the location of adsorption sites has been reported in the case of the interaction between O_2^- radicals and oxygen.[12]

It is worthy of note that admission of oxygen at room temperature did not affect the concentration of SO_2^-, since the formation of various cation radicals is known to be greatly enhanced by the presence of oxygen.[4,7,21-23] Since adsorbed oxygen is generally considered to work as an electron acceptor in the formation of cation radicals,[4,22,23] it is natural that oxygen does not enhance the formation of anion radicals, in which adsorbed molecules have to accept an electron from the surfaces.

Although the interaction of oxygen with SO_2^- radicals at room temperature is reversible and no decay of SO_2^- is observed within 2 hr, admission of 20 mmHg of oxygen at 200° led to the irreversible decay of the SO_2^- radicals. The intensity of the signal decreased to 5% of that before oxygen admission in 60 min. Since SO_2^- radicals are quite stable at 200° without oxygen as described above, the decay must be caused by a chemical reaction of SO_2^- with oxygen. The sample after the reaction showed only the signal due to SO_2^- radicals adsorbed on site B. These results strongly support the theory that oxygen is not easily accessible to site B.

Effect of the Calcination Temperature on SO_2^- Formation. The NH_4Y zeolites were evacuated at various temperatures for 5 hr and exposed to sulfur dioxide of 13 mmHg for 2.5 hr and esr measurements were carried out. The effect of calcination temperature on the formation of the SO_2^- radicals is shown in Figure 4. The radical amount increases considerably when the calcination temperature is raised from 500 to 600°. The radical amount attains its maximum at 600° and decreases over 650°. These results are qualitatively in agreement with the previous results on the effect of calcination temperature on the formation of trinitrobenzene or tetracyanoethylene anions on decationated zeolites.[8,9] This suggests that the same mechanism is operative for charge transfer. The formation of anion radicals is caused by a charge transfer from the basic sites (B) which are formed by the deamination and the following dehydroxylation of NH_4Y.

TABLE I: g Values of SO_2^- over Different Catalysts

	$g_{yy}(g_{\parallel})$	g_{zz}	$g_{xx}(g_{\perp})$	No. of spins/g
NH_4Y	2.008		2.002	1.2×10^{18}
	2.010		2.002	2×10^{17}
NaY	2.009	2.004	2.002	2×10^{17}
CaY	2.009		2.002	1×10^{17}
CoY	2.009		2.002	1×10^{17}
ZnY	2.010		2.002	
	2.008			7×10^{17}
HM	2.008		2.002	2×10^{17}
NH_4L	2.008		2.001	2×10^{18} $(9 \times 10^{18})^a$
Al_2O_3	2.008		2.002	3×10^{17}

[a] Adsorption of SO_2 at 100°.

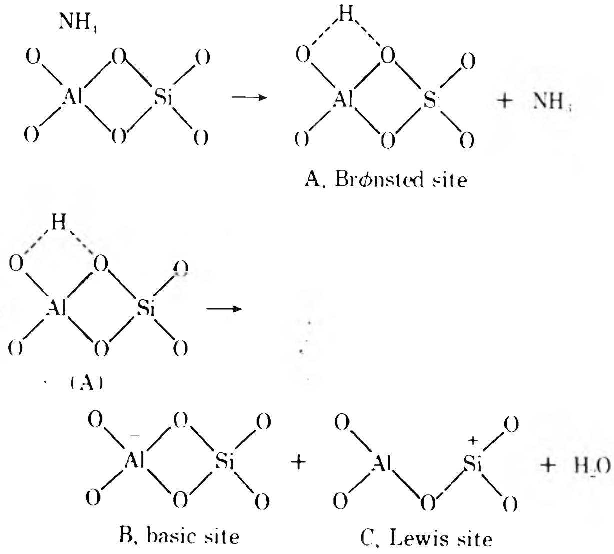

The mechanism of transformation of NH_4Y is well established by a variety of experimental methods.[24-26] The deamination of NH_4Y occurs around 300° and the dehydroxylation occurs around 500°. Turkevich and Ono[8,27] found that the catalytic activities for cracking of cumene and isomerization of xylene fall sharply when the calcination temperature exceeds 500°, and attributed the activity change to the loss of Brønsted sites (A) by dehydroxylation. The formation of cation radicals increases with dehydroxylation and the adsorption sites for cation radicals are considered to be Lewis sites (C).[1,4,9]

The number of the SO_2^- radicals for the sample calcined at 600° is 1.4×10^{18}/g, which is smaller than that from tetracyanoethylene anions adsorbed at room temperature.[9] The difference may be due to the difference in the electron affinities. Since the total adsorption amount of sulfur dioxide at the equilibrium pressure of 13 mmHg at 200° is 1.3×10^{20}/g, only about 1% of the adsorbed sulfur dioxide is in the form of the anion radicals. Decrease in the number of radicals over 650° is considered to be caused by the destruction of the zeolite framework.

The SO_2^- radicals are completely destroyed after the sample was exposed to water vapor of 21 mmHg for 1 hr.

Formation of SO_2^- Radicals on Various Catalysts. The formation of SO_2^- radicals on various catalysts was confirmed. The adsorption of sulfur dioxide was carried out at 200° for the samples treated at 600° for 5 hr. The observed

TABLE II: *g* **Values and the Hyperfine Splitting Constants of O_2^- on Zeolites**

	g_{xx}	g_{yy}	g_{zz}	a_{xx}	a_{yy}	a_{zz}	Ref
Decationated Y with preadsorbed SO_2^-	2.009 ± 0.001	2.002 ± 0.001	2.038 ± 0.001	4.5 ± 0.2	5.0 ± 0.5	5.8 ± 0.4	This work
Decationated mordenite with preadsorbed SO_2^-	2.010 ± 0.001	2.002 ± 0.001	2.040 ± 0.001	4.5 ± 0.4	6.2 ± 0.3	6.1 ± 0.1	This work
Decationated Y γ irradiated	2.009 ± 0.001	2.002 ± 0.001	2.038 ± 0.001	4.7 ± 0.5	5.7 ± 0.5	6.5 ± 0.5	11
AlHY γ irradiated	2.009 ± 0.001	2.003 ± 0.001	2.038 ± 0.001	4.8 ± 0.5	5.7 ± 0.5	6.5 ± 0.5	13

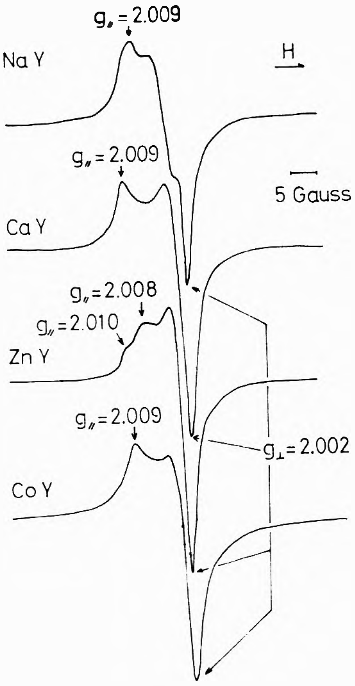

Figure 5. Esr spectra of SO_2^- radicals on various forms of Y zeolite.

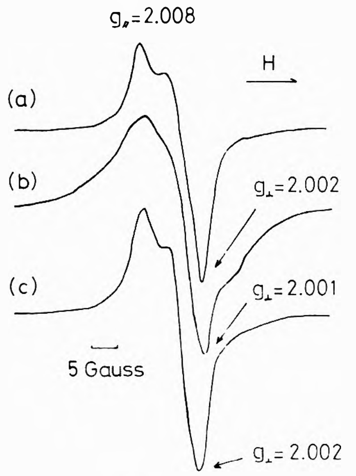

Figure 6. Esr spectra of SO_2^- radicals on (a) decationated mordenite, (b) decationated L, and (c) alumina.

spectra are illustrated in Figures 5 and 6, and their *g* values and radical amounts are listed in Table I.

It should be noted that SO_2^- radicals are formed even on NaY. The amount of radicals on NaY is about 10% of that on NH_4Y. The formation of radicals on NaY may be due to the presence of decationated sites in NaY. Flockhart et al.[9] found that the reduction of tetracyanoethylene occurred on NaY and suggested that the reducing agent was a hydroxyl ion. The metal exchanged zeolites (CaY, CoY, ZnY) and the decationated form of zeolites with different crystal structure (HM and NH_4L) also have reducing activity.

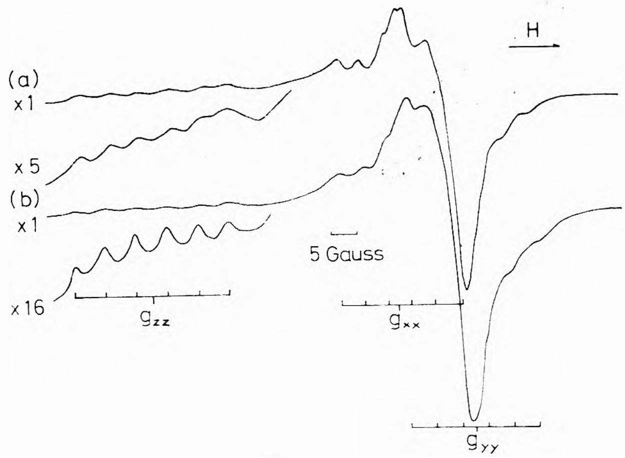

Figure 7. Esr spectra of O_2^- radicals superimposed on those of SO_2^- radicals: (a) decationated Y, (b) decationated mordenite.

The formation of SO_2^- radicals is also observed on alumina, but silica gel has no reducing activity.

It should be noted that the *g* values of the SO_2^- radicals studied in this work are all in the very narrow range ($g_\parallel$ = 2.008–2.010, $g_\perp$ = 2.001–2.002). This indicates that the nature of the adsorption center is considered to be very similar in all cases; the electronegative aluminum sites are responsible for charge transfer. In the cases of the SO_2^- radicals adsorbed on titanium exchanged Y zeolite, g_{yy} value is 2.004, quite different from that of the SO_2^- radicals on the catalysts studied in this work. In the former case, metal cations (Ti^{3+}) are considered to be adsorption centers for SO_2^- radicals.[15]

Formation of O_2^- Radicals on Zeolites with Preadsorbed SO_2^-. When the decationated Y zeolite with adsorbed SO_2^- radicals was kept in an oxygen atmosphere for 19 hr at room temperature and then the system was evacuated, small bumps were superimposed on the spectrum of SO_2^- radicals. These bumps are more clearly seen on prolonged contact with oxygen. Figure 7a shows the spectrum measured at −196° after 2 days contact with oxygen. The spectrum shows the hyperfine structure due to a ^{27}Al nucleus. This new signal is assigned to O_2^- radicals, since both the *g* values and the hyperfine splitting constants agree with O_2^- radicals on γ-irradiated zeolites[11,13] (Table II).

In the case of HM with preadsorbed SO_2^- radicals, O_2^- radicals are more easily formed. After the SO_2^- radicals were formed in an ordinary manner, the catalyst was exposed to 10 mmHg of oxygen for 30 min and then the system was evacuated for 5 min at room temperature. The sample gave the spectrum shown in Figure 7b. The *g* values and the hyperfine splitting constants are listed in Table II. The formation of O_2^- radicals was observed also on NH_4L zeolite.

Without preadsorbed SO_2^- radicals, the zeolites do not give O_2^- radicals after the same treatment. Thus, the mechanism of O_2^- formation is considered to be caused by a successive transfer of an electron in the following manner.

$$e^- + SO_2 \longrightarrow SO_2^-$$

$$SO_2^- + O_2 \longrightarrow O_2^- + SO_2$$

References and Notes

(1) D. N. Stamires and J. Turkevich, *J. Amer. Chem. Soc.*, **86**, 749 (1964).
(2) J. Turkevich, F. Nozaki, and D. N. Stamires, *Proc. Int. Congr. Catal., 3rd, 1964*, **1**, 586 (1965).
(3) A. E. Hirschler, W. C. Neikam, D. S. Barmby, and R. L. James, *J. Catal.*, **4**, 628 (1965).
(4) F. R. Dollish and W. K. Hall, *J. Phys. Chem.*, **71**, 1005 (1967).
(5) J. T. Richardson, *J. Catal.*, 9, 172 (1967).
(6) P. L. Corio and S. Shih, *J. Catal.*, **18**, 126 (1970).
(7) H. Tokunaga, Y. Ono, and T. Keii, *Bull. Chem. Soc. Jap.*, **45**, 3362 (1973).
(8) J. Turkevich and Y. Ono, *Advan. Catal.*, **20**, 135 (1969).
(9) B. D. Flockhart, L. Mcloughlin, and R. C. Pink, *J. Catal.*, **25**, 305 (1972).
(10) P. H. Kasai, *J. Chem. Phys.*, **43**, 3322 (1965).
(11) K. W. Wang and J. H. Lunsford, *J. Phys. Chem.*, **73**, 2069 (1969).
(12) K. W. Wang and J. H. Lunsford, *J. Phys. Chem.*, **74**, 1512 (1970).
(13) K. W. Wang and J. H. Lunsford, *J. Phys. Chem.*, **75**, 1165 (1971).
(14) T. Imai and H. W. Habgood, *J. Phys. Chem.*, **77**, 925 (1973).
(15) Y. Ono, K. Suzuki, and T. Keii, *J. Phys. Chem.*, **78**, 218 (1974).
(16) K. Sogabe, A. Hasegawa, Y. Yamada, and M. Miura, *Bull. Chem. Soc. Jap.*, **45**, 3362 (1972).
(17) J. M. de Lisle and R. M. Golding, *J. Chem. Phys.*, **43**, 3298 (1965).
(18) J. Schneider, B. Dischier, and A. Rauber, *Phys. Status Solidi*, **13**, 141 (1966).
(19) R. A. Schoonheydt and J. H. Lunsford, *J. Phys. Chem.*, **76**, 323 (1972).
(20) K. V. S. Rao and J. H. Lunsford, *J. Phys. Chem.*, **78**, 649 (1974).
(21) H. Imai, Y. Ono, and T. Keii, *J. Phys. Chem.*, **69** 1032 (1965).
(22) B. D. Flockhart, J. A. N. Scott, and R. C. Pink, *Trans. Faraday Soc.*, **62**, 730 (1966).
(23) B. D. Flockhart, I. R. Leith, and R. C. Pink, *J. Catal.*, **9**, 45 (1967).
(24) J. B. Uytterhoeven, L. G. Christner, and W. K. Hall, *J. Phys. Chem.*, **69**, 2117 (1965).
(25) J. Turkevich and S. Ciborowski, *J. Phys. Chem.*, **71**, 3208 (1967).
(26) J. W. Ward, *J. Catal.*, **9**, 225 (1967).
(27) J. Turkevich and Y. Ono, *Advan. Chem. Ser.*, **No. 102**, 315 (1971).

CNDO Model of Carbon Monoxide Chemisorbed on Nickel

G. Blyholder

Department of Chemistry, University of Arkansas, Fayetteville, Arkansas 72701 *(Received October 7, 1974)*

CNDO calculations have been made for the interaction of CO with (100) and (111) faces of clusters containing from 1 to 13 Ni atoms. Binding energies have been determined both with respect to location on the surface and distance from the surface. The parameters in the calculation were chosen for their ability to give reasonable geometric and electron properties for $Ni(CO)_4$ and Ni clusters. The most stable place for CO occurs with multicenter bonding of a carbon atom directly over the center of the hole formed by four surface atoms on the (100) face. The binding energy is not affected much by cluster size. Only the Ni atoms closest to the carbon atom contribute appreciably to the binding energy. Calculated trends in charges indicate that chemisorption of CO causes a negative surface potential in agreement with the experiment and that CO bonded directly over a surface atom has a charge similar to CO in $Ni(CO)_4$ while multicenter and bridge bonded CO is more negative. The relative charges and C–O bond orders correlate well with infrared spectra of chemisorbed CO. The bond orders indicate that Ni s and p orbitals and not d orbitals are primarily responsible for CO bonding to Ni.

I. Introduction

Experimental techniques have been developed to the point that papers regularly appear in the literature dealing with the interaction of small molecules and atoms with well-defined crystallographic planes of metals. While these works give considerable information about the structure of the surface atoms and the energetics of various adsorbed states of molecules, they have not led directly to a knowledge of the structure of the adsorption site and of the metal adsorbate bond angles and distances. Because of the importance of this detailed knowledge to understanding adsorption and catalysis a variety of theoretical models have been proposed to develop a picture of surface complexes which will account for the experimental observations. In this paper the application of a CNDO calculational model to CO adsorption on (100) and (111) faces of Ni is presented.

Theoretical models of chemisorption may be developed on a variety of levels.[1] Weinberg[2] has shown that an empirical bond-energy–bond-order correlation model of chemisorption leads to reasonable values of adsorption energies for a number of light gases and metals. General aspects of many electron theories of adsorption on metals have been reviewed by Schrieffer.[3] Complete ab initio quantum-mechanical treatments of metal crystal surfaces do not seem feasible at present but the great strength of some chemisorption bonds and the variation in behavior of different crystal faces suggest that calculations for a relatively small cluster of metal atoms plus an adsorbate will give a useful model of chemisorption. Grimley[4,5] has developed a formalism for discussing adsorption using perturbation theory and found that the concept of a surface compound is useful in this approach where it was found possible to assume values of interaction potentials which led to reasonable values for the C–Ni bond energy of adsorbed CO.

A molecular orbital model for chemisorbed CO[6] was originally introduced to rationalize infrared spectra of chemisorbed CO. This model which is adapted from MO theory for coordination complexes seeks to describe the role of various atomic and molecular orbitals in charge transfer to and from the metal and the consequences thereof. Using the overlap as an adjustible parameter Doyen and Ertl[7] have applied the Grimley formalism[4,5] to obtain values for the energy of adsorption of CO on different locations on single crystal planes of Ni. Some aspects of the orientation of CO with respect to Ni atoms at a surface have been examined with extended Hückel calculations by Robertson and Wilmsen.[8] Politzer and Kasten[9] have correlated CO infrared stretching frequencies for CO adsorbed on NiO with overlap populations derived from extended Hückel calculations. The CNDO procedure has been used to calculate the interaction energies of light atoms with a group of carbon atoms arranged as in a graphite lattice.[10] The widespread use of semiempitical molecular orbital methods to treat a wide variety of chemical structures has led to some general guidelines for their use. The exact values of quantities such as ionization potentials, spectral transition energies, and dipole moments are usually not accurate; close agreement between calculation and experiment being regarded as merely a happy accident. However, trends in values for similar compounds are often well reproduced by the calculations. Equilibrium bond angles and charge distributions are usually given more accurately than energies. The use of a EHMO procedure for metal clusters[11] calculates a large charge build-up on the central metal atom which should be avoided by CNDO calculations which explicitly contain electron–electron repulsion terms. Also the EHMO method has not usually been successful in giving equilibrium internuclear distances whereas the CNDO methods have.[12] The CNDO procedure used here has been shown[13] to give reasonable values for equilibrium internuclear distance, d band occupancy, binding energy, Fermi level, and d band width for clusters of up to 13 nickel atoms. The results[14] of this CNDO procedure for the interaction of a hydrogen atom with the (111) surface of a cluster of 10 nickel atoms indicated that the bonding involves mainly nickel s and p orbitals and that the most stable position for a hydrogen atom is over a surface hole. This CNDO procedure also gives a reasonable interpretation of the valence shell photoelectron spectrum of chemisorbed CO.[15]

2. Calculation Procedure

The starting point for CNDO (complete neglect of differential overlap) methods is Roothaan's[16] LCAO SCF equations, which are simplified by ignoring and approximating large numbers of integrals so that the computations for a large molecule can be carried out on a computer in a reasonable length of time, i.e., from a few minutes to 1 hr. The CNDO procedure used was basically a modification of that by Pople *et al.*[17–19] The modifications mainly consist in recognizing d orbitals as being sufficiently different from s and p orbitals as to require separate treatment. The diagonal F matrix elements are like those of Baetzold[20] in which the d orbitals have different orbital exponential coefficients from the s and p orbitals. In the off-diagonal F matrix elements a different parameter was used to represent the resonance integrals for d electrons from that used for s and p electrons as in the work of Clack *et al.*[21] Slater type orbitals were used. All valence shell electrons in the 3d, 4s, and 4p orbitals of nickel were included while all inner-shell electrons were treated as part of a nonpolarizable core. Closed shell calculations were done here because of the limitation on computer memory, but this is quite satisfactory since the main interest here is in ground state geometry and energies and not in magnetic properties which would require open shell calculations.

The molecular orbital ϕ_i is given by

$$\phi_i = \sum_{\mu} C_{\mu i} X_{\mu} \tag{1}$$

where $C_{\mu i}$ is the coefficient of the atomic orbital X_{μ} in molecular orbital i. The matrix equation

$$FC = CE \tag{2}$$

is solved with the diagonal matrix elements

$$\begin{aligned} F_{\mu\mu}{}^{A}(\mathrm{s}) = {} & -(1/2)(I_{\mathrm{s}}{}^{A} + A_{\mathrm{s}}{}^{A}) - (N_{\mathrm{s}}{}^{A} - 1/2)\gamma_{\mathrm{ss}}{}^{A} - \\ & N_{\mathrm{d}}{}^{A}\gamma_{\mathrm{ss'}}{}^{A} - (1/2)P_{\mu\mu}\gamma_{\mathrm{ss}}{}^{A} + \sum_{\lambda} P_{\lambda\lambda}\gamma_{\mu\lambda} - \\ & \sum_{B \neq A} (N_{\mathrm{s}}{}^{B}\gamma_{\mathrm{ss}}{}^{AB} + N_{\mathrm{d}}{}^{B}\gamma_{\mathrm{ss'}}{}^{AB}) \end{aligned} \tag{3}$$

$$\begin{aligned} F_{\mu\mu}{}^{A}(\mathrm{d}) = {} & -(1/2)(I_{\mathrm{d}}{}^{A} + A_{\mathrm{d}}{}^{A}) - N_{\mathrm{s}}{}^{A}\gamma_{\mathrm{s's}}{}^{A} - \\ & (N_{\mathrm{d}}{}^{A} - 1/2)\gamma_{\mathrm{s's'}}{}^{A} - (1/2)P_{\mu\mu}\gamma_{\mathrm{s's'}}{}^{A} + \sum_{\lambda} P_{\lambda\lambda}\gamma_{\mu\lambda} - \\ & \sum_{B \neq A} (N_{\mathrm{s}}{}^{B}\gamma_{\mathrm{s's}}{}^{AB} + N_{\mathrm{d}}{}^{B}\gamma_{\mathrm{s's'}}{}^{AB}) \end{aligned} \tag{4}$$

and the off-diagonal elements

$$F_{\mu\nu}{}^{AB} = (1/2)(\beta^{A} + \beta^{B})S_{\mu\nu} - (1/2)P_{\mu\nu}\gamma_{\mu\nu}{}^{AB} \tag{5}$$

where $I_{\mathrm{s}}{}^{A}$ is the ionization potential of an electron from an s orbital on atom A, A is the electron affinity, $N_{\mathrm{s}}{}^{A}$ is the total number of valence shell s and p electrons on atom A in the initial atom configuration, N_{d} is the number of d electrons in the initial configuration and

$$P_{\mu\nu} = 2\sum_{i} C_{\mu i} C_{\nu i} \tag{6}$$

with the sum being over occupied molecular orbitals. Since matrix eq 2 depends on the values of the coefficients, $C_{\mu i}$, which are calculated by solution of the matrix equation, the final solution is obtained by an iterative procedure where the coefficients from one solution are used to calculate a new solution for coefficients and total energy until two successive energies agree to within 10^{-4} atomic units.

The two center electron repulsion integrals are given by

$$\gamma_{\mathrm{ss'}}{}^{AB} = \int\int X_{\mathrm{s}}{}^{A}(1)\, X_{\mathrm{s}}{}^{A}(1)(1/r_{12}) X_{\mathrm{s'}}{}^{B}(2) X_{\mathrm{s'}}{}^{B}(2)\, \mathrm{d}\tau_1\, \mathrm{d}\tau_2. \tag{7}$$

where the integration is over all values of position coordinated $\mathrm{d}\tau_1$ and $\mathrm{d}\tau_2$ for electrons 1 and 2 in orbitals s and s′ on atomic orbitals X^A and X^B of atoms A and B respectively and r_{12} is the distance between electrons 1 and 2. The electron repulsion integrals involving only s orbitals are readily calculated so all p and d orbitals in electron repulsion integrals are replaced by s orbitals with the same orbital coefficient. In eq 3–5 the s and p orbitals are referred to with a subscript s and the d orbitals with a subscript s′. All d orbitals of an atom are treated as being equivalent. The notation $\gamma_{ss'}{}^{A}$ refers to the case where both orbitals s and s′ are on atom A. The resonance integrals, β, are treated as arbitrary constants. In eq 4 β^A is $\beta_d{}^A$ or $\beta_s{}^A$ depending on whether μ is a d or an s or p orbital and likewise for β^B.

The input parameters used for nickel atoms are listed in Table I. These were chosen on the basis of giving reasonable values of equilibrium bond length, d orbital occupancy, binding energy, Fermi level, and d band width for a cluster of six nickel atoms.[13] The basis for the parameter selection, the effect of parameter variation, and a fuller discussion of the development of the equations used here have been reported,[22] as there are no established CNDO parameters for transition metals. The carbon and oxygen atom parameters are those given by Pople *et al.*[12]

The calculations were performed on the Facom 230-60 computer at the Hokkaido University Computer Center.

3. Results

The results of calculations for the interaction of one CO molecule with various Ni clusters are given in Tables II–IV. The arrangements of the atoms in the clusters are given in Figure 1. The Ni lattice parameters used were based on a Ni–Ni nearest distance of 2.50 Å. Although the coordinates are rounded off in Figure 1 and in the tables, the input to the computer program contained the coordinates to six significant figures. In all cases, except for the one indicated on Table II, the C and O atoms are located on a line normal to the surface with a CO distance of 1.15 Å. In obtaining equilibrium distances for the CO molecule from the surface the energies were determined usually at 0.1-Å intervals. The binding energy is the difference in energy between the clusters with a CO molecule and the sum of the isolated CO molecule electronic energy plus the energy of the same Ni cluster without the CO molecule.

The results in Table III indicate that the most stable position for chemisorbed CO is with multicenter bonding on the (100) face. As the CO moves from directly over an atom toward a nearest neighbor to form a bridge bond the binding energy increases until the midpoint between the two atoms is reached. For a bridge bond the symmetrical bridge is the most stable. The equilibrium distance above the plane of the surface decreases as the CO goes from being above one atom to the symmetrical bridge position. Also indicated in Table III is that as the CO goes from the symmetrical bridge location to the symmetrical multicenter position the binding energy increases and the height above the surface plane decreases.

4. Discussion

The CNDO method and parameters used here give quite good values for the Ni–C equilibrium bond length in $Ni(CO)_4$ but the binding energy of CO to Ni is considerably too high. Table II shows a calculated equilibrium Ni–C distance of 1.8 ± 0.1 Å which is in good agreement with the experimental value of 1.82 Å.[23] The calculated binding energy per CO molecule in $Ni(CO)_4$ is 0.24 au whereas the experimental value is around 0.05 au. Likewise the binding energies for chemisorbed CO in Table II of 3.5 to 8.4 eV are considerably above the experimental chemisorption energies reported in the range of 1.4–2 eV.[24,25] In these CNDO calculations the parameters have not been optimized for CO adsorption on Ni but rather parameters previously selected for other situations were used. For C and O the standard parameters of Pople *et al.*[12] which fit CH and OH units but give too large binding energies for CH_4, H_2O, CO, CO_2, etc. were used. The Ni parameters used were those previously used to fit Ni clusters.[13] Undoubtedly better binding energies could be obtained by optimizing the parameters for the CO and Ni system.

As noted in the Introduction the most useful result of approximate calculations is not absolute values but trends. For CO adsorbed directly above one Ni atom the binding energy is not a strong function of the cluster size. In Table II the binding energy stays about constant for 1 to 13 atom clusters; the special case of CO on an exposed Ni atom in

TABLE I: Nickel Atom Parameters for an Initial Configuration of $3d^8$, $4s^2$, $4p^0$; β, Resonance Integral; ξ, Orbital Exponential Coefficient; *I*, Ionization Potential; and *A*, Electron Affinity

β_s	−6 eV
β_d	−10 eV
ξ_s	1.8
ξ_d	2.5
$(I_s + A_s)/2$	4.3 eV
$(I_p + A_p)/2$	1.3 eV
$(I_d + A_d)/2$	10.0 eV

TABLE II: CNDO Calculations for CO Interacting with Ni Clusters Having the CO Directly Over a Ni Atom

Type of cluster[a]	Binding of energy CO, au	Charge on CO, e	Ni–C[b] distance
$Ni(CO)_4$	0.24	+0.20	1.8*
Linear Ni CO	0.23	+0.14	1.8*
(100) planar Ni_5CO (1, 2, 4–6)	0.29	+0.18	1.8*
(100) cluster Ni_9CO (1, 2, 4–10)	0.24	+0.21	1.8
(100) cluster $Ni_{13}CO$ (1–13)	0.31	+0.22	1.8
(111) planar Ni_7CO (1–7)	0.27	+0.19	1.8
(111) cluster $Ni_{10}CO$ (1–10)	0.27	+0.22	1.8
(100) Ni_4NiCO (1–4)[c]	0.13	+0.28	1.8*
(100) Ni_4NiCO bent (1–4)[d]	0.22	+0.23	1.8
(111) Ni_5NiCO (1–5)[e]	0.13	+0.19	1.8

[a] The numbers in parentheses after each Ni cluster refer to the atom numbers in Figure 1. [b] The asterisk indicates equilibrium distance determined. [c] The fifth Ni atom has *x*, *y*, *z* coordinates 1.25, 1.25, 1.77 Å and the CO molecule is located linearly above it. [d] Same arrangement as in *c* except that the line on which the NiCO are located is at 45° to the surface normal. The Ni atom position is unchanged. [e] The sixth Ni atom has *x*, *y*, *z* coordinates 0, 1.44, 2.04 Å and the CO molecule is located linearly above it.

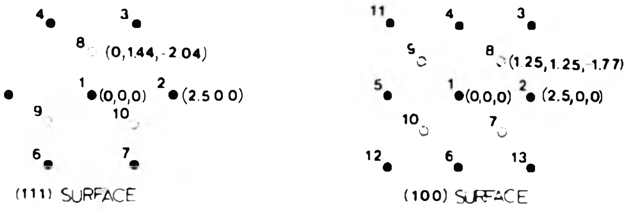

Figure 1. Atom coordinates and numbering for Ni clusters. Open circles indicate subsurface atoms.

TABLE III: CNDO Calculations for CO Interaction with Ni Clusters Having the CO in Bridge and Multicenter Locations

Type of cluster	Binding energy of CO, au	Charge on CO, e	Coordinates of C atom[a]
(100) Ni_5CO (1–4,8) CO over atom	0.21	+0.21	0, 0, 1.8*
(100) Ni_5CO (1–4,8) asymmetric bridge	0.22	+0.19	0.25, 0, 1.8*
(100) Ni_5CO (1–4,8) asymmetric bridge	0.29	+0.08	0.75, 0, 1.6*
(100) Ni_5CO (1–4,8) asymmetric bridge	0.35	+0.03	1.0, 0, 1.5*
(100) Ni_5CO (1–4, 8) symmetric bridge	0.39	0.00	1.25, 0, 1.4*
(100) Ni_5CO (1–4,8) multicenter asym	0.41	+0.05	1.25, 0.25, 1.4*
(100) Ni_5CO (1–4,8) multicenter asym	0.61	+0.11	1.25, 1.0, 0.7*
(100) Ni_5CO (1–4,8) multicenter sym	0.70	+0.16	1.25, 1.25, 0.6*
(100) Ni_4CO (1–4) symmetric bridge	0.39	+0.06	1.25, 0, 1.5*
(111) Ni_6CO (1–5, 8) symmetric bridge	0.39	+0.10	0.625, 1.08, 1.3*
(111) Ni_6CO (1–5,8) CO over subsurface Ni	0.46	+0.06	0, 1.4, 1.3*
(111) Ni_6CO (1–5, 8) CO over hole	0.48	+0.09	1.25, 0.72, 1.3*

[a] The asterisk indicates equilibrium distance above surface determined.

the last three lines of Table II being an exception. This is true for both (100) and (111) planar and three-dimensional clusters included in Table II. This result indicates that the cluster size taken for the calculations is not affecting the results greatly. This lends credence to representing some, but certainly not all, aspects of chemisorption by calculations with small clusters.

Comparison of the binding energies of CO in Tables II and III indicates that a bridge bond with the carbon atom between two Ni atoms and a multicenter bond with the carbon atom over a hole formed by three or four surface atoms are more stable than the bond with the C atom directly over a surface atom. The multicenter bond is more stable than the bridge bond. The LEED pattern for CO on the (100) Ni face shows an ordered C(2 × 2) pattern which is consistent with the multicenter bonding location. Tracy[24] proposed such a structural model for the LEED pattern while Park and Farnsworth[26] proposed a bridge structure for the C(2 × 2) LEED pattern.

The binding energy for a bridge CO structure on the (100) face is seen in Table III to be about 56% of the maximum binding energy for the symmetric multicenter position. Since the bridge location is at the highest potential energy for a CO molecule moving along the minimum energy path between two multicenter positions, the activation energy for diffusion over a sparsely covered (100) surface would be expected to be about 44% of the maximum experimental binding energy of 30 kcal/mol[24] or about 13 kcal/mol.

While most of the clusters representing the (100) face contained five Ni atoms, some calculations with a four atom cluster were made as indicated in Table III. When the fifth Ni atom located below the centroid of the four surface atoms is missing the equilibrium distance of the CO above the surface plane is not appreciably changed nor is the binding energy appreciably changed for both the bridge and multicenter positions. In the multicenter location the distance from the carbon atom to the Ni atom in the subsurface layer is about 2.4 Å which is considerably longer than the Ni–C distance of about 1.9 Å to the surface atoms. Thus only the Ni atoms closest to the CO affect the CO binding energy.

The CO interaction with the (111) face of a six atom cluster with the CO in a multicenter position over the hole formed by three surface atoms has a binding energy about 2/3 of that for the (100) face as shown in Table III. Preliminary data have been quoted[7] as giving a lower binding energy for CO on the (111) face than for the (100) face of Ni. There are two kinds of triangular surface holes on the (111) face; one with and one without an atom directly below the center of the hole. As indicated in Table III, the difference in binding energy for these two sites is small. This result is in keeping with the fact that the Ni–C distance is 3.3 Å to the subsurface Ni atom while the equilibrium distance to the surface atoms is only about 1.9 Å.

Some aspects of the binding of a CO molecule to an exposed Ni atom which is the only atom in its plane above a (100) or (111) plane are given in Table II. When the CO molecule is located directly above the exposed Ni atom the resulting binding energy of 0.13 au is only about half of that obtained when the Ni atom is part of the main top layer. One might have expected a higher binding energy for CO to such an exposed surface atom but this was not found for both the (100) and (111) surfaces. However, when the CO molecule was tilted at a 45° angle to the surface normal, the binding energy to the exposed atom of 0.22 *au is* about that for a bonding site directly over an atom in the surface layer.

For the parameters used these calculations do not give good values for absolute charges on atoms but the trend in a series is consistent with experimental observations. Ab initio calculations[27] for $Ni(CO)_4$ have the Ni atom slightly positive and the CO ligands slightly negative while the CNDO method and parameters used here give a charge of +0.2 e on the CO ligands. For CO attached to a cluster of Ni atoms the charge on the CO given in Table II is about the same if the CO is directly over one Ni atom. Normalized to $Ni(CO)_4$ these calculations indicate chemisorbed CO would have a negative charge. This is in accord with the experimental observaton that chemisorbed CO produces a negative surface potential.[28] The relative calculated charges for CO interacting with different sites on the clusters are also in accord with the observed infrared bands for chemisorbed CO, which are broad bands in the region of 2075 and 1935 cm^{-1}.[29] In the general molecular orbital model of ligand or chemisorbed CO, the infrared band position is shifted to lower frequencies as more electron density is transferred onto the CO unit in orbitals which are antibonding in the CO π system.[6,29] The asymmetric C–O stretch in molecular $Ni(CO)_4$ occurs at about 2058 cm^{-1}.[30] This corresponds with the high-frequency band of chemisorbed CO and the CNDO calculations give very similar charges on the CO unit in $Ni(CO)_4$ and adsorbed directly over a surface atom. For multicenter bonded CO the calculations put

TABLE IV: Bond Orders for CO Interacting with Ni Clusters

Type of cluster	Ni–C bond order				C–O bond order	
		s, p	d	Total		
$Ni(CO)_1$	σ	0.57	0.05	0.62	σ	0.72
	π	0.07	0.07	0.14	π	0.42
	Total	0.64	0.12	0.76	Total	1.14
(100) Ni_5CO	σ	0.55	0.06	0.61	σ	0.72
CO directly over Ni	π	0.08	0.09	0.17	π	0.40
	Total	0.63	0.15	0.78	Total	1.12
(100) Ni_5CO	$\sigma + \pi$	1.95	0.44	2.39	σ	0.68
multicenter					π	0.26
					Total	0.94

more negative charge on the CO which will give lower infrared frequencies corresponding to the several bands making up the very broad absorption feature centered at 1935 cm^{-1}.

The infrared band positions for chemisorbed CO may also be correlated with the bond orders in Table IV calculated from the molecular orbital coefficients. The C–O bond order for CO directly over a surface atom is about the same as in $Ni(CO)_4$, thus agreeing with the assignment of the 2075-cm^{-1} band to this structure. For multicenter bonded CO the C–O bond order is only 83% of that for $Ni(CO)_4$, thus strengthening the assignment of the 1935-cm^{-1} feature to multicenter and bridge bonded CO. The main drop in bond order occurs in the π bond order which fits the general molecular orbital picture of the π bonding system having a large influence on the infrared band position.

The calculated bond orders indicate that the Ni s and p orbitals are primarily responsible for the Ni–C bond with the d orbitals making only a small contribution to the bond order. This result is somewhat at variance with the past great emphasis that has been placed on the role of d electrons in chemisorption. Indeed, the case of Ni may be different from other transition metals in this respect and even here the d orbitals are important in determining the charge distribution. The importance of the Ni s and p orbitals is not confined to CO chemisorption as both CNDO[14] and extended Hückel[11] calculations indicate that the bond order for H atom adsorption on Ni is due mainly to Ni s and p orbitals. Of course one needs to be cautious of the results of semiempirical calculations, particularly those such as the relative importance of different orbitals which could be greatly affected by the choice of parameters. One fact that lends credence to the importance of the Ni s and p orbitals is that an ab initio calculation for $Ni(CO)_4$[27] also indicates the s and p orbitals make a larger contribution to the Ni–C bond order than do the d orbitals. This CNDO method reproduces that result for $Ni(CO)_4$.

The adsorption of CO on Ni has been treated previously by other approximate theoretical methods. Since all of the methods are approximate, they all have their advantages and disadvantages. An extended Hückel procedure was used by Robertson and Wilmsen[8] to examine some different orientations of CO on clusters of Ni atoms. They found a bridge CO structure to be more stable than a linear Ni CO system which these CNDO calculations agree with, but they apparently did not consider the multicenter position which the CNDO procedure gives as the most stable. As used the extended Hückel calculations give an energy minimum for the adsorbed CO at an asymmetric position between two Ni atoms. This result is probably a result of the carbon atom being maintained at a constant distance above the surface as it was moved between two Ni atoms to determine the energy minimum. In the CNDO calculation (Table III) the energy minimum is symmetrically located between the two Ni atoms and at this location the carbon atom is closer to the surface plane than when directly over one Ni atom. This points out one of the advantages of the CNDO method over the extended Hückel which Robertson and Wilmsen stated was not useful for determining bond lengths. They used a constant distance of the carbon atom over the surface whereas in the CNDO calculation the energy minimum with respect to vertical displacement of the CO was determined for each location on the surface grid. However, the extended Hückel method certainly comes closer to the absolute values of the adsorption energy than does the CNDO procedure with the parameters used here.

In the application by Doyen and Ertl[7] of the perturbation formalism developed by Grimley to CO chemisorption the binding energy of CO to the surface is normalized at one location to the observed chemisorption energy and the variations in binding energy as a function of surface location determined. Thus the question of an absolute determination of binding energy does not arise. The results of Doyen and Ertl and the CNDO results are in good agreement as to the location of the maximum and minimum energy sites. Charge distributions were not discussed in their paper. The binding energy in their formalism is proportional to an overlap integral which was determined using only Ni d orbitals so nominally they attributed the bonding to only Ni d orbitals. The CNDO results indicate s and p orbitals are also important, perhaps even more important than d orbitals. However since the s and p orbitals make up a spherically symmetric distribution about the Ni nuclei as do the d orbitals, the resulting binding energy distribution as a function of surface position would be about the same for s and p overlap use as it was for d orbital use. Thus their main results are independent of whether one attributes the binding to s and p or to d orbitals. The CNDO procedure has the advantage of furnishing a natural basis for discussing the relative involvement of different orbitals while the perturbation formalism used by Doyen and Ertl takes into account the influence of extended metal properties on the chemisorption band.

Since exact ab initio calculations for chemisorption are too difficult at present, I believe all types of approximate calculations should be done. While one cannot place too much faith in any one result of a single approximate method, those results on which several approximate methods agree, such as has now been obtained for relative binding energies of CO on different Ni sites, are likely to be correct.

Acknowledgment. Partial support from the U.S. National Science Foundation in a grant under the Japan–U.S. Cooperative Science Program is acknowledged with thanks. The author is also appreciative of grants for computing time from the Research Institute for Catalysis at Hokkaido University and from the Graduate School at the University of Arkansas. This research was also partially supported by National Science Foundation Grant No. GP-24757.

References and Notes

(1) G. Blyholder, "Modern Aspects of Electrochemistry", Vol. 8, J. O'M. Bockris and B. E. Conway, Ed., Plenum Press, New York, N.Y., 1972, Chapter 1.
(2) W. H. Weinberg, *J. Vac. Sci. Tech.*, **10**, 89 (1973).
(3) J. R. Schrieffer, *J. Vac. Sci. Tech.*, **9**, 561 (1972).
(4) T. B. Grimley, "Molecular Processes on Solid Surfaces", E. Drauglis, *et al.*, Ed., McGraw-Hill, New York, N.Y., 1969, p 299.
(5) T. B. Grimley, *J. Vac. Sci. Tech.*, **8**, 31 (1971).
(6) G. Blyholder, *J. Phys. Chem.*, **68**, 2772 (1964).
(7) G. Doyen and G. Ertl, *Surface Sci.*, **43**, 197 (1974).
(8) J. C. Robertson and C. W. Wilmsen, *J. Vac. Sci. Tech.*, **9**, 901 (1972).
(9) P. Politzer and S. D. Kasten, *Surface Sci.*, **36**, 186 (1973).
(10) A. J. Bennett, B. McCarroll, and R. P. Messmer, *Phys. Rev. B*, **3**, 1397 (1971).
(11) D. J. M. Fassaert, H. Verbeek, and A. Van der Avoird, *Surface Sci.*, **29**, 501 (1972).
(12) J. A. Pople and D. L. Beveridge, "Approximate Molecular Orbital Theory", McGraw-Hill, New York, N.Y., 1970.
(13) G. Blyholder, *Surface Sci.*, **42**, 249 (1974).
(14) G. Blyholder, *Chem. Commun.*, 625 (1973).
(15) G. Blyholder, *J. Vac. Sci. Tech.*, accepted for publication.
(16) C. C. J. Roothaan, *Rev. Mod. Phys.*, **23**, 69 (1951).
(17) J. A. Pople, D. P. Santry, and G. A. Segal, *J. Chem. Phys.*, **43**, S129 (1965).
(18) J. A. Pople and G. A. Segal, *J. Chem. Phys.*, **43**, S136 (1965); **44**, 3289 (1966).
(19) D. P. Santry and G. A. Segal, *J. Chem. Phys.*, **47**, 158 (1967).
(20) R. C. Baetzold, *J. Chem. Phys.*, **55**, 4335 (1971).
(21) D. W. Clack, N. S. Hush, and J. R. Yandle, *J. Chem. Phys.*, **57**, 3503 (1972).
(22) G. Blyholder, accepted by *J. Res. Instit Catal., Hokkaido Univ.*
(23) L. O. Brockway and P. C. Cross, *J. Chem. Phys.*, **3**, 828 (1935).
(24) J. C. Tracy, *J. Chem. Phys.*, **56**, 2736 (1972).
(25) R. R. Ford, *Adv. Catal.*, **21**, 51 (1970)
(26) R. L. Park and H. E. Farnsworth, *J. Chem. Phys.*, **43**, 2351 (1965).
(27) I. H. Hillier and V. R. Saunders, *Mol. Phys.*, **22**, 1025 (1971).
(28) R. V. Culver and F. C. Tompkins, *Adv. Catal.*, **11**, 67 (1959).
(29) G. Blyholder and M. Allen, *J. Am. Chem. Soc.*, **91**, 3158 (1969).
(30) L. H. Jones, *J. Chem. Phys.*, **28**, 1215 (1958).

COMMUNICATIONS TO THE EDITOR

An Infrared Study of Some Reactions with Reactive Sites on Dehydroxylated Silica

Publication costs assisted by Imperial Oil Limited

Sir: A previous infrared spectroscopic study of the reactions of BCl_3 and of BF_3 on silica[1,2] indicated that a new reactive site was formed as the isolated SiOH groups were removed by thermal degassing under vacuum. This new site was associated with the growth of bands in the background spectrum of silica at 908 and 888 cm^{-1} (see ref 2) as the intensity of the 3748-cm^{-1} SiOH band decreased in intensity and was presumed to be a strained siloxane bridge although proof was lacking. In the present communication, a study of the chemisorption of H_2O, NH_3, and of CH_3OH on highly dehydroxylated silica has provided further evidence that this site corresponds to a siloxane type site which forms when the degassing temperature under vacuum is greater than 400°. In addition a new type of SiOH species is formed following the reaction of the aforementioned molecules with these sites.

Details of silica sample disk preparation[3] (10 mg of SiO_2/cm^2) and of the reaction cell[4] have been described elsewhere. All adsorption reactions were carried out at room temperature.

Following admission of 10 Torr of H_2O to a silica sample which had been degassed at 1100° under vacuum the bands at 908/888 cm^{-1} immediately disappeared and a new broad band at 3741 cm^{-1} appeared as a shoulder on the side of the normal isolated SiOH band at 3748 cm^{-1} (Figure 1A). When the sample was titrated with small incremental doses of H_2O (1–5 μmol) the 908/888 cm^{-1} bands disappeared in proportion to the growth in intensity of the 3741-cm^{-1} band but the intensity of the band at 3748 cm^{-1} did not change.

When a degassed deuterated silica (normal SiOD band at 2764 cm^{-1}) was similarly titrated with H_2O only the broad 3741-cm^{-1} band was observed (Figure 1B) and its half-width was about 19 cm^{-1}. When D_2O was added to a hydrogen containing silica, the corresponding broad band appeared at 2758 cm^{-1}. Upon adding $H_2{}^{18}O$ (98.6% oxygen-18) a very broad ($\nu_{1/2} \simeq 30$ cm^{-1}) band appeared at 3735 cm^{-1} (Figure 1C) with shoulders to low and high wave number. This band could be reconstructed from the sum of two identical broad bands with half-widths of 19 cm^{-1} centered at 3741 and 3730 cm^{-1}, one corresponding to a $Si^{16}OH$ and the other to a $Si^{18}OH$ (Figure 1D). [The ^{18}O isotope shift[2] for the 3748-cm^{-1} SiOH band is 11 cm^{-1}.]

Using NH_3 for the titration, a somewhat more symmetrical and narrower ($\nu_{1/2} = 12$ cm^{-1}) band appeared at 3741 cm^{-1} (Figure 1E) as the 908/888 cm^{-1} bands disappeared and these changes were accompanied by the parallel growth of infrared bands at 3540, 3450, and 1550 cm^{-1} due the $SiNH_2$ groups.[5] An identical band at 3741 cm^{-1} also appeared when CH_3OH was used and bands due to $SiOCH_3$ were detected in the νCH region.[6]

The 908/888-cm^{-1} bands were just detectable if the degassing temperature was 400°, as was the broad 3741-cm^{-1} band if H_2O or NH_3 was added. With higher degassing temperatures, all bands increased in intensity indicating the formation of an increasing number of reactive sites with increasing degassing temperatures up to a maximum of about 1200° (the softening point of quartz) when the silica was totally dehydroxylated.

Prolonged evacuation at room temperature or up to about 300° did not result in any alteration of the intensity

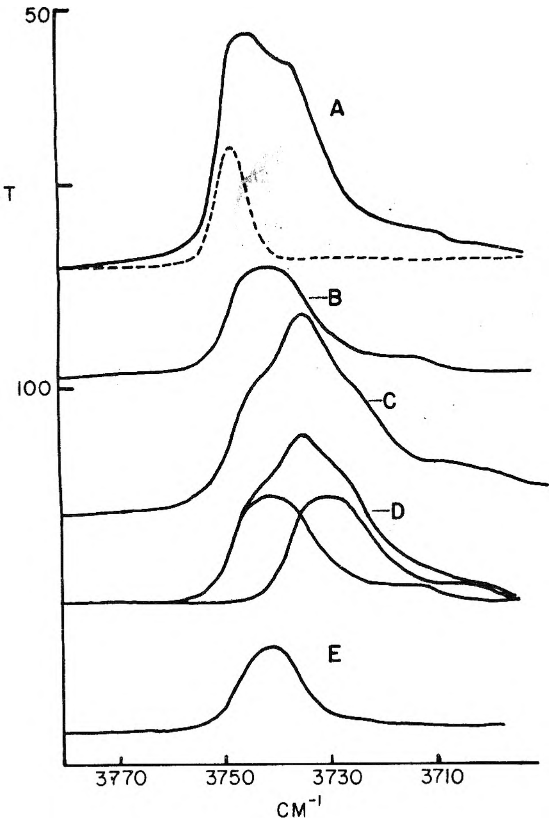

Figure 1. (A) Dashed line represents the residual 3748-cm^{-1} SiOH band on a silica which had been degassed under vacuum at about 1100°. Solid line spectrum was obtained after admitting 10 Torr of H_2O at 20° and evacuating the excess. (B) After adding 5 μmol of H_2O to a degassed deuterated silica. (C) After adding $H_2{}^{18}O$ to a degassed deuterated silica. (D) Taking two spectra as in B, displacing one by 11 cm^{-1} to 3730 cm^{-1}, and summing the two (see text). (E) After adding 5 μmol of NH_3 to a degassed deuterated silica and evacuating the excess. The % *T* scale refers to Figure A.

of the 3741-cm^{-1} band (or of the bands due to $SiNH_2$ when present) but with increasing temperatures (>400°) the 3741-cm^{-1} band diminished in intensity (as did the $SiNH_2$ bands) and the 908/888-cm^{-1} bands reappeared.

At no stage in this work were any bands observed between 2400 and 2000 cm^{-1} which could be attributed to the formation of SiH containing species. Further, no reaction took place between degassed silica and C_2H_4, HCN, HCl, O_2, H_2, or PH_3.

Assuming that the new site corresponds to a "reactive" siloxane bridge site, the stoichiometry for reaction could be represented as follows:

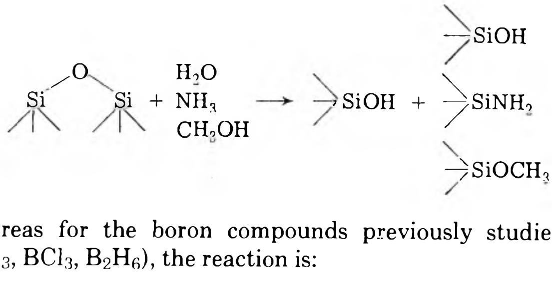

whereas for the boron compounds previously studied[1,2] (BF_3, BCl_3, B_2H_6), the reaction is:

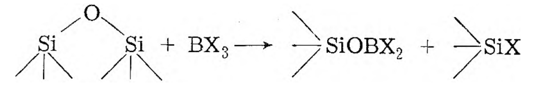

For reaction with $H_2{}^{18}O$ a pair of broad SiOH bands are to be expected with equal intensities and separated by 11 cm^{-1}.

It is difficult to account for the results on the assumption that the surface is oxygen deficient and contains Si radical sites (further, no ESR signals have been detected for degassed samples[2]) or are

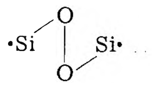

type sites involved as has been postulated by Low from the pyrolysis of methylated silica.[7] We have also considered the possibility that geminal functional groups are formed and that the somewhat broader band at 3741 cm^{-1} when H_2O is the reactant is due to coupling between the identical $Si(OH)_2$ groups. However, we have rejected this since the peak position and band width remained constant for any H/D ratio (e.g. and 1:9 H_2O–D_2O mixture should give a spectrum in the νOH region which contains 95% SiOH–SiOD pairs and only 5% SiOH–SiOH pairs). Nonetheless, the unusual breadth and slight low wave number shift of the 3741-cm^{-1} band relative to the 3748-cm^{-1} SiOH band might reflect a very weak type of hydrogen bond interaction with the neighboring SiOH, $SiNH_2$, or $SiOCH_3$ groups, or it might simply be a reflection of some unusual geometry.

The existence of reactive siloxane bridge sites which are formed as a result of the thermal dehydroxylation of silica has been suggested by others.[8-11] Such sites might account for many of the anomalies (i.e., high surface chlorine values) which have been noted in studies of the chlorination of degassed silica by hydrogen sequestering agents.[12,13] We also note that the 400° pretreatment for the initial appearance of these sites coincides with maximum temperature to which silica gels can be heated before rehydration becomes somewhat irreversible and the onset of hydrophobicity starts.[14] Further details of our investigations of the nature of these sites will be reported later.

Acknowledgment. Support for this work was provided by Imperial Oil Ltd. and by the National Research Council of Canada.

References and Notes

(1) B. A. Morrow and A. Devi, *Chem. Commun.*, 1237 (1971).
(2) B. A. Morrow and A. Devi, *J. Chem. Soc., Faraday Trans. 1*, **68**, 403 (1972).
(3) B. A. Morrow and I. A. Cody, *J. Phys. Chem.*, **77**, 1465 (1973).
(4) B. A. Morrow and P. Ramamurthy, *J. Phys. Chem.*, **77**, 3052 (1973).
(5) G. A. Blomfield and L. H. Little, *Can. J. Chem.*, **51**, 1771 (1973).
(6) B. A. Morrow, *J. Chem. Soc., Faraday Trans. 1*, **70**, 1527 (1974).
(7) M. J. D. Low, *J. Catal.*, **32**, 103 (1974).
(8) J. Kunavicz, P. Jones, and J. A. Hockey, *Trans. Faraday Soc.*, **67**, 848 (1971).
(9) R. J. Peglar, F. H. Hampleton, and J. A. Hockey, *J. Catal.*, **20**, 309 (1971).
(10) E. Borello, A. Zecchine, and C. Morterra, *J. Phys. Chem.*, **71**, 2938, 2945 (1967).
(11) C. Clark-Monks and B. Ellis, *J. Colloid Interface Sci.*, **44**, 37 (1973).
(12) M. L. Hair and W. Hertl, *J. Phys. Chem.*, **73**, 2372 (1969).
(13) M. L. Hair and W. Hertl, *J. Phys. Chem.*, **77**, 2070 (1973).
(14) G. J. Young, *J. Colloid Interface Sci.*, **13**, 67 (1958).

Department of Chemistry
University of Ottawa
Ottawa, Canada K1N 6N5

B. A. Morrow*
I. A. Cody

Received January 6, 1975

Fragmentation of α-Alkoxyalkyl Radicals. An Electron Paramagnetic Resonance Study

Publication costs assisted by the Institut fur Strahlenchemie im Max-Planck-Institute für Kohlenforschung

Sir: From product studies of reactions involving α-alkoxyalkyl radicals it has been inferred[1-5] that in many cases these radicals undergo a C–O bond scission (β scission) to yield a carbonyl compound and an alkyl radical:

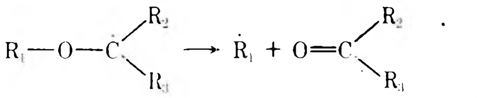

$$R_1{-}O{-}\dot{C}(R_2)(R_3) \rightarrow \dot{R}_1 + O{=}C(R_2)(R_3) \qquad (1)$$

An analogous fragmentation reaction has been observed to occur with α-dialkoxyalkyl and α-hydroxy-α-alkoxyalkyl radicals.[6-12]

So far, however, there have been no attempts to directly demonstrate the occurrence of reaction 1 by physical methods such as EPR. In previous EPR work on ether radicals, emphasis was placed on characterization of the primary radicals formed by H abstraction[13-17] and, with one notable exception involving the methyloxiranyl radical,[18] radicals formed by fragmentation of these species were not observed.

Product studies on the liquid-phase uv photolysis of *tert*-butyl methyl ether[19] and di-*tert*-butyl ether[4] at room temperature had indicated that the *tert*-butoxyisopropyl radical (R_1 = *tert*-butyl, R_2 = R_3 = methyl) fragments quantitatively according to (1) whereas the homologous *tert*-butoxymethyl radical (R_1 = *tert*-butyl, R_2 = R_3 = H) is stable with respect to fragmentation under these conditions. EPR studies were expected to yield supporting information on this and analogous systems.

Alkoxyalkyl radicals were produced by photolyzing di-*tert*-butyl peroxide (3 vol %) in benzene containing 5–7.5 vol % of the ethers **1–10** (Table I). The photolytically formed *tert*-butoxy radicals abstract hydrogen from the ethers to yield *t*-BuOH and α-alkoxyalkyl radicals which may be stable under the experimental conditions or fragment according to (1). The results obtained with various ethers are summarized in Table I. In the series of *tert*-butyl ethers (**1–3**) the radical derived from **1** does not fragment at 30° whereas with **3** only the fragment radical is observed at the lowest attainable temperature of 0°. **2** occupies its expected place in this series, the primary radical being the only one observable at 0° whereas considerable fragmentation is found at 30°. It is suggested that (a) F and B strain[20] in the primary radical and (b) the stabilizing influence of the alkyl group on the carbonyl bond of the fragmentation product are responsible for this trend. Concerning the latter, it may be estimated by Benson's method of group increments[21] that the stabilization of the carbonyl group effected by substituting CH_3 for H in formaldehyde (i.e., in going from formaldehyde to acetone) is of the order of 3.8 kcal/mol. From this it may be inferred that the rate of fragmentation of the primary species derived from **3** should be between 100 and 1000 times larger than that of the primary radical derived from **1**.

The primary radicals formed on H abstraction from the cumyl ethers **4** and **5** begin to show fragmentation at 0° (Figure 1). In this series, the fragmentation process is clear-

TABLE I: Radicals Observed on H Abstraction from Various Ethers

No.	Ether	Temp. °C	Radicals detected	Structure	Coupling constants, mT
1	t-BuOCH$_3$	0 and 30	t-BuO$\dot{C}$H$_2$	t-BuO$\dot{C}$H$_2$	$a_\alpha = 1.66(2)$, $a_{CH_3} = 0.03(9)$
2	t-BuOCH$_2$CH$_3$	0	t-BuO$\dot{C}$HCH$_3$	t-BuO$\dot{C}$HCH$_3$	$a_\alpha = 1.35$, $a_\beta = 2.16(3)$, $a_{CH_3} = 0.02(9)$
		30	t-BuO$\dot{C}$HCH$_3$, (CH$_3$)$_3\dot{C}$	(CH$_3$)$_3\dot{C}$	$a_\beta = 2.27(9)$
3	t-BuOCH(CH$_3$)$_2$	0	(CH$_3$)$_3\dot{C}$	(CH$_3$)$_3\dot{C}$	$a_\beta = 2.27(9)$
4	PhC(CH$_3$)$_2$OCH$_3$	0 and 30	PhC(CH$_3$)$_2$O$\dot{C}$H$_2$, Ph$\dot{C}$(CH$_3$)$_2$	PhC(CH$_3$)$_2$O$\dot{C}$H$_2$	$a_\alpha = 1.70(2)$
				Ph$\dot{C}$(CH$_3$)$_2$	$a_\beta = 1.60(6)$, $a_o = 0.47(2)$, $a_m = 0.16(2)$, $a_p = 0.55$
5	PhC(CH$_3$)$_2$OCH$_2$CH$_3$	0 and 30	PhC(CH$_3$)$_2$O$\dot{C}$HCH$_3$, Ph$\dot{C}$(CH$_3$)$_2$	PhC(CH$_3$)$_2$O$\dot{C}$HCH$_3$	$a_\alpha = 1.42$, $a_\beta = 2.19(3)$
6	PhCH$_2$OCH$_2$Ph	0 and 30	Ph$\dot{C}$HOCH$_2$Ph	Ph$\dot{C}$HOCH$_2$Ph	$a_\alpha = 1.52$, $a_{OCH_2} = 0.14(2)$, $a_1 = 0.15_7$, $a_2 = 0.16_3$, $a_3 = 0.46$, $a_4 = 0.51$, $a_5 = 0.58$
7	PhCH$_2$OCH$_3$	0 and 30	Ph$\dot{C}$HOCH$_3$	Ph$\dot{C}$HOCH$_3$	$a_\alpha = 1.51$, $a_{OCH_3} = 0.14(3)$, $a_1 = 0.15$, $a_2 = 0.16$, $a_3 = 0.45$, $a_4 = 0.50$, $a_5 = 0.57$
8	PhCH$_2$OCH$_2$CH$_3$	0 and 30	Ph$\dot{C}$HOCH$_2$CH$_3$, Ph$\dot{C}$H$_2$	Ph$\dot{C}$HOCH$_2$CH$_3$	$a_\alpha = 1.52$, $a_{OCH_2} = 0.14(2)$, $a_1 = 0.15_5$, $a_2 = 0.16_5$, $a_3 = 0.45$, $a_4 = 0.50$, $a_5 = 0.58$
				Ph$\dot{C}$H$_2$	$a_\alpha = 1.63(2)$, $a_o = 0.51(2)$, $a_m = 0.18(2)$, $a_p = 0.62$
9	PhCH$_2$OCH(CH$_3$)$_2$	0 and 30	Ph$\dot{C}$HOCH(CH$_3$)$_2$, Ph$\dot{C}$H$_2$	Ph$\dot{C}$HOCH(CH$_3$)$_2$	$a_\alpha = 1.51$, $a_{OCH<} = 0.10$, $a_{CH_3} = 0.01(6)$ $a_1 = 0.15_5$, $a_2 = 0.16_5$, $a_3 = 0.45$, $a_4 = 0.50$, $a_5 = 0.58$
10	Ph$_3$COCH$_3$	5	Ph$_3\dot{C}$	Ph$_3\dot{C}$	$a_o = 0.25(6)$, $a_m = 0.11(6)$, $a_p = 0.28(3)$

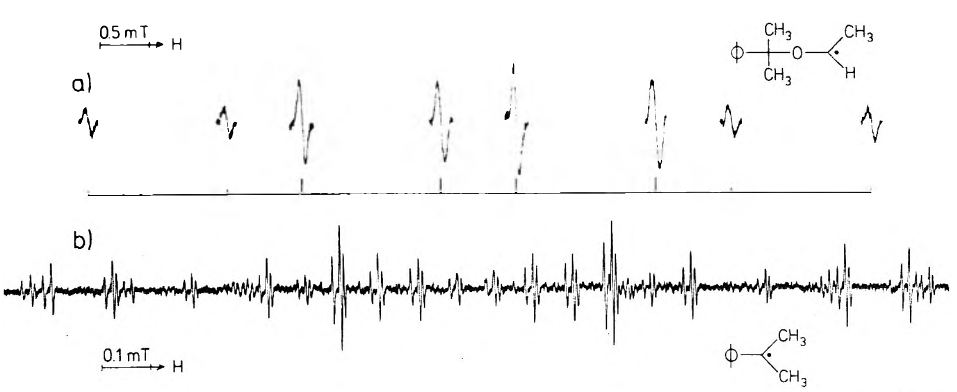

Figure 1. Radicals observed on H abstraction from cumyl ethyl ether in benzene at 0°: (a) spectrum of $PhC(CH_3)_2O\dot{C}HCH_3$ recorded at 1-mW microwave power and 0.05 mT modulation amplitude; (b) central part of the spectrum of $Ph\dot{C}(CH_3)_2$ showing second-order structure. The spectrum was recorded using a microwave power of 0.2 mW and a modulation amplitude of 0.004 mT.

ly facilitated by resonance stabilization of the product radical which amounts to more than 11.2 kcal/mol.[22,23] The effect is even more pronounced with the radical produced from **10** which shows complete fragmentation at 5°. With the primary radical from **5** the activation energy of fragmentation was determined, using the method described by Hamilton and Fischer,[24] to be 8 ± 1 kcal/mol.

In the series of benzyl ethers (**6–9**) fragmentation does not seem to occur if the primary radical is of the benzyl type. With **7**, exclusive H abstraction at the benzylic carbon is observed. With **8** and **9**, however, H abstraction from the ethyl and isopropyl groups, respectively, seems to take place in addition to H abstraction from the benzylic carbon. This is concluded from the presence of the fragmentation products of the expected primary radicals. The latter radicals could not be identified unambiguously due to interference with the intense lines from the benzyl type radicals.

References and Notes

(1) C. Walling and M. F. Mintz, *J. Am. Chem. Soc.*, **89**, 1515 (1967).
(2) C. Walling and J. A. McGuiness, *J. Am. Chem. Soc.*, **91**, 2053 (1969).
(3) J. W. Timberlake and M. L. Hodges, *Tetrahedron Lett.*, 4147 (1970).
(4) H.-P. Schuchmann and C. von Sonntag, *Tetrahedron*, **29**, 3351 (1973).
(5) M. E. Snook and G. A. Hamilton, *J. Am. Chem. Soc.*, **96**, 860 (1974).
(6) E. S. Huyser, *J. Org. Chem.*, **25**, 1820 (1960).
(7) E. S. Huyser and D. T. Wang, *J. Org. Chem.*, **27**, 4616 (1962).
(8) E. S. Huyser and D. T. Wang, *J. Org. Chem.*, **29**, 2720 (1964).
(9) V. Hartmann, C. von Sonntag, and D. Schulte-Frohlinde, *Z. Naturforsch. B*, **25**, 1394 (1970).
(10) B. Maillard, M. Cazaux, and R. Lalande, *Bull. Soc. Chem. Fr.*, 467 (1971).
(11) C. von Sonntag and M. Dizdaroglu, *Z. Naturforsch. B*, **28**, 367 (1973).
(12) C. von Sonntag, K. Neuwald, and M. Dizdaroglu, *Radiat. Res.*, **58**, 1 (1974).
(13) P. L. Kolker, J. Chem. Soc., 5929 (1964).
(14) P. L. Kolker and W. A. Waters, *J. Chem. Soc.*, 1136 (1964).
(15) W. T. Dixon, R. O. C. Norman, and A. Buley, *J. Chem. Soc.*, 3625 (1964).
(16) L. E. Burchill and P. W. Jones, *Can. J. Chem.*, **49**, 4005 (1971).
(17) A. Hudson and K. D. J. Root, *Tetrahedron*, **25**, 5311 (1969).
(18) G. Behrens and D. Schulte-Frohlinde, *Angew. Chem.*, **85**, 993 (1973); *Angew. Chem., Int. Ed. Engl.*, **12**, 932 (1973).
(19) H.-P. Schuchmann and C. von Sonntag, *Tetrahedron*, **29**, 1811 (1973).
(20) C. Rüchardt, *Angew. Chem.*, **82**, 845 (1970).
(21) S. W. Benson, "Thermochemical Kinetics", Wiley, New York, N.Y., 1968, p 180.
(22) D. J. Bogan and D. W. Setser, *J. Am. Chem. Soc.*, **96**, 1950 (1974).
(23) R. Walsh, D. M. Golden, and S. W. Benson, *J. Am. Chem. Soc.*, **88**, 650 (1966).
(24) E. J. Hamilton and H. Fischer, *Helv. Chim. Acta*, **56**, 795 (1973).

Institut für Strahlenchemie
im Max-Planck-Institut für Kohlenforschung
D-433 Mülheim/Ruhr
West Germany

S. Steenken*
H.-P. Schuchmann
C. von Sonntag

Received October 10, 1974

PHYSICAL PHENOMENA

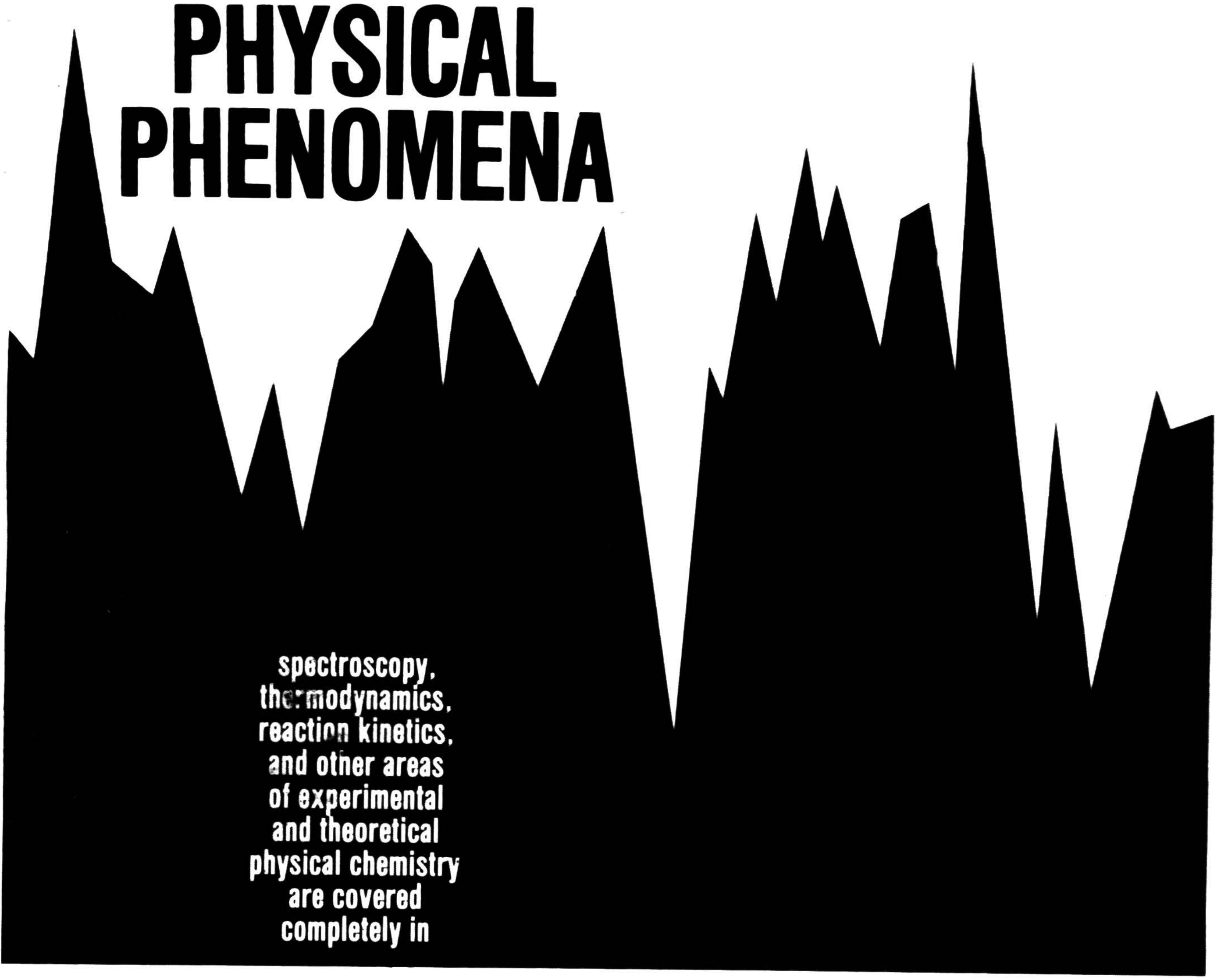

spectroscopy,
thermodynamics,
reaction kinetics,
and other areas
of experimental
and theoretical
physical chemistry
are covered
completely in

THE JOURNAL OF PHYSICAL CHEMISTRY

The biweekly JOURNAL OF PHYSICAL CHEMISTRY includes over 25 papers an issue of original research by many of the world's leading physical chemists. Articles, communications, and symposia cover new concepts, techniques, and interpretations. A "must" for those working in the field or interested in it, the JOURNAL OF PHYSICAL CHEMISTRY is essential for keeping current on this fast moving discipline. Complete and mail the coupon now to start your subscription to this important publication.

The Journal of Physical Chemistry
American Chemical Society
1155 Sixteenth Street, N.W.
Washington, D.C. 20036

1975

Yes, I would like to receive the JOURNAL OF PHYSICAL CHEMISTRY at the one-year rate checked below:

	U.S.	*Canada***	*Latin America***	*Other Nations***
ACS Member One-Year Rate*	☐ $20.00	☐ $24.50	☐ $24.50	☐ $25.00
Nonmember	☐ $80.00	☐ $84.50	☐ $84.50	☐ $85.00

Bill me ☐ Bill company ☐ Payment enclosed ☐

Air freight rates available on request.

Name ____________________

Street ____________________ Home ☐ Business ☐

City ____________ State ____________ Zip ____________

Journal subscriptions start on January '75

*NOTE: Subscriptions at ACS member rates are for personal use only. **Payment must be made in U.S. currency, by international money order, UNESCO coupons, U.S. bank draft, or order through your book dealer.

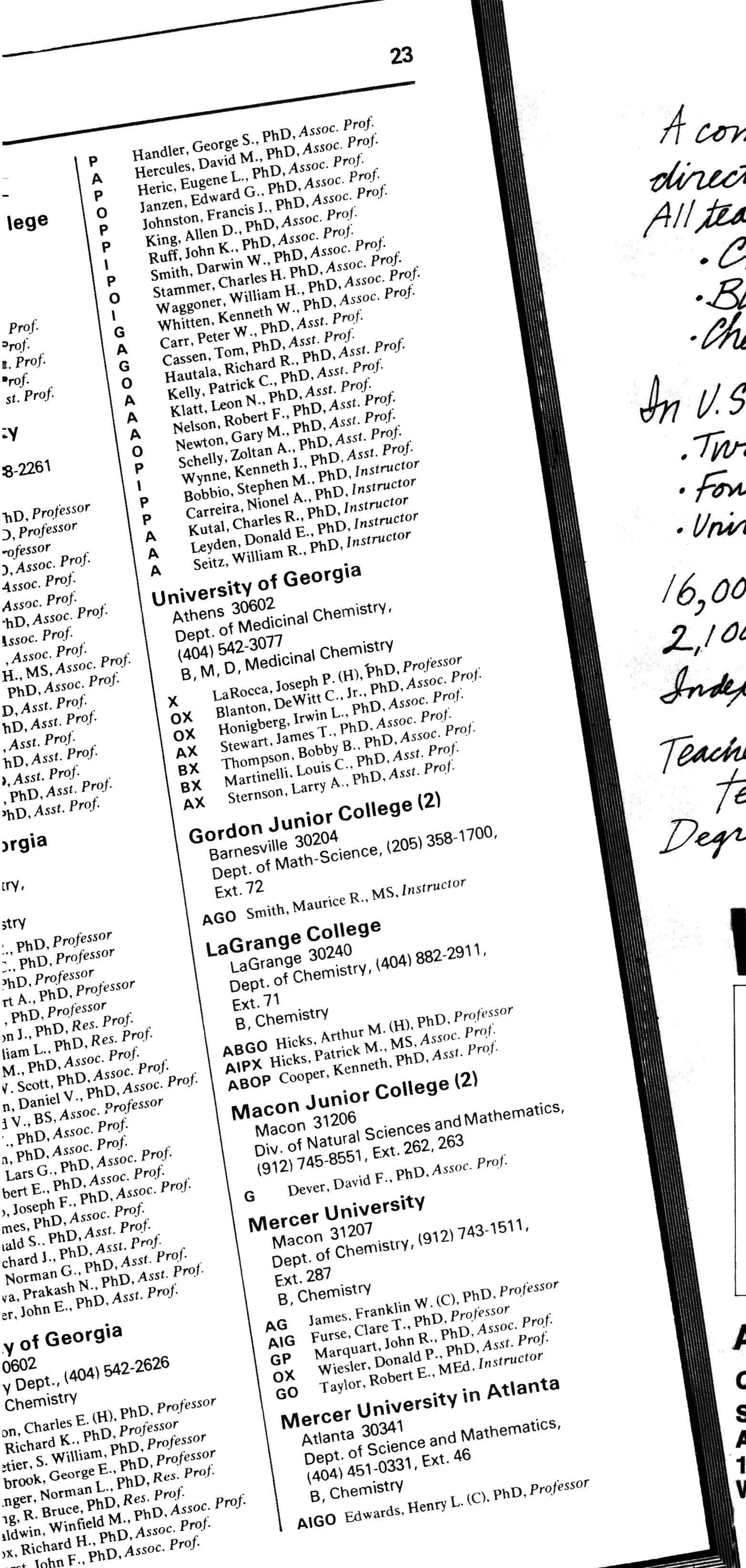

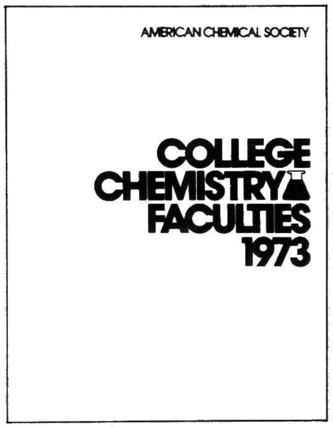
AMERICAN CHEMICAL SOCIETY
COLLEGE CHEMISTRY FACULTIES 1973